université PARIS-SACLAY

Design and Optimization of Higher Order Mode Couplers for the Superconducting Cavities of the PERLE Energy Recovery Linac

Conception et optimisation de coupleurs de modes d'ordre supérieur pour les cavités supraconductrices de l'accélérateur à récupération d'énergie PERLE

Thèse de doctorat de l'université Paris-Saclay

École doctorale n° 576, Particules, Hadrons, Énergie et Noyau : Instrumentation, Imagerie, Cosmos et Simulation (PHENIICS)
Spécialité de doctorat : Physique des accélérateurs

Graduate school : Physique. Référent : Faculté des sciences d'Orsay

Thèse préparée dans l'unité de recherche **IJCLab** (Université Paris-Saclay/CNRS), sous la direction de **Fabian ZOMER**, Professeur, Université Paris-Saclay, le co-encadrement de **Guillaume OLRY**, Ingénieur de recherche, IJCLab, **Patricia DUCHESNE**, Ingénieure de recherche, IJCLab, et **Haipeng WANG**, Chercheur, Jefferson Lab

Thèse soutenue à Paris-Saclay, le 21 octobre 2024, par

Carmelo Barbagallo

Composition du Jury

Membres du jury avec voix délibérative

Achille STOCCHI Professeur, Université Paris-Saclay	Président
Ursula VAN RIENEN Professeure, Universität Rostock	Rapporteure & Examinatrice
Carsten WELSCH Professeur, University of Liverpool	Rapporteur & Examinateur
Enrico CENNI Chercheur, CEA Saclay IRFU/DACM	Examinateur
Anne-Marie VALENTE-FELICIANO Chercheuse, Jefferson Lab	Examinatrice

université PARIS-SACLAY

ÉCOLE DOCTORALE
Particules, hadrons, énergie et noyau : instrumentation, imagerie, cosmos et simulation (PHENIICS)

Titre: Conception et optimisation de coupleurs de modes d'ordre supérieur pour les cavités supraconductrices de l'accélérateur à récupération d'énergie PERLE

Mots clés: PERLE, ERL, BBU, coupleurs HOM, impédance, mesures RF

Résumé: PERLE (Powerful Energy Recovery Linac for Experiments) est un accélérateur linéaire à récupération d'énergie (ERL) basé sur la technologie à cavité radiofréquence supraconductrice qui sera installé au Laboratoire de Physique des 2 Infinis Irène Joliot-Curie (IJCLab) en France. Avec une puissance de faisceau cible de 10 MW, PERLE vise à démontrer le fonctionnement multi-tour à haute intensité en onde continue pour valider des options pour les futures machines à haute énergie, telles que l'ERL de 50 GeV proposé pour LHeC (Large Hadron electron Collider) et FCC-eh (Future Circular electron-hadron Collider), et à accueillir des expériences dédiées en physique des particules et en nucléaire. Dans les ERLs à haute intensité, l'instabilité de Beam Breakup (BBU), résultant de l'interaction entre le faisceau et les modes d'ordre supérieur (HOMs) des cavités, est une préoccupation majeure pour un fonctionnement stable. Les HOMs induits par le faisceau peuvent augmenter la charge thermique de la cavité à température cryogénique et causer des instabilités du faisceau. Des coupleurs HOM sont installés dans les tubes de faisceau de la cavité pour absorber l'énergie des HOMs et atténuer ces effets. Cette thèse présente la conception et l'optimisation de plusieurs coupleurs HOM coaxiaux pour les cavités elliptiques en Nb avec 5 cellules à 801,58 MHz de la configuration PERLE ERL à 500 MeV. La transmission RF des coupleurs HOM a été optimisée pour améliorer l'amortissement des HOMs les plus dangereux. Les coupleurs HOM optimisés ont été intégrés dans des groupes d'extrémité pour simuler leur performance d'amortissement et leur comportement thermique. Les coupleurs HOM optimisés ont été imprimés en 3D en époxy et revêtus de cuivre. Des mesures RF à faible puissance ont été effectuées sur les coupleurs HOM produits installés dans des cavités en cuivre de type PERLE pour valider leur performance d'amortissement et proposer plusieurs groupes d'extrémité pour la cavité PERLE avec 5 cellules afin d'atténuer les HOMs en dessous des limites d'instabilité BBU.

Title: Design and Optimization of Higher Order Mode Couplers for the Superconducting Cavities of the PERLE Energy Recovery Linac

Keywords: PERLE, ERL, BBU, HOM couplers, Impedance, RF measurements

Abstract: The Powerful Energy Recovery Linac for Experiments (PERLE) is an energy recovery linac (ERL) facility based on superconducting radio-frequency (SRF) technology to be hosted at the Laboratoire de Physique des 2 Infinis Irène Joliot-Curie (IJCLab) in France. With a target beam power of 10 MW, PERLE aims to demonstrate the high-current, continuous wave, multi-pass operation to validate options for future high-energy machines, such as the 50 GeV ERL proposed for the Large Hadron electron Collider (LHeC) and the Future Circular electron-hadron Collider (FCC-eh), and host dedicated particle physics and nuclear experiments. In high-current ERLs, the regenerative Beam Breakup (BBU), emerging from the beam and cavity Higher Order Modes (HOMs) interaction, is a major concern for their stable operation. Beam-induced HOMs can increase the cavity heat load at cryogenic temperature and cause beam instabilities. HOM couplers are installed in the cavity beam pipes to absorb HOM energy and mitigate these effects. This thesis presents the design and optimization of several coaxial HOM couplers for the 5-cell 801.58 MHz elliptical Nb cavities of the 500 MeV PERLE ERL configuration. The RF transmission of the HOM couplers was optimized to enhance the damping of the most dangerous HOMs. The optimized HOM couplers were integrated into endgroups to simulate their damping performance and thermal behavior. The optimized HOM couplers were 3D-printed in epoxy and copper-coated. Low-power RF measurements were conducted on the produced HOM couplers installed in copper PERLE-type cavities to validate their damping performance and propose several endgroups for the PERLE 5-cell cavity to mitigate HOMs below the BBU instability limits.

To Giuliana

Acknowledgements

I would like to thank my supervisors at IJCLab, Fabian Zomer, Guillaume Olry, and Patricia Duchesne, for granting me the opportunity to pursue this thesis and for their support and guidance. I also wish to thank Walid Kaabi and Achille Stocchi for giving me the opportunity to work on the PERLE project.

My special gratitude goes to Haipeng Wang, my PhD advisor at JLab, for his enduring guidance, patience, foresight, and encouragement throughout my academic journey. The countless discussions and his invaluable experience have enabled me to develop my career in the field of accelerator physics. I am also grateful to Robert Rimmer from JLab for his keen interest in my PhD work, valuable suggestions, and support.

During the exceptional time being part of Radio-Frequency Group at JLab for conducting HOM measurements, I deeply appreciated the full support of Gunn-Tae Park, Jiquan Guo, Sarah Overstreet, James Henry, Steve Castagnola, Gregory Grose, Eduard Drachuk, Mingqi Ge, Anne-Marie Valente-Feliciano, Gianluigi Ciovati, Vince Pope and all the colleagues from the machine shop and Superconducting Radio-Frequency structure lab who accommodated all my needs. A special gratitude appertains to Sadiq Setiniyaz for having helped me through numerous discussions on beam dynamics analyses and his friendly support.

I am grateful to my CERN colleagues who collaborated on my PhD projects. I thank Shahnam Gorgi Zadeh for numerous insightful discussions in numerical simulations. I have appreciated the support of Frank Gerigk, Simon Barrière, Romain Gérard, Sebastien Clement, Pierre Maurin, Olivier Choisnet, and Jean-Philippe Rigaud for their contributions to the production of the HOM coupler prototypes at CERN.

My thanks also extend to my former colleagues at IJCLab, Gilles Olivier and Samuel Roset, and all others who directly or indirectly supported my PhD thesis. I especially acknowledge Luc Perrot for his guidance, support, and insightful discussions, and for his meticulous review of my thesis over several months.

I am deeply thankful to my parents, Antonino and Giuseppina, and my sister, Cristina, for their emotional support. Above all, my immeasurable gratitude goes to my wife, Giuliana, my better half, my best friend, and the love of my life. She not only encouraged me to pursue a PhD but also accompanied and sustained me through every challenge over the years with her invaluable love.

Contents

Acronyms **viii**

Introduction **1**

1 Electromagnetic theory and RF cavity principles **5**
1.1 Maxwell's equations . . . 5
1.1.1 Material equations . . . 6
1.1.2 Wave equations . . . 7
1.1.3 Helmholtz equations . . . 8
1.2 RF fields in cavities . . . 10
1.2.1 Eigenmodes of a pillbox cavity . . . 11
1.2.2 Eigenmodes of an elliptical cavity . . . 14
1.3 Figures of merit for RF cavities . . . 16
1.3.1 Fundamental mode frequency . . . 16
1.3.2 Lorentz force and voltage . . . 17
1.3.3 Geometric shunt impedance . . . 18
1.3.4 Cavity impedance . . . 20
1.3.5 Loss factor . . . 20
1.3.6 Power dissipation and surface resistance . . . 21
1.3.7 Quality factor . . . 23

2 RF cavity design for PERLE **27**
2.1 The PERLE accelerator . . . 27
2.2 The PERLE elliptical cavity . . . 30
2.2.1 RF design parameters of the cavity . . . 31
2.2.2 HOMs of the cavity . . . 37
2.3 Static and dynamic heat losses . . . 40
2.4 Input RF power . . . 42
2.4.1 Optimization with respect to tuning for energy recovery . . . 42
2.4.2 Optimization with respect to cavity coupling for energy recovery 44
2.4.3 Input power for the PERLE cavity . . . 44

3 Beam breakup instability studies **49**
3.1 Beam breakup instabilities . . . 49
3.2 Beam breakup instability thresholds . . . 50
3.2.1 Transfer Matrix . . . 50
3.2.2 Threshold current . . . 51
3.2.3 Impedance threshold . . . 52
3.2.4 Critical external quality factor . . . 53
3.3 Regenerative BBU studies in PERLE . . . 54
3.3.1 Impedance and external quality factor requirements . . . 55
3.3.2 Maximum achievable current . . . 57
3.3.3 BBU-tracking model . . . 59

4 HOM coupler design and fabrication **63**
4.1 HOM couplers . . . 63
4.1.1 Coaxial HOM couplers . . . 65
4.1.2 Waveguide couplers . . . 67
4.1.3 Beamline absorbers . . . 68
4.1.4 HOM coupler selection for PERLE . . . 69
4.2 Coaxial HOM coupler optimization . . . 69
4.2.1 Optimization method for RF transmission . . . 70
4.2.2 Probe-type PERLE coupler . . . 73
4.2.3 Hook-type PERLE coupler . . . 78
4.2.4 DQW-type PERLE coupler . . . 83
4.2.5 Summary of HOM coupler optimization results . . . 88
4.3 HOM coupler prototyping . . . 89
4.3.1 Mechanical design for coaxial HOM couplers . . . 89
4.3.2 3D printing for HOM coupler fabrication . . . 90
4.3.3 Copper electroplating of epoxy-based HOM couplers . . . 92
4.3.4 3D-scanning measurements on HOM couplers . . . 94
4.3.4.1 3D-scanning of the hook-type coupler prototype . . . 94
4.3.4.2 3D-scanning of the probe-type coupler prototype . . . 96
4.3.4.3 3D-scanning of the DQW coupler prototype . . . 101
4.3.5 Niobium 3D-printed HOM couplers . . . 107

5 HOM-damping and RF-heating analyses **109**
5.1 Numerical methods for impedance calculation . . . 109
5.1.1 Wakefields and wake impedance . . . 110
5.1.2 Eigenmode impedance . . . 113
5.2 Beam-induced HOM power calculation . . . 114
5.2.1 HOM power in damped RF cavities . . . 114
5.2.2 Propagation of HOM power through the cavity ports . . . 118
5.3 Five-cell cavity at 801.58 MHz for PERLE . . . 119

5.3.1 Longitudinal and transversal impedance . . . 122
5.3.2 Average HOM power . . . 124
5.3.3 HOM power . . . 125
5.3.3.1 Five-cell cavity with coaxial HOM-couplers . . . 125
5.3.3.2 Five-cell cavity with coaxial HOM-couplers and BLAs 127
5.4 RF-heating analyses on coaxial HOM coupler . . . 132
5.4.1 Heat transfer in cavities and couplers . . . 133
5.4.2 Dynamic heat load on the HOM coupler . . . 134
5.4.2.1 Electric and magnetic fields . . . 137
5.4.2.2 Power deposition and maximum temperature . . . 140

6 RF cavity fabrication 147
6.1 Elliptical cavity manufacturing . . . 147
6.1.1 Deep-drawing . . . 147
6.1.2 Springback effect and coining . . . 149
6.2 Dumbbell measurements . . . 152
6.2.1 Dumbbell measuring setup . . . 152
6.2.2 Theoretical framework for dumbbell measurements . . . 153
6.2.3 Target frequency and trimming coefficient simulations . . . 155
6.2.4 Trimming measurement summary . . . 158
6.3 Cavity assembly . . . 159
6.4 Bead-pull measurements . . . 160

7 RF measurements on PERLE HOM couplers and cavities 165
7.1 Theoretical background for RF measurements of cavity modes . . . 165
7.1.1 Coupler basic parameters . . . 166
7.1.1.1 Undriven cavity . . . 167
7.1.1.2 Driven cavity . . . 168
7.1.1.3 Scattering matrix . . . 170
7.1.2 HOM measurements for a cavity with a HOM coupler . . . 171
7.1.2.1 Theoretical framework . . . 172
7.1.2.2 HOM measurement procedure . . . 173
7.2 Low power RF measurements on 801.58 MHz cavities . . . 175
7.2.1 The measurement setup . . . 176
7.2.2 2-cell elliptical copper cavity . . . 177
7.2.2.1 Frequency spectrum and deviation . . . 178
7.2.2.2 Probe-type coupler: HOM measurements and simulations 180
7.2.2.3 Hook-type coupler: HOM measurements and simulations 183
7.2.2.4 DQW-type coupler: HOM measurements and simulations 186
7.2.2.5 Influence of the coupler antenna tilt . . . 188
7.2.2.6 Summary of the HOM measurement results for the 2-cell cavity . . . 190

7.2.3 5-cell elliptical copper cavity 191
7.2.3.1 Frequency spectrum and deviation 191
7.2.3.2 Bead-pull measurements 195
7.2.3.3 Unloaded quality factor 196
7.2.3.4 HOM-damping measurements and simulations 198

Conclusions and perspectives **203**

A 5-cell cavity and HOM couplers for PERLE **207**

Symbols **213**

Bibliography **245**

Résumé étendu en français **247**

Acronyms

AC	Alternating Current
ALICE	Accelerators and Lasers In Combined Experiments
BP	Beam pipe
BBU	Beam Breakup
BCS	Bardeen-Cooper-Schrieffer
BLA	Beamline absorber
BNL	Brookhaven National Laboratory
CAD	Computer-Aided Design
CBETA	Cornell-BNL ERL Test Accelerator
CDR	Conceptual Design Report
CEBAF	Continuous Electron Beam Accelerator Facility
cERL	Compact ERL
CERN	Conseil Européen pour la Recherche Nucléaire
Cu	Copper
CW	Continuous Wave
DC	Direct Current
DQW	Double Quarter Wave
EBW	Electron Beam Welding
EM	Electromagnetic
eRHIC	Electron-Relativistic Heavy Ion Collider
ERL	Energy Recovery Linac
FCC-ee	Future Circular electron-positron Collider
FCC-eh	Future Circular electron-hadron Collider
FEL	Free Electron Laser
FEM	Finite Element Method
FIT	Finite Integration Technique
FM	Fundamental Mode
FP	Field Probe
FPC	Fundamental Power Coupler
He	Helium
HL-LHC	High-Luminosity LHC
HOM	Higher Order Mode
HTR	High-Heat Resistant

IC	Inner Conductor
ICB	The Carnot de Bourgogne Interdisciplinary Laboratory
ID	Identity
IJCLab	Laboratoire de Physique des 2 Infinis Irène Joliot-Curie
IP	Interaction Point
IR	Infrared
JLab	Jefferson Lab
KEK	High Energy Accelerator Research Organization
LANL	Los Alamos National Laboratory
LHC	The Large Hadron Collider
LHeC	The Large Hadron electron Collider
LINAC	Linear Accelerator
MESA	Mainz Energy-recovering Superconducting Accelerator
Nb	Niobium
Nb_3Sn	Niobium-Tin
OC	Outer Conductor
OFHC	Oxygen-Free High Thermal Conductivity
PEC	Perfect Electric Conductor
PMC	Perfect Magnetic Conductor
PERLE	Powerful Energy Recovery Linac for Experiments
R&D	Research and Development
RF	Radio Frequency
RMS	Root Mean Square
RRR	Residual Resistivity Ratio
SC	Superconducting
SCA	Superconducting Accelerator
S-DALINAC	Superconducting Darmstadt Electron Linear Accelerator
SiC	Silicon carbide
SiC-W	Silicon carbide to Tungsten braze
SP	Sequence Preserving
SPL	Superconducting Proton Linac
SR	Synchrotron Radiation
SRF	Superconducting Radio Frequency
TE	Transverse Electric
TEM	Transverse Electromagnetic
TM	Transverse Magnetic
UV	Ultraviolet
VNA	Vector Network Analyzer
W-Ti	Tungsten to Titanium braze
WG	Waveguide
4DQW	Four DQW couplers
2P2H	Two Probe and two Hook couplers

Introduction

Particle accelerators have been extensively employed throughout the 20th century in various fields, including industry, medicine, and fundamental research. Notable applications include Synchrotron Radiation (SR) X-ray sources and Free Electron Lasers (FELs), which generate photon beams for studies in atomic and molecular physics and biology, in addition to hadron and electron-ion colliders for nuclear and particle physics research. Historically, storage rings have fulfilled the demand for highly coherent, high-average-brightness photon beams [1]. Nevertheless, their performance is limited by the equilibrium between radiation damping and quantum excitation, which limits the minimum achievable emittance and bunch length. Linear accelerators (Linacs) can produce beams with low emittance, small energy spread, and a short bunch length. However, their usage is limited to accelerating low average current beams (on the order of mA or less) due to the expensive radio-frequency (RF) power requirements. Nowadays, Energy Recovery Linacs (ERLs) are an attractive accelerator concept for generating high-current electron beams with significantly reduced RF power requirements compared to traditional linacs [2]. ERLs combine the efficiency comparable to a storage ring with the superior beam characteristics of a linac, positioning them as a promising option for a number of applications in future light sources.

The notion of energy recovery was introduced by M. Tigner [3] in 1965, initially for its implementation in a collider. It is based on the principle that RF cavity fields, by properly timing the arrival of electron bunches in the linac, can accelerate and decelerate the same beam [2]. The simplest layout of an ERL involves a single recirculation. An electron beam is injected into the linac from a high-brightness photo-injector and accelerated through RF cavities. If the recirculation path length is designed to be an integer plus half of the RF accelerating field wavelength, after being used, the beam returns to the linac 180° out of phase with respect to the RF field and is decelerated through the RF cavities. The energy of the decelerated beam is recovered and used to accelerate successive electron bunches. Subsequently, the decelerated beam exits the linac with an energy approximately equal to the injection energy and is directed to a beam dump. The decelerated beam cancels the beam-loading of the accelerated beam, enabling the acceleration of high-current beams with minimal RF power consumption.

In 1986, the concept of energy recovery was verified at the Stanford Superconducting Accelerator FEL (SCA/FEL) [4] and shortly thereafter at the Los Alamos National

Laboratory (LANL) FEL [5]. More recently, the Infrared Demonstration Free Electron Laser (IR Demo FEL) facility at the Jefferson Lab (JLab) has demonstrated the recirculation of a 5 mA beam up to 48 MeV of energy, producing 2.1 kW of IR light available for users [6]. The rebuild of its recirculation arcs and the increase of the electron energy enabled the recirculation of a 9 mA beam at up to 150 MeV [7]. The IR Upgrade FEL at JLab has operated with over 1.1 MW of beam power while requiring only about 300 kW of RF power [8], highlighting the emphasis on power saving as a motivation behind constructing an ERL [2]. In a time where energy sobriety is crucial and energy sustainability is vital for society, minimizing energy consumption is a priority challenge for future accelerators. Therefore, ERLs represent an essential step toward the future sustainability of high-energy physics applications.

Energy Recovery Linac landscape

The fundamentals of ERL technology have now been demonstrated globally. Since the first demonstration of energy recovery [4], several ERLs have been designed, constructed, and operated worldwide. The key parameters of an ERL are the electron beam current, which is proportional to the luminosity, and the beam power [9]. Figure 1 provides an overview of the worldwide past, present, and future proposed ERL facilities, comparing them based on electron beam energy and average beam current.

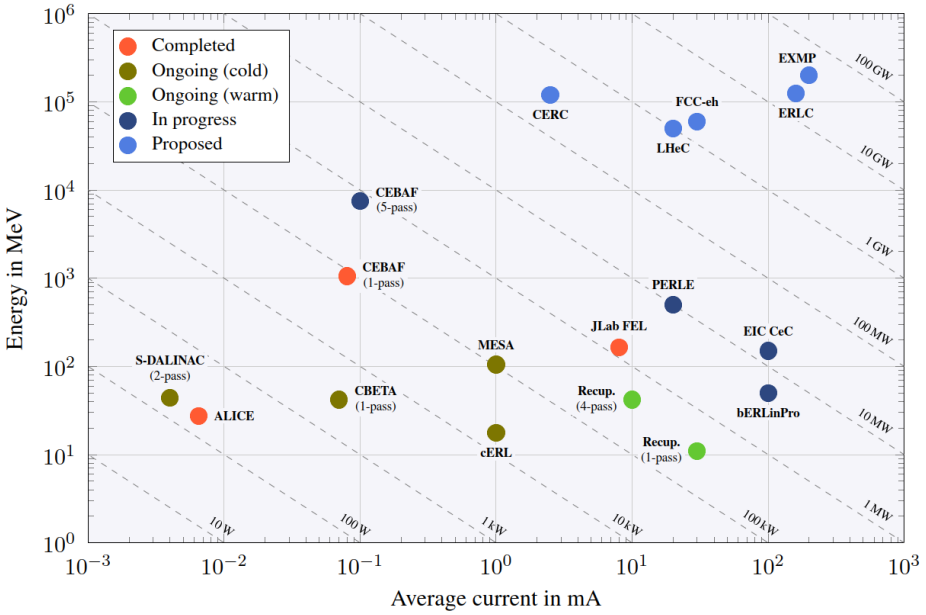

Figure 1: Overview of past, present, and future proposed worldwide ERL facilities. The illustration compares the ERLs based on the electron beam energy as a function of the beam current. Dashed diagonal lines represent the constant beam power. The figure is taken from [9] and falls under the Creative Commons Attribution 4.0 (CC BY 4.0) license (https://creativecommons.org/licenses/by/4.0/).

Three ERL facilities have been completed: the ALICE (Accelerators and Lasers In Combined Experiments) ERL [10] at Daresbury; the Continuous Electron Beam Accelerator Facility (CEBAF), a 1-pass ERL that has achieved the highest energy ever of 1 GeV [11, 12]; the JLab FEL [7], which has reached the highest current of 10 mA among all SRF ERLs. Nowadays, three ERLs operate with a beam power of up to hundreds of kilowatts: the Superconducting Darmstadt Electron Linear Accelerator (S-DALINAC) [13], the Cornell-BNL ERL Test Accelerator (CBETA) [14] at Cornell, and the compact ERL (cERL) [15] at KEK. The Mainz Energy-recovering Superconducting Accelerator (MESA) [16] is expected to have the first beam in the near future.

For the next generation of high-current ERLs, utilizing Superconducting Radio-Frequency (SRF) linac cavities is the most efficient solution to significantly reduce the power consumption [17, p. 45]. In the coming decades, four SRF ERL facilities are expected to be built to achieve beam power levels in the tens of megawatts and pave the way for developing and constructing gigawatts accelerator complexes for high-energy physics studies. In this context, the Powerful Energy Recovery Linac for Experiments (PERLE) [18], which is discussed in this thesis, is the only proposal for a multi-pass continuous wave (CW) ERL with 10 MW circulating beam power. The 20 mA electron beam will be boosted in energy through SRF cavities in three recirculation passes to achieve the target beam energy of 500 MeV. The PERLE facility is planned to be hosted at the Laboratoire de Physique des 2 Infinis Irène Joliot-Curie (IJCLab) in Orsay. It will serve as a demonstrator to gain the necessary experience required for the development of the Large Hadron-electron Collider (LHeC) [19, 20] at CERN. Furthermore, it will open the door for the next generation of compact and yet powerful ERLs suitable for applications requiring high-energy and high-current beams, such as inverse Compton scattering, high-energy ion cooling sources, and electron-ion colliders.

Motivation and aim of the thesis

In high-current multi-pass ERLs, such as PERLE, regenerative beam breakup (BBU) constitutes a performance-limiting phenomenon for stable operation [2]. This effect emerges from the interaction between the circulating electron beam and the parasitic excited cavity modes, known as Higher Order Modes (HOMs). Beam-induced monopole HOMs can increase the cryogenic load of the linac, while dipole HOMs can deflect the beam during subsequent ERL passes. To mitigate BBU, the upcoming generation of high-current ERL necessitates SRF cavities with strong HOM-damping requirements [21]. Nowadays, various concepts to damp potentially dangerous cavity HOMs can be used. Existing damping solutions primarily utilize coaxial and waveguide HOM couplers, beamline absorbers, or any of their combinations mounted on the cutoff beam pipe of the cavities to absorb HOMs.

This thesis aims to design, build, test, and analyze coaxial HOM couplers for the cavities of PERLE. The ultimate goal is to propose HOM-damping options to damp cavity HOMs and ensure the stable operation of the ERL. Several designs of coaxial

HOM couplers were analyzed and optimized based on the frequency spectrum of the PERLE cavity to meet BBU requirements. The performance of the HOM-damped cavity has been numerically evaluated. The optimized HOM couplers were fabricated, installed, and tested individually and as multi-coupler combinations at room temperature on PERLE-type cavity prototypes to assess their damping performances. Simulations were validated by comparing them with results obtained from the RF prototype measurements.

Structure of the thesis

Chapter 1 discusses the basic principles of the electromagnetic theory and RF cavities. Chapter 2 presents the PERLE accelerator complex and the 801.58 MHz 5-cell elliptical cavity proposed for its SRF linacs. The RF design parameters and the HOM spectrum of the PERLE cavity are discussed. The cavity's static and dynamic heat losses and its power requirements are also evaluated. The BBU instability phenomenon is presented in Chapter 3. The longitudinal and transverse impedance thresholds are calculated for the PERLE cavity, along with an estimate of the maximum achievable beam current.

Chapter 4 presents an overview of the existing HOM-damping mechanisms, such as HOM couplers and beamline absorbers, used to extract HOM power from the cavities. The optimization of the RF transmission of three designs of coaxial HOM couplers is described. The processes involved in 3D-printing and surface copper-coating techniques used to fabricate the optimized HOM couplers are detailed, along with the metrological measurements conducted on their primary components.

Chapter 5 first establishes a theoretical framework on longitudinal and transverse wake impedances and beam-induced HOM power. Numerical techniques employed to compute the above-mentioned quantities are also discussed. The optimized HOM couplers are combined in two different damping structures (or HOM endgroups) and compared in terms of impedance and HOM power extraction. HOM power absorption via beamline absorbers is also addressed. Finally, the dynamic heat load on the coupler surfaces is evaluated, and several cooling techniques are proposed to prevent the risk of loss of superconductivity in both the HOM couplers and the cavity.

Chapter 6 presents the first copper 5-cell 801.58 MHz PERLE-cavity prototype manufactured within the framework of this thesis to validate the HOM-damping performance of two HOM-coupler endgroups. The fabrication process and the geometrical deviations on the cavity cells due to manufacturing tolerances are described. Dumbbell measurements and the trimming process performed on the cells to tune the cavity to its operating frequency are also discussed. Additionally, bead-pull measurements performed on the 5-cell cavity are presented. Chapter 7 presents the low-power RF measurements conducted on the copper 2-cell and 5-cell 801.58 MHz PERLE-type cavities equipped with the manufactured HOM-couplers. The survey includes the frequency spectrum evaluation, bead-pull measurements of relevant HOMs, and measurements of the HOM-damping performance for the HOM coupler prototypes.

1 Electromagnetic theory and RF cavity principles

This chapter briefly introduces the foundations of electromagnetic field theory and presents the mathematical equations that govern the fields in RF cavities. The fundamental parameters that characterize the effectiveness of RF structures in accelerating particle bunches are introduced, with particular emphasis on SRF cavities.

1.1 Maxwell's equations

Maxwell's equations are a set of coupled partial differential equations that form the foundation of electromagnetic theory [22]. They describe the interdependence and variations of the electric and magnetic fields, charges, and currents over a given spatial domain $\mathbf{\Omega}$. The differential formulation of Maxwell's equations for general time-varying electromagnetic fields is provided by

$$\nabla \cdot \mathbf{D}(\mathbf{r}, t) = \rho(\mathbf{r}, t), \tag{1.1}$$

$$\nabla \cdot \mathbf{B}(\mathbf{r}, t) = 0, \tag{1.2}$$

$$\nabla \times \mathbf{E}(\mathbf{r}, t) = -\frac{\partial}{\partial t}\mathbf{B}(\mathbf{r}, t), \tag{1.3}$$

$$\nabla \times \mathbf{H}(\mathbf{r}, t) = \mathbf{J}(\mathbf{r}, t) + \frac{\partial}{\partial t}\mathbf{D}(\mathbf{r}, t), \tag{1.4}$$

where $\mathbf{D}(\mathbf{r}, t)$ denotes the electric flux density, $\rho(\mathbf{r}, t)$ the electric charge density, $\mathbf{B}(\mathbf{r}, t)$ the magnetic flux density, $\mathbf{E}(\mathbf{r}, t)$ the electric field strength, $\mathbf{H}(\mathbf{r}, t)$ the magnetic field strength and $\mathbf{J}(\mathbf{r}, t)$ the electric current density. The symbol $\nabla\cdot$ represents the divergence operator, which contains spatial derivatives, while $\nabla\times$ is the curl operator, which computes the rotation of a vector field around a point within a given domain. The electric current density $\mathbf{J}(\mathbf{r}, t)$ can be expressed as the combination of individual current densities produced by different sources, as follows [23, p. 2]

$$\mathbf{J}(\mathbf{r},t) = \mathbf{J}_\mathrm{c}(\mathbf{r},t) + \mathbf{J}_\mathrm{i}(\mathbf{r},t) = \sigma\mathbf{E}(\mathbf{r},t) + \mathbf{J}_\mathrm{i}(\mathbf{r},t). \tag{1.5}$$

Here, $\mathbf{J}_\mathrm{c}(\mathbf{r},t)$ is the conduction electric current density arising in materials with electric conductivity σ. $\mathbf{J}_\mathrm{i}(\mathbf{r},t)$ denotes the impressed electric current density provided by an external source, such as the beam current supplied to an accelerating cavity.

1.1.1 Material equations

To apply Maxwell's equations at a macroscopic level, it is necessary to establish the relationships between electromagnetic (EM) fields in material media [23, pp. 41-51]. The material equations describe the interaction between EM fields and matter as

$$\mathbf{D}(\mathbf{r},t) = \varepsilon_0\mathbf{E}(\mathbf{r},t) + \mathbf{P}(\mathbf{r},t), \tag{1.6}$$

$$\mathbf{B}(\mathbf{r},t) = \mu_0(\mathbf{H}(\mathbf{r},t) + \mathbf{M}(\mathbf{r},t)), \tag{1.7}$$

where $\varepsilon_0 \approx 8.854 \times 10^{-12}\,\mathrm{F/m}$ is the vacuum permittivity, $\mathbf{P}(\mathbf{r},t)$ the electric polarization vector, $\mu_0 \approx 4\pi \times 10^{-7}\,\mathrm{H/m}$ is the permeability of vacuum and $\mathbf{M}(\mathbf{r},t)$ the magnetic polarization vector. The electric polarization vector $\mathbf{P}(\mathbf{r},t)$ characterizes the electric polarization of a material in the presence of an external electric field. Conversely, the magnetic polarization vector $\mathbf{M}(\mathbf{r},t)$ represents the magnetic polarization of a material in the presence of an external magnetic field [24].

The polarization vectors $\mathbf{P}(\mathbf{r},t)$ and $\mathbf{M}(\mathbf{r},t)$ are related to the electric and magnetic fields, respectively, via the following expressions

$$\mathbf{P}(\mathbf{r},t) = \varepsilon_0\chi_\mathrm{e}\mathbf{E}(\mathbf{r},t), \tag{1.8}$$

$$\mathbf{M}(\mathbf{r},t) = \chi_\mathrm{m}\mathbf{H}(\mathbf{r},t), \tag{1.9}$$

where χ_e and χ_m are two dimensionless quantities referred to as electric susceptibility and magnetic susceptibility, respectively. Substituting the equation (1.8) into equation (1.6), and the equation (1.9) into equation (1.7), results in

$$\mathbf{D}(\mathbf{r},t) = \varepsilon_0\mathbf{E}(\mathbf{r},t) + \varepsilon_0\chi_\mathrm{e}\mathbf{E}(\mathbf{r},t) = \varepsilon_0\underbrace{(1+\chi_\mathrm{e})}_{\varepsilon_\mathrm{r}}\mathbf{E}(\mathbf{r},t), \tag{1.10}$$

$$\mathbf{B}(\mathbf{r},t) = \mu_0(\mathbf{H}(\mathbf{r},t) + \chi_\mathrm{m}\mathbf{H}(\mathbf{r},t)) = \mu_0\underbrace{(1+\chi_\mathrm{m})}_{\mu_\mathrm{r}}\mathbf{H}(\mathbf{r},t), \tag{1.11}$$

where ε_r and μ_r are the material-dependent relative permittivity and relative permeability, respectively. These are dimensionless quantities defined as

$$\varepsilon_\mathrm{r} = \frac{\varepsilon}{\varepsilon_0}, \tag{1.12}$$

$$\mu_\mathrm{r} = \frac{\mu}{\mu_0}, \tag{1.13}$$

where ε is the permittivity and μ is the permeability of the material. This leads to the constitutive relations for a linear material in its most common form

$$\mathbf{D}(\mathbf{r}, t) = \varepsilon \mathbf{E}(\mathbf{r}, t), \tag{1.14}$$

$$\mathbf{B}(\mathbf{r}, t) = \mu \mathbf{H}(\mathbf{r}, t). \tag{1.15}$$

These constitutive relations allow us to address free currents and charges exclusively without explicitly accounting for polarization vectors in the material. For homogeneous materials, the values of ε and μ remain constant throughout the material. In the case of isotropic materials, the quantities ε and μ are scalar values, while in anisotropic materials, they are represented by tensors. In the remainder of this thesis, the materials under investigation are assumed to be linear and homogeneous.

1.1.2 Wave equations

The resolution of both electric and magnetic field strengths can be achieved by uncoupling the equations (1.3) and (1.4) and raising them to second-order differential equations [23, p. 99]. First, the curl of both equations is taken, and then Schwarz's theorem is applied

$$\nabla \times \nabla \times \mathbf{E}(\mathbf{r}, t) = \nabla \times \left[-\frac{\partial}{\partial t} \mathbf{B}(\mathbf{r}, t) \right] = -\frac{\partial}{\partial t} \nabla \times \mathbf{B}(\mathbf{r}, t), \tag{1.16}$$

$$\nabla \times \nabla \times \mathbf{H}(\mathbf{r}, t) = \nabla \times \left[\mathbf{J}(\mathbf{r}, t) + \frac{\partial}{\partial t} \mathbf{D}(\mathbf{r}, t) \right] = \nabla \times \mathbf{J}(\mathbf{r}, t) + \frac{\partial}{\partial t} \nabla \times \mathbf{D}(\mathbf{r}, t). \tag{1.17}$$

The right-hand side of both equations can be simplified by employing equations (1.15) and (1.14) as follows

$$\nabla \times \nabla \times \mathbf{E}(\mathbf{r}, t) = -\mu \frac{\partial}{\partial t} \nabla \times \mathbf{H}(\mathbf{r}, t) = -\mu \frac{\partial}{\partial t} \mathbf{J}(\mathbf{r}, t) - \varepsilon \mu \frac{\partial^2}{\partial t^2} \mathbf{E}(\mathbf{r}, t), \tag{1.18}$$

$$\nabla \times \nabla \times \mathbf{H}(\mathbf{r}, t) = \nabla \times \mathbf{J}(\mathbf{r}, t) + \varepsilon \frac{\partial}{\partial t} \nabla \times \mathbf{E}(\mathbf{r}, t) = \nabla \times \mathbf{J}(\mathbf{r}, t) - \varepsilon \mu \frac{\partial^2}{\partial t^2} \mathbf{H}(\mathbf{r}, t). \tag{1.19}$$

Utilizing the following vector identity

$$\nabla \times (\nabla \times \mathbf{A}) = \nabla(\nabla \cdot \mathbf{A}) - \nabla^2 \mathbf{A}, \tag{1.20}$$

where ∇^2 is the Laplace operator applied to the vector field $\mathbf{A}$, and recalling (1.1) and (1.2) together with the constitutive relations for a homogeneous material, the equations (1.18) and (1.19) can be rewritten as

$$\nabla^2 \mathbf{E}(\mathbf{r}, t) - \varepsilon\mu \frac{\partial^2}{\partial t^2} \mathbf{E}(\mathbf{r}, t) = \mu \frac{\partial}{\partial t} \mathbf{J}(\mathbf{r}, t) + \frac{1}{\varepsilon} \nabla \rho(\mathbf{r}, t), \tag{1.21}$$

$$\nabla^2 \mathbf{H}(\mathbf{r}, t) - \varepsilon\mu \frac{\partial^2}{\partial t^2} \mathbf{H}(\mathbf{r}, t) = -\nabla \times \mathbf{J}(\mathbf{r}, t). \tag{1.22}$$

Equations (1.21) and (1.22) are uncoupled second-order differential equations commonly referred to as the vector wave equations for $\mathbf{E}(\mathbf{r}, t)$ and $\mathbf{H}(\mathbf{r}, t)$ fields.

1.1.3 Helmholtz equations

The analysis of wave equations can be simplified when considering time-harmonic vector EM fields using the phasor notation. This representation allows for substituting instantaneous quantities in the time domain with corresponding phasor quantities in the frequency domain. Let $\mathbf{E}(\mathbf{r}, t)$ be a time-harmonic electric field described as

$$\mathbf{E}(\mathbf{r}, t) = \mathbf{E}_0(\mathbf{r}) \cos[\omega t + \phi_0(\mathbf{r})], \tag{1.23}$$

where $\mathbf{E}_0(\mathbf{r})$ is the amplitude vector of the electric field, ω the angular frequency and $\phi_0(\mathbf{r})$ the initial phase angle of the cosine function [25, p. 17-18]. The time-harmonic electric field can be equivalently expressed as

$$\mathbf{E}(\mathbf{r}, t) = \Re\{\underline{\mathbf{E}}(\mathbf{r}) \mathrm{e}^{j\omega t}\}, \tag{1.24}$$

where the complex-valued quantity $\underline{\mathbf{E}}(\mathbf{r}) = \mathbf{E}_0(\mathbf{r}) \mathrm{e}^{j\phi_0(\mathbf{r})}$ represents the electric field phasor and $j = \sqrt{-1}$ is the imaginary unit. Therefore, the wave equations for time-harmonic fields can be reformulated as

$$\nabla^2 \underline{\mathbf{E}} + \omega^2 \varepsilon\mu \underline{\mathbf{E}} = j\omega\mu \underline{\mathbf{J}} + \frac{1}{\varepsilon} \nabla \underline{\rho}, \tag{1.25}$$

$$\nabla^2 \underline{\mathbf{H}} + \omega^2 \varepsilon\mu \underline{\mathbf{H}} = -\nabla \times \underline{\mathbf{J}}. \tag{1.26}$$

Here, the spatial dependence of the phasors on the coordinate $\mathbf{r}$ is omitted for brevity. This notation is consistently used throughout the thesis when discussing time-harmonic fields. Employing the equations (1.5), (1.3), and (1.15) in phasor notation, the equations (1.25) and (1.26) can be rewritten as

$$\nabla^2\underline{\mathbf{E}} - \underbrace{(-\omega^2\varepsilon\mu + j\omega\sigma\mu)}_{\underline{\gamma}^2}\underline{\mathbf{E}} = j\omega\mu\underline{\mathbf{J}}_\mathrm{i} + \frac{1}{\varepsilon}\nabla\underline{\rho}, \tag{1.27}$$

$$\nabla^2\underline{\mathbf{H}} - (-\omega^2\varepsilon\mu + j\omega\sigma\mu)\underline{\mathbf{H}} = -\nabla\times\underline{\mathbf{J}}_\mathrm{i}. \tag{1.28}$$

Equations (1.27) and (1.28) are commonly referred to as the vector wave equations for $\underline{\mathbf{E}}$ and $\underline{\mathbf{H}}$, also known as the inhomogeneous Helmholtz equations. The terms on the right-hand side of these equations represent the source of the fields. The quantity $\underline{\gamma}$ represents the propagation constant of the wave, which is expressed as [23, p. 139]

$$\underline{\gamma} = \alpha_\gamma + j\beta_\gamma = \sqrt{-\omega^2\mu\varepsilon + j\omega\mu\sigma}. \tag{1.29}$$

Here, the real part of $\underline{\gamma}$ is known as the attenuation constant α_γ, which represents the attenuation factor of the wave. Conversely, the imaginary part is referred to as the phase constant β_γ, indicating the phase change experienced by the wave as it propagates through the medium. By squaring the equation (1.29) and equating the real and imaginary parts from both sides, we can reduce it to

$$\alpha_\gamma^2 - \beta_\gamma^2 = -\omega^2\mu\varepsilon, \tag{1.30}$$

$$2\alpha_\gamma\beta_\gamma = \omega\mu\sigma. \tag{1.31}$$

The expressions for α_γ and β_γ are then obtained by solving (1.30) and (1.31) simultaneously [23, p. 142]

$$\alpha_\gamma = \omega\sqrt{\mu\varepsilon}\left\{\frac{1}{2}\left[\sqrt{1+\left(\frac{\sigma}{\omega\varepsilon}\right)^2}-1\right]\right\}^{1/2}, \tag{1.32}$$

$$\beta_\gamma = \omega\sqrt{\mu\varepsilon}\left\{\frac{1}{2}\left[\sqrt{1+\left(\frac{\sigma}{\omega\varepsilon}\right)^2}+1\right]\right\}^{1/2}. \tag{1.33}$$

For non-excited source-free ($\underline{\mathbf{J}}_\mathrm{i} = 0$ and $\underline{\rho} = 0$) and lossless media ($\sigma = 0$), the equations (1.27) and (1.28) can be simplified to the well-known homogeneous Helmholtz equations

$$\nabla^2\underline{\mathbf{E}} + \omega^2\mu\varepsilon\underline{\mathbf{E}} = \mathbf{0}, \tag{1.34}$$

$$\nabla^2\underline{\mathbf{H}} + \omega^2\mu\varepsilon\underline{\mathbf{H}} = \mathbf{0}. \tag{1.35}$$

In this case, the propagation constant is purely imaginary (i.e., $\alpha_\gamma = 0$), and the phase constant can be expressed as

$$\beta_\gamma = \omega\sqrt{\mu\varepsilon}. \tag{1.36}$$

In the literature, the phase constant is often denoted by the wave number k, which is defined as

$$k = \frac{2\pi}{\lambda}, \tag{1.37}$$

where λ is the wavelength of a plane wave in the considered medium [23, p. 102]. This leads to a more concise form of the homogeneous Helmholtz equations

$$\nabla^2\underline{\mathbf{E}} + k^2\underline{\mathbf{E}} = \mathbf{0}, \tag{1.38}$$

$$\nabla^2\underline{\mathbf{H}} + k^2\underline{\mathbf{H}} = \mathbf{0}. \tag{1.39}$$

For the remainder of the problem formulation, we will focus exclusively on EM waves propagating with harmonic behavior in a vacuum. In this context, $\varepsilon = \varepsilon_0$ and $\mu = \mu_0$, satisfying the relationship $c^2\varepsilon_0\mu_0 = 1$, where c represents the speed of light in vacuum.

1.2 RF fields in cavities

RF cavities are structures employed in particle accelerators to accelerate charged particles along their longitudinal axis. The accelerated particles interact with the resonating cavity's EM fields, referred to as eigenmodes or modes of the cavity. Let a cavity be described by a closed, perfectly conducting metallic structure filled with a vacuum. Furthermore, no sources are considered. The cavity eigenmodes are determined by solving the homogeneous Helmholtz equations

$$\nabla^2\underline{\mathbf{E}}_n + k_n^2\underline{\mathbf{E}}_n = \mathbf{0} \text{ on } \mathbf{\Omega}_\mathrm{v}, \tag{1.40}$$

$$\nabla^2\underline{\mathbf{H}}_n + k_n^2\underline{\mathbf{H}}_n = \mathbf{0} \text{ on } \mathbf{\Omega}_\mathrm{v}, \tag{1.41}$$

where $\mathbf{\Omega}_\mathrm{v}$ represents the vacuum-filled inner volume of the cavity. The solutions of this set of equations are characterized by the field patterns $\underline{\mathbf{E}}_n$ and $\underline{\mathbf{H}}_n$ and the resonant angular frequency $\omega_n = k_n/\sqrt{\varepsilon_0\mu_0}$ of the nth eigenmode. The fields at the surface of the perfect conductor must also satisfy the following perfect electric conductor boundary (PEC) conditions

$$\mathbf{n} \times \underline{\mathbf{E}}_n = \mathbf{0} \text{ and } \mathbf{n} \cdot \underline{\mathbf{H}}_n = \mathbf{0} \text{ on } \partial\mathbf{\Omega}_{\mathrm{v,PEC}}, \tag{1.42}$$

where $\mathbf{n}$ is the vector normal to the perfect electric conducting boundary $\partial\mathbf{\Omega}_{\mathrm{v,PEC}}$. The

PEC boundary condition implies that the tangential component of the electric field and the normal component of the magnetic field on the PEC surface are zero. A perfect magnetic conductor (PMC) boundary condition is applied at the boundaries where the normal component of the electric field and the tangential component of the magnetic field vanish, and is expressed as

$$\mathbf{n} \cdot \underline{\mathbf{E}}_n = \mathbf{0} \text{ and } \mathbf{n} \times \underline{\mathbf{H}}_n = \mathbf{0} \text{ on } \partial\mathbf{\Omega}_{\mathrm{v,PMC}}. \tag{1.43}$$

where $\partial\mathbf{\Omega}_{\mathrm{v,PMC}}$ represents the perfect magnetic conducting boundary. The surface impedance boundary condition extends the equations (1.42) when a finite electric conductivity is considered [26]

$$\mathbf{n} \times \underline{\mathbf{E}}_n = \underline{Z}_{\mathrm{s}} \mathbf{n} \times \underline{\mathbf{H}}_n \text{ on } \partial\mathbf{\Omega}_{\mathrm{v}}, \tag{1.44}$$

where $\underline{Z}_{\mathrm{s}}$ is the frequency-dependent surface impedance of the material. Subsection 1.3.6 provides more details on the surface impedance. A general solution to the problem formulation is given in [27, pp. 297-306].

In this thesis, the cavities made of superconducting material are modeled with the interior domain assumed to be vacuum and the conducting walls treated as perfect electric conductors (PEC). This assumption approximates the RF behavior of a cavity made of highly conductive material and operating under vacuum conditions. However, the surface impedance boundary condition is applied to account for losses at the interface between cavity walls and the inner vacuum volume. For example, this applies to the modeling of normal conducting cavities. Similarly, this condition can be employed when simulating the losses on superconducting surfaces, which are significantly lower than those in normal conducting cavity walls.

1.2.1 Eigenmodes of a pillbox cavity

Numerical methods are typically employed to evaluate the eigenmodes of a realistic cavity, even when the cavity is rotationally symmetric. The Finite Element Method (FEM) and the Finite Integration Technique (FIT) are widely used in commercial software, such as CST Studio Suite® [28] (briefly CST), to numerical solve Maxwell's equations. A detailed description of FEM and FIT methods is provided in [29, Ch. 5] and [25, Ch. 2.3], respectively.

Helmholtz equations could be solved analytically only for simple structures. The simplest rotationally symmetric cavity that allows for an analytical solution is the pillbox cavity [17, pp. 40-42]. This structure is a hollow cylinder with conducting walls and can sustain infinite resonant EM modes. The standing-wave eigenmodes propagating in z-direction, which is assumed to be the longitudinal direction in a cavity, can be divided into four main categories:

(i) Transverse electric (TE) modes, with the z-component of the electric field being

zero $\underline{E}_z = 0$ and the z-component of the magnetic field $\underline{H}_z \neq 0$.

(ii) Transverse magnetic (TM) modes, with $\underline{H}_z = 0$ and $\underline{E}_z \neq 0$.

(iii) Transverse electromagnetic (TEM) modes are purely transverse, with the z-component of both electric and magnetic field strengths being zero.

(iv) Hybrid modes, with the z-component of both electric and magnetic field strengths being non-zero.

Modes of a rotationally symmetric cavity are usually classified according to their spatial field variation in TE_{mnp} and TM_{mnp} modes, where the integer indexes m, n, and p denote the azimuthal φ, radial r, and longitudinal z directions, respectively. The complete set of TM_{mnp} modes is given by [30, pp. 252-406]

$$\underline{E}_\varphi = \underline{E}_0 \frac{m k_z}{k_r^2 r} \sin(k_z z) J_m(k_r r) \sin(m\varphi), \tag{1.45}$$

$$\underline{E}_r = -\underline{E}_0 \frac{k_z}{k_r} \sin(k_z z) J'_m(k_r r) \cos(m\varphi), \tag{1.46}$$

$$\underline{E}_z = \underline{E}_0 \cos(k_z z) J_m(k_r r) \cos(m\varphi), \tag{1.47}$$

$$\underline{H}_\varphi = j\underline{H}_0 \frac{\omega_{mnp}}{c k_r} \cos(k_z z) J'_m(k_r r) \cos(m\varphi), \tag{1.48}$$

$$\underline{H}_r = j\underline{H}_0 \frac{m\omega_{mnp}}{c k_r^2 r} \cos(k_z z) J_m(k_r r) \sin(m\varphi). \tag{1.49}$$

Here, J_m and J'_m represent the mth order Bessel function and its derivative, respectively. Additionally, $\underline{E}_0 = Z_0 \underline{H}_0$, where $Z_0 = \sqrt{\mu_0/\varepsilon_0} \approx 376.7\ \Omega$ is the impedance of free space. The terms $\underline{E}_0$ and $\underline{H}_0$ are the amplitude of the electric and magnetic field strengths, respectively. A set of TE_{mnp} modes similar to those in (1.45)–(1.49) can be derived. The terms k_r and k_z are denoted as the longitudinal and radial propagation constants, respectively. These two constants are related to the resonant angular frequency ω_{mnp} of the considered mode via the dispersion equation

$$\omega_{mnp} = c\sqrt{k_r^2 + k_z^2}. \tag{1.50}$$

For a pillbox cavity with length L_p and radius R_p (see Figure 1.1), the resonant angular frequencies ω_{mnp} of the TM and TE modes are given by

$$\omega_{mnp}^{(\mathrm{TM})} = c\sqrt{\left(\frac{u_{mn}}{R_\mathrm{p}}\right)^2 + \left(\frac{p\pi}{L_\mathrm{p}}\right)^2}, \tag{1.51}$$

$$\omega_{mnp}^{(\mathrm{TE})} = c\sqrt{\left(\frac{u'_{mn}}{R_\mathrm{p}}\right)^2 + \left(\frac{p\pi}{L_\mathrm{p}}\right)^2}, \tag{1.52}$$

where u_{mn} and u'_{mn} are the nth root of the mth order Bessel function and its derivative, respectively. The electric field is employed in particle accelerators to accelerate the beam, while the magnetic field is utilized to bend its trajectory. TE modes have zero longitudinal electric fields and, therefore, cannot accelerate a particle beam. The TM modes are of interest since they could accelerate particles. However, only TM modes with azimuthal order $m = 0$, namely TM_{0np} modes, can accelerate a beam in an accelerator due to their non-zero electric field along the cavity axis. Among the TM_{0np} modes, the TM_{010} mode is typically selected for accelerating particles in RF cavities [17, p. 41]. The TM_{010} mode is denoted as the fundamental mode (FM) of the accelerating cavities. The electric field of the TM_{010} is purely longitudinal (see Figure 1.1 (a)), and its magnetic field is null at the cavity axis (see Figure 1.1 (b)).

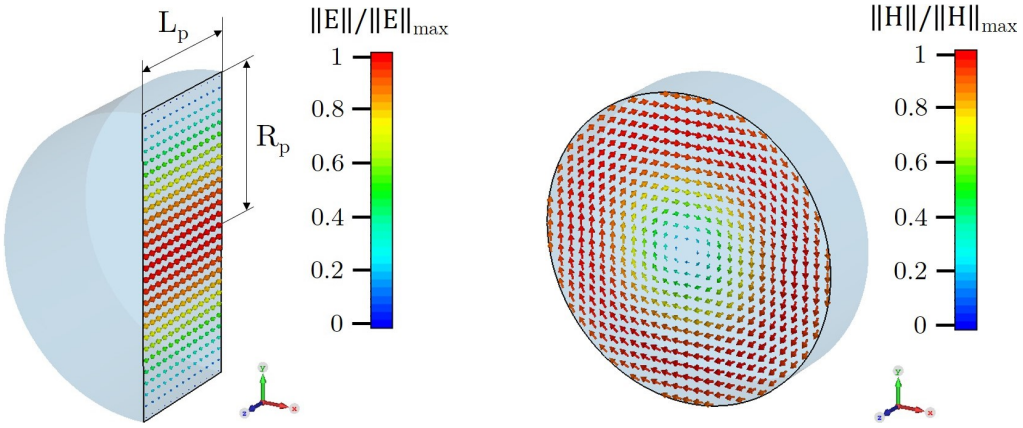

(a) Electric field **(b)** Magnetic field

Figure 1.1: Maps of the electric field (a) and magnetic field (b) for the TM_{010} mode in a 3D pillbox cavity model simulated using CST.

The TM_{010} mode in a pillbox cavity possesses the lowest eigenfrequency. The ensemble of modes with a frequency higher than the TM_{010} mode are denoted as higher order modes (HOMs) [31]. A mode with index $m = 0$ is referred to as monopole, $m = 1$ as dipole, $m = 2$ as quadrupole, $m = 3$ as sextupole, and so forth. The TM monopole modes, i.e., TM_{0np} modes, possess a non-zero longitudinal electric field along the cavity axis and can be easily excited by a beam passing through the cavity. The TM_{011} mode is typically considered the most dangerous monopole HOM. The TE monopole modes, namely TE_{0np} modes, do not feature a longitudinal electric field component along the cavity axis. Consequently, they do not pose significant risks to beam stability, even when not adequately damped. The TM dipole modes, i.e., TM_{1np} modes, possess a strong longitudinal electric field component off-axis and a net deflecting field on-axis. The TE dipole modes, i.e., TE_{1np} modes, do not possess a longitudinal electric field on-axis while featuring a transverse electric field on-axis. These modes are undesirable in accelerating cavities because they can deflect the beam, potentially causing undesired

resonant effects. Typically, the TM_{110} and TE_{111} modes are the most dangerous among the dipole modes.

1.2.2 Eigenmodes of an elliptical cavity

The pillbox cavity is a theoretical shape that is suitable only for analytical calculations. To enable the beam to enter, accelerate, and exit the cavity, two beam pipes must be added to a practical cavity [17, pp. 37, 40]. When incorporating beam pipes, it is crucial to ensure that the cutoff frequency of the TM_{01} beam pipe mode exceeds the cavity FM frequency. This ensures that the accelerating mode field cannot propagate out of the cavity, except for only minor field leakage into the beam pipe. The elliptical cavity (see Figure 1.2) is a suitable concept for accelerating particles in superconducting structures to velocities close to the speed of light [32]. This cavity design features an elliptical profile, which allows for mitigating the cavity's peak surface electric and magnetic fields. This reduces the risk of undesired emission of electrons from the cavity surface or a significant temperature rise in the cavity walls, which could ultimately result in the loss of superconductivity. More details on the elliptical RF cavity design will be provided in Chapter 2.

RF fields of an elliptical cavity deviate from the pure pillbox cavity fields. As a result, closed analytical expressions for the RF fields are not feasible, and numerical codes are needed for RF field computations. The same nomenclature as in the pillbox cavity case is still used for mode identification if the cavity fields are not severely perturbed with respect to the pillbox configuration. Figures 1.2 (a) and (b) depict the electric field distribution of the FM (TM_{010} mode) and TE_{111} dipole mode in a single-cell elliptical cavity computed using CST, respectively.

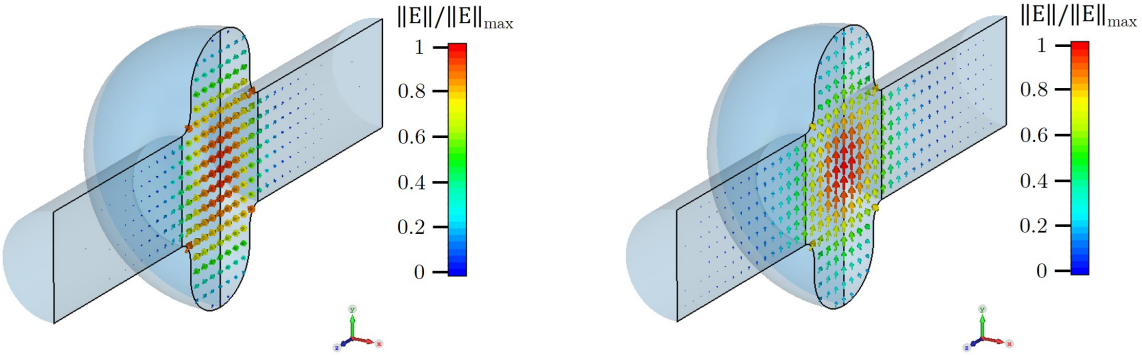

(a) Electric field of TM_{010} mode

(b) Electric field of TE_{111} mode

Figure 1.2: Electric field maps of the TM_{010} mode (FM) (a) and the TE_{111} dipole mode (b) in a 3D single-cell elliptical cavity simulated using CST.

The net acceleration of the beam can be enhanced by employing a multi-cell cavity, which is a combination of multiple cavity cells. Their behavior can be modeled as

that of a group of coupled oscillators. Additional details on the circuit model for a multi-cell cavity are provided in [17, pp. 129-134]. In a multi-cell cavity, multiple modes of excitation exist for a given mode, which together form the mode passband. The relative field amplitude in the ith cavity cell of a mode n belonging to a mode passband is given by [17, pp. 132]

$$v_i^{(n)} = \sqrt{\frac{2 - \delta_{n,N_{\text{cell}}}}{N_{\text{cell}}}} \sin\left[n\pi\left(\frac{2i-1}{2N_{\text{cell}}}\right)\right], \tag{1.53}$$

where $\delta_{n,N_{\text{cell}}}$ is the Kronecker delta[1], with N_{cell} representing the number of cavity cells, and the indexes $i = 1, ..., N_{\text{cell}}$ and $n = 1, ..., N_{\text{cell}}$ denoting the number of cell and modes, respectively. The modes within the same passband are further distinguished based on the particular phase advance per cavity cell period. Assuming periodic boundary conditions, the dispersion relation can be derived as [33, p. 110]

$$\omega_n = \frac{\omega_{\text{p},0}}{\sqrt{1 + k_{\text{cc}}\cos(\phi_n)}}, \tag{1.54}$$

where $\omega_{\text{p},0}$ is the lowest angular frequency in the passband, k_{cc} is the cell-to-cell coupling factor, and $\phi_n = n\pi/N_{\text{cell}}$ is the phase advance per cell of the mode n in the considered mode passband. The phase advance between neighboring cells for standing wave cavities can take only values ranging from 0 to π. For $k_{\text{cc}} \ll 1$, the cell-to-cell coupling factor is given by [34]

$$k_{\text{cc}} = 2\frac{\omega_{\text{p},\pi} - \omega_{\text{p},0}}{\omega_{\text{p},\pi} + \omega_{\text{p},0}} \cdot 100\%, \tag{1.55}$$

where $\omega_{\text{p},\pi}$ is the highest angular frequency in the passband. Equation (1.54) accounts for the dependency of the eigenfrequency on the phase advance in a multi-cell cavity. The mode spacing increases with a stronger cell-to-cell coupling factor, while it decreases as the number of cells increases. The TM_{010} passband in a five-cell cavity is composed of the following modes: TM_{010}-$\pi/5$, TM_{010}-$2\pi/5$, TM_{010}-$3\pi/5$, TM_{010}-$4\pi/5$ and TM_{010}-π. Figure 1.3 (a) illustrates the dispersion curve of the TM_{010} passband of an 801.58 MHz five-cell cavity. The TM_{010}-π mode is commonly employed for particle beam acceleration in multi-cell RF cavities. The electric field of the TM_{010}-π mode features equal magnitude and opposite direction between neighboring cells. Consequently, the particle beam is accelerated in the same direction as it passes along the cavity axis [17, p. 3]. The electric field distribution of the TM_{010}-π mode of an 801.58 MHz five-cell cavity is depicted in Figure 1.3 (b).

[1] $\delta_{n,n} = 1$ and $\delta_{n,i} = 0$ when $n \neq i$.

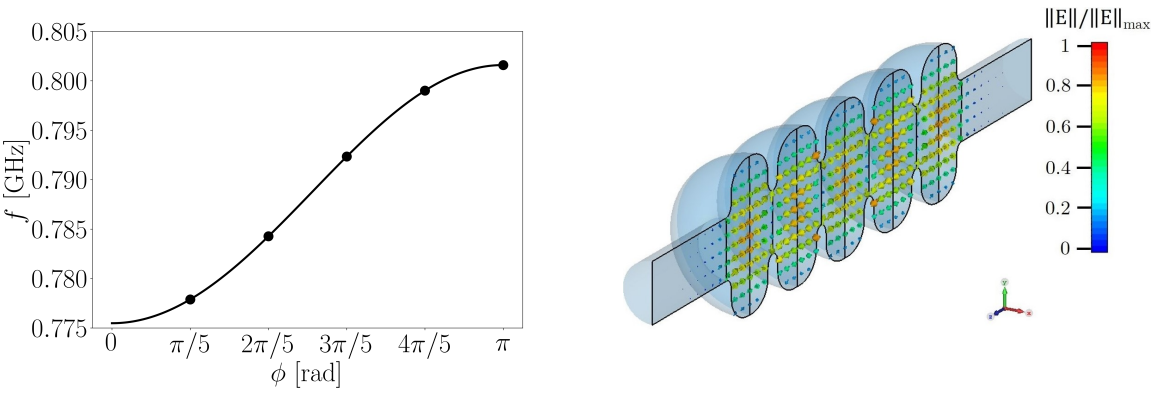

(a) TM_{010} passband **(b)** Electric field of TM_{010}-π mode

Figure 1.3: Dispersion curve of the TM_{010} passband in a five-cell cavity (a). Electric field of FM mode (b) in a 3D 801.58 MHz five-cell elliptical cavity simulated using CST.

1.3 Figures of merit for RF cavities

The relevant properties of eigenmodes can be derived for more realistic cavity shapes from the behavior of the ideal pillbox cavity [17]. This section concisely discusses some important quantities, usually called figures of merit, that guide the design of an RF cavity.

1.3.1 Fundamental mode frequency

The fundamental mode, often denoted as the TM_{010} mode, is commonly employed in RF cavities, including elliptical cavities, for accelerating charged particle beams. This mode is preferred because it typically possesses the lowest eigenfrequency, which is denoted as f_0 [17, p. 41]. The typical operating frequency of a cavity ranges from several hundred MHz to a few GHz. The choice of cavity frequency is essential for any project and depends on various technical and economic factors. The decision also relies on the availability of suitable RF sources and devices at the selected frequency. The length of a cavity cell is proportional to half the wavelength at the FM frequency as

$$L_{\text{cell}} = \beta \frac{\lambda_0}{2}, \tag{1.56}$$

where λ_0 is the wavelength of the FM, and β represents the ratio of the particle velocity to the speed of light in vacuum[2]. The wavelength at FM frequency is defined as the distance between two corresponding points in the FM electromagnetic wave, and it is given by

[2]For a charge traveling at the speed of light, β=1.

$$\lambda_0 = \frac{c}{f_0}. \tag{1.57}$$

Consequently, the size of the cavity scales inversely with the operating frequency. In superconducting cavities, the surface resistance, which is associated with surface losses, approximately scales proportionally with the square of the frequency. Subsection 1.3.6 provides additional details on the surface resistance. Therefore, very high frequencies are not preferred for such cavities. Low frequencies also facilitate the minimization of beam instabilities caused by wakefields. Utilizing a low operating frequency results in larger cavities, which can be costly and challenging to manufacture [17, p. 12].

1.3.2 Lorentz force and voltage

Assume a unit charge q traveling at the speed of light along the z-axis in the presence of an EM field. The Lorentz force contribution of a mode n acting on the moving charge is described by

$$\underline{\mathbf{F}}_n = q(\underline{\mathbf{E}}_n + c\hat{\mathbf{z}} \times \underline{\mathbf{B}}_n)\mathrm{e}^{jk_n z} = q\big[(\underline{E}_{x,n} - c\underline{B}_{y,n})\hat{\mathbf{x}} + (\underline{E}_{y,n} + c\underline{B}_{x,n})\hat{\mathbf{y}} + \underline{E}_{z,n}\hat{\mathbf{z}}\big]\mathrm{e}^{jk_n z}, \tag{1.58}$$

where $k_n = \omega_n/c$ is the wave number[3] of mode n, and $z = ct$ is the charge position. The electric field's force applied to the charged particle does not depend on the particle's velocity and aligns with the direction of the electric field strength. In contrast, the force exerted on a charged particle due to the magnetic field is perpendicular to the particle's direction of motion and depends on its velocity. Therefore, the electric field is commonly employed to accelerate particles to high energies, while the magnetic field is typically used to change the direction of moving charged particles.

The charged particle experiences a voltage in the longitudinal direction while passing through the cavity, denoted as accelerating voltage, which is calculated by direct integration of the longitudinal force as

$$\underline{V}_{\parallel,n}(x,y) = \int_0^{L_{\mathrm{cav}}} \underline{E}_{z,n}(x,y,z)\mathrm{e}^{jk_n z}\,\mathrm{d}z, \tag{1.59}$$

where $\underline{E}_{z,n}(x,y,z)$ is the longitudinal electric field along the particle's trajectory, and the integral is evaluated across the length L_{cav} of the considered cavity. The accelerating voltage for the FM of a cavity is calculated as

$$V_{\mathrm{acc}} = \left|\underline{V}_{\parallel,0}(0,0)\right| = \left|\int_0^{L_{\mathrm{cav}}} \underline{E}_{z,0}(0,0,z)\mathrm{e}^{jk_0 z}\,\mathrm{d}z\right|, \tag{1.60}$$

[3]The wave number is generally defined as $k_n = \omega_n/\beta c$ with β being the ratio of the particle velocity to the speed of light.

where the index 0 refers to the FM. It is also useful to describe the average accelerating field experienced by the beam, E_{acc}, over the active length of the cavity, L_{act}, known as the cavity accelerating gradient [17, p. 43]

$$E_{\mathrm{acc}} = \frac{V_{\mathrm{acc}}}{L_{\mathrm{act}}}. \tag{1.61}$$

The active length represents the cavity region where the electric field is predominant. In an elliptical cavity accelerating particle at $\beta = 1$, the active length can be approximated as

$$L_{\mathrm{act}} = N_{\mathrm{cell}} \frac{\lambda_0}{2}, \tag{1.62}$$

where N_{cell} is the number of cells of the cavity. This distance typically does not include the length of the beam pipe, where the FM field decays before reaching the beam pipe entries. In the elliptical cavity, the active length is usually called iris-to-iris length.

Similarly, the effective transverse voltages $\underline{V}_{\perp \mathrm{x},n}$ and $\underline{V}_{\perp \mathrm{y},n}$ experienced by the moving charge can be calculated by directly integrating the deflecting force in the x and y directions, respectively, as

$$\underline{V}_{\perp \mathrm{x},n}(x,y) = \int_0^{L_{\mathrm{cav}}} \left(\underline{E}_{x,n}(x,y,z) - c\underline{B}_{y,n}(x,y,z)\right) \mathrm{e}^{jk_n z} \,\mathrm{d}z, \tag{1.63}$$

$$\underline{V}_{\perp \mathrm{y},n}(x,y) = \int_0^{L_{\mathrm{cav}}} \left(\underline{E}_{y,n}(x,y,z) + c\underline{B}_{x,n}(x,y,z)\right) \mathrm{e}^{jk_n z} \,\mathrm{d}z. \tag{1.64}$$

The transverse and longitudinal voltages can be directly related to each other via the Panofsky-Wenzel theorem [35]

$$\underline{\mathbf{V}}_{\perp,n} = \frac{j}{k_n} \nabla_\perp \underline{V}_{\parallel,n}, \tag{1.65}$$

where $\underline{\mathbf{V}}_{\perp,n}$ is the transverse voltage vector of the mode n, and $\nabla_\perp$ is the transverse gradient operator.[4] Equation (1.65) is valid when the PEC boundary condition is applied at both ends of the cavity, represented by the two longitudinal coordinates $z = 0$ and $z = L_{\mathrm{cav}}$ [17, p. 342].

1.3.3 Geometric shunt impedance

The geometric shunt impedance, denoted as R/Q, relates the accelerating voltage to the stored energy within the cavity. The longitudinal geometric shunt impedance of a mode n can be expressed as [17, p. 47]

[4] In the literature [36, p. 295], depending on the used convention, the relationship between the longitudinal and transverse voltage can be found with a negative sign, i.e., $\underline{\mathbf{V}}_{\perp,n} = -\frac{j}{k_n} \nabla_\perp \underline{V}_{\parallel,n}$.

$$(R/Q)_{\parallel,n} = \frac{\left|\underline{V}_{\parallel,n}(0,0)\right|^2}{\omega_n U_n}, \tag{1.66}$$

where U_n is the energy contribution of the mode n stored in the cavity calculated from

$$U_n = \frac{1}{2}\mu_0 \iiint_\Omega \left|\underline{\mathbf{H}}_n\right|^2 \mathrm{d}V = \frac{1}{2}\varepsilon_0 \iiint_\Omega \left|\underline{\mathbf{E}}_n\right|^2 \mathrm{d}V, \tag{1.67}$$

where Ω is the cavity volume. Equation (1.66) utilizes the linac definition of R/Q, which is twice the value of the circuit definition. The geometric shunt impedance depends only on the cavity geometry. This quantity measures the effectiveness of the cavity in transferring its stored energy to the beam. Additionally, it is also indicative of the beam-mode coupling within the cavity. To minimize the power dissipation in the cavity walls by the FM, the aim is to maximize the value of $(R/Q)_\parallel$ for the accelerating mode, commonly indicated as $(R/Q)_{\parallel,0}$, while minimizing it for the monopole HOMs. Indeed, in the latter case, a higher value of $(R/Q)_\parallel$ corresponds to a greater excitation induced by charges passing through the cavity. Modes with azimuthal order $m > 1$ exhibit no longitudinal electric field component on the beam axis, resulting in $(R/Q)_\parallel = 0$ for such modes.

In analogy to equation (1.66), the transversal geometric shunt impedance of a mode n can be derived as [17, p. 342]

$$(R/Q)_{\perp,n} = \frac{\left|\underline{\mathbf{V}}_{\perp,n}\right|^2}{\omega_n U_n} = \underbrace{\frac{\left|\underline{V}_{\perp \mathrm{x},n}(0,0)\right|^2}{\omega_n U_n}}_{(R/Q)_{\perp \mathrm{x},n}} + \underbrace{\frac{\left|\underline{V}_{\perp \mathrm{y},n}(0,0)\right|^2}{\omega_n U_n}}_{(R/Q)_{\perp \mathrm{y},n}}, \tag{1.68}$$

where $(R/Q)_{\perp \mathrm{x},n}$ and $(R/Q)_{\perp \mathrm{y},n}$ represent the transversal components of the R/Q of a mode n, respectively. In RF cavities with rotational symmetry, dipole mode degeneracy occurs, meaning that dipole modes have the same resonant frequency and can be oriented at any arbitrary azimuthal angle. Therefore, the transversal geometric shunt impedance, as defined in the equation (1.68), is independent of the azimuthal angle of the mode n, and it can be approximated to

$$(R/Q)_{\perp,n} = \max[(R/Q)_{\perp \mathrm{x},n}, (R/Q)_{\perp \mathrm{y},n}]. \tag{1.69}$$

Using the Panofsky-Wenzel theorem, the transversal geometric shunt impedance can be approximated as follows

$$(R/Q)_{\perp,n} \approx \frac{\left|\underline{V}_{\parallel,n}(x_\mathrm{p},0) - \underline{V}_{\parallel,n}(0,0)\right|^2}{\omega_n U_n k_n^2 x_\mathrm{p}^2} + \frac{\left|\underline{V}_{\parallel,n}(0,y_\mathrm{p}) - \underline{V}_{\parallel,n}(0,0)\right|^2}{\omega_n U_n k_n^2 y_\mathrm{p}^2}, \tag{1.70}$$

where x_p and y_p represent the transverse position of the particle in x and y directions,

respectively. The unit of longitudinal and transversal geometric shunt impedances defined above is Ω. A definition that is independent of the transverse displacement of the particle can be obtained by multiplying both sides of the equation (1.70) by k_n, which converts the unit of the transversal geometric shunt impedance to Ω/m. Monopole modes do not provide any transverse momentum on the beam axis. Consequently, $(R/Q)_\perp$ vanishes on the beam axis. Minimizing $(R/Q)_\perp$ of dipole modes is crucial for reducing the transverse instabilities induced by the beam passing through the cavity.

1.3.4 Cavity impedance

The impedance of a cavity is a quantity that establishes a relationship between the beam current and the voltage induced within the cavity. The behavior of narrow-band resonances in a cavity can be effectively described using a parallel *RLC* circuit [36, p. 292]. This applies to all trapped modes, i.e., modes that reside below the lowest cutoff frequency of waveguide (WG) modes in the beam pipe. More details on the beam pipe cutoff frequency and trapped modes will be provided in Chapter 2. Assuming that the modes n of a cavity are orthogonal to each other, the longitudinal impedance of the cavity could be expressed as [37]

$$Z_\parallel(\omega) = \sum_n \frac{1}{2} \frac{(R/Q)_{\parallel,n} Q_n}{1 + jQ_n \delta_{\omega_n}}, \tag{1.71}$$

where $\delta_{\omega_n} = (\omega/\omega_n - \omega_n/\omega)$. Here Q_n represents the quality factor of mode n, defined from an *RLC* circuit model via the resonance bandwidth as [33, p. 132]

$$Q_n = \frac{\omega_n}{\Delta\omega_n}, \tag{1.72}$$

where $\Delta\omega_n$ is the angular power bandwidth. The factor $1/2$ included in equation (1.71) refers to using the linac definition of the geometric shunt impedance. Similarly, the transverse impedance can be calculated as

$$Z_\perp(\omega) = \sum_n \frac{1}{2} \frac{(R/Q)_{\perp,n} k_n Q_n}{1 + jQ_n \delta_{\omega_n}}. \tag{1.73}$$

Additional details on calculating the cavity impedance in the frequency and time domains will be provided in Chapter 5.

1.3.5 Loss factor

The fraction of energy deposited by a traversing point charge q into the mode n of a cavity is given by [17, p. 333]

$$U_{q,n} = k_{\parallel,n} q^2. \tag{1.74}$$

Here, the quantity $k_{\parallel,n}$ represents the modal longitudinal loss factor, which can be defined as

$$k_{\parallel,n} = \frac{\left|\underline{V}_{\parallel,n}(0,0)\right|^2}{4U_n} = \frac{\omega_n}{4}(R/Q)_{\parallel,n}. \tag{1.75}$$

The longitudinal loss factor is often expressed in V/pC. The modal loss factor is intricately related to the definition of power loss caused by a beam in a cavity. Section 5.2 will provide more details on this relationship. Similar to equation (1.75), given the definition (1.70) of transverse geometric shunt impedance, the kick factor of the mode n can be derived as [37]

$$k_{\perp,n} = \frac{\omega_n}{4} k_n (R/Q)_{\perp,n}. \tag{1.76}$$

The kick factor describes the transverse momentum experienced by the bunch while passing through the cavity. It is commonly expressed in units of V/(pCm).

1.3.6 Power dissipation and surface resistance

RF modes resonating inside the cavity dissipate energy in a thin conducting layer of the cavity surface due to its finite conductivity. For a mode n, the power dissipated on the cavity walls is given by

$$P_{\mathrm{c},n} = \frac{1}{2} R_\mathrm{s} \iint_\Sigma \left|\underline{\mathbf{H}}_{\mathrm{tan},n}\right|^2 \mathrm{d}S, \tag{1.77}$$

where $\underline{\mathbf{H}}_{\mathrm{tan},n}$ is the magnetic field strength tangential to the interior cavity surface Σ for the considered mode [23, p. 567].[5] The surface resistance for a normal conductor is defined as [17, pp. 78-79]

$$R_\mathrm{s} = \sqrt{\frac{\omega\mu}{2\sigma}}. \tag{1.78}$$

It represents the real part of the surface impedance $\underline{Z}_\mathrm{s}$, which can be approximated for a normal conductor as

$$\underline{Z}_\mathrm{s} \approx \sqrt{\frac{j\omega\mu}{\sigma}} = \sqrt{\frac{\omega\mu}{2\sigma}}(1+j) = R_\mathrm{s} + jX_\mathrm{s}, \tag{1.79}$$

where the imaginary part X_s is referred to as reactance. The RF fields can penetrate a normal conductor for a typical distance called the skin depth, which can be

[5] We are assuming that the surface resistance does not vary spatially across the entire cavity surface.

approximated for a good conductor ($\omega\varepsilon \ll \sigma$) as

$$\delta_\mathrm{s} \approx \sqrt{\frac{2}{\omega\mu\sigma}}. \tag{1.80}$$

In particular, the skin depth quantifies the distance over which the wave intensity decreases to $1/e \approx 0.37$ of its initial value [23, p. 140]. Equation (1.80) leads to a more compact expression of the surface resistance as follows

$$R_\mathrm{s} = \frac{1}{\sigma\delta_\mathrm{s}}. \tag{1.81}$$

The resistance of a normal conductor is directly proportional to the square root of the frequency. Furthermore, as the temperature of the conductor is reduced, its resistance decreases. The surface resistance of a Copper (Cu) cavity, operating at room temperature within the MHz frequency range, typically falls in the order of a few mΩ [17, p. 45].

For a superconductor, the electrical resistance to DC currents abruptly falls to zero once the material is cooled below a characteristic critical temperature T_c. Superconducting materials display different critical temperatures depending on their composition. For instance, Nb and Nb_3Sn exhibit a critical temperature of 9.2 K and 18.3 K, respectively [38]. Dissipation occurs for all $T > 0$ K when a superconductor is exposed to RF currents, although the effect is minimal compared to the normal conducting state. In this case, the surface resistance may qualitatively be understood by the so-called two-fluid model [17, p. 85]. Assuming a time-varying EM field exponentially decaying when penetrating a superconductor according to the London equations [39], the surface impedance of a superconductor can be written as

$$\underline{Z}_\mathrm{s} = R_\mathrm{s} + jX_\mathrm{s} = \frac{1}{2}\omega^2\mu_0^2\sigma_\mathrm{n}\lambda_\mathrm{L}^3 + j\omega\mu_0\lambda_\mathrm{L}, \tag{1.82}$$

where σ_n is the electric conductivity in the normal conducting state and λ_L represents the London penetration depth [17, p. 86]. The surface resistance is strictly linked to the purity of the material, which is indicated by the Residual Resistivity Ratio (RRR)[6] [41]

$$\mathrm{RRR} = \frac{\sigma(0\ \mathrm{K})}{\sigma(300\ \mathrm{K})} \approx \frac{\sigma(10\ \mathrm{K})}{\sigma(300\ \mathrm{K})}. \tag{1.83}$$

High-purity Nb cavities feature RRR $\geq$ 300, while RRR $= 100 - 150$ and RRR $= 60$ are typical values for medium and low-purity Nb cavities, respectively [42]. A common resistivity ratio value for a high gradient Nb cavity is RRR $= 300$ [40].

The temperature dependence of the surface resistance may be derived from the

[6] In the literature, several definitions of RRR exist, reflecting the use of different measurement approaches. For example, RRR $= \sigma(4.2\ \mathrm{K})/\sigma(300\ \mathrm{K})$ [40]. Additionally, this ratio is often defined using the electric resistivity of the material.

temperature-dependent London penetration depth described by [43]

$$\lambda_{\mathrm{L}}^2(T) \propto \frac{1}{1-\left(\frac{T}{T_{\mathrm{c}}}\right)^4}, \tag{1.84}$$

which applies for $T \ll T_{\mathrm{c}}$. Furthermore, the proportionality to σ_{n} of the surface resistance leads to an exponential correlation with the temperature, valid for $T < T_{\mathrm{c}}/2$, which is

$$R_{\mathrm{s}} \propto \omega^2 \lambda_{\mathrm{L}}^3 \ell \mathrm{e}^{-\Delta/k_{\mathrm{B}}T}. \tag{1.85}$$

Here, T is the temperature, ℓ represents the electron mean free path, 2Δ is the energy gap of the superconductor, and $k_{\mathrm{B}} = 1.38 \times 10^{-23}$ J/K is the Boltzmann constant [44]. An implicit formulation has been developed by Mattis and Bardeen [45] based on the BCS theory [46], allowing for quantitative predictions of the surface resistance of a superconductor. As a result, the surface resistance of a superconductor at RF frequencies is defined as

$$R_{\mathrm{s}} = R_{\mathrm{BCS}}(T) + R_{\mathrm{res}} = A_{\mathrm{s}} \frac{\omega^2}{T} \mathrm{e}^{-\Delta/k_{\mathrm{B}}T} + R_{\mathrm{res}}, \tag{1.86}$$

where A_{s} is a material-dependent constant and R_{res} is the residual resistance, which is influenced by surface impurities and trapped magnetic flux. Typical R_{s} values for Nb cavities range from 100 nΩ to 10 nΩ [17, p. 9]. A well-prepared Nb surface typically exhibits a residual resistance in the order of few nΩ [17, p. 75]. The R_{BCS} proportionally increases with the square of the frequency, while it exponentially decreases with temperature. A conventional expression used to calculate the R_{BCS} for Nb is

$$R_{\mathrm{BCS}}[\Omega] = 2 \times 10^{-4} \frac{1}{T[\mathrm{K}]} \left(\frac{f[\mathrm{GHz}]}{1.5}\right)^2 \mathrm{e}^{-17.67/T[\mathrm{K}]}, \tag{1.87}$$

where f is the RF frequency in GHz [17, p. 88]. The exponential reduction of the surface resistance with the temperature implies that operating at low temperatures, such as 2 K for Nb cavities, minimizes RF losses in an SRF cavity. Due to their significantly small power loss on the cavity walls, superconducting cavities can achieve high-accelerating fields. Therefore, SRF cavities are preferred to Cu cavities in applications that demand a high continuous-wave accelerating field (on the order of tens of MV/m).

1.3.7 Quality factor

The quality factor Q is a dimensionless quantity associated with the power loss in accelerating cavities, defined as [17, p. 45]

$$Q = \frac{\omega U}{P_{\text{loss}}}. \tag{1.88}$$

It quantifies the number of RF cycles needed to dissipate the energy stored within the cavity. Power loss in a cavity can emerge from multiple mechanisms, including conductive loss P_{c} and external loss P_{ext}. The total quality factor of a mode n, denoted as the loaded quality factor $Q_{\text{L},n}$, is calculated according to [36, p. 56]

$$\frac{1}{Q_{\text{L},n}} = \frac{1}{Q_{0,n}} + \frac{1}{Q_{\text{ext},n}} = \frac{P_{\text{c},n}}{\omega_n U_n} + \frac{P_{\text{ext},n}}{\omega_n U_n}. \tag{1.89}$$

Here, $Q_{0,n}$ represents the unloaded quality factor or intrinsic quality factor of a mode n, related to the power dissipated into the cavity walls due to finite conductivity. An important figure of merit for accelerating cavities is the unloaded quality factor of the FM, denoted as Q_0, which can be expressed as [17, p. 45]

$$Q_0 = \frac{\omega_0 U_0}{P_{\text{c},0}} = \frac{\omega_0 \mu_0 \iiint_\Omega \left|\underline{\mathbf{H}}_0\right|^2 \mathrm{d}V}{R_{\text{s}} \iint_\Sigma \left|\underline{\mathbf{H}}_{\text{tan},0}\right|^2 \mathrm{d}S}. \tag{1.90}$$

Considering the equations (1.59) and (1.66), the power dissipated in the cavity walls by the FM can be written as

$$P_{\text{c},0} = \frac{V_{\text{acc}}^2}{(R/Q)_{\parallel,0} Q_0}, \tag{1.91}$$

where $(R/Q)_{\parallel,0}$ and Q_0 are the longitudinal geometric shunt impedance and the intrinsic quality factor of the FM, respectively. The unloaded quality factor depends on both the material properties and the geometry of the cavity. This yields the following definition of geometric factor

$$G = \frac{\omega_0 \mu_0 \iiint_\Omega \left|\underline{\mathbf{H}}_0\right|^2 \mathrm{d}V}{\iint_\Sigma \left|\underline{\mathbf{H}}_{\text{tan},0}\right|^2 \mathrm{d}S} = Q_0 R_{\text{s}}, \tag{1.92}$$

which represents the geometry-dependent part of the unloaded quality factor. Equation (1.92) highlights the inverse proportionality of the quality factor with the surface resistance. The typical value of the Q_0 for Cu cavities is in the order of 10^4, while superconducting cavities can achieve significantly higher Q_0 values in the order of 10^{10} [47]. The RF losses can also be rewritten using equation (1.92) in the form

$$P_{\text{c},0} = \frac{V_{\text{acc}}^2 R_{\text{s}}}{(R/Q)_{\parallel,0} G}. \tag{1.93}$$

The quantity $(R/Q)_{\parallel,0} G$, which is purely geometry-dependent, is typically minimized in an SRF cavity design optimization process for large-scale accelerators working in CW mode to reduce the RF power losses into the Helium (He) bath.

The external coupling mechanisms are quantified by the external quality factor Q_{ext}, which relates the stored energy within the cavity U to the power P_{ext} that propagates out of the cavity through the beam pipe or the couplers. For superconducting cavities, due to the immensely larger Q_0, the value of Q_{ext} is dominant in equation (1.89), leading to the assumption that $Q_{\text{L}} \approx Q_{\text{ext}}$. In other words, in superconducting cavities, the external quality factor Q_{ext} is typically determined by the loaded quality factor Q_{L}. The HOMs that exhibit minimal external loss are typically trapped inside the cavity. They are considered particularly problematic due to their large $Q_{\text{ext}} > 10^5$. For such modes, damping through external coupling mechanisms, such as HOM couplers, is required to ensure beam stability and prevent excessive power dissipation on the cavity walls. More details about couplers and HOM-damping are provided in Chapters 4 and 5, respectively. It is also useful to define the coupling parameter, β, which is the ratio of the power lost by external coupling mechanisms and the power dissipated into the cavity walls [36, p. 56][7]

$$\beta = \frac{P_{\text{ext}}}{P_{\text{c}}} = \frac{Q_0}{Q_{\text{ext}}}. \tag{1.94}$$

The coupling factor indicates how strongly an external coupling mechanism, such as a HOM coupler, interacts with the cavity EM fields. If the β is large, it indicates that a significant amount of power is leaking out of the coupler compared to the power being dissipated in the cavity walls. Additional details on the coupling factor are provided in Chapter 7.

[7] We use β here to represent the coupling parameter. This thesis also employs the same symbol for the relative velocity β. It is usually clear from the context which quantity is being referred to.

2 RF cavity design for PERLE

This chapter focuses on the proposed design of the five-cell 801.58 MHz superconducting RF cavity intended for the PERLE energy recovery linac. An overview of the PERLE accelerator complex, along with the main RF cycle and beam parameters, is provided. Subsequently, the optimized design of the five-cell elliptical cavity proposed for PERLE and its main figures of merit are presented. Given the importance of identifying high-R/Q HOMs for beam stability and cavity refrigeration requirements in high-current ERLs, this chapter also includes a numerical eigenmode investigation to detect potentially dangerous HOMs near the beam spectral lines. Finally, the static and dynamic heat losses and the required input power per cavity are presented.

2.1 The PERLE accelerator

The multi-pass ERL PERLE, depicted in Figure 2.1, is arranged in a racetrack topology featuring two parallel superconducting linacs, each containing an 82.2 MeV cryomodule hosting four 5-cell elliptical Niobium (Nb) cavities operating at 801.58 MHz [48].

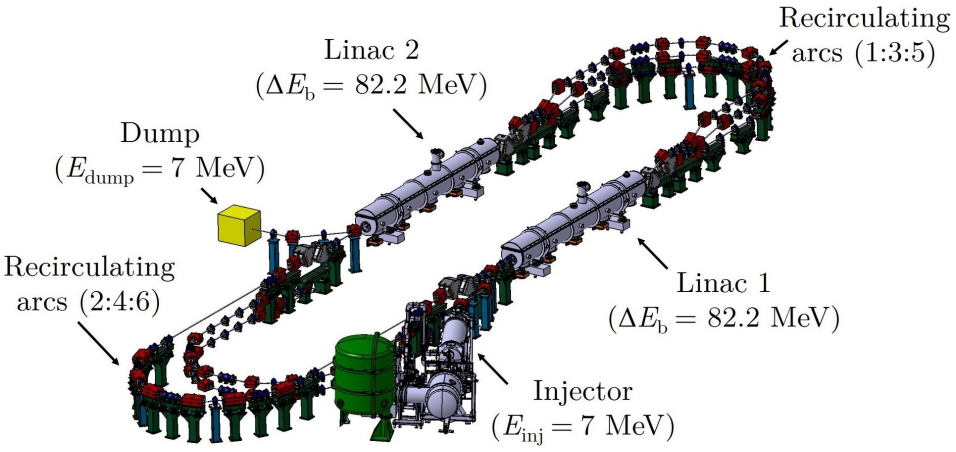

Figure 2.1: The PERLE accelerator complex layout, consisting of two parallel superconducting linacs, each hosting an 82.2 MeV cryomodule, achieving 500 MeV in three passes [49].

Three vertically stacked recirculating arcs are placed on each side of the accelerator configuration. The spreader/recombiner section connects the linacs to the arcs. The spreaders are located after each linac to separate beams of different energies and direct them toward the respective arcs. Conversely, the recombiners merge beams of different energies into the same trajectory before entering the next linac [50]. Two experimental areas at the interaction points (IPs) will complete the accelerator complex. Figure 2.2 illustrates the top and side views of the PERLE accelerator. The total length of the straight and spreader/recombiner sections is 29 m. The distance between the two straight sections is 5.5 m. The arcs are separated by a vertical distance of 45 cm between each of them. The total footprint of the accelerator is 29 m × 5.5 m × 0.9 m.

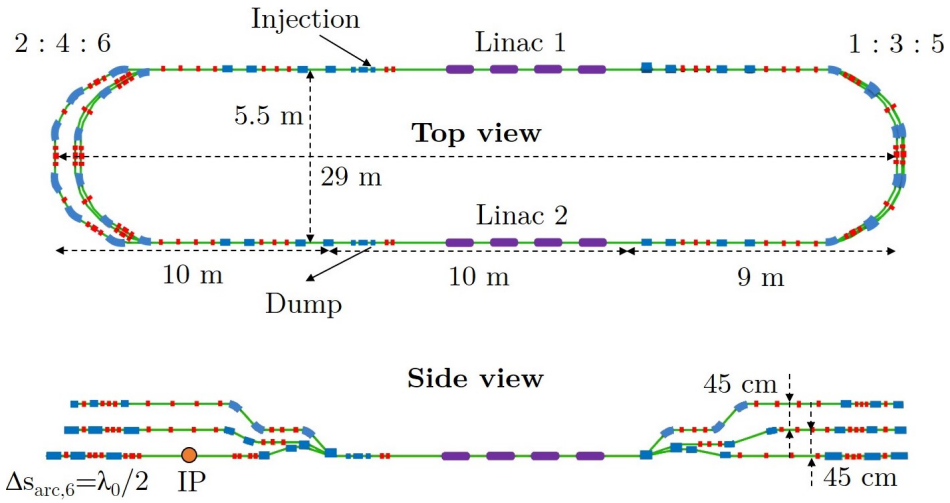

Figure 2.2: Top and side views of the 500 MeV PERLE accelerator complex. The four RF cavities hosted in each cryomodule are indicated in purple. The dipole and quadrupole magnets are depicted in blue and red, respectively. The orange dot depicts one of the two interaction points. The figure is adapted from [48] and falls under the Creative Commons Attribution 4.0 (CC BY 4.0) license (https://creativecommons.org/licenses/by/4.0/).

A flexible momentum compaction lattice, whose details are provided in [51], is employed for the six arcs. PERLE is a 6-pass ERL, which includes three accelerating and three decelerating passes. The 20 mA electron beam is injected into the ERL from a photo-injector at an energy of 7 MeV. The CW beam is boosted in energy by each of the two 82.2 MeV cryomodules. Hence, the target beam energy of approximately 500 MeV is achieved in three recirculation passes. The length of each arc's path is selected to be an integer of the RF wavelength, with the exception of arc 6 at the highest energy pass, whose length is extended by $\Delta s_{\mathrm{arc},6} = \lambda_0/2$ to shift the RF phase from accelerating to decelerating, allowing the operation in energy recovery mode. Following an experiment at target energy, the beam is decelerated in three consecutive passes back to the injection energy. During this phase, the beam energy is effectively transferred back to the SRF system, and the final 7 MeV beam is then directed toward

the beam dump. It is worth noting that, since PERLE features six passes, the current passing through the cavity during its operation is six times the 20 mA injected current, i.e., $I_{\mathrm{b,op}} = 120$ mA. The last detailed studies on the beam dynamics-driven design for PERLE are reported in [48]. Table 2.1 summarizes the main parameters of the RF cycle and the beam parameters for the 500 MeV version of PERLE. The term $t_0 = 1/f_0$ represents the time period of the FM wave. The bunch spacing is represented as $t_{\mathrm{b}} = 1/f_{\mathrm{b}}$, where f_{b} is the bunch repetition frequency. The number of oscillations of the RF field during one cycle of the bunch repetition is denoted as the number of waves per cycle, and it is given by $n_{\mathrm{wave}} = f_0/f_{\mathrm{b}}$.

Table 2.1: RF cycle and beam parameters for the 500 MeV version of PERLE [48].

Parameter	Symbol	Unit	Value
Number of passes	N_{p}	1	6
Injection beam energy	E_{inj}	MeV	7
Energy gain per linac	ΔE_{b}	MeV	82.2
Average beam current	$I_{\mathrm{b,0}}$	mA	20
Operating beam current	$I_{\mathrm{b,op}}$	mA	120
Bunch charge	Q_{b}	pC	500
Longitudinal bunch length	σ_z	mm	3
Normalized emittance	$\gamma\varepsilon_{x,y}$	mm mrad	6
RF frequency	f_0	MHz	801.58
Time period of RF wave	t_0	ns	1.25
Wavelength at RF frequency	λ_0	m	0.374
Bunch repetition frequency	f_{b}	MHz	40.08
Bunch spacing	t_{b}	ns	25
Number of waves per cycle	n_{wave}	1	20
Duty factor		1	CW

The 500 MeV PERLE ERL configuration, as illustrated in Figure 2.1, will be constructed in two phases. Initially, a 250 MeV version comprising one cryomodule and three straight sections on the opposite side will be built. The injection line and beam dump will be on the same side in this configuration. Subsequently, the 250 MeV version will be upgraded to the final 500 MeV version. This strategy aims to reduce initial costs, allowing for faster construction and shorter commissioning time. This thesis will focus solely on the 500 MeV version of PERLE. Further details on the layout and lattice design of the 250 MeV version of PERLE are reported in [52]. A detailed description of the main components initially foreseen for the PERLE ERL, including the electron source and injector, the RF cavity and cryomodule designs, and related experiments, can be found in the PERLE Conceptual Design Report (CDR) [18] and in the most recent document [53]. This thesis exclusively focuses on the Nb cavity design suitable for high-gradient CW operation in the 500 MeV PERLE ERL and the related HOM couplers designed to extract potentially dangerous HOMs from the cavity.

2.2 The PERLE elliptical cavity

Elliptical cavities in the medium and high-β ranges are extensively employed in particle accelerator applications. These cavities are proved to be well-suited for future high-energy accelerators and energy recovery linacs [54]. It is convenient for medium and large-scale accelerators to employ multi-cell cavities rather than single-cell cavities to achieve the required accelerating voltage [21]. This choice reduces costs associated with the required auxiliary components, such as HOM couplers, input couplers, tuners, and so forth. Some designs of superconducting elliptical cavities have been conceived and manufactured for high-current ERLs. Notable examples include the 5-cell 704 MHz cavity for the Electron-Relativistic Heavy Ion Collider (eRHIC) [55], the 5-cell 748.5 MHz high-current cavity developed at JLab for the ERL Free Electron Laser (ERL-FEL) [56], and the 7-cell 1300 MHz cavity for Cornell ERL main linac [57].

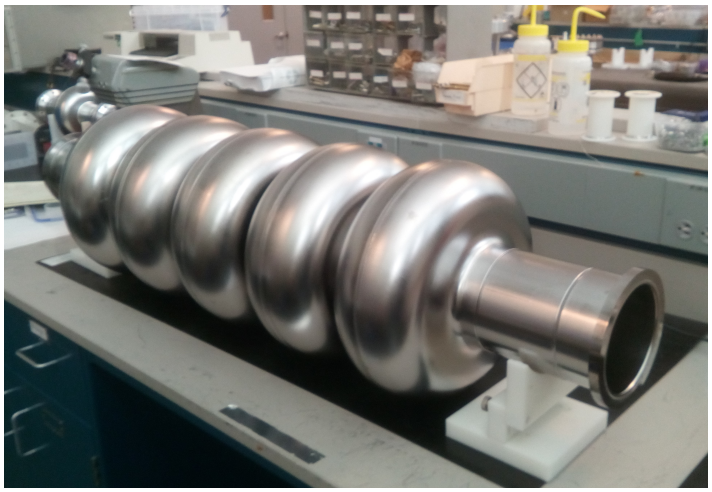

Figure 2.3: Bulk Nb prototype of PERLE cavity fabricated at JLab [58].

For high-current accelerators, using five-cell cavities represents a good compromise between balancing HOM-damping performances and the required cavity length, especially at low operating frequencies (around 800 MHz). In the framework of the collaboration between CERN and JLab for the Large Hadron electron Collider (LHeC) and the Future Circular Collider (FCC) studies (FCC-eh and FCC-ee), JLab has proposed an 801.58 MHz Nb five-cell elliptical cavity design suitable for ERL at high beam currents and future high-energy accelerators [58]. JLab's cavity design has been chosen as the baseline for the two superconducting linac cryomodules of the PERLE ERL, which is proposed as a testbed to demonstrate the principles of the LHeC and FCC-eh. The 801.58 MHz Nb five-cell elliptical cavity fabricated at JLab in 2018 is depicted in Figure 2.3.

The operating frequency of the 5-cell PERLE cavity is 801.58 MHz, which corresponds to the 20th harmonic of the bunch repetition frequency $f_b = 40.08$ MHz [58]. This choice of FM mode frequency aligns with the RF systems under development at CERN and minimizes beam-beam interactions. The cells are made of fine-grain Nb with RRR = 250. The cavity wall thickness is 4 mm, which provides relatively good cavity stiffness. The 5-cell Nb cavity was tested at high power in a vertical cryostat at 2 K temperature, reaching an accelerating field of around 30.1 MV/m at the ultimate quench field of 126 mT. A quench occurs when the superconductivity in the cavity walls is lost due to surface losses. High Q_0-values were reached in the high-field regime, preserving a record unloaded quality factor of $Q_0 = 3{\times}10^{10}$ up to $E_{acc} = 27$ MV/m without applying nitrogen-doping or nitrogen-infusion techniques. This set a new record unloaded quality factor at 2 K in the high field regime of SRF cavities resonating at around 800 MHz. Additional details on the production and high-power RF test results at 2 K of this cavity are provided in [58, 59].

2.2.1 RF design parameters of the cavity

The JLab 5-cell cavity design for high-current ERL was conceived in 2015 at JLab [59]. The parametrization detailed in [60] was used in this thesis to reconstruct the 5-cell elliptical cavity design using CST, as depicted in Figure 2.4.

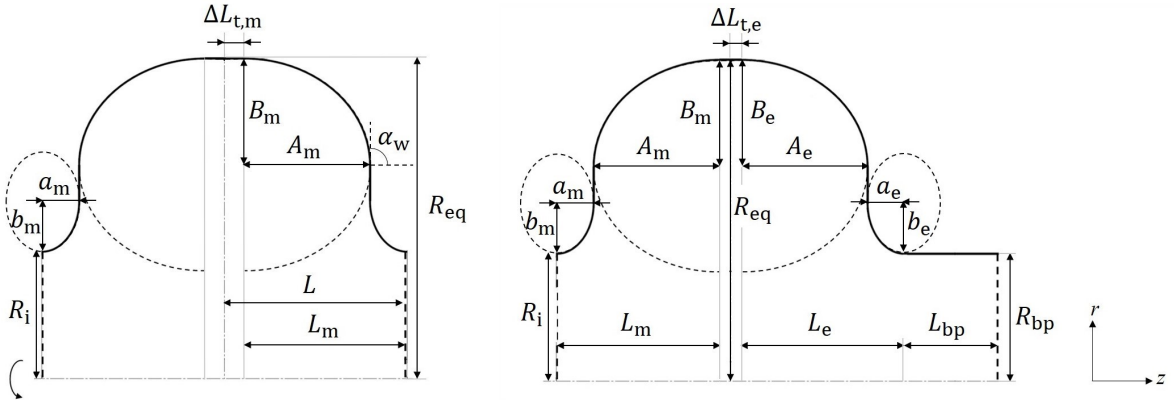

(a) Middle-cell **(b)** End-cell

Figure 2.4: Geometrical parameters of the middle-cell (a) and end-cell (b) of an elliptical cavity. The inner shape of the left-hand half end-cell is identical to that of the half middle-cells. The half end-cell connected to the beam pipe can have a slightly changed design. The geometry is axisymmetric around the centerline. The beam pipe length L_{bp} is not to scale.

The shape of the elliptical cavity cells is exclusively defined by eight parameters: A_k, B_k, a_k, b_k, α_w, L_k, R_{eq}, and R_i, where the index "k" = "m" for the middle-cells and "k" = "e" for the end-cells. Typically, the optimization of the cavity shape aims to determine a specific set of these parameters to balance all key performance parameters

related to RF, thermal, mechanical, and beam-dynamics aspects. The only fixed parameter that remains constant during the optimization process is the half-cell length L. For high-β cavities ($\beta \approx 1$), the theoretical half-cell length is proportional to a quarter of the wavelength at the FM frequency [17, p. 3]

$$L = \frac{\beta\lambda_0}{4}. \tag{2.1}$$

The length L determined by the equation (2.1) ensures that the particle beam experiences maximum acceleration in the same direction as it moves from one cell to the next. The theoretical half-cell length of an 801.58 MHz cavity operating at $\beta = 1$ is 93.5 mm. It is worth noting that in the actual design, the length L may deviate slightly from its theoretical value. Nonetheless, it is important to guarantee that the operating frequency and integrated cavity voltage are preserved despite this slight difference. Table 2.2 reports the optimized geometrical parameters of the middle and end-cells of the 5-cell cavity for the PERLE project. The listed parameters refer to the cavity design at its FM warm frequency of 798.45 MHz. The cavity design at warm frequency considers a tuning rationale to hit the target operating frequency at 2 K, also called cavity cold frequency, at the desired cavity length [61]. The tuning rationale involves several factors, including the frequency shift due to the estimated springback effect after cell stamping (see Subsection 6.1.2), the presence of non-homogeneous bulk material, the final chemistry applied to the cavity, and the impact of the cavity cool-down and evacuation. To simulate the cavity at its actual operating frequency, the warm design geometry can be scaled to ensure that the frequency of the FM aligns with the cold frequency at 2 K, which is 801.58 MHz for the 5-cell cavity for PERLE.

Table 2.2: Geometrical parameters of the middle and end-cells of the five-cell elliptical cavity for PERLE [62]. The listed parameters refer to the cavity design at its FM warm frequency of 798.45 MHz.

A_m [mm]	B_m [mm]	a_m [mm]	b_m [mm]	L_m [mm]	$\Delta L_\mathrm{t,m}$ [mm]	R_eq [mm]	R_i [mm]	α_w [degree]
64.454	54.579	19.10	25.92	83.554	10	163.98	65	90
A_e [mm]	B_e [mm]	a_e [mm]	b_e [mm]	L_e [mm]	$\Delta L_\mathrm{t,e}$ [mm]	L_bp [mm]	R_bp [mm]	L_bp [mm]
64.454	54.579	19.10	25.92	83.554	5.595	195.5	65	195.50

The geometrical parameters defining the elliptical cavity shape have been optimized with the primary objective of minimizing two key performance parameters: $E_\mathrm{pk}/E_\mathrm{acc}$, which represents the ratio of the peak electric field on the cavity surface to the cavity accelerating gradient, and $B_\mathrm{pk}/E_\mathrm{acc}$, which depicts the ratio of the peak magnetic field on the cavity surface to the accelerating gradient [58, 59]. Lower values of $E_\mathrm{pk}/E_\mathrm{acc}$

shifts the potential electron field emission onset to higher operating fields [17, p. 43]. The electron field emission is a phenomenon that limits the accelerating performance of an SRF cavity [33, p. 159]. It consists of the emission of electrons from the cavity walls in the presence of a strong surface electric field. The emitted electrons absorb RF energy and lower the Q_0 of the cavity. Lower values of $B_{\mathrm{pk}}/E_{\mathrm{acc}}$ reduce the surface losses on the cavity walls, shifting the quench field limit to higher operating fields. Superconducting cavities can quench when the temperature-dependent critical surface magnetic field is exceeded. The critical surface magnetic field for Nb cavities operating at temperatures ranging from 2 K to 4.2 K is approximately 200 mT. For SRF accelerators operating in CW mode, the critical magnetic field is the major limiting factor due to the risk of a cavity quench. Therefore, a so-called low-loss cavity design is required. An angle $\alpha_{\mathrm{w}} > 90°$ results in an higher $B_{\mathrm{pk}}/E_{\mathrm{acc}}$. Choosing an angle $\alpha_{\mathrm{w}} < 90°$ results in a re-entrant cavity contour. While a re-entrant shape may not raise concerns for normal conducting cavities, it is unfavorable for SRF cavities because chemical residues could be difficult to remove from a re-entrant surface during the necessary high-pressure water rinsing [58, 59]. The cells of the optimized five-cell cavity for PERLE feature a wall slope angle of $\alpha_{\mathrm{w}} = 90°$, which minimizes the ratio $B_{\mathrm{pk}}/E_{\mathrm{acc}}$ and represents a trade-off to balance all the other critical performance parameters, such as $E_{\mathrm{pk}}/E_{\mathrm{acc}}$. The chosen angle $\alpha_{\mathrm{w}} = 90°$ simultaneously increases the product $(R/Q)_{\parallel,0}G$, contributing to lower the RF power losses into the He bath at a given accelerating gradient (see equation (1.93)). Figures 2.5 (a) and (b) illustrate the electric and magnetic field distributions for the FM of the 801.58 MHz 5-cell cavity, respectively. The fields are scaled to the nominal accelerating gradient of 22.4 MV/m. The peak surface electric field is 50.46 MV/m, and the peak surface magnetic field is 96.32 mT.

The choice of the cavity iris aperture ($2R_{\mathrm{i}}$) significantly impacts the RF parameters of the cavity [21]. Both parameters $E_{\mathrm{pk}}/E_{\mathrm{acc}}$ and $B_{\mathrm{pk}}/E_{\mathrm{acc}}$ decrease as the cavity iris aperture diminishes. This improves the product $(R/Q)_{\parallel,0}G$, consequently reducing surface losses. However, this comes with the drawback of a larger loss factor $k_{\parallel}$ (see equation (5.20)), which increases the beam-induced HOM power (see equation (5.17)), and a decrease in the cell-to-cell coupling factor k_{cc}, which indicates the strength of the cell-to-cell coupling for each HOM field pattern. Typically, a relatively large cell-to-cell coupling factor is required, particularly as the number of cavity cells, N_{cell}, increases. The RF field amplitudes within beam pipes, where HOM couplers are installed, increase for larger k_{cc}-values. Consequently, a small cavity iris aperture compromises the HOM-damping efficiency. Lowering the iris aperture also reduces the cavity stiffness. This holds true particularly for cavities with straight walls ($\alpha_{\mathrm{w}} = 90°$), since the ratio between the cavity equator radius R_{eq} and the iris radius R_{i} is increased. The chosen relatively large iris radius $R_{\mathrm{i}} = 65$ mm represents a good compromise for balancing the cavity performance when compared to existing cavity designs [21]. It is worth noting that in an optimized cavity shape for a given R_{i}, the ratio $B_{\mathrm{pk}}/E_{\mathrm{acc}}$ cannot be further lowered without increasing $E_{\mathrm{pk}}/E_{\mathrm{acc}}$, and vice-versa. However, expanding the beam pipe diameter ($2R_{\mathrm{bp}}$) beyond the end-cell iris aperture can preserve both ratios.

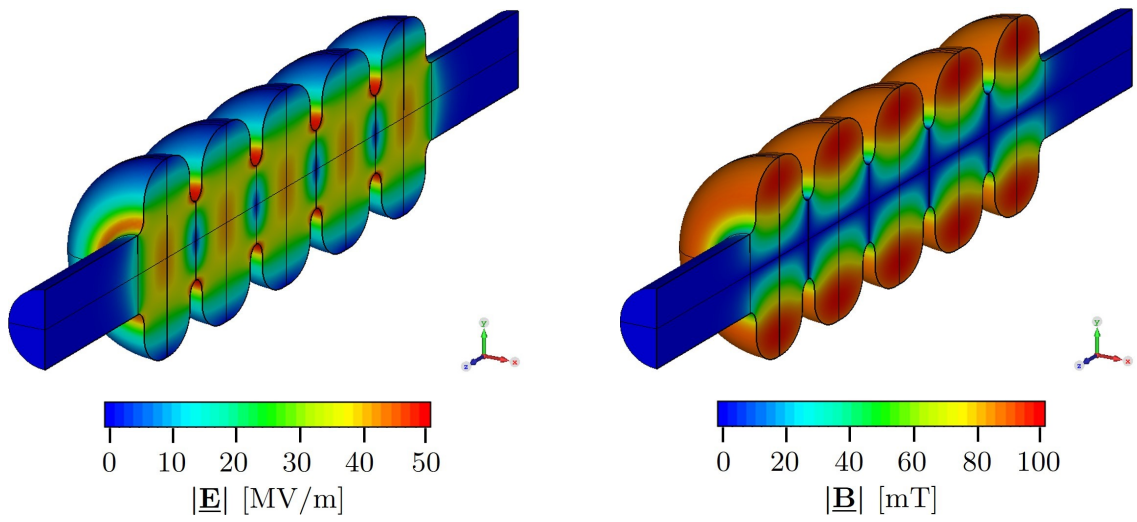

(a) Electric field **(b)** Magnetic flux density

Figure 2.5: Electric (a) and magnetic (b) field distributions for the fundamental mode of the PERLE cavity simulated using CST. The field magnitudes are scaled to the nominal accelerating gradient of 22.4 MV/m.

The beam pipe radius R_{bp} is selected in an RF cavity to ensure that the FM cutoff frequency $f_{\text{cut}}^{(\text{TM}_{01})}$ of the considered beam pipe resides above the FM frequency of the cavity. This keeps the FM electromagnetic field inside the cavity, with minimal leakage into the beam pipe. Referring to the more generalized case of a cylindrical resonator [33, pp. 30-32], the cutoff frequencies of the TM_{mn} and TE_{mn} modes for a beam pipe with radius R_{bp} can be derived from the equations (1.51) and (1.52) as

$$f_{\text{cut}}^{(\text{TM}_{mn})} = c\frac{u_{mn}}{R_{\text{bp}}}, \tag{2.2}$$

$$f_{\text{cut}}^{(\text{TE}_{mn})} = c\frac{u'_{mn}}{R_{\text{bp}}}. \tag{2.3}$$

The nth root of the mth order Bessel function, u_{mn}, and its derivative, u'_{mn}, are reported in Table 2.3 for $m = 0, 1, 2$ and $n = 1, 2, 3$.

Table 2.3: Zeros of the mth order Bessel function and its derivative.

	u_{mn}				u'_{mn}		
m \ n	1	2	3	m \ n	1	2	3
0	2.405	5.520	8.654	0	3.832	7.016	10.174
1	3.832	7.016	10.173	1	1.841	5.331	8.536
2	5.136	8.417	11.620	2	3.054	6.706	9.970

The choice of the beam pipe radius is also related to the definition of TM_{mnp} modes and TE_{mnp} trapped modes, which resonate within the cavity cells at frequencies lower than their respective TM_{mn} and TE_{mn} beam pipe cutoff frequencies. These modes exhibit exponentially decaying fields, with low-frequency modes often possessing the highest R/Q values. Consequently, trapped modes require mitigation through HOM-damping mechanisms (refer to Chapter 4) [21]. Modes resonating at frequencies beyond their cutoff frequencies are referred to as traveling modes, as they can propagate through the beam pipe tubes, facilitating their damping. Larger beam pipe radii offer the advantage of lowering beam tube cutoff frequencies, enabling HOMs to escape the cavity through the beam pipe and reducing their quality factors. In the case of the PERLE cavity design, it was decided to maintain a beam pipe radius of $R_{\mathrm{bp}} = 65$ mm, equivalent to the radius of the cavity iris. This choice was considered a well-balanced compromise between RF and HOM-damping performances. The selected beam pipe radius of 65 mm for the PERLE cavity yields cutoff frequencies of 1.77 GHz and 1.35 GHz for the TM_{01} and TE_{11} modes, respectively. Therefore, mode passbands ringing in the 5-cell PERLE cavity below their cutoff frequencies, such as the TM_{011} or TE_{111} passbands, remain trapped inside the cavity. More details about the most dangerous HOM passbands of the 5-cell PERLE cavity are provided in Subsection 2.2.2. The beam pipe length is selected to ensure that the field of FM mode is predominantly attenuated before reaching the beam pipe ends. The 5-cell cavity for PERLE is designed with a beam pipe length that is three times the size of the beam pipe radius, i.e., $L_{\mathrm{bp}} = 3R_{\mathrm{bp}}$.

The 5-cell cavity design for PERLE features middle half-cells and end half-cells with the same elliptical contour [58]. This allows for a single deep-drawing die for cavity prototyping, minimizing tooling costs. Chapter 6 provides details on the RF elliptical cavity fabrication. The cell equators include a flat section, denoted as $\Delta L_{\mathrm{t,m}}$ and $\Delta L_{\mathrm{t,e}}$ for the middle half-cells and end half-cells, respectively. These flat sections are trimmed during dumbbell measurements (refer to Section 6.2) to provide the required field flatness for the accelerating mode. For a multi-cell cavity with a fixed $\beta = v/c$, the cavity field flatness is an important figure of merit, quantifying the uniformity of the energy distribution across adjacent cells. It can be determined using the peak axial electric field as [63]

$$\eta_{\mathrm{ff}} = 1 - \frac{E_{\mathrm{p,max}} - E_{\mathrm{p,min}}}{\frac{1}{N_{\mathrm{cell}}} \sum_{i=1}^{N_{\mathrm{cell}}} E_{\mathrm{p},i}}, \tag{2.4}$$

where N_{cell} denotes the number of cavity cells, $E_{\mathrm{p,max}}$ and $E_{\mathrm{p,min}}$ are the maximum and minimum cell peak axial electric field in the cavity, respectively, and $E_{\mathrm{p},i}$ is the peak axial electric field in the ith cell. The field flatness, as expressed in the equation (2.4), describes the maximum field variation of the peak axial electric field across the cavity cells along the center axis, and it quantifies the field quality associated with the FM. A field flatness of 100% indicates a uniform distribution of the electric field maxima along the cavity axis. The simulated field flatness of the 5-cell cavity is 99%. Section 6.4 provides additional details about a multi-cell cavity's simulated and measured field

flatness. The simulated field profile of the TM_{010}-π mode of the 5-cell PERLE cavity is depicted in Figure 2.6. The main RF parameters of the 801.58 MHz five-cell bare cavity, i.e., without external damping mechanisms, are summarized in Table 2.4.

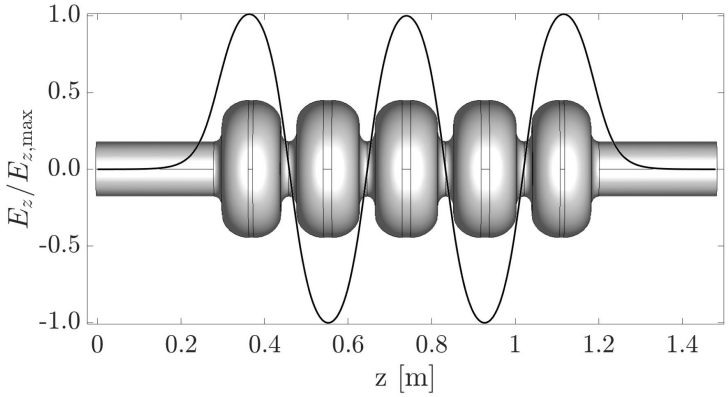

Figure 2.6: Normalized on-axis electric field amplitude of the TM_{010}-π mode at 801.58 MHz in the 5-cell bare-cavity for PERLE.

Table 2.4: RF figures of merit of the 5-cell cavity for PERLE.

Parameter	Symbol	Unit	Value
Operating frequency	f_0	MHz	801.58
Number of cells	N_{cell}	1	5
Active length	L_{act}	mm	917.92
Equator radius	R_{eq}	mm	163.98
Iris radius	R_{i}	mm	65
Beam pipe radius	R_{bp}	mm	65
Wall slope angle of the cell	α_{w}	degree	90
Nominal accelerating gradient	E_{acc}	MV/m	22.4
Nominal accelerating voltage	V_{acc}	MV	20.6
Quality factor at nominal gradient	Q_0	1	3×10^{10}
Longitudinal geometric shunt impedance of FM ($\beta = 1$)	$(R/Q)_{\parallel,0}$	Ω	523.6
$(R/Q)_{\parallel,0}$ per number of cells	$(R/Q)_{\parallel,0}/N_{\text{cell}}$	Ω	104.7
Geometry factor	G	Ω	274.6
Power dissipated by the FM in the cavity walls	$P_{\text{c},0}$	W	26.9
Total longitudinal loss factor ($\sigma_z = 3$ mm)	$k_{\parallel}$	V/pC	2.304
Cell-to-cell coupling factor	k_{cc}	%	2.93
Field flatness	η_{ff}	%	99
$N_{\text{cell}}^2/k_{\text{cc}}$ ratio	$N_{\text{cell}}^2/k_{\text{cc}}$	1	854
$E_{\text{pk}}/E_{\text{acc}}$ ratio (middle cell)	$E_{\text{pk}}/E_{\text{acc}}$	1	2.26
$B_{\text{pk}}/E_{\text{acc}}$ ratio (middle cell)	$B_{\text{pk}}/E_{\text{acc}}$	mT/(MV/m)	4.3
TE_{11} cutoff frequency for R_{bp}	$f_{\text{cut}}^{(\text{TE}_{11})}$	GHz	1.35
TM_{01} cutoff frequency for R_{bp}	$f_{\text{cut}}^{(\text{TM}_{01})}$	GHz	1.77

2.2.2 HOMs of the cavity

This section presents the analysis of the HOM spectrum of the 5-cell 801.58 MHz bare cavity for PERLE, which is one of the most important properties of a cavity. The eigenmode simulations, performed using CST, focus on cavity monopole and dipole modes, which hold significant importance in high-current ERL due to their potential impact on its performance. Higher order modes with high (R/Q)-values are of particular interest, as an elevated value of R/Q corresponds to a more amplified excitation induced by the circulating beam. If not adequately damped, monopole modes can lead to high HOM power loss (see Chapter 5) in SRF cavities, while dipole modes can cause transverse beam instabilities (see Chapter 3). Modes with frequencies close to beam harmonics are also particularly relevant. When a HOM is near a beam harmonic, the induced voltage may become significant, leading to potential beam instabilities. Therefore, during the design phase of an SRF cavity for high-current CW operation, it is essential to ensure that HOMs are kept sufficiently far from strong beam current harmonics [18]. Figure 2.7 illustrates the R/Q of the most relevant monopole and dipole passbands of the 5-cell 801.58 MHz cavity. The longitudinal geometric shunt impedance $(R/Q)_{\parallel}$ is calculated for the TM monopole modes, while the transversal geometric shunt impedance $(R/Q)_{\perp}$ is computed for the TM and TE dipole modes. Additionally, it compares HOM resonant frequencies with respect to the PERLE beam current spectrum, corresponding to the filling pattern and bunch timing presented in Figure 3.8 in Chapter 3 and calculated using the beam parameters listed in Table 2.1.

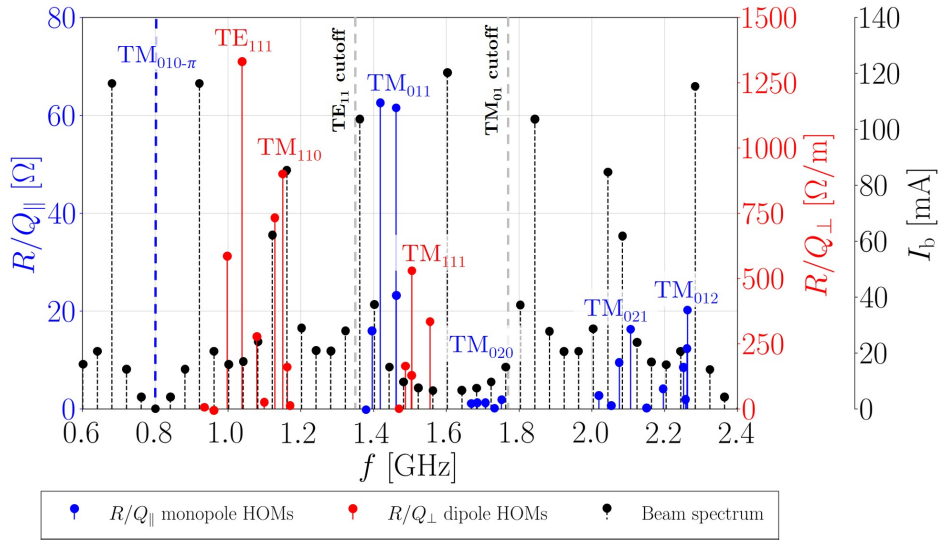

Figure 2.7: $(R/Q)_{\parallel}$ (blue lollipops) and $(R/Q)_{\perp}$ (red lollipops) of the most relevant monopole and dipole HOMs, respectively, of the 5-cell 801.58 MHz cavity until 2.4 GHz. Twenty-five monopole modes and fifteen dipole modes are shown. A blue-dashed line indicates the FM frequency. Gray-dashed lines represent the TM_{01} and TE_{11} beam pipe cutoff frequencies. Black-dashed lollipops depict the PERLE beam current spectrum.

The monopole passbands TM_{011} and TM_{020} and the dipole passbands TE_{111}, TM_{110} and TM_{111} are confined within the cavity's cells. The phase advance per cell of TE_{111}, TM_{020} and TM_{012} modes takes values from $\pi/5$ to π, while the phase of TM_{011}, TM_{110} and TM_{021} modes shifts from π to $\pi/5$. The trapped HOMs can limit the stable operation of the ERL. Consequently, they require strong damping to reduce their impedance $(R/Q)Q_{\mathrm{L}}$ below the beam instability limits and meet beam dynamics requirements (see Chapters 3 and 5). The monopole passband TM_{011} possesses the highest longitudinal geometric shunt impedance among the trapped monopole modes. Specifically, the longitudinal R/Q-values of the TM_{011}-$3\pi/5$ mode at 1.42 GHz and TM_{011}-$2\pi/5$ mode at 1.46 GHz are 62 Ω and 61 Ω, respectively. It is worth noting that some modes can become trapped within the cavity cells even if their resonant frequency is above their corresponding cutoff frequency. The TM_{012}-π mode, located at approximately 2.26 GHz, is relatively confined within the middle cells of the five-cell cavity, exhibiting a longitudinal geometric shunt impedance of 20 Ω. The two dipole passbands TE_{111} and TM_{110} exhibit the highest transversal geometric shunt impedance among the confined dipole modes. In particular, the TE_{111}-$4\pi/5$ mode at 1.03 GHz and TM_{110}-$3\pi/5$ mode at 1.51 GHz possess transversal R/Q-values of 1.3 $\times 10^3$ Ω/m and 893 Ω/m, respectively. The normalized electric field maps of some of the trapped high-(R/Q) monopole and dipole modes are illustrated in Figure 2.8.

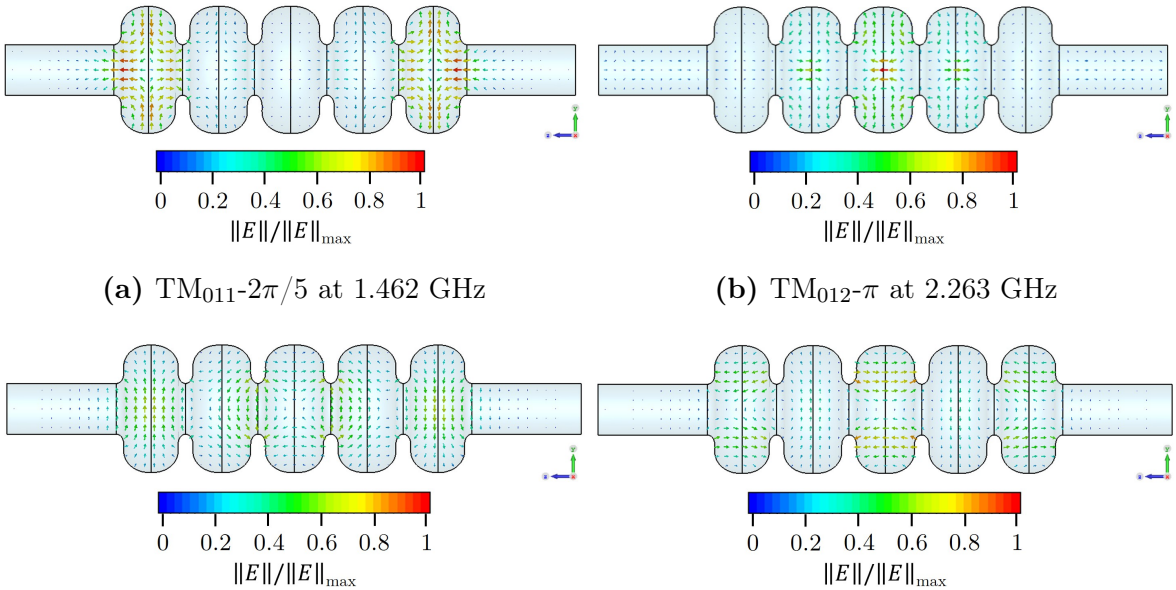

(a) TM_{011}-$2\pi/5$ at 1.462 GHz

(b) TM_{012}-π at 2.263 GHz

(c) TE_{111}-$4\pi/5$ at 1.039 GHz

(d) TM_{110}−$3\pi/5$ at 1.151 GHz

Figure 2.8: Cross-sectional view of the normalized electric field norm for significant monopole ((a) and (b)) and dipole HOMs ((c) and (d)) of the 5-cell 801.58 MHz bare cavity simulated using CST Studio Suite®. The phase advance is denoted for each mode.

Figure 2.7 illustrates that the modes with the highest R/Q values are kept sep-

arated from the main beam spectral lines, located at multiples of the fundamental mode frequency. This reduces concerns about potential voltage buildup from resonant interactions between HOMs and the beam spectrum lines with the highest current magnitude. While each cavity of a cryomodule is tuned to the fundamental mode frequency, the resonant frequency of the HOMs can change from one cavity to another because of manufacturing tolerances, typically within the range of several MHz for the HOMs [64] (refer to Subsection 6.1.2). Therefore, quantifying the frequency shift between the resonant frequencies of the analyzed modes and the closest lower and higher bunch harmonics is crucial for identifying potentially dangerous HOMs. Figures 2.9 (a) and (b) depict the calculated frequency shift between the investigated monopole and dipole modes, respectively, and their closest lower and higher bunch harmonics.

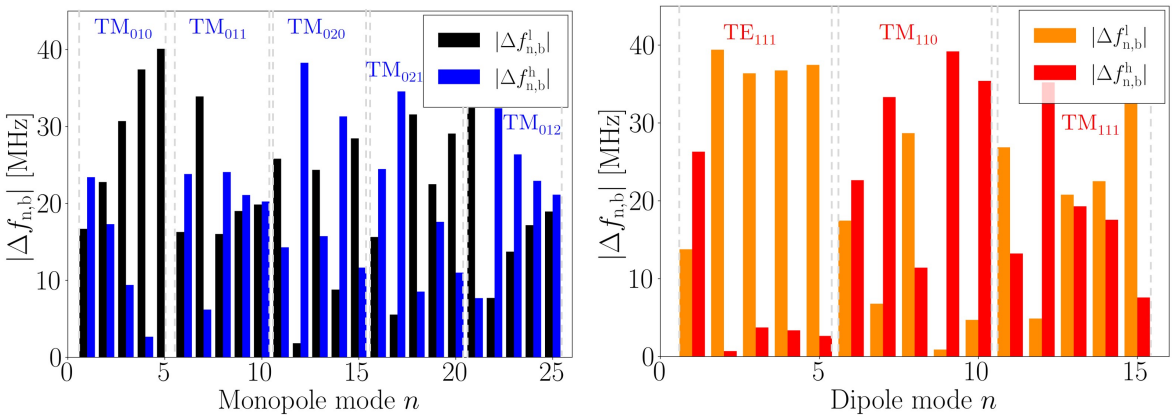

(a) Monopole modes **(b)** Dipole modes

Figure 2.9: Frequency shift between the resonant frequency of a mode n and its closest lower and higher bunch harmonics. The absolute difference between the mode frequency and its closest lower-frequency harmonic $|\Delta f^{\mathrm{l}}_{n,\mathrm{b}}|$ is represented in black for monopole modes (a) and orange for dipole modes (b), respectively. Similarly, the frequency shift to the nearest higher-frequency harmonic $|\Delta f^{\mathrm{h}}_{n,\mathrm{b}}|$ is depicted in blue for monopole modes (a) and red for dipole modes (b). The resonant frequency associated with each mode n is depicted in Figure 2.7.

The frequency shift of monopole HOMs ranges from 1.81 MHz to 38.26 MHz. The monopole HOMs with $(R/Q)_{\parallel} > 10\ \Omega$ are separated by at least 10 MHz from the nearest beam harmonic. For instance, the monopole modes TM_{011}-$3\pi/5$ (at 1.42 GHz) and TM_{011}-$2\pi/5$ (at 1.46 GHz) are positioned 16 MHz and 19 MHz away, respectively, from their closest beam current line. The relatively confined TM_{012}-π (at 2.26 GHz) is 19 MHz away from its closest beam harmonic. This frequency separation may be sufficient to exclude the possibility of resonant effects between the beam and the HOMs. The TM_{020}-$2\pi/5$ (at 1.68 GHz) mode presents a frequency shift from the closest current line of only 1.81 MHz. However, its proximity to its nearest bunch harmonic should not be a concern due to its low longitudinal geometric shunt impedance, $(R/Q)_{\parallel} = 0.9\ \Omega$. The frequency shift of dipole HOMs varies from 0.7 MHz to 39 MHz. While the mode

TE_{111}-$2\pi/5$ at 0.96 GHz, which shows a minimum frequency shift of only 0.7 MHz, should not pose any concern because of its low-$(R/Q)_\perp$ value of 0.1 Ω/m, the relatively low frequency shift of 3 MHz for the high-$(R/Q)_\perp$ TE_{111}-$3\pi/5$ and TE_{111}-$4\pi/5$ modes (at 0.99 GHz and 1.04 GHz, respectively) from their closest beam line needs to be monitored during the different stages of cavity manufacturing. The same might apply to the TM_{110}-$4\pi/5$ mode (at 1.13 GHz), whose frequency shift from the nearest harmonic is about 7 MHz. Subsection 7.2.3 provides details on the analysis of the HOM frequency deviation of the manufactured 5-cell Cu cavity prototype for PERLE.

2.3 Static and dynamic heat losses

The power consumption of the cryogenic system significantly influences the operational costs of an ERL [65]. Estimating the required power from the cryogenic system requires the evaluation of the static and dynamic heat losses in the cryomodule [66]. Static heat losses occur when the linac cryomodule components are at their design operating temperatures. Static losses are associated with inadequate insulation of the linac's cold components from their surroundings. Static losses exist even when no RF power is supplied to the cavities. They include conduction through radiation and conduction fluxes through supports, pipes, beamline HOM loads, and so forth [65, 67]. Dynamic heat losses emerge during the cavity operation due to the power dissipation caused by induced RF currents within the cavity surfaces.

The power dissipated in the walls of an SRF cavity by the FM, as given in the equation (1.91), constitutes the most relevant dynamic power loss in the He bath and represents the largest dynamic heat load in the cryomodule. For the 5-cell PERLE cavity, the power dissipation by the FM in the cavity walls at the nominal accelerating gradient ($E_{\mathrm{acc}} = 22.4$ MV/m) is $P_{\mathrm{c},0} = 26.9$ W. Given that the dynamic power loss by the FM is inversely proportional to the cavity Q_0, the quality factor becomes the primary cost driver in terms of dynamic cryogenic losses [66]. Therefore, minimizing dynamic heat losses is crucial for maintaining low costs associated with He refrigeration. The total AC wall power required to remove the static losses, P_{st}, and dynamic heat losses, P_{dyn}, from the cryomodule can be approximated as [66, 68]

$$P_{\mathrm{t,AC}} \approx \frac{1}{\eta_{\mathrm{c}}\eta_{\mathrm{t}}} \underbrace{P'_{\mathrm{st}} \frac{V_{\mathrm{RF}} L_{\mathrm{cav}}}{E_{\mathrm{acc}} L_{\mathrm{act}}}}_{P_{\mathrm{st}}} + \frac{1}{\eta_{\mathrm{c}}\eta_{\mathrm{t}}} \underbrace{V_{\mathrm{RF}} \frac{E_{\mathrm{acc}} L_{\mathrm{act}}}{(R/Q)_{\parallel,0} Q_0}}_{P_{\mathrm{dyn}}} . \tag{2.5}$$

Here, $V_{\mathrm{RF}} = V_{\mathrm{acc}} N_{\mathrm{cav}}$ represents the total required voltage for the cavities within the cryomodule, where N_{cav} is the number of cavities. The term η_c is the Carnot efficiency, which is defined as [17, p. 48]

$$\eta_{\mathrm{c}} = \frac{T_{\mathrm{bath}}}{T_{\mathrm{amb}} - T_{\mathrm{bath}}}, \tag{2.6}$$

where T_{bath} is the cavity operating temperature and T_{amb} is the ambient temperature. For $T_{\mathrm{bath}} = 2$ K and $T_{\mathrm{amb}} = 300$ K, the Carnot efficiency is $\eta_{\mathrm{c}} = 6.7 \times 10^{-3}$. The technical efficiency of the cryogenic plant, depicted as η_{t}, is estimated to be 20% at 2 K and 30% at 4.5 K operation [66]. The term P'_{st} represents the static losses per unit length, which are around 8 W/m at 500 MHz and vary approximately inversely with the square root of the FM frequency [69]. Therefore, the static losses per unit length are $P'_{\mathrm{st}} \approx 6.3$ W/m at 801.58 MHz. The static heat losses increase with the number of cavities. For a lower E_{acc}, more cavities are needed to attain the voltage V_{RF}, consequently leading to an increase of the static loss [66]. Conversely, dynamic heat losses increase proportionally with the accelerating gradient. Moreover, they depend on the $(R/Q)_{\parallel,0}$ and the material-dependent Q_0. It is worth noting that in the estimation of P_{dyn} in equation (2.5), only the dynamic losses related to the FM are considered. The undamped beam-induced power of trapped modes below their respective cutoff frequencies can increase dynamic heat losses in the cavity walls. HOM couplers are employed to decrease the external quality factor of HOMs and consequently lower the HOM power dissipated in the cavity walls. For a damped trapped HOM n, the ratio between the undamped HOM power $P_{\mathrm{nd},n}$ and the extracted HOM power $P_{\mathrm{ext},n}$ for the considered mode can be approximated as

$$\frac{P_{\mathrm{nd},n}}{P_{\mathrm{ext},n}} \approx \frac{Q_{\mathrm{ext},n}}{Q_{0,n}}. \tag{2.7}$$

However, the undamped HOM power is considered a small fraction in HOM-damped SRF cavities compared to the dynamic heat loss caused by the FM. For a HOM possessing a $Q_{0,n}$-value in the order of 10^{10} and a typical $Q_{\mathrm{ext},n}$ in the order of 10^5, the undamped HOM power will be 10^5 times lower than the extracted HOM power for the considered mode. Consequently, the undamped HOM power can be neglected when estimating the total AC wall power in an SRF cryomodule. Table 2.5 summarizes the estimated total static and dynamic heat losses and AC wall power for the four 5-cell Nb cavities within a PERLE cryomodule.

Table 2.5: Static and dynamic losses and AC wall power for the four 5-cell cavities of PERLE. Dividing the listed values by $N_{\mathrm{cav}} = 4$ returns the power requirements for a single 5-cell cavity.

Parameter	Symbol	Unit	Value
Required voltage	V_{RF}	MV	82.2
Static losses	P_{st}	W	37.4
Dynamic losses	P_{dyn}	W	107.5
Static losses scaled to the net cryogenic plant efficiency	$P_{\mathrm{st}}/(\eta_c\eta_t)$	kW	27.9
Dynamic losses scaled to the net cryogenic plant efficiency	$P_{\mathrm{dyn}}/(\eta_c\eta_t)$	kW	80.1
Total AC wall power	$P_{\mathrm{t,AC}}$	kW	108

A comparison of the losses associated with individual cavities between the PERLE and Cornell ERL cryomodules [70] is presented to provide a more comprehensive international context. The Cornell cryomodule consists of six 7-cell, 1.3 GHz Nb cavities operating at 1.8 K. Each cavity in the Cornell ERL achieves a nominal accelerating gradient of 16.2 MV/m with a required voltage of 13.1 MV. The $(R/Q)_{\parallel,0}$ and Q_0 values are 774 Ω and $2{\times}10^{10}$, respectively. The dynamic power losses are 11.1 W for the Cornell cavity and 26.9 W for the PERLE cavity, while the static power losses are approximately 6.5 W and 9.4 W, respectively. The total AC wall power required per cavity is around 14.6 kW and 27.1 kW for the Cornell cavity and the PERLE cavity, respectively. The lower losses observed in the Cornell cavity can primarily be attributed to its lower accelerating gradient compared to the PERLE cavity. Additional information on the RF figures of merit, power losses, and requirements of the Cornell ERL cryomodule is provided in [70].

2.4 Input RF power

The input power represents the amount of power supplied to an RF system. The input coupler, or Fundamental Power Coupler (FPC), has the role of transferring the RF power from a generator to the cavity and the beam [17, p. 403]. The FPC has to compensate for the losses in the cavity walls due to the RF field and beam energy losses. The loaded Q must be optimized for the linac cavities of an ERL to deal with energy recovery and microphonics. In the following, a set of expressions to determine the power supplied by the generator to a cavity in the case of an ERL is presented [71]. The derived equations allow for determining the optimum setting of the cavity parameters (coupling factor, loaded Q, and static detuning) when operating under beam loading and in the presence of microphonics.

2.4.1 Optimization with respect to tuning for energy recovery

In a multi-pass ERL, the bunch train consists of a number of accelerating bunches and decelerating bunches passing through the cavity during its operation. These bunches collectively contribute to the total beam current seen by the cavity. The total beam current $\underline{I}_\mathrm{b}$ could be obtained by summing the resulting accelerating current $\underline{I}_\mathrm{b,acc}$ and decelerating current $\underline{I}_\mathrm{b,dec}$ vectors as

$$\underline{I}_\mathrm{b} = \underline{I}_\mathrm{b,acc} + \underline{I}_\mathrm{b,dec} = I_\mathrm{b,0} \left(\sum_{i=1}^{N_\mathrm{b,acc}} \mathrm{e}^{j\psi_{\mathrm{acc},i}} + \sum_{k=1}^{N_\mathrm{b,dec}} \mathrm{e}^{j\psi_{\mathrm{dec},k}} \right), \tag{2.8}$$

where $I_\mathrm{b,0}$ is the average beam current or ERL injection current, $N_\mathrm{b,acc}$ the total number of accelerating bunches, $N_\mathrm{b,dec}$ the total number of decelerating bunches, and $\psi_{\mathrm{acc},i}$

and $\psi_{\mathrm{dec},k}$ represent the angular position of the ith accelerating bunch and the kth decelerating bunch, respectively.

The input power required in a cavity for accelerating a beam with a total current of magnitude I_b, at a phase ψ_b with respect to the crest of the FM electric field, could be written as [71]

$$P_\mathrm{in} = \frac{P_{\mathrm{c},0}}{4\beta}\left\{(1+\beta+b)^2 + [(1+\beta)\tan(\psi) - b\tan(\psi_\mathrm{b})]^2\right\}, \tag{2.9}$$

where β is the cavity coupling factor and $P_{\mathrm{c},0}$ the power dissipated in the cavity walls by the FM. In the equation (2.9), the term $\tan(\psi)$ represents the total amount of detuning, which is given by

$$\tan(\psi) = -2Q_{\mathrm{L},0}\frac{\delta f_0 - \delta f_\mathrm{m}}{f_0}, \tag{2.10}$$

where ψ is the tuning angle, δf_0 is the static detuning, δf_m the microphonic detuning, and $Q_{\mathrm{L},0} = Q_0/(1+\beta)$ is the loaded quality factor of the FM mode at frequency f_0. The term b represents the ratio between the power absorbed by the beam and the power dissipated in the cavity walls

$$b = \frac{I_\mathrm{b}(R/Q)_{\parallel,0}Q_0\cos(\psi_\mathrm{b})}{V_\mathrm{acc}}. \tag{2.11}$$

Substituting the equations (2.10) and (2.11) into equation (2.9) and using the definition of intrinsic cavity bandwidth $\Delta f_0 = f_0/Q_0$, the input power for a cavity can be rewritten as

$$P_\mathrm{in} = \frac{P_{\mathrm{c},0}}{4\beta}\left\{(1+\beta+b)^2 + \left[\frac{2\delta f_0}{\Delta f_0} + \frac{2\delta f_\mathrm{m}}{\Delta f_0} + b\tan(\psi_\mathrm{b})\right]^2\right\}. \tag{2.12}$$

The amount of static detuning required to minimize the input power is given by

$$\delta f_0 = -\frac{\Delta f_0}{2} b\tan(\psi_\mathrm{b}), \tag{2.13}$$

which is independent of the coupling factor β. This term includes the Lorentz force detuning and mechanical tuner static detuning. Finally, in the absence of microphonics, the input power at optimum tuning is provided by

$$P_\mathrm{in} = \frac{P_{\mathrm{c},0}}{4\beta}(1+\beta+b)^2. \tag{2.14}$$

2.4.2 Optimization with respect to cavity coupling for energy recovery

In the presence of microphonics, the input power at optimum tuning can be written as

$$P_{\text{in}} = \frac{P_{\text{c},0}}{4\beta}\left\{(1+\beta+b)^2 + \left[\frac{2\delta f_{\text{m}}}{\Delta f_0}\right]^2\right\}, \tag{2.15}$$

where δf_{m} is the amount of microphonic detuning. The optimum coupling factor, and consequently the optimum loaded quality factor $Q_{\text{L},0}$, could be derived by differentiating the equation (2.15) with respect to β and equating it to zero as

$$\beta_{\text{opt}} = \sqrt{(b+1)^2 + \left(\frac{2\delta f_{\text{m}}}{\Delta f_0}\right)^2}. \tag{2.16}$$

The input power at optimum coupling is obtained by substituting the optimum coupling factor β_{opt} into the equation (2.15) as

$$P_{\text{in}} = \frac{P_{\text{c},0}}{2}\left[(b+1) + \sqrt{(b+1)^2 + \left(\frac{2\delta f_{\text{m}}}{\Delta f_0}\right)^2}\right]. \tag{2.17}$$

In the absence of a beam ($b = 0$), the equations (2.16) and (2.15) become

$$\beta_{\text{opt}} = \sqrt{1 + \left(\frac{2\delta f_{\text{m}}}{\Delta f_0}\right)^2}, \tag{2.18}$$

and

$$P_{\text{in}} = \frac{P_{\text{c},0}}{2}\left[1 + \sqrt{1 + \left(\frac{2\delta f_{\text{m}}}{\Delta f_0}\right)^2}\right]. \tag{2.19}$$

2.4.3 Input power for the PERLE cavity

The linac cavities of PERLE are expected to operate at a gradient of 22.4 MV/m. The generator power is expected to be fed into each cavity by a Superconducting Proton Linac (SPL) type power coupler, which is able to deliver 500 kW of power in CW operation [72]. Based on the latest bunching PERLE scenario, the ERL can be operated on-crest to deliver to the interaction points a bunch with minimal energy spread [48, 73]. Under these conditions, the particles travel within the linac on the crest of the FM electric field, maximizing the utilization of the entire available gradient. A beam on the accelerating crest is defined at $\psi_{\text{acc}} = 0°$, while a beam on the decelerating crest is set at $\psi_{\text{dec}} = 180°$. When the phase difference between accelerating and decelerating beams

is 180°, the magnitude of the beam current vector $\underline{I}_\mathrm{b}$ is null, and the phase with respect to the RF crest ψ_b is zero. This condition corresponds to a zero-beam loading scenario ($b = 0$) [74]. Lorentz force detuning or microphonic effects can detune the cavity, increasing the input power needed to maintain the accelerating field in the cavity. Other bunching scenarios currently under study for PERLE [48, 73] could foresee the off-crest acceleration of the beam in at least one linac to have a longitudinal match that increases the beam peak current from the injector to the interaction points. Consequently, the beam loading is no longer null, and the linac cavities must be detuned by the amount of static detuning δf_0 to minimize the generator power. In the following, we investigate the scenario of zero-beam loading with on-crest operation ($\psi_\mathrm{acc} = 0°, \psi_\mathrm{dec} = 180°$) of the linac, and two possible scenarios of off-crest operation: ($\psi_\mathrm{acc} = 11.1°, \psi_\mathrm{dec} = 188.6°$) and ($\psi_\mathrm{acc} = 13.6°, \psi_\mathrm{dec} = 188.6°$).

Due to the energy gain and synchronization requirements, all $N_\mathrm{b,acc}$ accelerating bunches share the same accelerating phase ψ_acc, and all $N_\mathrm{b,dec}$ decelerating bunches have a common decelerating phase ψ_dec. Therefore, the equation (2.8) simplifies to

$$\underline{I}_\mathrm{b} = \underline{I}_\mathrm{b,acc} + \underline{I}_\mathrm{b,dec} = I_\mathrm{b,0}(N_\mathrm{b,acc}\mathrm{e}^{j\psi_\mathrm{acc}} + N_\mathrm{b,dec}\mathrm{e}^{j\psi_\mathrm{dec}}). \tag{2.20}$$

Figure 2.10 (a) illustrates in a polar plot the resulting accelerating and decelerating currents for the three investigated cases, along with the position of the bunches with respect to the RF crest. Figure 2.10 (b) depicts the corresponding required input power at optimum tuning and in the absence of microphonics for the 5-cell PERLE cavity as a function of the cavity loaded Q. The input power curves are obtained for $(R/Q)_{\parallel,0} = 523.6\ \Omega$, nominal accelerating voltage $V_\mathrm{acc} = 20.6$ MV and $Q_0 = 3 \times 10^{10}$.

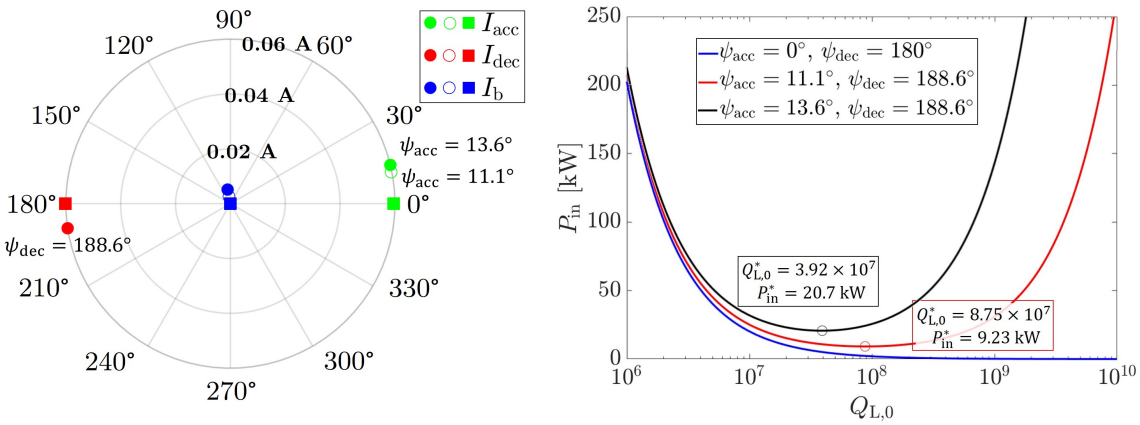

(a) Beam current and phase

(b) Input power at optimum tuning

Figure 2.10: (a) Polar plot showing the phase (in degrees) and current (in amperes) of accelerating (red) and decelerating bunches (red) in the studied on-crest (squares) and off-crest (circles) scenarios. The resulting beam loading in both cases is marked in blue. Input power at optimum tuning and $\delta f_\mathrm{m} = 0$ as a function of Q_L for the three studied cases (b).

In the case of on-crest operation, the magnitude of the total current is null, and the input power needs to compensate only for the power dissipated on the cavity walls ($P_{\mathrm{in}} = P_{\mathrm{c},0} = 26.9$ W). For the ERL off-crest operation ($\psi_{\mathrm{acc}} = 11.1°, \psi_{\mathrm{dec}} = 188.6°$), the optimum detuning value is -26.2 Hz, and the cavity requires $P^*_{\mathrm{in}} = 9.23$ kW at $Q^*_{\mathrm{L},0} = 8.75 \times 10^7$. In the off-crest scenario ($\psi_{\mathrm{acc}} = 13.6°, \psi_{\mathrm{dec}} = 188.6°$), the optimum detuning value is -52.23 Hz, and the cavity necessitates $P^*_{\mathrm{in}} = 20.7$ kW at $Q^*_{\mathrm{L},0} = 3.92 \times 10^7$. The minimum point of each curve indicates the optimum loaded quality factor and the corresponding minimum input power per cavity. Any deviation from $Q^*_{\mathrm{L},0}$ leads to an increase in the input power required to preserve the accelerating field in the cavity. The choice of the loaded-Q value relies not only on the beam loading but also on the value of the cavity bandwidth $\Delta f_{3\mathrm{dB}} = f_0/Q_{\mathrm{L},0}$. The cavity bandwidth at optimum detuning is 9.16 Hz and 20.45 Hz for the ($\psi_{\mathrm{acc}} = 11.1°, \psi_{\mathrm{dec}} = 188.6°$) and ($\psi_{\mathrm{acc}} = 13.6°, \psi_{\mathrm{dec}} = 188.6°$) off-crest scenarios, respectively. The cavity bandwidth must be higher than the microphonic detuning for an SRF cavity, which is typically lower than 100 Hz [75]. Consequently, the $Q_{\mathrm{L},0}$ has to be lowered by approximately one order of magnitude to increase the cavity bandwidth to values higher than 100 Hz.

Finally, one major figure of merit in an ERL is the ratio between the klystron power and the beam power

$$\eta_{\mathrm{b}} = \frac{P_{\mathrm{kly}}}{P_{\mathrm{b}}} \approx \frac{1.26 P_{\mathrm{in}}}{N_{\mathrm{b,acc}} I_{\mathrm{b},0} V_{\mathrm{acc}} \cos(\psi_b)}, \tag{2.21}$$

where P_{kly} is the klystron power. The factor of 1.26 is chosen to ensure that the klystron operates below its -1 dB saturation point, thereby avoiding any distortion or non-linear effects in the amplification process. This ratio has to be kept small for efficient energy recovery in the ERL. Furthermore, a power overhead is required to compensate for perturbations caused by microphonics [76]. For PERLE in the on-crest ERL mode scenario ($\psi_b = 0$), the total beam power per cavity is roughly $P_{\mathrm{b}} \approx 1.23$ MW. Assuming $\eta_{\mathrm{b}} = 0.1$, the minimum required klystron power per cavity is approximately $P_{\mathrm{kly}} \approx 123$ kW. Consequently, the estimated input power per cavity is $P_{\mathrm{in}} \approx 97.86$ kW. Therefore, the loaded-Q has to be lowered with respect to the value at optimum detuning to meet the estimated input power requirements.

Figures 2.11 (a) and (b) depict the input power at optimum detuning as a function of the cavity $Q_{\mathrm{L},0}$ in the case of on-crest operation and one of the two discussed off-crest scenarios ($\psi_{\mathrm{acc}} = 13.6°$, $\psi_{\mathrm{dec}} = 188.6°$) for different microphonic detuning values, respectively. If the maximum available power per cavity is around 123 kW, in the case of on-crest operation, choosing a $Q_{\mathrm{L},0}$ between 2.5×10^6 and 4×10^6 could allow controlling microphonic detuning up to 100 Hz. Assuming a microphonic detuning of $\delta f_{\mathrm{m}} = 60$ Hz, the required input power per cavity is 92.36 kW for $Q_{\mathrm{L},0} = 2.5 \times 10^6$ and 68.79 kW for $Q_{\mathrm{L},0} = 4 \times 10^6$. In the case of off-crest operation ($\psi_{\mathrm{acc}} = 13.6°, \psi_{\mathrm{dec}} = 188.6°$) and for the same amount of microphonic detuning, the needed input power per cavity is 103.05 kW for $Q_{\mathrm{L},0} = 2.5 \times 10^6$ and 79.68 kW for $Q_{\mathrm{L},0} = 4 \times 10^6$. The cavity bandwidth for these

two loaded-Q values exceeds the microphonic detuning of 100 Hz, with values of 320 Hz and 200 Hz, respectively. Employing a fixed input coupler with a $Q_{\mathrm{L},0}$ in the range from 2.5×10^6 to 4×10^6 could present a valuable solution for PERLE in the studied scenarios. Although a higher $Q_{\mathrm{L},0}$ offers the advantage of reducing the input power requirement, it comes with the trade-off of reduced cavity bandwidth. Conversely, a lower $Q_{\mathrm{L},0}$ enhances the cavity bandwidth but will necessitate a higher input power. Finally, controlling microphonic effects with a Ferro-Electric Fast Reactive Tuner (FE-FRT) can reduce the amount of required input power per cavity in the ERL [77].

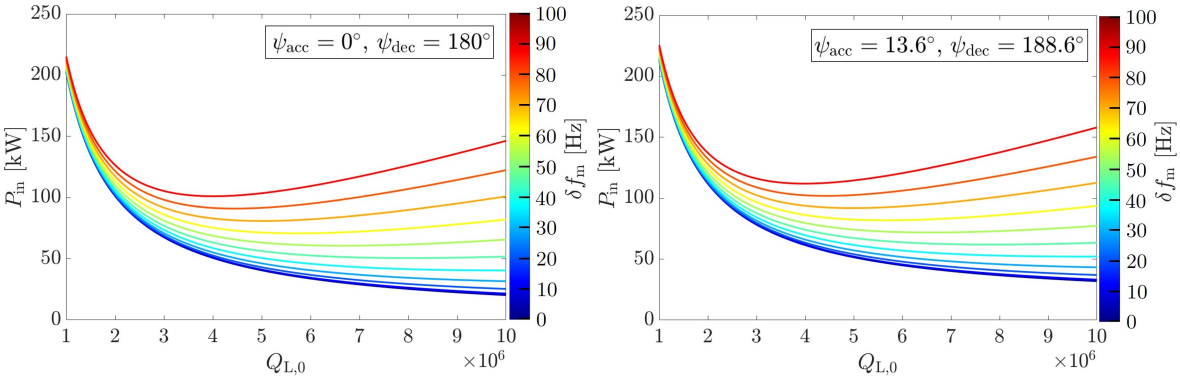

(a) On-crest operation **(b)** Off-crest operation

Figure 2.11: Input power at optimum tuning as a function of the cavity loaded Q for different microphonic detuning values: on-crest operation (a) and one possible scenario of off-crest operation (b).

3 Beam breakup instability studies

This chapter investigates the Beam Breakup (BBU) instability phenomenon in an ERL. The objective is to estimate the longitudinal and transverse impedance limits beyond which beam instabilities can rise during multi-pass ERL operation. The evaluation of the impedance thresholds is crucial for determining the required loaded quality factor Q_{L} for each relevant HOM, which ultimately drives the optimization of the HOM coupler design. Additionally, the threshold current, which represents the maximum achievable beam current in the machine, is evaluated.

3.1 Beam breakup instabilities

Energy recovery linacs offer the potential for operation with high beam current and simultaneously low emittance. A widely recognized limitation on the achievable beam current in an ERL is the occurrence of beam breakup instabilities. This phenomenon can emerge from the interaction between the traversing beam and the HOMs of an RF accelerating cavity at a sufficiently high current. BBU instabilities can be classified into two main categories: cumulative [17, p. 346] and regenerative [78] instabilities. The cumulative BBU effect involves the accumulation of beam deflection over a single pass in multiple accelerating structures. Cumulative BBU instabilities mainly occur in large-scale linacs or those operating at very high-current [79]. Therefore, they are out of the scope of this study. The main focus in high-current ERLs is on regenerative BBU, which occurs when the same bunch train passes through each RF cavity multiple times. This establishes a feedback loop between the recirculating beam and the HOM fields of a cavity, which closes when the beam returns to the same cavity during a subsequent pass in the ERL.

In a multi-pass machine, the beam experiences off-axis deflection caused by the transverse EM field generated by dipole modes during its initial pass. Consequently, the beam returns to the same cavity with a transverse offset in subsequent passes. It then exchanges energy with dipole HOMs that further deflect successive bunches. If the average beam current surpasses a threshold current, denoted as I_{th}, the feedback loop between the beam position offset and the dipole fields can become unstable. In the event that dipole HOMs are not adequately damped, the amplitude of dipole fields can undergo exponential growth until bunches hit the beam pipe, eventually resulting

in the loss of the beam. This effect is commonly known as transverse BBU instability, which is the primary limiting stability mechanism in ERLs [2].

Similarly, longitudinal BBU instabilities can arise when the excitation of monopole modes by the beam induces a change in the energy of the bunch. This leads to a shift in the arrival time of the bunch at the cavity [80]. Assuming an initial excitation of a longitudinal mode and perfectly spaced bunches entering a cavity on the first pass. The longitudinal mode modulates the energy of the bunches as they exit the cavity. If the isochronicity of the recirculation optics on the second or higher passes is not precisely maintained, the energy modulation experienced by the bunches is manifested as spacing modulation. As a result, a side-band current is generated, characterized by a frequency matching that of the exciting HOM. Therefore, the resulting current can amplify the excitation of the considered longitudinal HOM during subsequent passes, yielding an even higher induced current. In this case, the threshold condition for instability is satisfied when the excitation leads to a self-enhancement process through the induced current, which matches the original cavity excitation. It is important to note that in longitudinal BBU, the induced current can only reach a magnitude equivalent to the average beam current of the ERL before reaching saturation [81].

3.2 Beam breakup instability thresholds

This section first briefly introduces the concept of the transfer matrix in beam dynamics [82, p. 87]. The transfer matrix permits the representation of the bunch position within a system. Subsequently, an analytical formulation for calculating the BBU threshold current, impedance threshold, and external quality factor requirements in a multi-turn ERL is presented.

3.2.1 Transfer Matrix

Consider a charged particle traveling through a system. At any given position ζ along a nominal trajectory, the particle's state can be described using a vector (single-column matrix) $\mathbf{X}(\zeta)$, with

$$\mathbf{X}^{\mathrm{T}}(\zeta) = [x(\zeta), x'(\zeta), y(\zeta), y'(\zeta), l(\zeta), \Delta p/p]. \tag{3.1}$$

The terms of equation (3.1) are defined as follows: x is the horizontal position of the particle from the nominal trajectory; $x' = dx/d\zeta$ denotes the angle that the particle forms in the horizontal plane with respect to the nominal trajectory; y represents the vertical position of the particle from the nominal trajectory; $y' = dy/d\zeta$ is the angle that the particle forms in the vertical plane with respect to the nominal trajectory; $l(\zeta)$ is the path length difference between the arbitrary trajectory of the particle and its nominal trajectory; $\Delta p/p$ is the fractional momentum deviation of the particle from the nominal trajectory [83].

The 6×6 transfer matrix $\mathbf{M}$ is used to describe the transformation of the particle's state as it moves from an initial position ζ_i to a final position ζ_f via

$$\mathbf{X}(\zeta_\mathrm{f}) = \mathbf{M}\mathbf{X}(\zeta_\mathrm{i}). \tag{3.2}$$

The transfer matrix $\mathbf{M}$, at the first order in the equation (3.2), is used to map the particle's motion through accelerating structures, individual magnets, or drift distances. The matrix $\mathbf{M}$ can be extended to include second and high-order terms [84]. For an ERL, the energy of the bunches varies from one turn to the next. Therefore, the following study considers a transfer matrix for each turn to account for the energy variation of the bunch in the ERL [85].

3.2.2 Threshold current

The threshold current is the highest allowed beam current before the HOM voltage undergoes exponential growth, resulting in beam instabilities. An analytical formulation for the BBU threshold current can be derived by equating the energy dissipated on the cavity walls to the energy deposited by the beam into an HOM [78]. In the simple case of a single cavity containing a HOM n with frequency ω_n driving instability for a bunch in a two-pass ERL, the first-order analytical expression for the threshold current, which applies to both longitudinal and transverse BBU instabilities, is given by [2, 86, 87]

$$I_\mathrm{th} = -\frac{2E_\mathrm{b}}{e(R/Q)_n Q_{\mathrm{L},n} k_n M_{ij} \sin(\omega_n t_\mathrm{r})}, \tag{3.3}$$

where t_r is the recirculation time, E_b is the energy of the beam in the recirculation arc, M_{ij} is the $(i,\, j)$ element of the beam transfer matrix with $1 \leq i, j \leq 6$, e is the electron charge, $(R/Q)_n$ is the geometric shunt impedance of the considered HOM, $Q_{\mathrm{L},n}$ is its loaded quality factor, and $k_n = \omega_n/c$ defines its wave number with c the speed of light. When n refers to a dipole HOM, and $i, j = 1, 2$ or 3,4, the equation (3.3) returns the threshold current of the transverse BBU. If n denotes a monopole HOM, and $i, j = 5, 6$, the equation (3.3) gives the threshold current of the longitudinal BBU. Specifically, the terms M_{12} and M_{34} relate the angular kick imparted to the beam by a dipole HOM to the horizontal and vertical offset after one recirculation, respectively. The M_{56} term establishes a relationship between the change in beam energy and the time shift of the beam. Equation (3.3) is valid only when the condition $M_{ij} \sin(\omega_n t_\mathrm{r}) < 0$ is satisfied. If $M_{ij} \sin(\omega_n t_\mathrm{r}) > 0$, the first-order expansion of the analytical solution does not provide a physically significant threshold current. In such cases, pursuing a higher-order solution becomes necessary [88].

For a machine featuring more than two passes and two linacs, such as PERLE, whose layout is illustrated in Figure 3.1, the expression for the threshold current can be reformulated as [87, 89, 90]

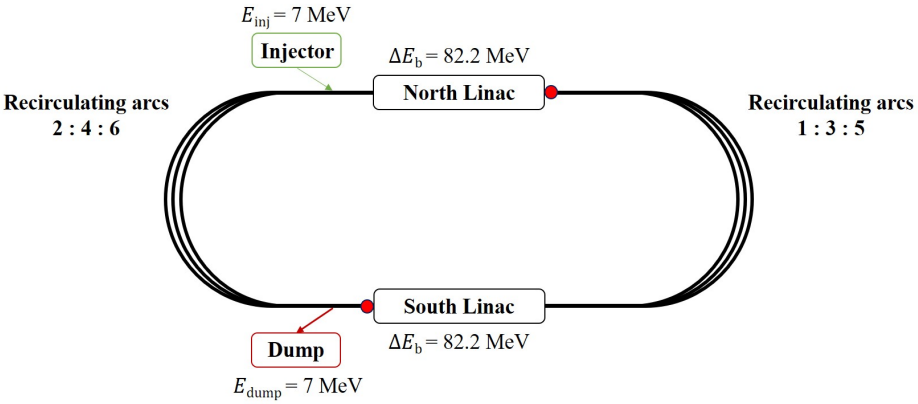

Figure 3.1: Schematic view of the 500 MeV PERLE layout. The accelerator complex comprises two parallel 82.2 MeV SC linacs, each hosting four 801.58 MHz 5-cell elliptical Nb cavities ($\beta = 1$), completed with three recirculating arcs on each side. The red dots indicate the linacs' exits, referred to as checkpoints in our analytical model. The terms "north Linac" and "south Linac" refer to "Linac 1" and "Linac 2" as shown in Figure 2.1.

$$I_{\mathrm{th}} = -\frac{2E_{\mathrm{b}}}{e(R/Q)_n Q_{\mathrm{L},n} k_n \sum_{m>l=1}^{N_{\mathrm{c}}} [(E_{\mathrm{b}}/E_{\mathrm{b}}^m) M_{ij}^{lm} \sin(\omega_n t_{\mathrm{r}}^{lm})]}, \tag{3.4}$$

where E_{b}^m is the beam energy at checkpoint m, M_{ij}^{lm} is the (i, j) element of the beam transfer matrix M^{lm} from checkpoint l to the consecutive checkpoint m, and t_{r}^{lm} is the recirculation time from checkpoint l to successive checkpoint m. In equation (3.4), N_{c} represents the overall number of checkpoints, depicting the exits of the linacs. For example, the indexes $m = 1$ and $m = 2$ represent the exit of the north linac and the exit of the south linac in the first turn, respectively; the indexes $m = 3$ and $m = 4$ depict the entry of the north linac and the exit of the south linac in the second turn, respectively, and so forth. This model is referred to as the multiple checkpoint analytical model [90].

3.2.3 Impedance threshold

It is common practice to compare the impedance of a cavity with the coupled-bunch instability limits. From the equation (3.4), the impedance requirement for a mode n in a multi-pass machine operating at a beam current $I_{\mathrm{b,op}}$ could be derived as

$$(R/Q)_n Q_{\mathrm{L},n} \leq \underbrace{-\frac{2E_{\mathrm{b}}}{eI_{\mathrm{b,op}} k_n \sum_{m>l=1}^{N_{\mathrm{c}}} [(E_{\mathrm{b}}/E_{\mathrm{b}}^m) M_{ij}^{lm} \sin(\omega_n t_{\mathrm{r}}^{lm})]}}_{Z_n^{\mathrm{th}}}. \tag{3.5}$$

The right-hand side term of equation (3.5) denotes the impedance threshold Z_n^{th}, which is the value of the impedance of a mode n beyond which multi-bunch instabilities arise.

The longitudinal impedance threshold of a monopole mode n can be obtained from equation (3.5), considering $i, j = 5, 6$, as follows

$$Z^{\mathrm{th}}_{\parallel,n} = (R/Q)_{\parallel,n} Q_{\mathrm{L},n} = -\frac{2E_{\mathrm{b}}}{eI_{\mathrm{b,op}} k_n \sum_{m>l=1}^{N_{\mathrm{c}}} [(E_{\mathrm{b}}/E^m_{\mathrm{b}}) M^{lm}_{56} \sin(\omega_n t^{lm}_{\mathrm{r}})]}. \tag{3.6}$$

Similarly, the transversal impedance threshold of a dipole mode n can be derived as

$$Z^{\mathrm{th}}_{\perp,n} = (R/Q)_{\perp,n} Q_{\mathrm{L},n} k_n = -\frac{2E_{\mathrm{b}}}{eI_{\mathrm{b,op}} \sum_{m>l=1}^{N_{\mathrm{c}}} [(E_{\mathrm{b}}/E^m_{\mathrm{b}}) M^{lm}_{ij} \sin(\omega_n t^{lm}_{\mathrm{r}})]}, \tag{3.7}$$

where $i, j = 1, 2$ for dipole modes with horizontal polarization, while $i, j = 3, 4$ for dipole modes with vertical polarization. The longitudinal impedance threshold is expressed in units of Ω and exhibits an inverse relationship with the resonance frequency. The transversal impedance threshold is defined in Ω/m and is independent of the resonance frequency. Moreover, impedance thresholds scale linearly with the beam energy and inversely with the beam current. The impedance threshold can be affected by a frequency spread between the cavities, which can emerge from operating conditions or manufacturing tolerances [91, 92]. In the following analysis, the impact of the frequency spread between cavities is not considered.

3.2.4 Critical external quality factor

The primary strategy to mitigate coupled-bunch instabilities in SRF cavities is to reduce the Q_{ext} of the cavity HOMs by employing HOM couplers and consequently minimize their impedance $(R/Q)Q_{\mathrm{L}}$. In SRF cavities, the critical Q_{ext} for monopole and dipole HOMs, beyond which BBU instabilities may occur, can be evaluated from the equations (3.6) and (3.7), respectively, as

$$Q^{\mathrm{th}}_{\mathrm{ext}\parallel,n} = \frac{Z^{\mathrm{th}}_{\parallel,n}}{(R/Q)_{\parallel,n}}, \tag{3.8}$$

$$Q^{\mathrm{th}}_{\mathrm{ext}\perp,n} = \frac{Z^{\mathrm{th}}_{\perp,n}}{(R/Q)_{\perp,n} k_n}. \tag{3.9}$$

This conservative approach establishes an optimization criterion for the damping performance of HOM couplers. The objective is to sufficiently suppress HOMs to avoid the potential occurrence of BBU instabilities in the ERL.

3.3 Regenerative BBU studies in PERLE

After the recent advancements on the beamline lattice for the 500 MeV PERLE version designed by A. Bogacz [93], regenerative BBU analytical studies have been performed as part of this thesis. The multiple checkpoint analytical model, described in Subsection 3.2.2, was implemented using a MATLAB [94] routine to calculate the impedance thresholds and the critical Q_{ext} for each concerned HOM at the operating beam current $I_{\text{b,op}} = 120$ mA. Furthermore, a subroutine was developed to estimate the threshold current for each selected cavity HOM, considering various Q_{ext} values.

Table 3.1: Significant monopole and dipole HOMs in the 801.58 MHz 5-cell PERLE cavity computed using CST Studio Suite®. The phase advance is denoted for each mode. Both longitudinal and transverse R/Q values are provided in units of Ω.

Monopole modes				Dipole modes			
No.	Mode n	f_n [GHz]	$R/Q_{\parallel}$ [Ω]	No.	Mode n	f_n [GHz]	$R/Q_{\perp}$ [Ω]
1	TM_{011}-π	1.379	0.007	1	TE_{111}-$\pi/5$	0.936	0.223
2	TM_{011}-$4\pi/5$	1.397	15.597	2	TE_{111}-$2\pi/5$	0.961	0.007
3	TM_{011}-$3\pi/5$	1.419	62.202	3	TE_{111}-$3\pi/5$	0.998	27.665
4	TM_{011}-$2\pi/5$	1.462	61.214	4	TE_{111}-$4\pi/5$	1.039	60.842
5	TM_{011}-$\pi/5$	1.463	22.870	5	TE_{111}-π	1.079	12.472
6	TM_{020}-$\pi/5$	1.669	0.739	6	TM_{110}-π	1.100	0.846
7	TM_{020}-$2\pi/5$	1.685	0.908	7	TM_{110}-$4\pi/5$	1.129	30.684
8	TM_{020}-$3\pi/5$	1.708	0.830	8	TM_{110}-$3\pi/5$	1.151	37.052
9	TM_{020}-$4\pi/5$	1.732	0.160	9	TM_{110}-$2\pi/5$	1.163	6.357
10	TM_{020}-π	1.752	1.525	10	TM_{110}-$\pi/5$	1.167	0.418
11	TM_{021}-$\pi/5$	2.020	2.413	11	TM_{111}-π	1.470	0.144
12	TM_{021}-$2\pi/5$	2.050	0.465	12	TM_{111}-$4\pi/5$	1.488	5.086
13	TM_{021}-$3\pi/5$	2.076	9.166	13	TM_{111}-$3\pi/5$	1.504	3.917
14	TM_{021}-$4\pi/5$	2.107	15.949	14	TM_{111}-$2\pi/5$	1.505	16.595
15	TM_{021}-π	2.153	0.246	15	TM_{111}-$\pi/5$	1.555	10.050
16	TM_{012}-$\pi/5$	2.197	3.850				
17	TM_{012}-$2\pi/5$	2.252	8.071				
18	TM_{012}-$3\pi/5$	2.258	1.487				
19	TM_{012}-$4\pi/5$	2.262	11.957				
20	TM_{012}-π	2.263	19.883				

The analysis considers as input the R/Q and frequency values for the most relevant monopole and dipole HOMs of the 5-cell PERLE bare-cavity up to approximately 2.3 GHz. These values were computed using CST Studio Suite® and are provided in Table 3.1. HOMs possessing R/Q-values greater than 10 Ω can potentially compromise beam stability. The parameters E_{b}^{m}, M_{12}, M_{34}, and M_{56}, as used in the analytical model and depicted in Figure 3.2, were calculated in OptiMX [95] based on the PERLE

beamline lattice [93]. The threshold current is periodic over HOM frequency due to the term $\sin(\omega_n t_{\mathrm{r}}^{lm})$. In this study, BBU calculations are made under the assumption that $\sin(\omega_n t_{\mathrm{r}}^{lm}) = 1$, representing a conservative scenario in which the equation (3.4) yields the lowest threshold current value.

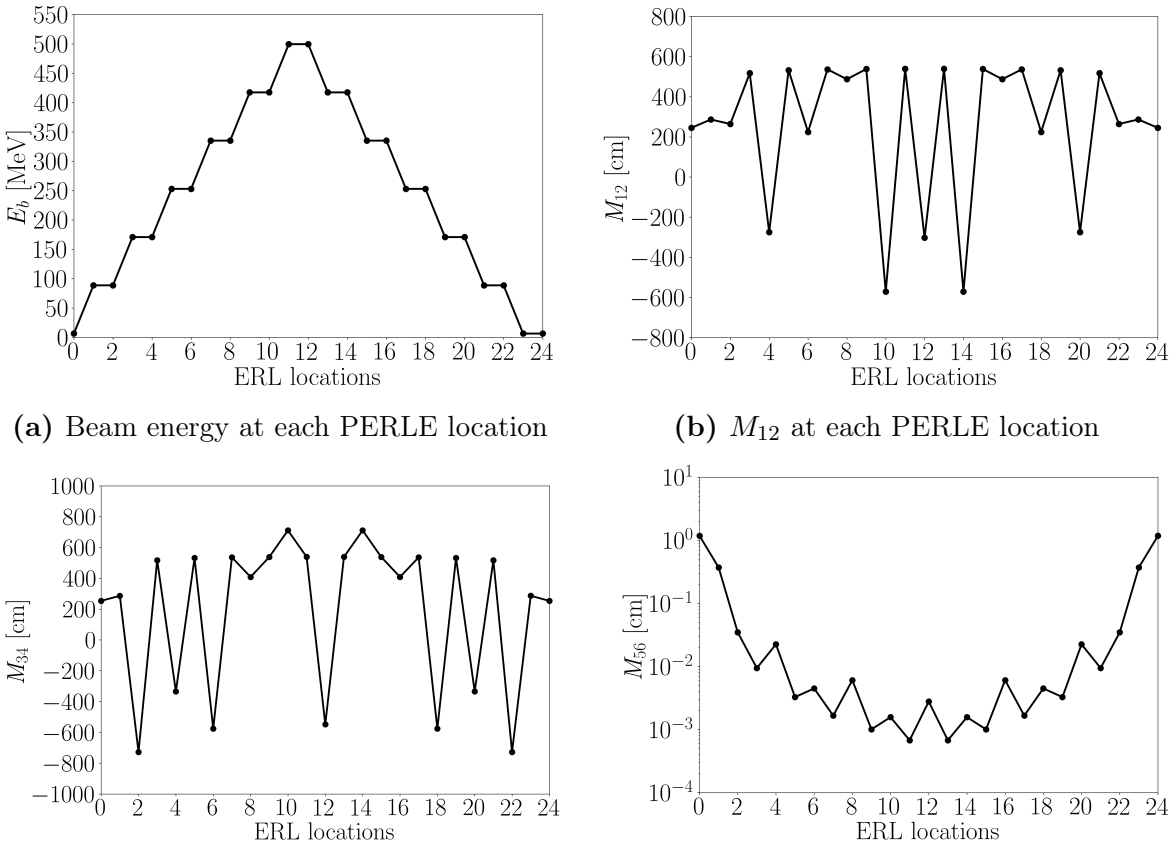

(a) Beam energy at each PERLE location

(b) M_{12} at each PERLE location

(c) M_{34} at each PERLE location

(d) M_{56} at each PERLE location

Figure 3.2: Beam parameters of the PERLE 500 MeV version vs. ERL locations. The beam acceleration stage extends from location 0 (entry of the north linac in the first turn) to location 12 (entry of the north linac in the fourth turn). The beam deceleration stage spans from location 12 to location 23, with the latter corresponding to the exit of the south linac in the sixth turn. Location 24 indicates the beam dump.

3.3.1 Impedance and external quality factor requirements

The main results of the BBU analytical studies for the analyzed HOMs, considering an operating beam current $I_{\mathrm{b,op}}$=120 mA, are depicted in Figures 3.3 and 3.4. The longitudinal and transversal impedances, calculated using equations (3.6) and (3.7), respectively, were fitted to capture the overall trend of the impedance thresholds, as shown in Figures 3.3 (a) and (b).

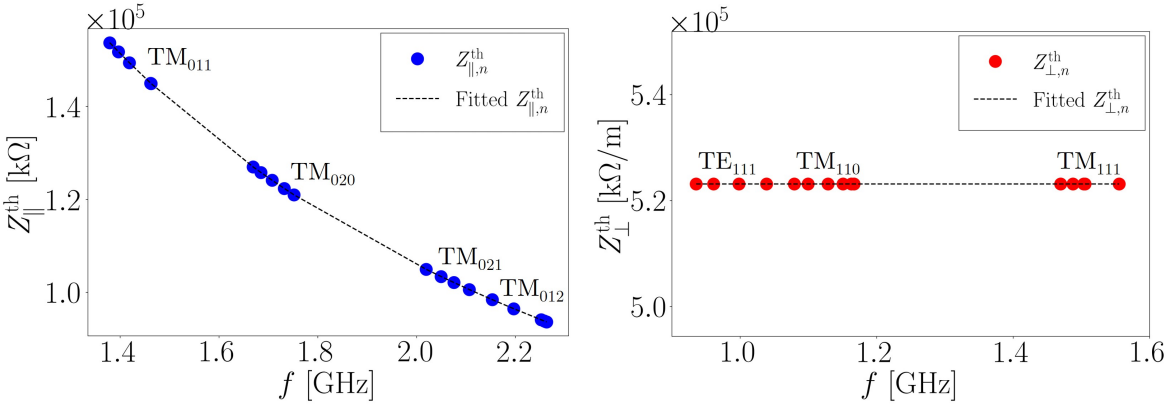

(a) Longitudinal impedance threshold **(b)** Transversal impedance threshold

Figure 3.3: Longitudinal (a) and transversal (b) impedance thresholds of the 5-cell PERLE cavity. The dashed lines correspond to the fitted impedance threshold curves, capturing the overall trend of the impedance threshold variation with respect to the frequency. The fit equation for the longitudinal impedance threshold is $Z_{\parallel}^{\text{th}}[\text{k}\Omega] = 2.12 \times 10^5 f^{-1}[\text{GHz}]$, with $R^2 = 1$. The transverse impedance threshold value is $Z_{\perp}^{\text{th}} = 5.23 \times 10^5$ kΩ/m and does not vary with frequency. The impedances are calculated considering an operating beam current of 120 mA.

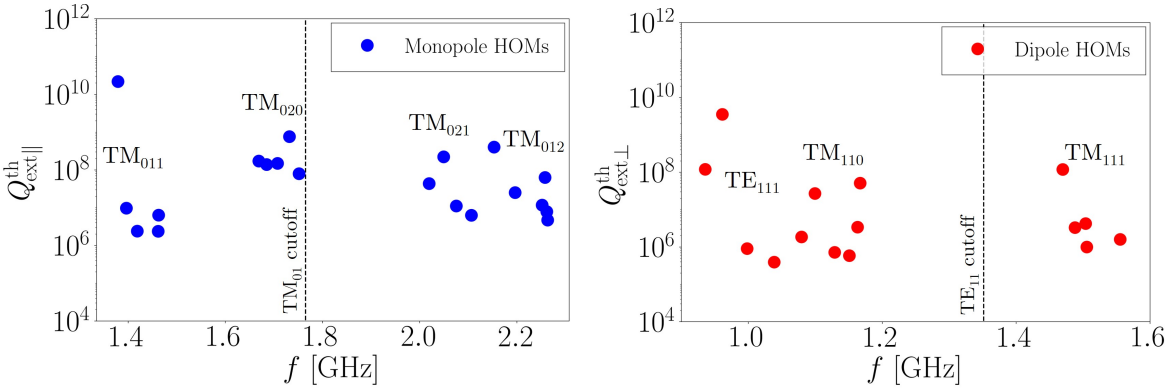

(a) Critical Q_{ext} for monopole HOMs **(b)** Critical Q_{ext} for dipole HOMs

Figure 3.4: Critical Q_{ext} values for monopole (a) and dipole (b) HOMs of the 5-cell PERLE cavity. The dashed vertical lines represent the cutoff frequencies of 1.77 GHz and 1.35 GHz for the TM_{01} and TE_{11} beam pipe modes, respectively. The critical Q_{ext} values are calculated considering an operating beam current of 120 mA.

Fitting the impedances mentioned above enables the extension of the general trend of the impedance thresholds across a broader frequency range of interest for the studied cavity. The longitudinal impedance threshold scales as $\propto 1/f$, while the transverse impedance threshold, expressed in Ω/m, remains constant regardless of the frequency.

The critical external quality factor values for each analyzed monopole and dipole

mode, calculated using equations (3.8) and (3.9), respectively, are illustrated in Figures 3.4 (a) and (b). As shown in Figure 3.4 (a), the TM_{011}-passband modes exhibit comparatively low critical Q_{ext} values in the order of 10^6, with the lowest value of $Q_{ext} = 2.36 \times 10^6$ possessed by the TM_{011}-$2\pi/5$ mode. The rather confined TM_{012}-π mode, which resides above the TM_{01} beam pipe cutoff frequency, presents similar external quality factor requirements as the trapped TM_{011}-type modes ($Q_{ext} = 4.57 \times 10^6$). The results for the most significant dipole modes, shown in Figure 3.4 (b), illustrate that the relatively low critical Q_{ext} values range between 10^5 and 10^6. Particularly, among the three analyzed dipole passbands, the lowest critical external quality factors are $Q_{ext} = 3.95 \times 10^5$ for the TE_{111}-$4\pi/5$ mode, $Q_{ext} = 5.85 \times 10^5$ for the TM_{110}-$3\pi/5$ mode, and $Q_{ext} = 9.87 \times 10^5$ for the TM_{111}-$2\pi/5$ mode.

The figure of merit concerning beam stability is the impedance $(R/Q)Q_L$, and not solely the loaded quality factor Q_L of a HOM. The modes possessing the highest impedances can limit the achievable stable beam current in a machine. Typically, higher values of (R/Q) will necessitate lower values of Q_L, and vice versa [21]. The TM_{011}-type HOMs typically exhibit the highest $(R/Q)_{\parallel}$ among all monopole modes. The most problematic dipole passbands are the TE_{111} and the TM_{110} due to their high-$(R/Q)_{\perp}$ values. For these modes, it is crucial to ensure that their Q_{ext} is at least one order of magnitude lower than the critical Q_{ext} determined from BBU analysis, to provide a safety margin against beam instabilities. This criterion could be considered as a guideline for designing the cavity's HOM couplers. The design of HOM couplers developed for the PERLE cavities will be covered in Chapter 4, while Chapter 5 will discuss their damping performance.

3.3.2 Maximum achievable current

The primary goal in an ERL is to push the BBU threshold current beyond the operating current $I_{b,op}$ to ensure safe operation. The aim is to provide a margin for a current higher than the nominal operational current. In the context of this analysis, the threshold current refers to the minimum beam current required for each HOM to initiate BBU instabilities in the machine. The threshold current has been estimated exclusively for dipole modes, as they impose the most significant limitation on the maximum achievable current in an ERL [2]. This estimation process requires a set of Q_{ext} values for each considered HOM to simulate a certain level of damping, in addition to the parameters listed in Table 3.1 and Figure 3.2, as inputs. Typical Q_{ext}-values in damped SRF cavities can range from 10^3 to 10^5 [17, 96]. In this context, it may be feasible to employ the same Q_{ext} value for all the analyzed modes in order to assess the trend of I_{th} across the different modes.

Figure 3.5 presents the threshold current as a function of different Q_{ext} values for each studied dipole HOM. The investigated modes show a threshold current higher than the target beam current. The results indicate that certain modes could constrain the maximum achievable beam current in the ERL. These are the TE_{111}-$4\pi/5$, TM_{110}-

$4\pi/5$, TM_{110}-$3\pi/5$ modes, labeled with index n equal to 4, 7, and 8, respectively, in Figure 3.5. For example, at $Q_{ext} = 10^5$, these modes exhibit I_{th}-values of 474 mA, 860 mA, and 702 mA, in the given order. The TE_{111}-$3\pi/5$ and TM_{111}-$2\pi/5$ modes (numbered as $n = 3$ and $n = 14$ in Figure 3.5) present a threshold current of 1 A and 1.2 A for the same Q_{ext} value, respectively.

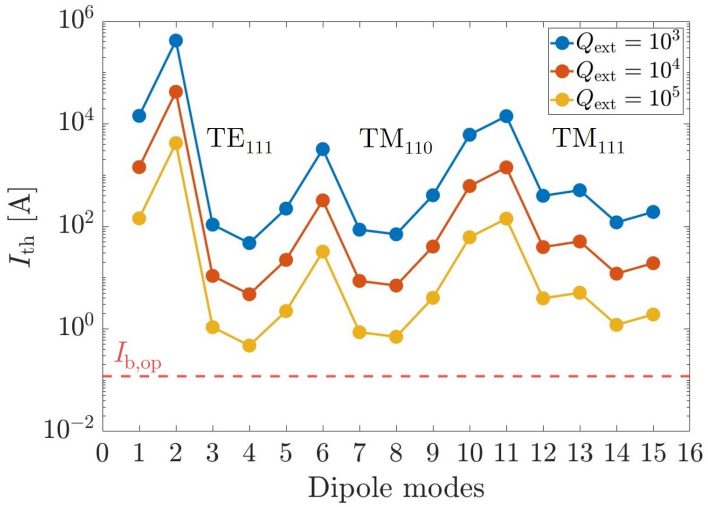

Figure 3.5: Threshold current for each analyzed dipole HOM with Q_{ext} values of 10^3, 10^4, and 10^5. The red dashed line corresponds to operating beam current $I_{b,op}$=120 mA for PERLE.

The key strategy to increase the threshold current involves lowering Q_{ext} of HOMs and their impedance through HOM couplers. However, a significant reduction of Q_{ext} might introduce additional complications related to intense HOM coupling, such as elevated RF-heating of couplers antenna (refer to Section 5.4). Other approaches include optimizing the optics of the ERL, which will consequently change the values of M_{ij} elements. Manufacturing errors, with fabrication tolerances in the order of hundreds of µm, could further change the average I_{th} of an ERL [97]. The threshold current can ultimately be calculated considering the Q_{ext} values for each HOM determined through simulations of a cavity equipped with specific HOM damping mechanisms. However, due to the limitations of the analytical model, these additional studies would require the use of particle-tracking codes, as will be discussed in Subsection 3.3.3. Recent studies have demonstrated that threshold currents of 2 A can be achieved in the PERLE ERL [98]. As BBU tracking studies are beyond the scope of this thesis, the next subsection will only present a comparison between the critical Q_{ext}-values obtained from the analytical model and those from a BBU-tracking code developed at Lancaster University [85].

3.3.3 BBU-tracking model

The primary objective of the described investigation has been to analytically derive a first-order estimation of the cavity impedance requirements. The aim was to establish an optimization criterion for HOM couplers in PERLE cavities (refer to Chapter 4). The used transfer matrix $\mathbf{M}$ reduces to M_{12} and M_{34} elements for horizontally and vertically polarized modes, respectively [99]. Therefore, the analytical model, as in the equation (3.3), utilizes M_{12} element to convert the horizontal mode kick to horizontal beam offset, while the M_{34} element translates the vertical mode kick to vertical beam offset. The M_{56} element converts the energy offset to longitudinal beam offset [100].

In a multi-turn ERL scenario, to model the mutual interaction between the bunches and the various HOMs within the same turn and across different turns, it is necessary to utilize established particle tracking codes, such as Bmad [101], or a novel BBU-tracking model developed at Lancaster University. In the context of beam dynamics studies carried out within the framework of the PERLE collaboration, BBU-tracking simulations were carried out at Lancaster University to benchmark the results of the analytical model presented in this thesis. Part of these results have been recently published in [48]. This BBU-tracking model can estimate the threshold current of an ERL featuring multiple cavities and the critical Q_{ext}-values of HOMs at a nominal beam current, considering the mutual interaction between multiple modes. It incorporates the interplay of all M_{ij} elements rather than relying only on M_{12}, M_{34}, and M_{56} elements. It also allows for the inclusion of filling patterns and bunch timing dependency.

The filling pattern is the sequence in which bunches are injected into the ERL ring during successive turns. The bunch timing, often referred to as bunch spacing, represents the temporal separation between adjacent bunches. The position occupied by the bunches on each turn can be represented using the concept of intra-packet blocks [48] (see Figure 3.6). For a 6-turn ERL, which includes three accelerating and three decelerating passes, the filling pattern {1 2 3 4 5 6} denotes that the first bunch goes to the first intra-packet block, the second bunch to the second block, and so forth.

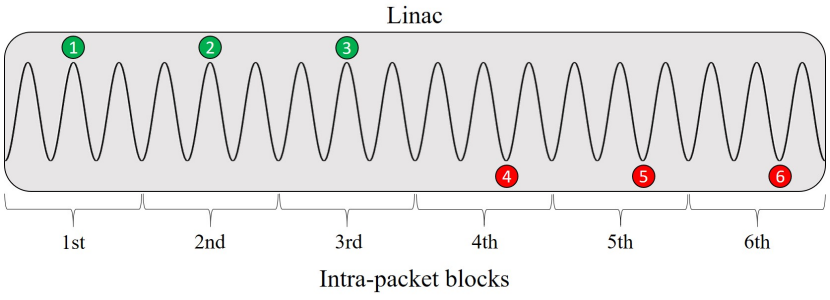

Figure 3.6: Intra-packet blocks and their associated RF cycles within a linac. The green and red bunches refer to accelerating and decelerating bunches, respectively.

The intra-packet blocks determine the fixed number of RF cycles between bunches.

These bunches together constitute a packet, and multiple packets of bunches fill the ERL, as depicted in Figure 3.7.

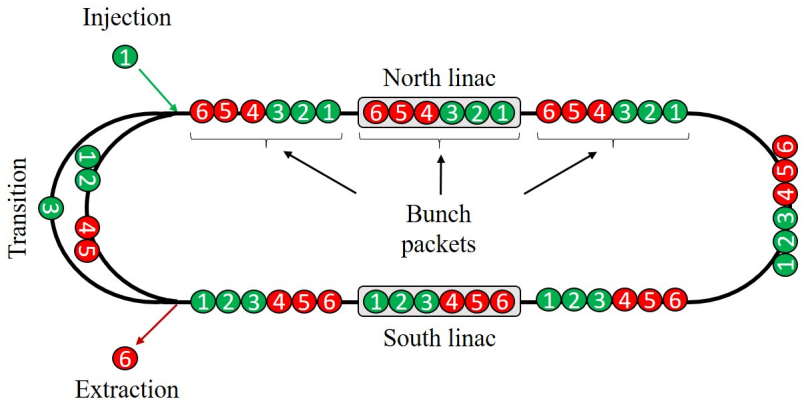

Figure 3.7: Filling of an ERL by multiple bunch packets. Bunches on the third turn pass through the transition arc, which introduces at least an additional half RF cycle delay. The figure is adapted to the PERLE ERL from [85]. The cited figure falls under the Creative Commons Attribution 4.0 (CC BY 4.0) license (https://creativecommons.org/licenses/by/4.0/).

In the simulations, the ERL is filled using a sequence preserving (SP) recirculation scheme [85, 102], which means the filling pattern remains the same for each turn. This ensures that the cavities in the linac constantly observe the same bunch-packets passing through. In an SP scheme, the bunch on its first turn advances to the block formerly occupied by the bunch on its second turn. The second bunch moves to the block previously occupied by the bunch on its third turn, and so on. In this manner, the block previously occupied by the bunch on its first turn is continuously available for injecting the new bunch, while the RF transient in the cavities is preserved during each turn. Figure 3.8 depicts the simulated SP filling pattern {1 4 2 5 3 6} and bunch timing for PERLE, combined with the normalized cavity voltage as a function of time.

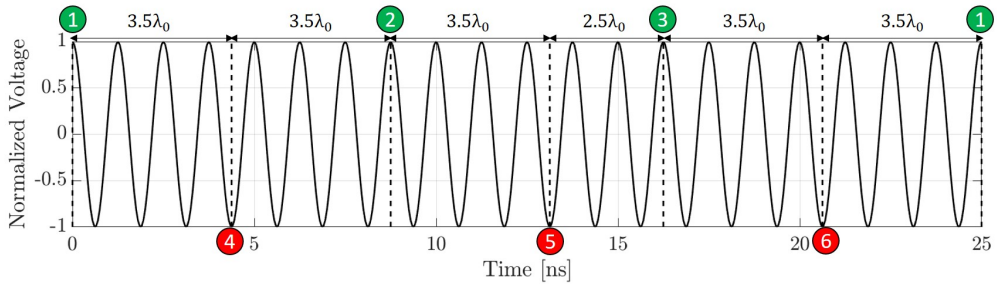

Figure 3.8: PERLE filling pattern {1 4 2 5 3 6} combined with the normalized cavity voltage as a function of time. The resulting alternating pattern of accelerating (green dots) and decelerating bunches (red dots) is depicted. The distance between bunches is indicated in terms of fundamental RF cycles, with $\lambda_0 = 0.374$ m.

This is currently considered as one of the suitable filling patterns for PERLE [103]. In the PERLE filling pattern {1 4 2 5 3 6}, bunch no. 1 represents the initial bunch, injected every 25 ns, during its first turn. Bunches 4, 2, 5, 3, and 6 depict the respective bunches in their 4th, 2nd, 5th, 3rd, and 6th turns. The acceleration stage in PERLE occurs in the 1st, 2nd, and 3rd turns, while deceleration takes place in the 4th, 5th, and 6th turns. According to the SP scheme, the first intra-packet block is always occupied by the bunch at the first turn, the second block by the bunch at the fourth turn, and so on. The space between bunches has also been chosen to be as uniform as possible, with alternating accelerating and decelerating bunches to mitigate beam loading. Figure 3.9 illustrates the comparison between the analytical model and Lancaster's BBU-tracking model for the critical Q_{ext} of the most problematic dipole passbands.

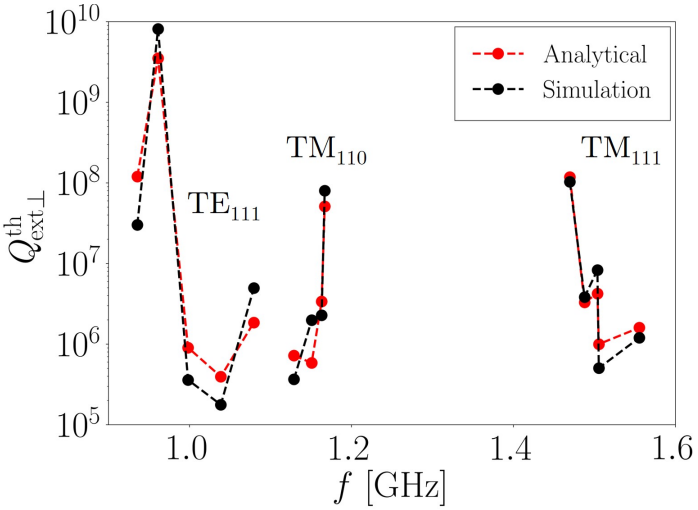

Figure 3.9: Critical Q_{ext} values for the first three dipole passbands calculated in the analytical model (red dots) and Lancaster's BBU-tracking model (black dots) for $I_{\text{b,op}}$=120 mA [48]. The figure falls under the Creative Commons Attribution 4.0 (CC BY 4.0) license (https://creativecommons.org/licenses/by/4.0/). The SP pattern {1 4 2 5 3 6} is employed for the calculations.

Results indicate a broad agreement and similar trends between the analytical model and Lancaster's BBU-tracking model [48]. Differences can be attributed to the fact that the analytical model does not account for the filling pattern, bunch timing dependency, or the interplay between modes. Nevertheless, the BBU analytical model remains a valid tool for providing a conservative first-order estimation of the impedance thresholds within the scope of establishing a design criterion for HOM couplers in this thesis. Further explorations beyond this scope are reserved for future investigation.

4 HOM coupler design and fabrication

Chapter 3 discussed the regenerative beam breakup (BBU) phenomenon, a crucial issue for continuous-wave high-current energy recovery linacs. As charged particles are accelerated along the cavity, they emit a specific amount of energy into the surrounding structure, exciting the cavity's higher-order modes. The multi-pass interaction between the electron beam and the cavity HOMs can limit the stable operation of the ERL. In particular, beam-induced monopole HOMs can increase the cryogenic losses of the linac, while dipole HOMs can deflect the beam during subsequent passes. To prevent the occurrence of multi-pass BBU instabilities, the next generation of ERLs, such as PERLE, calls for using SRF cavities with strong HOM-damping requirements [21]. Conventional HOM-damping mechanisms, such as coaxial HOM couplers, beamline absorbers (BLAs), and waveguides (WGs), can efficiently extract the HOM-induced power from the cavities. This chapter focuses on designing three coaxial HOM couplers to mitigate the effects of beam-induced HOMs in the 801.58 MHz 5-cell PERLE cavity. First, a brief introduction to traditional HOM-damping mechanisms is provided. Then, the procedure used to design the three analyzed HOM couplers and optimize their RF transmission is presented. Finally, the different phases for producing 3D-printed and copper-coated coupler prototypes are discussed.

4.1 HOM couplers

Higher Order Mode (HOM) couplers are devices attached to the accelerating cavities alongside the fundamental power coupler (FPC). The main role of the HOM couplers is to remove or dissipate unwanted HOM energy from a cavity [17, p. 28]. On the other hand, the primary function of the fundamental power coupler (or input coupler) is to supply power from the RF generator to the cavity at the fundamental mode (FM) frequency to accelerate the beam [17, p. 179]. Figure 4.1 shows a typical setup of a single-cell RF cavity with a HOM coupler and an FPC. The HOM couplers are designed to efficiently transmit RF signals at frequencies where high beam-impedance HOMs exist while effectively rejecting the fundamental mode. This ensures that HOM couplers operate to attenuate cavity higher-order modes without absorbing the energy of the FM.

The main objective of HOM couplers is to lower the external Q-value of high-R/Q cavity HOMs by enhancing the coupling to their pick-up antenna, thereby minimizing their impedance. The HOMs with the highest impedance are called "performance-limiting" modes, as they can limit the stable operation in an accelerator [21].

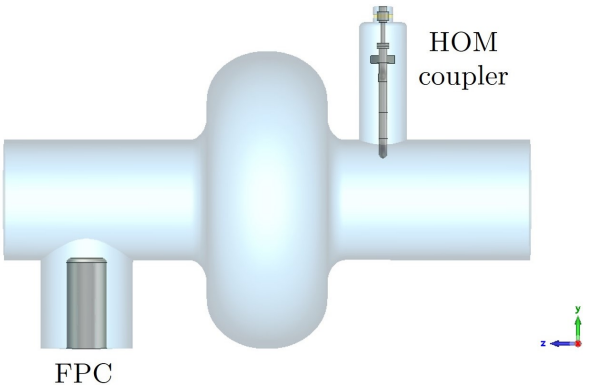

Figure 4.1: Scheme of a single-cell cavity equipped with a fundamental power coupler (FPC) (left-side) and a HOM coupler (right-side).

Several HOM-damper technologies have been developed in the accelerator community across different projects to mitigate beam-induced HOMs [104, 105, 106, 107, 108]. Existing HOM couplers can be classified into three categories as follows [21]: coaxial HOM couplers, waveguide (WG) couplers, and beamline absorbers (BLAs). In principle, HOM-damping schemes used in SRF cavities comprise coaxial HOM couplers, waveguide couplers, beamline absorbers, or any combination. These dampers are usually positioned outside the cavity. Recently, on-cell waveguide dampers have been explored for strong HOM-damping in novel high-current SRF single-cell cavities [21, 109]. In this case, the waveguides are connected to the cavity walls to extract trapped HOMs at the location where they are initially generated inside the cavity. However, since this novel damping technique has not yet been fully explored for multi-cell cavities and requires further study, it is not considered in this thesis.

The concept of cavity damping may vary, depending on several factors. These include the specific broadband or narrowband damping requirements for longitudinal and transverse HOMs, the dissipated power and related cooling demands, and the mechanical integration aspects within the cryomodule design. Coaxial HOM couplers or waveguide dampers are placed as close as possible to the cavity end-cells in damped cavities when the beam pipe aperture is not large enough to evacuate trapped modes. Among these beam-excitable modes, the first longitudinal HOM (TM_{011}) and the first two transverse HOMs (TE_{111} and TM_{110}) are the most problematic since they can possess the highest R/Q values. The fundamental power coupler (FPC) installed in the cavity beam pipe may also contribute to the HOM-damping. The conventional damping mechanisms are briefly presented in the following subsections.

4.1.1 Coaxial HOM couplers

Coaxial HOM couplers are conventionally designed with a coupling antenna that can exhibit either a dominant electric coupling or magnetic coupling with the EM field inside the cavity [110]. Typically, a probe antenna is employed for coupling with the electric field, while a loop-shaped antenna is used for coupling with the magnetic field. The coupling strength of probe couplers is quantified through the superposition between the excited fields from the inner conductor of the couplers and the fields existing inside the cavity. In loop-shaped couplers, the coupling strength is determined by the interaction between the excited magnetic fields perpendicular to the pick-up loop antenna and the magnetic field distribution associated with the considered mode. Additionally, hybrid designs combining characteristics of both probe and loop couplers can also be designed. Examples of coaxial HOM couplers are the broad-band probe-type and narrow-band hook-type couplers designed for the Large Hadron Collider (LHC) cavities at CERN (see Figure 4.2) [104].

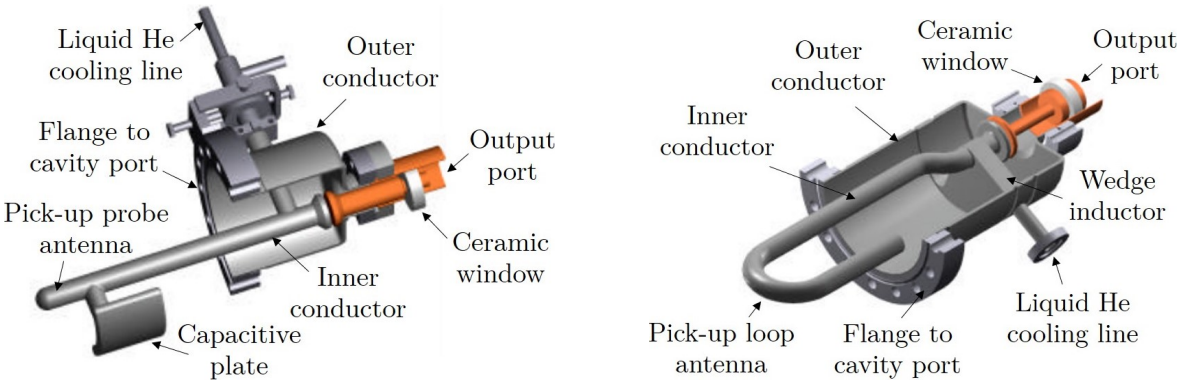

(a) Probe-type LHC coupler

(b) Hook-type LHC coupler

Figure 4.2: Coaxial HOM couplers developed for the LHC cavities: broad-band probe-type HOM coupler (a) and narrow-band hook-type HOM coupler (b) (figures adapted from [104]).

The LHC coaxial couplers were designed to handle up to 1 kW of HOM power [111]. They have been tested up to 800 W of HOM power [104]. Their inner conductor can be actively cooled via liquid He circuits to mitigate RF heating from the cavity modes (refer to Section 5.4). Two probe-type and hook-type coupler designs featuring two notches for the FM mode rejection were proposed in [96]. While the presence of a double notch reduces the sensitivity of FM rejection to geometrical perturbations, the complexity of the design makes the coupler manufacturing challenging. A recently designed HOM coupler is the Double Quarter Wave (DQW) coupler, which is intended for use in the High-Luminosity LHC (HL-LHC) DQW crab cavities (see Figure 4.3 (a)) [112]. The pick-up antenna of the DQW coupler can also be internally cooled by liquid He. The TESLA-type HOM coupler (see Figure 4.3 (b)) is another well-established coupler designed without liquid He circuits for low-duty cycle operations [106].

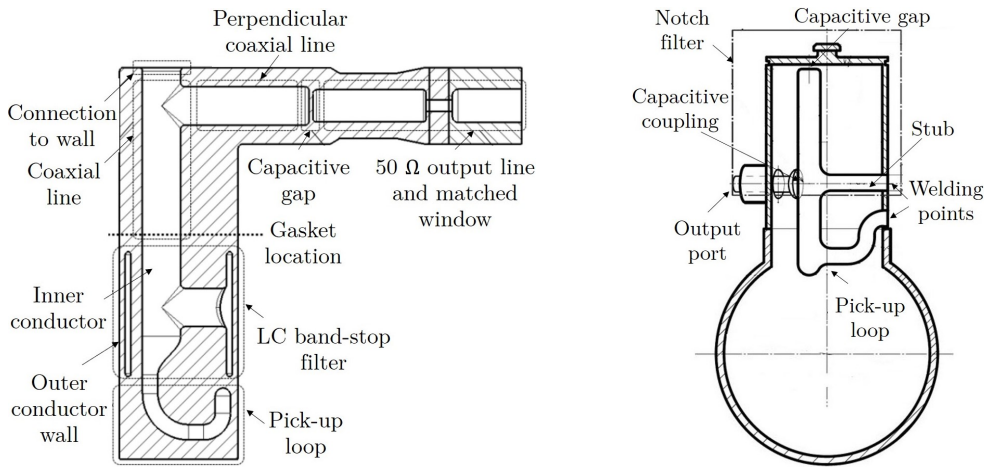

(a) DQW-type coupler **(b)** TESLA-type coupler

Figure 4.3: DQW-type HOM coupler (a) (figure adapted from [112]). Creative Commons Attribution 3.0 (CC BY 3.0) license (https://creativecommons.org/licenses/by/3.0/). All rights reserved. TESLA-type HOM coupler (b) (figure adapted from [113], ©IOP Publishing).

The coaxial HOM couplers are characterized by a compact design, which facilitates the cryomodule conception compared to other damping mechanisms [21]. The inner conductor (IC) and outer conductor (OC) are typically made from solid Nb to maintain the superconductivity during operation. Otherwise, the overheating caused by the absorbed HOM magnetic fields can lead to a thermal quench, potentially propagating to the HOM-endgroup (end-cell plus beam pipes with couplers) and the cavity. While coaxial HOM couplers offer advantages in terms of integration into the cryomodule, they may present challenges that must be addressed. Coaxial couplers can feature an intricate design that requires unconventional fabrication methods, like additive manufacturing (refer to Section 4.3). HOM couplers need stringent mechanical tolerances since fabrication errors can impact the FM mode rejection and damping performance. Typically, the mechanical tolerance of a HOM coupler should not be smaller than ± 0.2 mm to contain the cost of fabrication [96]. When coaxial HOM couplers are cooled down to their operating temperature, such as 2 K, the physical dimensions of their components can change. Consequently, the notch at the FM might be detuned, affecting its rejection. Another challenge is cooling the coupler inner conductor to counteract the overheating caused by the absorbed EM fields. This necessitates more sophisticated solutions for coaxial HOM couplers than waveguides or BLAs. HOM couplers can be cooled through conduction via direct contact between the stainless steel flange of the coupler port, which is in contact with the outer conductor of the coupler, and the He bath. The inner conductor could also be cooled through internal liquid He channels. Additionally, a single-crystal sapphire RF window can be incorporated in the output RF feedthrough, providing a direct heat path from the output antenna to a bulk copper sleeve in contact with the outer conductor of the HOM coupler [21]. More

details on the cooling of the HOM coupler will be provided in Section 5.4. Finally, multipacting, i.e., an accumulation of free electrons absorbing RF power [17, p. 179], can frequently occur when conditioning HOM couplers and RF cavities.

4.1.2 Waveguide couplers

Waveguide (WG) couplers are used to carry HOM power away from the cavity to an absorbing material at room or cryogenic temperature [21]. A notable application of this damping concept is the JLab 5-cell cavity designed for high-current ERLs and Free Electron Laser (FEL) light sources (see Figure 4.4). These cavities have two endgroups, each featuring three waveguides on both sides of the cavity. Five of these waveguides serve as HOM dampers, while one functions as the fundamental power coupler. The integration of WG couplers into the He vessel facilitates their cooling. The waveguides are bent and extended to broad-band Silicon carbide (SiC) ceramic and water-cooled absorber loads installed at room temperature, each capable of dissipating up to 4 kW of HOM power, resulting in a total dissipation of 20 kW per cavity. The 5-cell cavity used for the CEBAF 12 GeV upgrade is equipped with HOM waveguides immersed in the He bath within the cavity He vessel [114]. The utilization of absorbers at cryogenic temperature was considered for this cavity since the extracted HOM power was estimated to be only a few milliwatts.

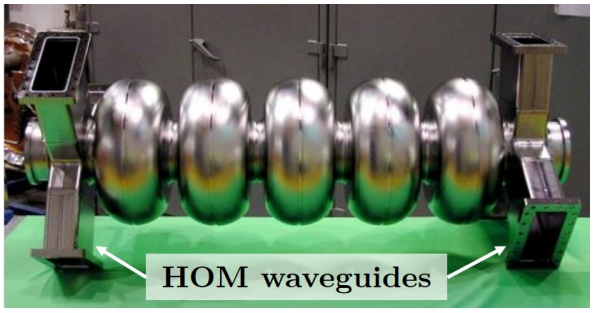

Figure 4.4: Photo of the JLab high-current Nb 748.5 MHz cavity [107]. Each cavity employs six HOM waveguides, with one serving as an FPC.

The WG dampers are characterized by a simple design. They are a commonly employed solution for the broadband damping of HOM and absorption of a few kW of HOM power at room temperature [21]. The major advantage of WG couplers is that an FM rejection filter is not required since the cutoff frequency of their first mode provides a natural rejection, being above the FM of the cavity. Moreover, their damping characteristics are less sensitive to geometrical variations than coaxial HOM couplers. Finally, multipacting occurs less frequently in WG couplers than in coaxial couplers. The main drawbacks are their considerable size, which complicates the cryomodule design, and the management of the high static heat load introduced into the cryostat.

4.1.3 Beamline absorbers

Beamline absorbers (BLAs) are hollow cylinders made of microwave-absorbing materials, such as lossy ferrites, or ceramic tiles, such as SiC. They present a broad-band behavior and are placed at the cavity ends, typically in the cavity-interconnecting region, to damp the cavity HOMs propagating through the beam pipes. The utilization of BLAs often implies enlarging the beam pipes to facilitate the propagation of even the lowest frequency HOMs from the cavity toward the absorbers [21]. BLAs also incorporate a Cu jacket with cooling channels for water or He circulation to cool down the absorber and mitigate the RF heating from the absorbed HOM power. An example of BLA application is the SiC brazed to Tungsten (SiC-W) HOM beamline absorber developed at Cornell University for ERL applications, shown in Figure 4.5. The Cornell's HOM absorber is cooled down by a circulating 80 K, 3 bar, forced-flow helium stream through stainless steel pipes, ensuring the absorber's capability to handle up to 400 W of HOM power [108].

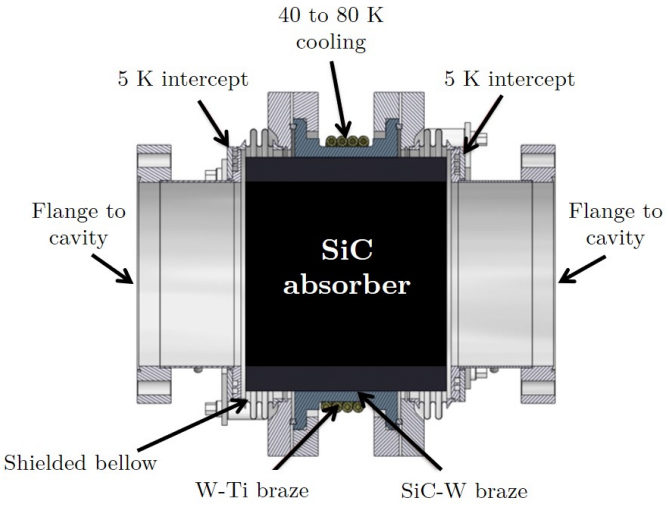

Figure 4.5: Cross-section of HOM absorber for Cornell's ERL main linac (adapted from [108]). The absorber is made of SiC and is cooled down through the He stream circulating through the stainless steel pipes. The 5 K intercepts at the flange transitions prevent RF heating of the cavity endgroups. The figure falls under the Creative Commons Attribution 3.0 (CC BY 3.0) license (https://creativecommons.org/licenses/by/3.0/).

Beamline absorbers have the advantage of featuring an axisymmetric design that allows propagating HOMs with different polarizations. Their damping characteristics are less sensitive to geometrical variations than coaxial HOM couplers and WG dampers. However, BLAs also exhibit some disadvantages. If the HOM power load is in the order of several hundred watts, the absorbers must be placed outside the cryostat to reduce the heat load. The positioning of absorbers between cavities is challenging when the aim is to minimize the cryostat length, as the cold-to-warm transition is required be-

tween cavities [21]. However, BLAs can also be installed at the end of the cryomodules rather than between cavities with fewer mechanical restrictions to damp HOMs that leave the cryomodule through the end beam pipes [115]. Subsection 5.3.3.2 discusses HOM power extraction through BLAs in the 5-cell 801.58 MHz PERLE cavity.

4.1.4 HOM coupler selection for PERLE

The proposed damping approach for the PERLE cavities involves using either a combination of re-designed and optimized versions of LHC coaxial HOM couplers or DQW couplers on the beam pipe tubes to damp beam-induced HOMs. The inclusion of BLAs has also been considered to absorb EM fields of HOMs escaping the cavities through the beam pipes. Due to mechanical restrictions, the double-notch version of the LHC HOM couplers and the TESLA-type HOM couplers had to be excluded. WG dampers were not considered for inclusion in the PERLE cavities due to their bulkiness, which would complicate the cryomodule design. Moreover, waveguides might be considered excessive in terms of damping for the PERLE operating beam current ($I_{\mathrm{b,op}} = 120$ mA). They are typically utilized in cavities capable of accelerating up to Ampère beam current levels, such as the Ampère class cavities designed at JLab for operation in ERLs and FELs [116]. In the following, our primary focus will be optimizing the RF characteristics of the selected designs of coaxial HOM couplers. HOM-damping performance and RF heating in coaxial HOM couplers will be addressed in Chapter 5.

4.2 Coaxial HOM coupler optimization

This section focuses on optimizing the RF transmission of three designs of coaxial HOM couplers: the probe (P), the hook (H), and the DQW couplers. The probe-type and hook-type coupler designs presented in [115, 117] are selected as a starting point for optimizing their transmission characteristics based on the HOM spectrum of the 5-cell 801.58 MHz PERLE cavity. The same approach is applied to the DQW coupler presented in [112, 115], after rescaling it from 400 MHz to 801.58 MHz. The results of the HOM coupler optimization for PERLE were partially presented in [49]. The three coupler designs are optimized to obtain high transmission at frequencies where cavity HOMs with a high level of longitudinal and transversal impedance exist without compromising the FM efficiency. The primary objective is to achieve, for selected coupler designs, a transmission ideally higher than -15 dB for the high impedance TM_{011}, TE_{111}, TM_{110} modes to guarantee sufficient HOM-damping within these mode passbands. These HOMs usually reside below the corresponding beam tube cutoff frequencies and possess high R/Q values. The TM_{01}, TE_{11}, and TM_{11} cutoff frequencies of the considered 65 mm radius beam pipe are 1.77 GHz, 1.35 GHz, and 2.81 GHz, respectively. The cutoff frequencies of TM_{01} and TM_{11} beam pipe modes are calculated using the equation (2.2) and the corresponding u_{mn}-values reported in Table 2.3. The

cutoff frequency of TE_{11} beam pipe mode is computed employing the equation (2.3) and the associated u'_{mn}-value reported in Table 2.3. On the other hand, the transmission at the FM frequency should be the lowest possible, preferably lower than -90 dB, to ensure effective FM rejection. Figure 4.6 shows the longitudinal and transversal impedance of the single-cell, two-cell, and five-cell PERLE-type cavities built on the basis of the parameters provided in Table 2.2, and tuned to the cold frequency of 801.58 MHz. The peaks correspond to the HOM with high impedance values that must be damped using HOM couplers. The rather confined TM_{012}-π mode at 2.26 GHz exhibits high-impedance, which cannot be reduced using coaxial HOM-coupler, as it resonates considerably above the TM_{01} beam tube cutoff. However, its impedance could be reduced by modifying the elliptical profile of the end-cells to improve the mode coupling to the beam pipe [21]. The RF transmission of the HOM couplers is optimized on the basis of the HOM spectrum of the 801.58 MHz five-cell cavity. Since the impedance spectra of the corresponding 801.58 MHz two-cell cavity are similar to those of the five-cell cavity, the optimized HOM couplers could also be used for damping the corresponding mode passbands in the two-cell cavity (refer to Subsection 7.2.2).

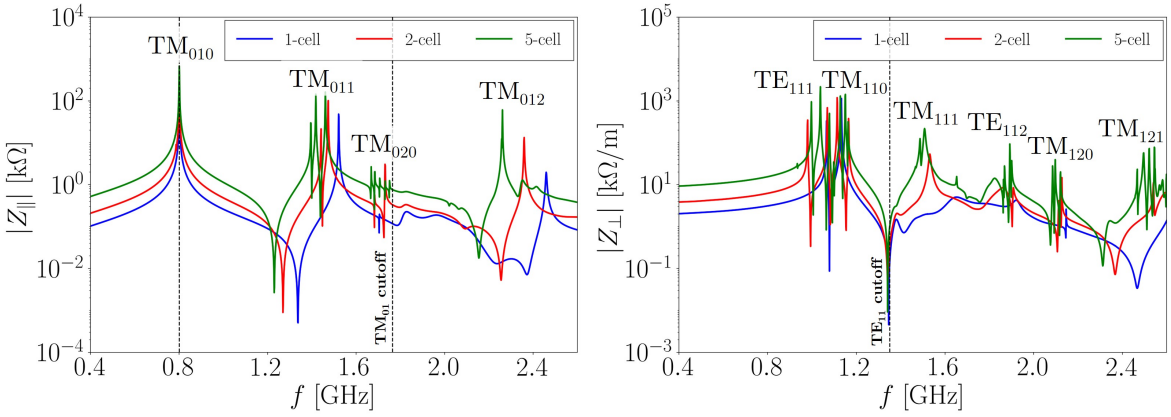

(a) Longitudinal impedance **(b)** Transversal impedance

Figure 4.6: Longitudinal (a) and transversal (b) impedance of the 1-cell (blue), 2-cell (red), and 5-cell (green) 801.58 MHz PERLE cavities. The dashed vertical lines in (a) and (b) represent the cutoff frequency of the TM_{01} and TE_{11} beam pipe modes, which are 1.77 GHz and 1.35 GHz, respectively. The mode passband nomenclature is given. The wake impedance is calculated for the bare cavities, and the peaks are not fully resolved due to the truncated simulated wake potential (refer to Subsection 5.1.1).

4.2.1 Optimization method for RF transmission

The standard approach for optimizing the RF transmission of a HOM coupler involves simplifying the cavity and coupler structure into a lumped element circuit [118]. This methodology, based on the principle of filter design [119], allows for obtaining the

desired transmission characteristics of the coupler. Successively, each circuit element can be translated into the corresponding component of the 3D model of the HOM coupler [118]. For example, coaxial lines can be modeled as linear elements, capacitors as gaps between surfaces, and straight rods connecting the inner and outer conductors as inductors. This method is computationally faster than a standard 3D EM solver and illustrates the influence of each circuit parameter on the transmission curves. The coupler transmission characteristics can be fine-tuned in a second step using a 3D EM solver, such as CST Studio Suite®. On the other hand, the circuit optimization method has some limitations. For example, it does not consider the presence of all geometrical details of the coupler. Moreover, when designing HOM couplers with complicated geometry, the analogy between the elements of the lumped model and parts of the 3D geometry becomes challenging. In this thesis, the HOM coupler transmission has been optimized using a 3D geometry and the frequency domain solver of CST (see Subsections 4.2.2, 4.2.3 and 4.2.4). The equivalent circuit of each coupler is shown solely to facilitate the analogy between circuit elements and coupler components.

The optimization of the coupler geometry is aimed at determining a specific set of geometric parameters to achieve high transmission for the relevant cavity HOMs without compromising the FM rejection. The computational domain for optimizing the coupler transmission in the frequency domain could include the cavity and the HOM coupler. However, this method is computationally expensive. This thesis closely follows the time-saving approach for optimizing HOM couplers introduced by S. Gorgi Zadeh in [115], which involves modeling only the coupler connected to the cavity's beam pipe, as depicted in Figure 4.7. The beam pipe is cut at the intersection with the cavity, and the resulting surface is terminated with a waveguide (WG) port, enabling the excitation of the first three modes of a circular WG: the horizontal and vertical polarizations of the TE_{11} dipole mode and the TM_{01} monopole mode. The resulting field patterns closely reproduce the field inside the cavity. The FM couples to the TM_{01} WG mode, while both trapped TE_{111} and TM_{110} modes couples to the two polarizations of TE_{11} beam pipe mode [120]. The WG port, which terminates the output port of the coupler, excites only its first mode, the zero-cutoff frequency TEM mode.

In this thesis, the port at the beam pipe is designated as port 1, and the port at the output of the HOM coupler as port 2. The transmission between the modes excited at port 1 and the first mode of port 2 is studied with the $S_{i(k),j(l)}$ parameter, which denotes the S-parameter between the mode k and l of ports i and j, respectively [115]. Additional details on the S-parameters are given in Subsection 7.1.1.3. Three S-parameters can be analyzed: $S_{1(3),2(1)}$, represents the coupling or monopole transmission between the third mode of port 1 (TM_{01}) and the first mode of port 2 (TEM). $S_{1(1),2(1)}$ denotes the coupling or dipole transmission between the first mode of port 1 (first polarization of TE_{11} mode) and the TEM mode of port 2. Similarly, $S_{1(2),2(1)}$ indicates the coupling or dipole transmission between the second mode of port 1 (second polarization of TE_{11} mode) and the TEM mode of port 2. In the following, only the dipole polarization yielding higher transmission is studied and optimized, i.e.,

either $S_{1(1),2(1)}$ or $S_{1(2),2(1)}$ [115]. Due to the 90° phase offset between the fields of the two dipole polarizations, an additional identical coupler can be installed in a cavity and rotated accordingly or by an appropriate angle to couple the second polarization of the dipole modes. The details about the number of required couplers in an HOM-damped cavity, their location in the beam pipe, and angular position with respect to the beam axis are provided in Section 5.3.

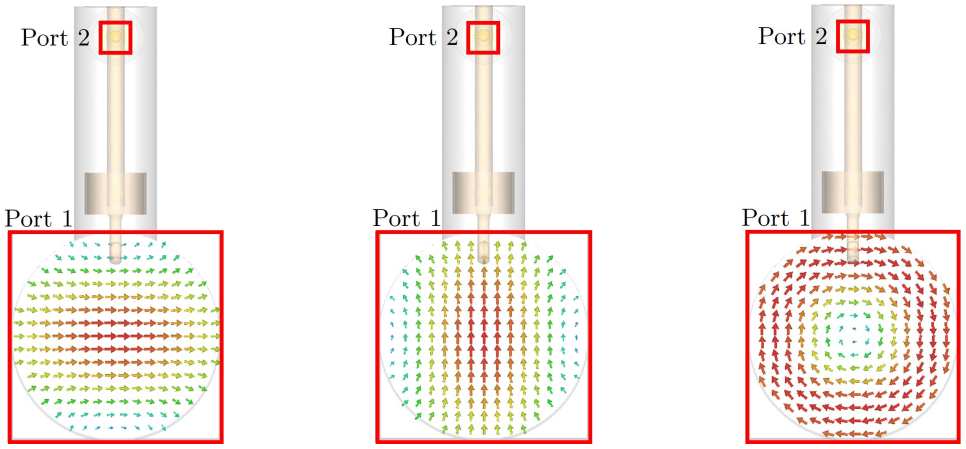

(a) TE_{11} mode **(b)** TE_{11} mode **(c)** TM_{01} mode

Figure 4.7: CST 3D setup of a HOM coupler. Port 1 is the beam pipe port, while port 2 is the coupler output port. The electric field of the first (a) and second polarization (b) of the TE_{11} mode and the magnetic field of the TM_{01} mode at the beam pipe port are depicted.

4.2.2 Probe-type PERLE coupler

The probe-type PERLE coupler was designed to predominantly damp the TM_{011} monopole passband of the 801.58 MHz 5-cell PERLE cavities. Figures 4.8 (a) and (b) depict the probe-type coupler equivalent circuit for electric coupling and the corresponding 3D geometry, respectively.

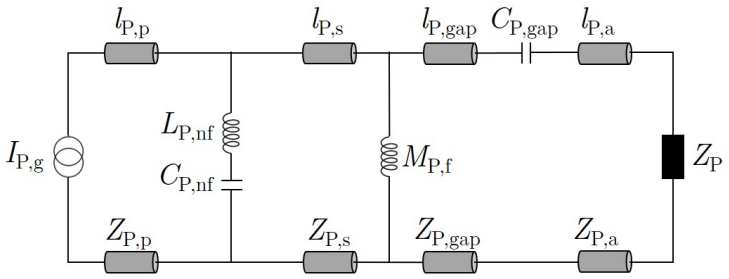

(a) Equivalent circuit of the probe-type coupler - Electric coupling

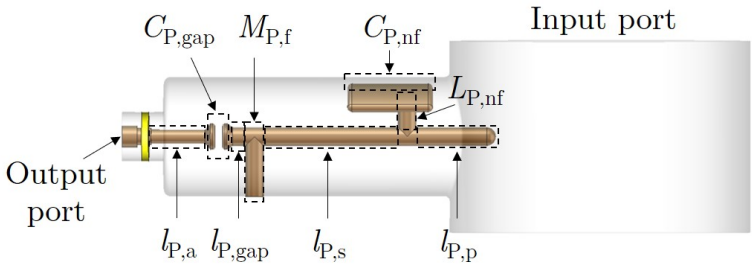

(b) Lateral view of the 3D probe-type coupler

Figure 4.8: Equivalent circuit of the probe-type coupler for electric coupling [115, 117] (a). Lateral view of the derived 3D geometry from the equivalent circuit (b). The capacitances $C_{P,i}$, inductances $L_{P,i}$, coupling inductance $M_{P,i}$, and coaxial transmission lines with length $l_{P,i}$ and characteristic impedances $Z_{P,i}$ are highlighted. Z_P represents the 50 Ω characteristic impedance of the output line.

The probe-type coupler includes a pick-up probe antenna to mainly couple the electric field inside the cavity [115, 117]. The coupler equivalent model consists of three resonant circuits connected to the current source $I_{P,g}$. The first circuit is composed of the lumped elements $l_{P,p}$, $L_{P,nf}$ and $C_{P,nf}$. The transmission line $l_{P,p}$ increases the real part of the impedance seen by the cavity field. The combination of inductance $L_{P,nf}$ and capacitance $C_{P,nf}$ forms the notch filter to reject the FM transmission. The coupling inductance $M_{P,f}$ interconnects the transmission line $l_{P,s}$ and the third resonant circuit composed by $l_{P,gap}$, $C_{P,gap}$ and $l_{P,a}$. The derivation of the probe-type coupler circuit elements based on the HOM-damping requirements of a cavity is provided in [121].

This thesis only describes the lumped elements of the equivalent circuit to facilitate the analogy with coupler components.

Considering the parametrization depicted in Figure 4.8 (b) and the probe-type coupler presented in [115] as a starting point, a detailed 3D geometry of the probe-type coupler has been optimized. This geometry is parameterized as shown in Figure 4.9. The capacitive plate is oriented to face the input port of the cavity. The geometrical parameters are tuned using the CST optimizer to increase the coupler transmission at the TM_{011} monopole passband, spanning from 1.379 GHz to 1.463 GHz, while simultaneously rejecting the FM transmission at 801.58 MHz. Yet, the probe coupler design can also provide mode mitigation at higher frequencies. The inner diameter of the coupler port $d_{P,2}$ is fixed at 51.5 mm, corresponding to one of the standard inner diameters of the port connecting the coupler to the beam pipe. The diameters of the inner conductor $d_{P,7}$, $d_{P,8}$ and $d_{P,9}$ should be sufficiently large to enable the fabrication of cooling channels. The ratio between $d_{P,1}$ and $d_{P,3}$ should be chosen to yield a fixed impedance of 50 Ω, matching the impedance of the output RF cable required for extracting the HOM power. The length $l_{P,3}$ does not significantly affect the RF transmission as the coupler is terminated with a matched load [115].

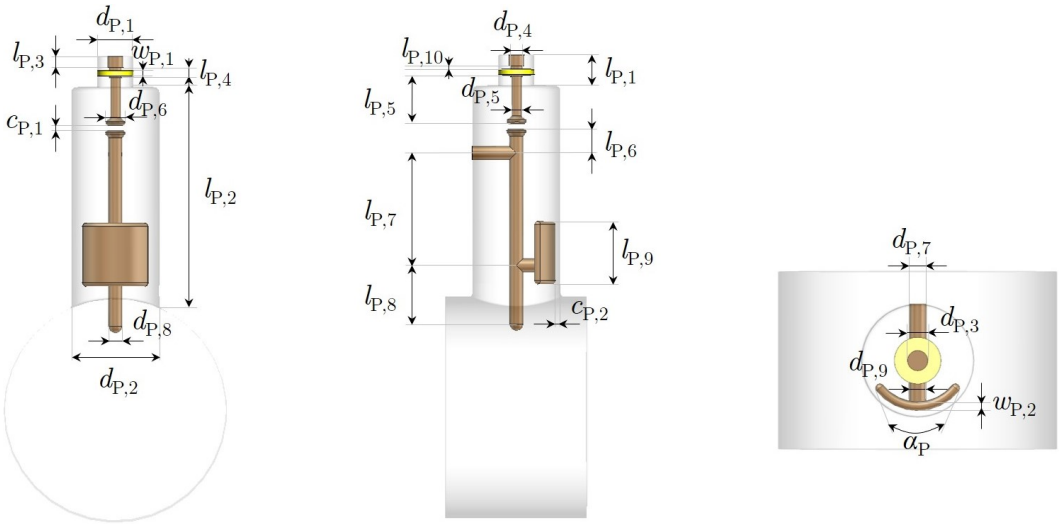

Figure 4.9: CST model and geometrical parameters of the probe-type PERLE coupler.

The subsequent steps closely follow the S-parameter tuning procedure for a probe-type coupler described in [115]. The sensitivity analysis has been performed on the geometrical parameters to assess their impact on both the monopole and the higher dipole transmissions. The parameters are varied around the values of the final optimized geometry (see Table 4.1). Figures 4.10 and 4.11 illustrate the dependency of the S-curves on selected geometrical parameters. First, the parameters with global influence on the S-parameters are tuned, such as $l_{P,1}$, $l_{P,5}$, $l_{P,7}$ and $d_{P,6}$. Then, those with local influence on the transmission are adjusted. The parameters $l_{P,8}$, $d_{P,2}$ and

$d_{P,9}$ affect the transmission up to the TM_{01} beam pipe cutoff frequency at 1.77 GHz. Conversely, $l_{P,9}$ and $d_{P,8}$ influence the S-curves up to the TE_{11} beam pipe cutoff frequency at 1.35 GHz. For any change in the values of $l_{P,4}$, $l_{P,5}$, $l_{P,6}$, $l_{P,7}$, $l_{P,8}$ and $c_{P,1}$, the total length $l_{P,2}$ is adjusted to keep a nominal penetration depth of 20 mm into the 65 mm radius beam pipe. Changing $l_{P,8}$ and $d_{P,9}$ affects the inductive part of the FM notch filter, i.e., $L_{P,nf}$ in the circuit. The FM notch tuning is performed by changing the values of $l_{P,9}$, $w_{P,2}$, $c_{P,2}$ and α_P, which represents $C_{P,nf}$ in the equivalent circuit.

Table 4.1: Optimized geometrical parameters of the probe-type PERLE coupler design.

$l_{P,1}$ [mm]	$l_{P,2}$ [mm]	$l_{P,3}$ [mm]	$l_{P,4}$ [mm]	$l_{P,5}$ [mm]	$l_{P,6}$ [mm]	$l_{P,7}$ [mm]	$l_{P,8}$ [mm]	$l_{P,9}$ [mm]	$l_{P,10}$ [mm]	$w_{P,1}$ [mm]	$w_{P,2}$ [mm]
18.0	123.5	6.5	6.0	27.6	9.6	13.8	34.3	36.8	2.0	3.0	4.0
$d_{P,1}$ [mm]	$d_{P,2}$ [mm]	$d_{P,3}$ [mm]	$d_{P,4}$ [mm]	$d_{P,5}$ [mm]	$d_{P,6}$ [mm]	$d_{P,7}$ [mm]	$d_{P,8}$ [mm]	$d_{P,9}$ [mm]	$c_{P,1}$ [mm]	$c_{P,2}$ [mm]	α_P [degree]
21.2	51.5	9.2	7.4	6.0	11.3	8.0	8.0	8.0	3.3	2.8	56.5

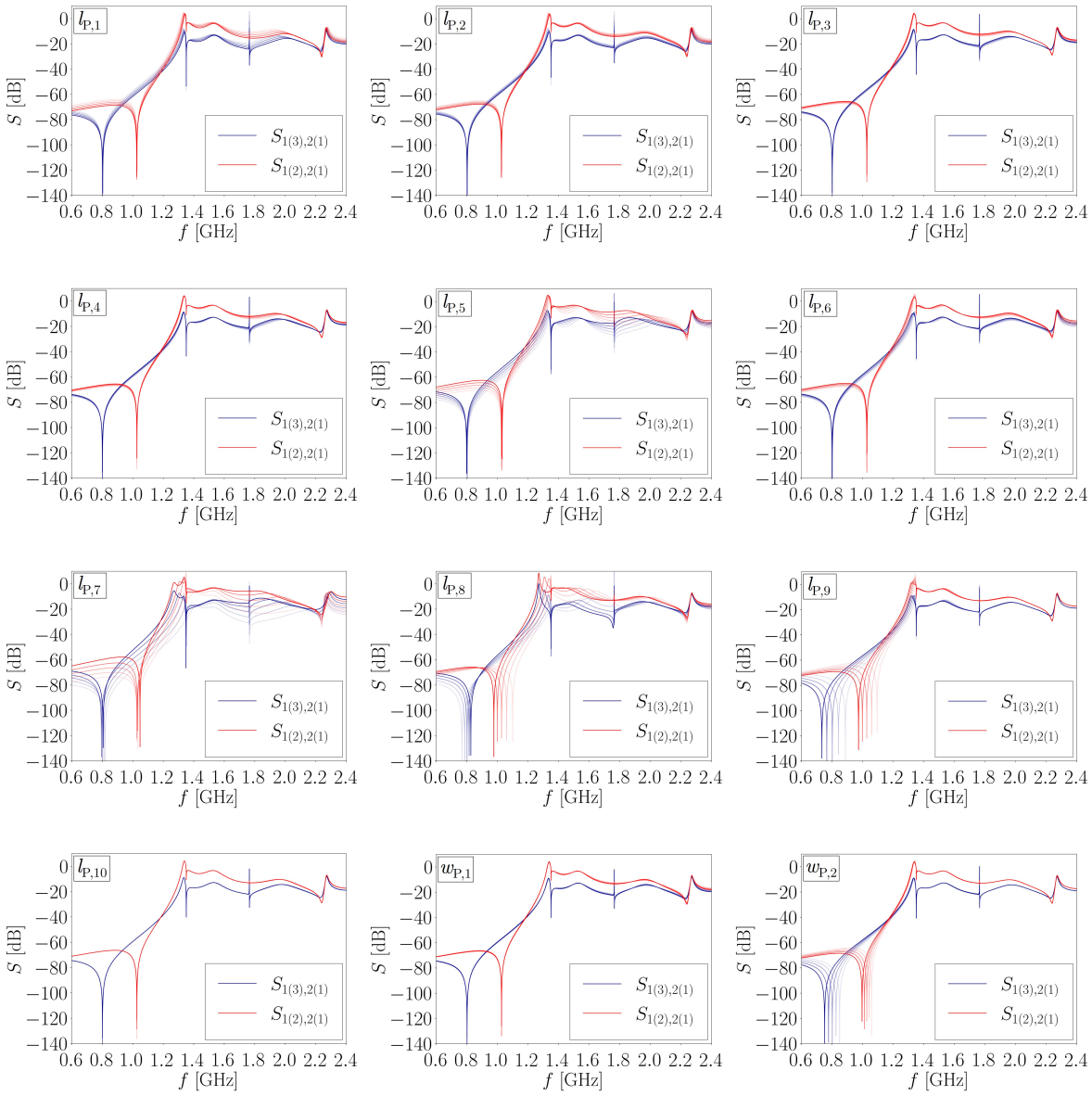

Figure 4.10: Dependency of the S-parameters on the geometrical parameters of the probe-type coupler. The TM_{01}-TEM and TE_{11}-TEM transmissions from the beam pipe port (port 1) and the output HOM coupler port (port 2) are depicted in blue and red, respectively. The geometrical parameters are changed within a range from -20% (light color) to +20% (dark color) around their nominal values provided in Table 4.1.

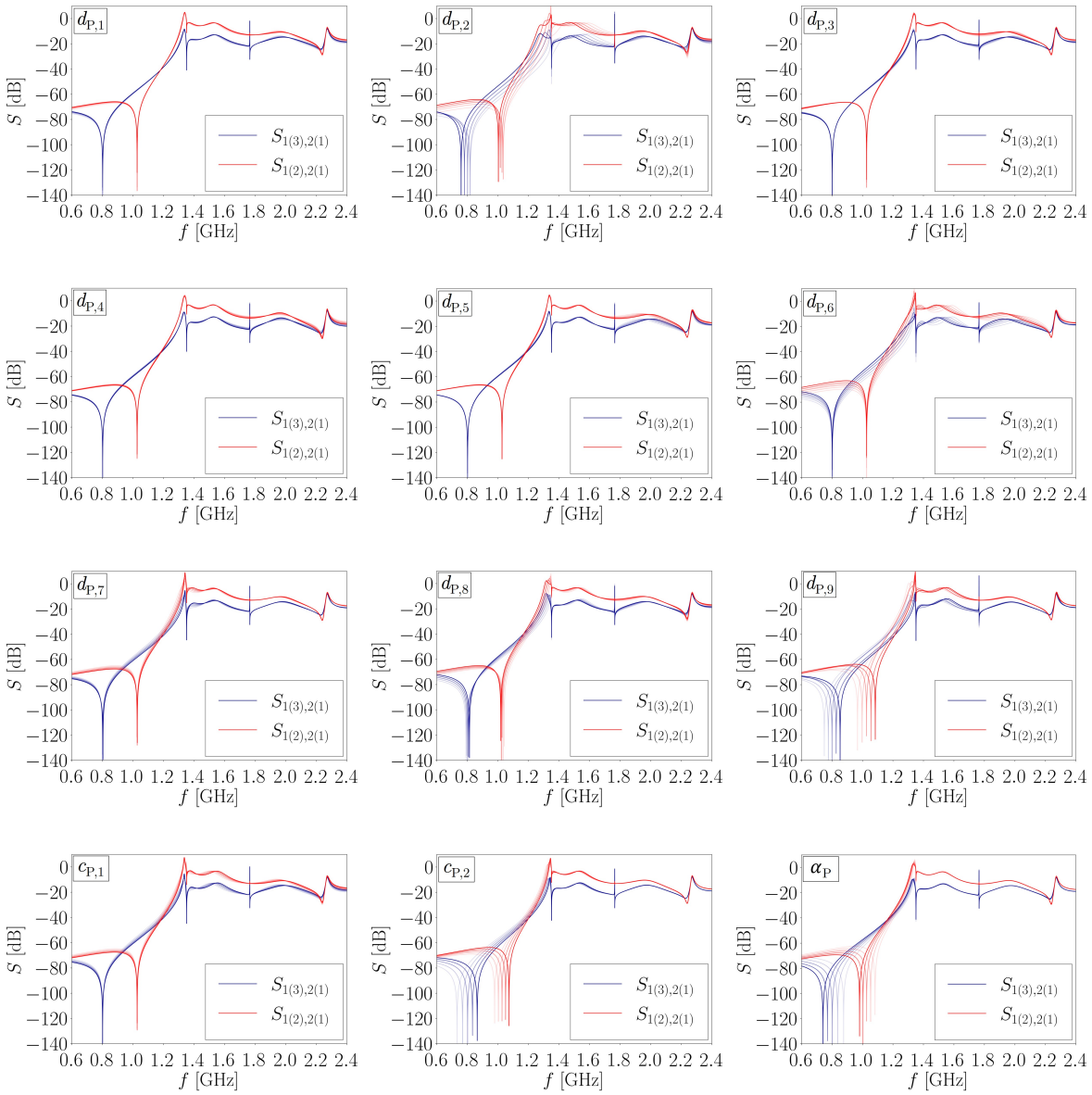

Figure 4.11: Dependency of the S-parameters on the geometrical parameters of the probe-type coupler. The TM_{01}-TEM and TE_{11}-TEM transmissions from the beam pipe port (port 1) and the output HOM coupler port (port 2) are depicted in blue and red, respectively. The geometrical parameters are changed within a range from -20% (light color) to +20% (dark color) around their nominal values provided in Table 4.1, except $d_{P,2}$, which is varied by ±10% because of space limitations.

4.2.3 Hook-type PERLE coupler

The hook-type PERLE coupler was designed to primarily damp the TE_{111} and TM_{110} dipole passbands of the 801.58 MHz 5-cell PERLE cavities. The hook-type coupler lumped circuit model for the electric coupling and the corresponding 3D geometry are illustrated in Figures 4.12 (a) and (b), respectively.

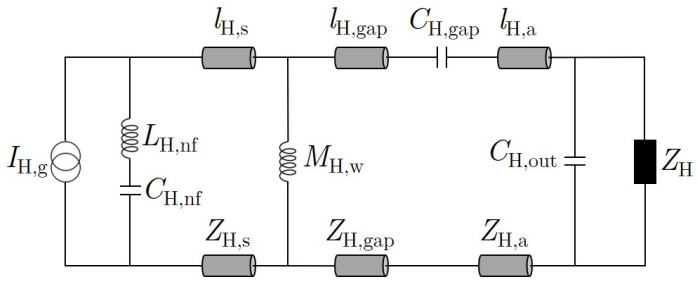

(a) Equivalent circuit of the hook-type coupler - Electric coupling

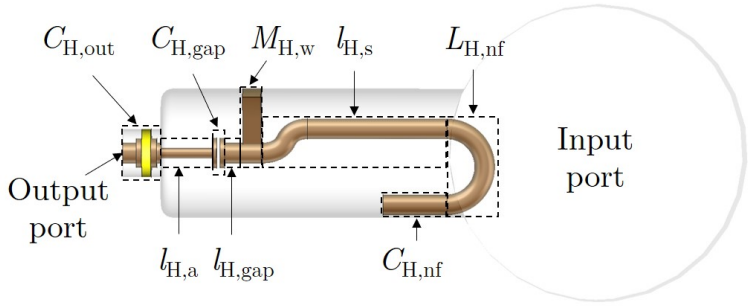

(b) Lateral view of the 3D hook-type coupler

Figure 4.12: Equivalent circuit model of the hook-type coupler for electric coupling [115, 117] (a). Lateral view of the derived 3D geometry from the equivalent circuit (b). The highlighted regions denote the specific locations of capacitances $C_{H,i}$, inductances $L_{H,i}$, coupling inductance $M_{H,i}$, and coaxial transmission lines with length $l_{H,i}$ and characteristic impedances $Z_{H,i}$ in the equivalent circuit. Z_H represents the 50 Ω characteristic impedance of the transmission line connected to the coupler output port.

This coupler features a pick-up loop to couple EM fields inside the cavity [115, 117]. The electric coupling induces a displacement current on the coupler's surface, and it is represented by a current source $I_{H,g}$ in the lumped circuit model. Conversely, in the case of magnetic coupling, a voltage is induced by the magnetic field traversing the pick-up loop. A voltage source in the equivalent circuit model can represent the induced voltage. The equivalent circuit of the hook-type coupler for magnetic coupling is reported in [117]. The combination of inductance $L_{H,nf}$ and capacitance $C_{H,nf}$ forms the notch filter to reject the FM. A coupling inductance $M_{H,w}$ is utilized to interconnect

two resonant circuits, both tuned to increase the impedance seen by the current source and, consequently, enhance the HOM power extraction at the frequencies of the TE_{111} and TM_{110} dipole modes [115]. The hook-type coupler lumped elements' derivation based on HOM-damping requirements of a cavity is given in [121].

The hook-type coupler described in [115] has been considered as the initial basis for the optimization process. The parameterized model of the hook-type coupler design for the PERLE 801.58 MHz cavities, optimized using CST, is shown in Figure 4.13.

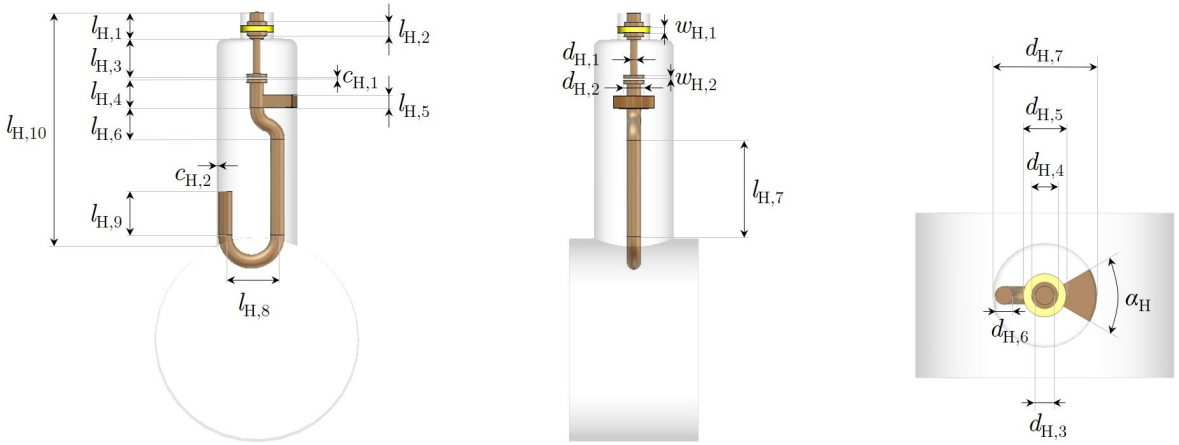

Figure 4.13: CST model and geometrical parameters of the hook-type PERLE coupler.

The active surface of the pick-up loop is oriented to be parallel to the magnetic field of the beam pipe TM_{01} mode to exclude the magnetic coupling to the cavity FM [118]. The geometrical parameters are tuned using the CST frequency domain solver to increase the coupler transmission at the TE_{111} and TM_{110} dipole mode passbands, which range from 0.936 GHz to 1.167 GHz, while rejecting the FM transmission at 801.58 MHz. However, certain parameters are subject to engineering constraints. The diameter $d_{H,7}$ is fixed at 51.5 mm, as for the probe-type PERLE coupler. The diameter $d_{H,6}$ should be maximized to facilitate the fabrication of a hollow inner conductor if internal cooling by liquid helium is foreseen. The ratio between $d_{H,5}$ and $d_{H,3}$ ensures a 50 Ω impedance. The length $l_{H,1}$ has no significant impact on the coupler transmission since it is terminated with matched impedance [115].

The S-parameter tuning procedure for a hook-type coupler described in [115] is used in the following. To tune the HOM coupler geometry, the influence of each geometrical parameter on both monopole and the higher dipole transmissions between ports is first analyzed. Figures 4.14 and 4.15 depict the dependency of the S-curves on specific geometrical parameters, which are varied around the values of the final tuned geometry, detailed in Table 4.2. Similar to the probe-type coupler, initially, parameters with a broad influence on the S-parameters are optimized, such as $l_{H,7}$ and $l_{H,8}$. For any modification of the parameters $l_{H,3}$, $l_{H,4}$, $l_{H,6}$, $l_{H,7}$ and $c_{H,1}$, which change the total length of the coupler inner conductor, the total length $l_{H,10}$ is adjusted

accordingly to maintain a nominal penetration depth of 20 mm into the 65 mm radius beam pipe. Adjusting the parameter $l_{\mathrm{H},7}$ mainly impacts the peaks of S-parameters in the frequency range of the dipole passbands of interest without significantly changing the FM rejection. The capacitance gap $c_{\mathrm{H},1}$ is kept constant for any variation of the distance $l_{\mathrm{H},8}$, and vice versa. Increasing the parameter $l_{\mathrm{H},8}$ enhances the inductive part of the notch filter ($L_{\mathrm{H,nf}}$ in the equivalent circuit), lowering its frequency. After optimizing the parameters with global influence on the S-parameters, those with a local effect on the transmission, such as $l_{\mathrm{H},3}$, $l_{\mathrm{H},4}$, $l_{\mathrm{H},6}$, $d_{\mathrm{H},2}$, $d_{\mathrm{H},6}$, $c_{\mathrm{H},1}$ and α_{H}, are optimized. In particular, the length $l_{\mathrm{H},3}$, the diameter $d_{\mathrm{H},2}$, the capacitive gap between the upper and lower parts of the inner conductor $c_{\mathrm{H},1}$ and the angle α_{H} of the coupling inductance part contribute in shaping the peaks of the S-parameter in the frequency range of interest. Finally, the FM notch is tuned at 801.58 MHz through the capacitive gap $c_{\mathrm{H},2}$ and the length $l_{\mathrm{H},9}$, whose combination corresponds to the capacitance $C_{\mathrm{H,nf}}$ of the FM notch filter in the lumped circuit model [115]. The geometrical parameters of the tuned hook-type coupler design for the PERLE 801.58 MHz cavity are reported in Table 4.2.

Table 4.2: Optimized geometrical parameters of the hook-type PERLE coupler design.

$l_{\mathrm{H},1}$ [mm]	$l_{\mathrm{H},2}$ [mm]	$l_{\mathrm{H},3}$ [mm]	$l_{\mathrm{H},4}$ [mm]	$l_{\mathrm{H},5}$ [mm]	$l_{\mathrm{H},6}$ [mm]	$l_{\mathrm{H},7}$ [mm]	$l_{\mathrm{H},8}$ [mm]	$l_{\mathrm{H},9}$ [mm]	$l_{\mathrm{H},10}$ [mm]	$w_{\mathrm{H},1}$ [mm]
16.8	9.0	24.5	18.0	8.0	20.4	61.3	33.5	28.1	132.1	4.0
$w_{\mathrm{H},2}$ [mm]	$d_{\mathrm{H},1}$ [mm]	$d_{\mathrm{H},2}$ [mm]	$d_{\mathrm{H},3}$ [mm]	$d_{\mathrm{H},4}$ [mm]	$d_{\mathrm{H},5}$ [mm]	$d_{\mathrm{H},6}$ [mm]	$d_{\mathrm{H},7}$ [mm]	$c_{\mathrm{H},1}$ [mm]	$c_{\mathrm{H},2}$ [mm]	α_{H} [degree]
2.0	4.5	13.5	9.2	13.0	21.2	9.1	51.5	1.5	1.0	60

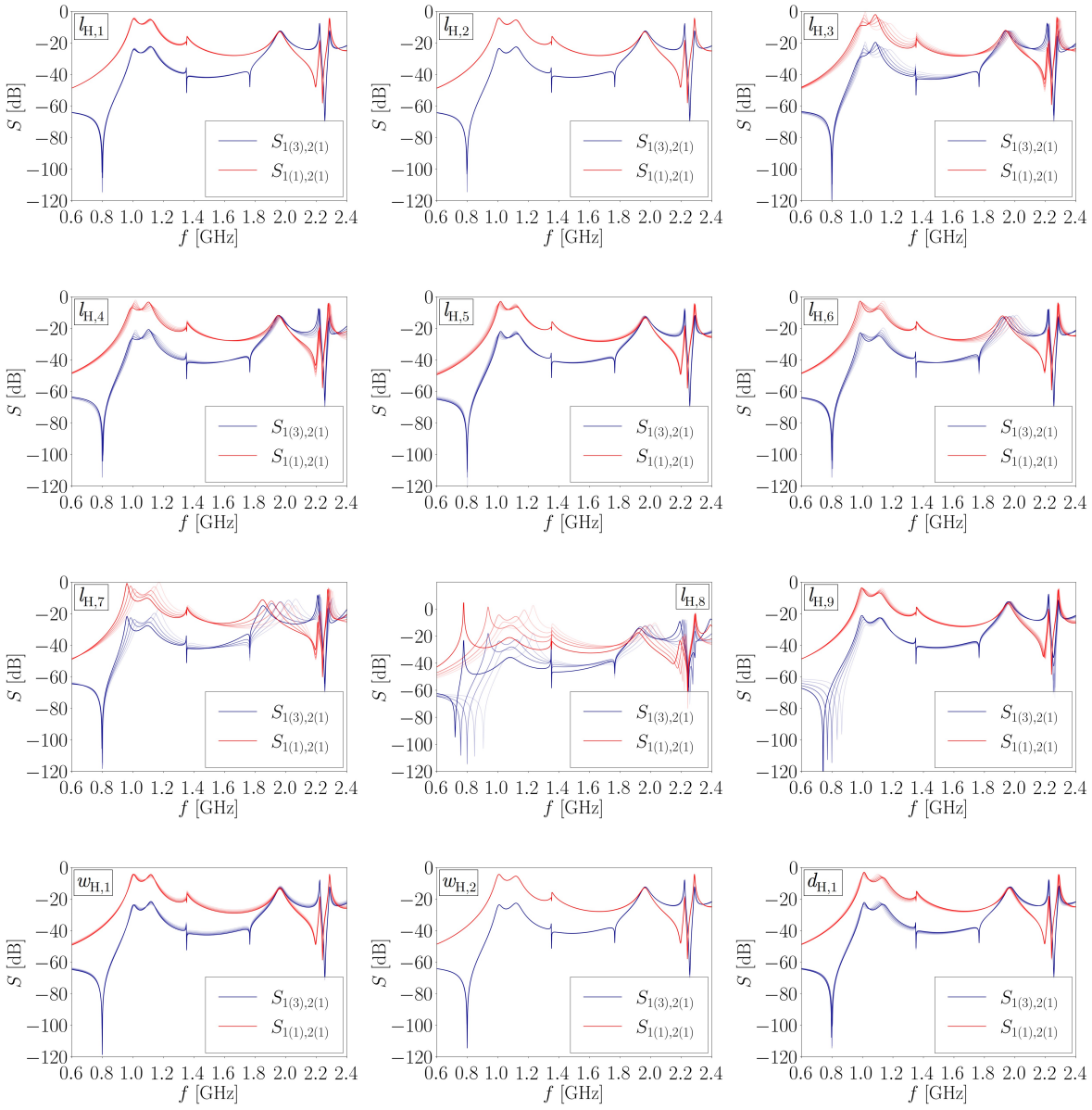

Figure 4.14: Dependency of the S-parameters on the geometrical parameters of the hook-type coupler. The TM_{01}-TEM and TE_{11}-TEM transmissions from the beam pipe port (port 1) and the output HOM coupler port (port 2) are depicted in blue and red, respectively. The geometrical parameters are varied within a range from -20% (light color) to +20% (dark color) around their nominal values provided in Table 4.2, except $d_{H,7}$, which is changed by ±10% because of space limitations.

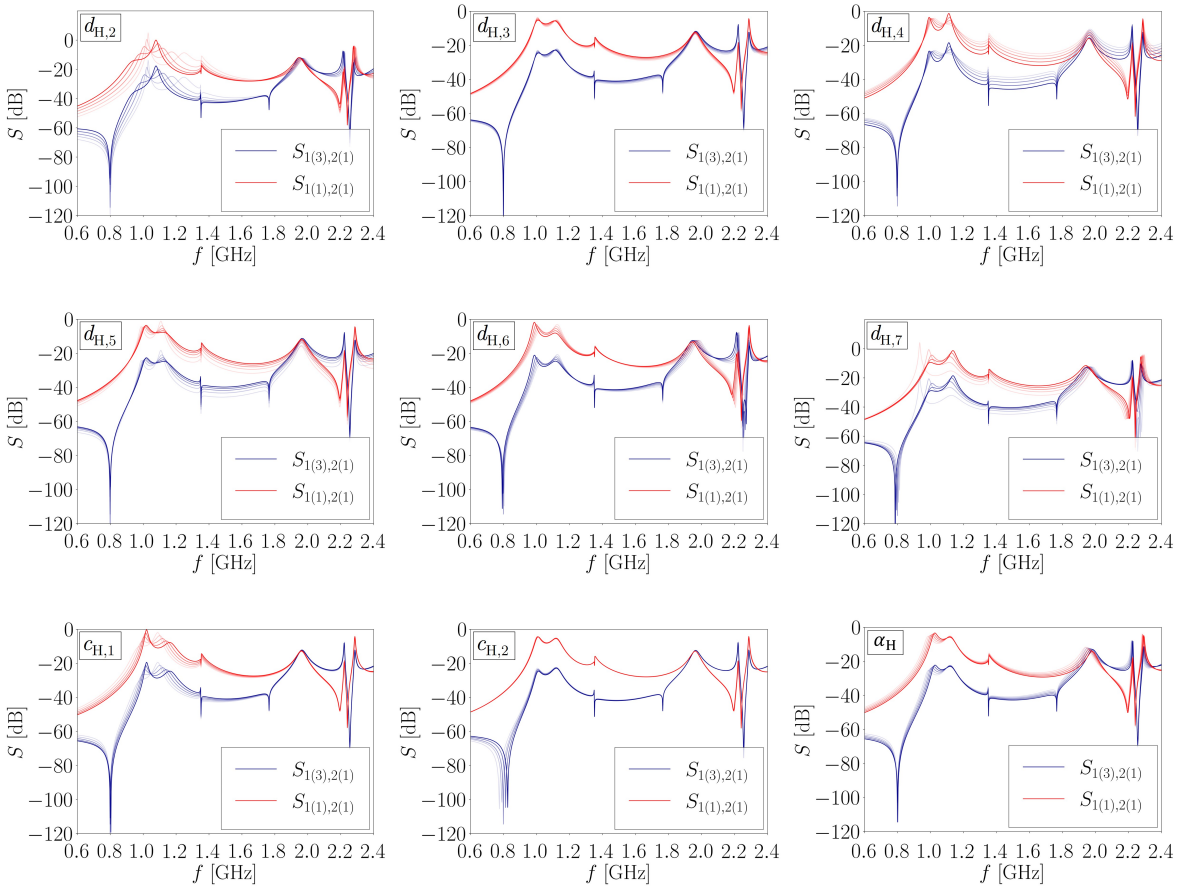

Figure 4.15: Dependency of the S-parameters on the geometrical parameters of the hook-type coupler. The TM_{01}-TEM and TE_{11}-TEM transmissions from the beam pipe port (port 1) and the output HOM coupler port (port 2) are depicted in blue and red, respectively. The geometrical parameters are changed within a range from -20% (light color) to +20% (dark color) around their nominal values listed in Table 4.2.

4.2.4 DQW-type PERLE coupler

The DQW-type PERLE coupler was conceived as a unique design to mainly damp the TM_{011} monopole passband, along with both the TE_{111} and TM_{110} dipole passbands of the 801.58 MHz 5-cell PERLE cavities. The DQW coupler lumped circuit model for the electric coupling and the corresponding 3D geometry are depicted in Figures 4.16 (a) and (b), respectively.

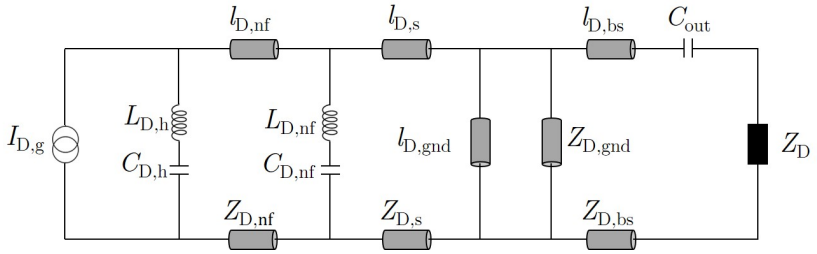

(a) Equivalent circuit of the DQW-type coupler - Electric coupling

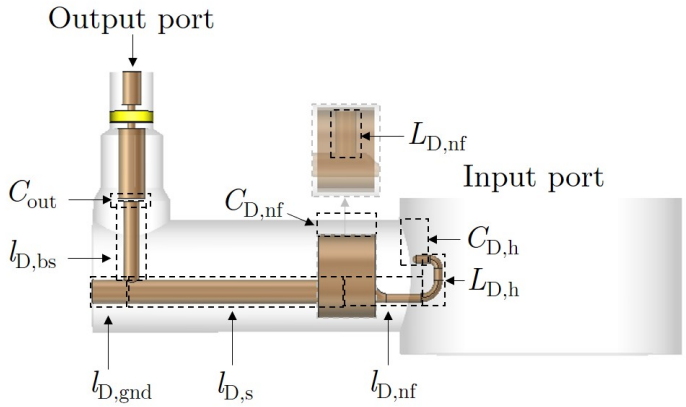

(b) Lateral view of the 3D DQW-type PERLE coupler

Figure 4.16: Equivalent circuit model of the DQW coupler for electric coupling [122] (a). Lateral view of the derived 3D geometry from the equivalent circuit (b). The highlighted regions denote the locations of capacitances $C_{D,i}$, inductances $L_{D,i}$, and coaxial transmission lines with length $l_{D,i}$ and characteristic impedances $Z_{D,i}$ in the equivalent circuit. Z_D represents the 50 Ω impedance of the transmission line connected to the coupler output port.

The DQW coupler features a hook-shaped pick-up antenna to couple EM fields inside the cavity [115, 122]. In the equivalent circuit, the electric coupling is modeled by a current source $I_{D,g}$. The pick-up antenna is represented by the combination of capacitance $C_{D,h}$ and the inductance $L_{D,h}$. This initial segment of the circuit is connected via the transmission line $l_{D,nf}$ to the FM notch filter, characterized by the capacitance $C_{D,nf}$ and the inductance $L_{D,nf}$. The FM notch filter resembles a capacitive

jacket connected to the central inner conductor shaft via an inductive stub [115]. This part is followed by the shaft transmission line $l_{\mathrm{D,s}}$ connected to the ground and coupled with the bent straight section $l_{\mathrm{D,bs}}$. This transmission line couples to the 50 Ω output line via the capacitance C_{out}. The derivation of the circuit elements of the DQW-type coupler is reported in [122]. Similarly to the probe-type and hook-type couplers, the lumped elements are presented to facilitate the analogy with coupler components. The parameterized 3D model of the DQW coupler optimized using CST is depicted in Figure 4.17.

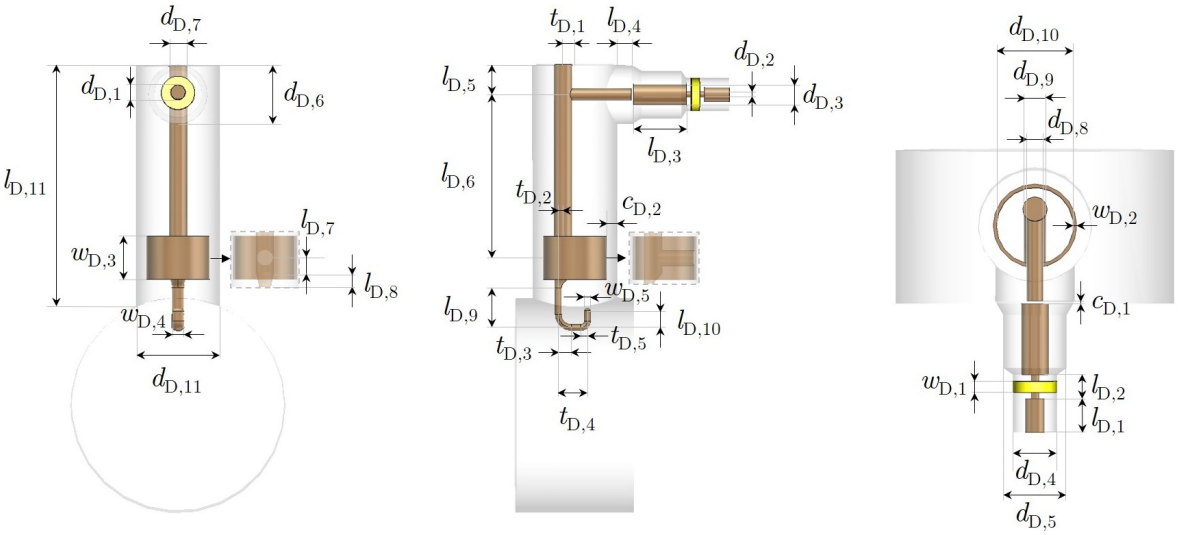

Figure 4.17: CST model and geometrical parameters of the DQW-type PERLE coupler.

The DQW-type coupler described in [115, 122] has been selected as a starting point for the optimization process. The pick-up antenna is oriented to face the cavity input port to enhance the monopole mode damping. The geometrical parameters are optimized for enhancing the S-parameters at the TM_{011}, TE_{111} and TM_{110} passbands, while at the same time rejecting the FM transmission at 801.58 MHz. The coupler design can also provide enough damping for higher frequency modes, such as the TM_{111} dipole mode at around 1.5 GHz. The inner diameter of the port $d_{\mathrm{D,11}}$ is fixed at 51.5 mm, as in the designed hook-type and probe-type couplers. The diameter of the central shaft $d_{\mathrm{D,7}}$, the diameter of the adjacent horizontal rod $d_{\mathrm{D,8}}$, and the axes $w_{\mathrm{D,4}}$ and $w_{\mathrm{D,5}}$ of the loop-shaped pick-up antenna should be large enough to ease the manufacturing of channels in case liquid helium cooling is foreseen. The ratio between $d_{\mathrm{D,4}}$ and $d_{\mathrm{D,1}}$ should be chosen to deliver a fixed line impedance of 50 Ω. The length $l_{\mathrm{D,1}}$ has no relevant impact on the coupler transmission because it is terminated with matched impedance [115].

The S-parameter optimization procedure for a DQW-type coupler described in [115] is used in the following. A sensitivity analysis of the S-parameters on the geometrical parameters was conducted. Figure 4.18 and 4.19 depicts the S-parameter dependency

on selected geometrical parameters. The parameters are changed around the values of the final optimized geometry, given in Table 4.3. Similar to the other two analyzed HOM couplers, initially, the parameters with a global influence on the S-parameters, such as $l_{\mathrm{D},4}$, $l_{\mathrm{D},6}$, $l_{\mathrm{D},9}$, $d_{\mathrm{D},6}$, $d_{\mathrm{D},7}$, $d_{\mathrm{D},8}$, $t_{\mathrm{D},1}$ and $t_{\mathrm{D},4}$ are tuned. The value of length $l_{\mathrm{D},6}$ strongly influences the shape and the location of the S-parameter peaks, especially at the TE_{111} and TM_{011} passbands. This parameter also determines the penetration depth of the antenna into the beam pipe, which is fixed at 20 mm. Varying the diameter of the central shaft $d_{\mathrm{D},7}$ mainly affects the S-parameter peaks at the first two dipole passbands, while its distance from the axis of the coupler $t_{\mathrm{D},1}$ mainly influences the transmission at the TE_{111} dipole passband and also causes detuning of the FM notch. The longitudinal length of the hook-shaped antenna $t_{\mathrm{D},4}$, the diameters $d_{\mathrm{D},6}$ and $d_{\mathrm{D},8}$, and the lengths $l_{\mathrm{D},4}$ and $l_{\mathrm{D},9}$ globally affect the coupler transmission without significantly detuning the FM notch. Subsequently, the geometrical parameters with local influence on the coupler transmission, such as $c_{\mathrm{D},1}$, $l_{\mathrm{D},7}$, $l_{\mathrm{D},8}$, $l_{\mathrm{D},10}$, and $d_{\mathrm{D},5}$ are adjusted. Both parameters $l_{\mathrm{D},7}$ and $l_{\mathrm{D},8}$ are tuned to shape the S-parameter peak of the TM_{110} dipole passband. The diameter $d_{\mathrm{D},5}$, the length of pick-up tip $l_{\mathrm{D},10}$ and the capacitive gap $c_{\mathrm{D},1}$ are tuned to adjust the transmission peaks of both the TM_{110} and TM_{011} passbands. The diameter of the inductive stub $d_{\mathrm{D},9}$ mainly impacts the S-parameter peak of the TE_{111} passband and significantly changes the inductive effect of the notch at FM frequency. Consequently, the tuning of the notch at 801.58 MHz is performed by changing the values $c_{\mathrm{D},2}$ and $w_{\mathrm{D},3}$, which approximates the capacitance $C_{\mathrm{D,nf}}$ in the equivalent circuit [115]. The geometrical parameters of the tuned DQW-type coupler design for the PERLE 801.58 MHz cavity are listed in Table 4.3.

Table 4.3: Optimized geometrical parameters of the DQW-type PERLE coupler design.

	$l_{\mathrm{D},1}$	$l_{\mathrm{D},2}$	$l_{\mathrm{D},3}$	$l_{\mathrm{D},4}$	$l_{\mathrm{D},5}$	$l_{\mathrm{D},6}$	$l_{\mathrm{D},7}$	$l_{\mathrm{D},8}$	$l_{\mathrm{D},9}$	$l_{\mathrm{D},10}$	$l_{\mathrm{D},11}$	$d_{\mathrm{D},1}$
[mm]	15.0	11.0	33.2	8.7	17.9	98.6	8.0	10.0	24.1	10.0	140.7	8.7
	$d_{\mathrm{D},2}$	$d_{\mathrm{D},3}$	$d_{\mathrm{D},4}$	$d_{\mathrm{D},5}$	$d_{\mathrm{D},6}$	$d_{\mathrm{D},7}$	$d_{\mathrm{D},8}$	$d_{\mathrm{D},9}$	$d_{\mathrm{D},10}$	$d_{\mathrm{D},11}$	$t_{\mathrm{D},1}$	$t_{\mathrm{D},2}$
[mm]	3.6	12.3	20.0	28.6	35.9	11.0	7.1	9.6	35.3	51.5	7.0	3.0
	$t_{\mathrm{D},3}$	$t_{\mathrm{D},4}$	$t_{\mathrm{D},5}$	$w_{\mathrm{D},1}$	$w_{\mathrm{D},2}$	$w_{\mathrm{D},3}$	$w_{\mathrm{D},4}$	$w_{\mathrm{D},5}$	$c_{\mathrm{D},1}$	$c_{\mathrm{D},2}$		
[mm]	8.0	17.7	4.0	5.0	1.5	26.0	7.2	4.0	1.2	6.6		

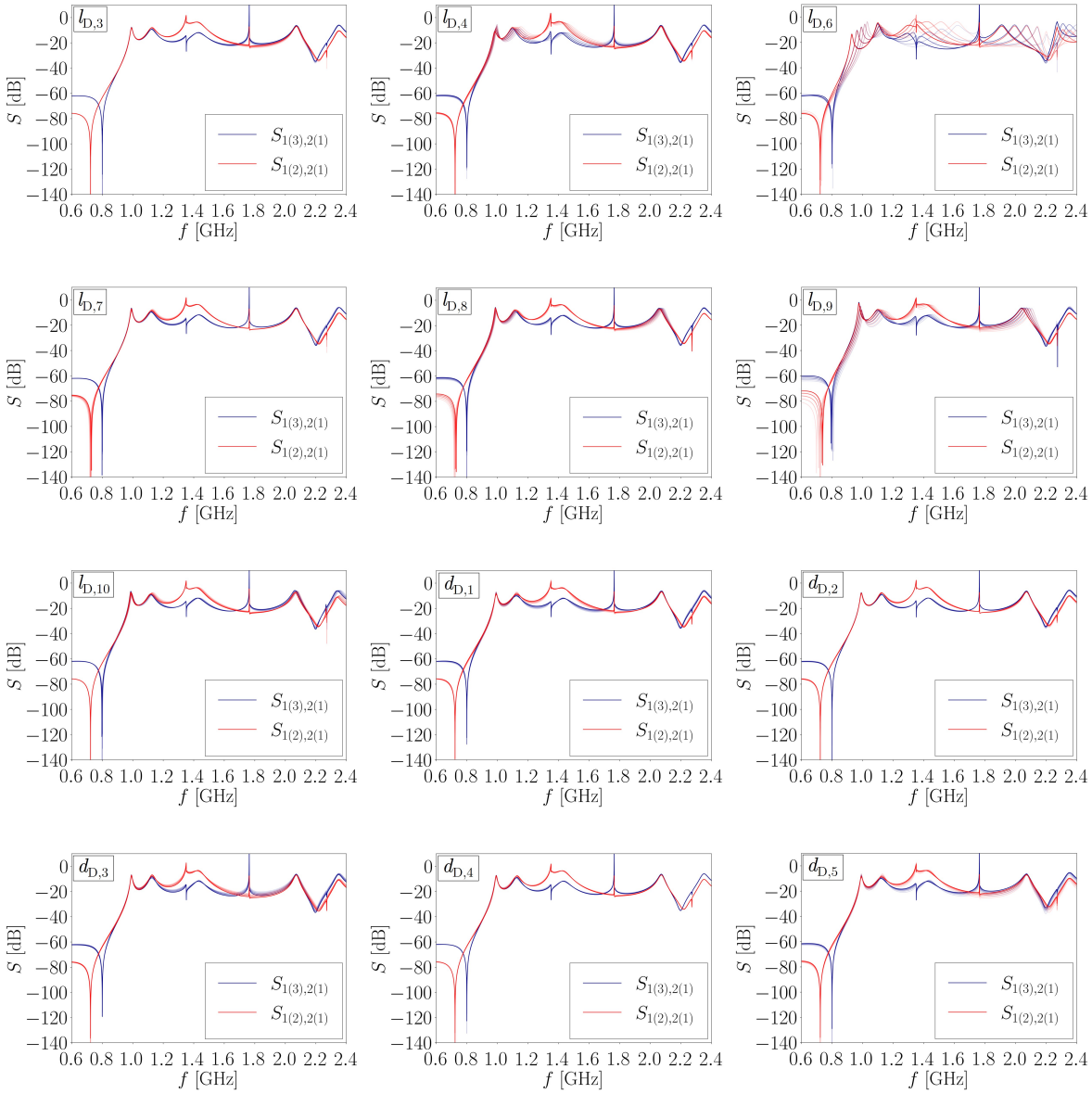

Figure 4.18: Dependency of the S-parameters on the geometrical parameters of the DQW-type coupler. The TM_{01}-TEM and TE_{11}-TEM transmissions from the beam pipe port (port 1) and the output HOM coupler port (port 2) are depicted in blue and red, respectively. The geometrical parameters are varied within a range from -20% (light color) to +20% (dark color) around their nominal values provided in Table 4.3.

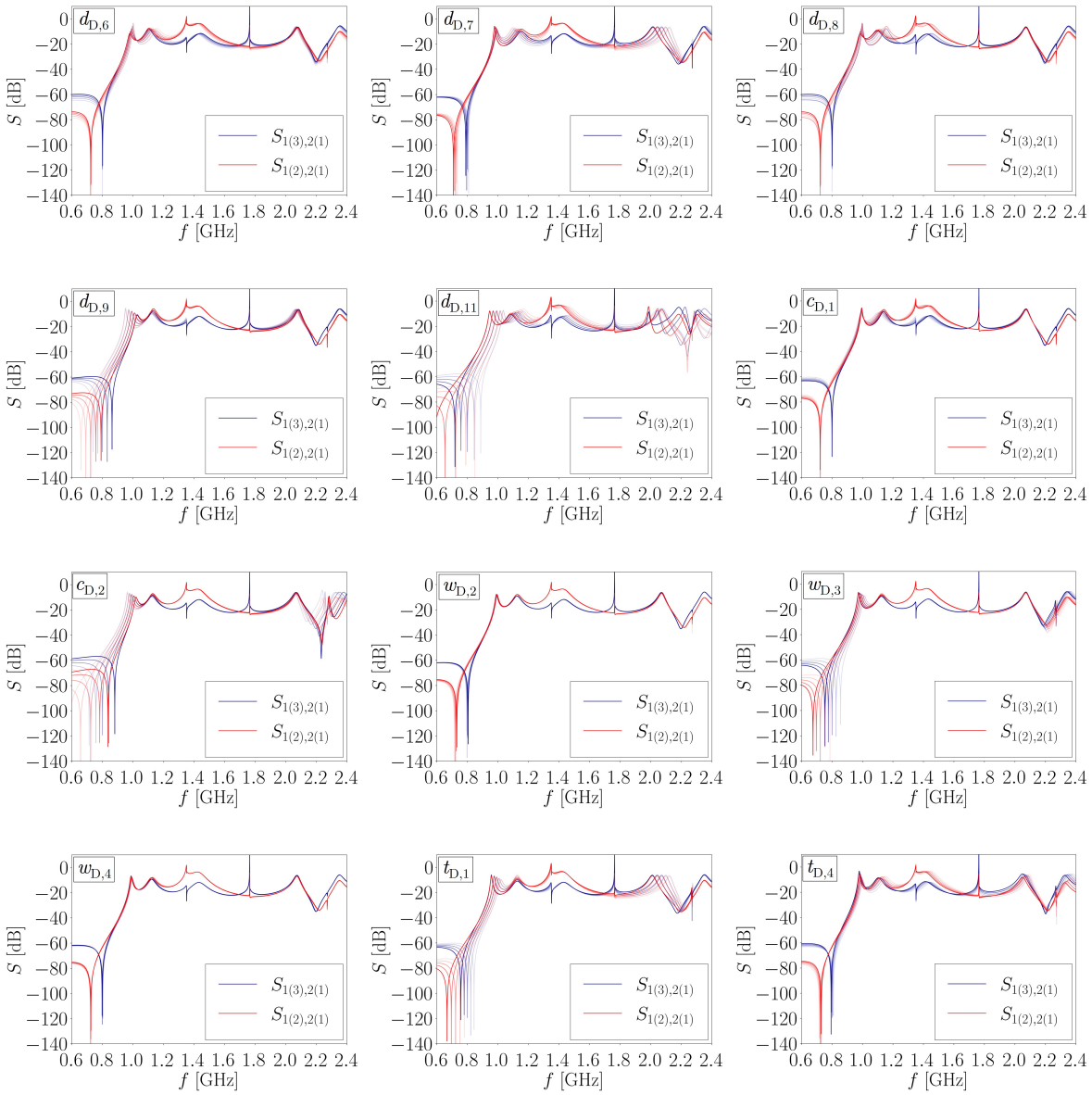

Figure 4.19: Dependency of the S-parameters on the geometrical parameters of the DQW-type coupler. The TM_{01}-TEM and TE_{11}-TEM transmissions from the beam pipe port (port 1) and the output HOM coupler port (port 2) are depicted in blue and red, respectively. The geometrical parameters are changed within a range from -20% (light color) to +20% (dark color) around their nominal values provided in Table 4.3, except $d_{D,11}$, which is varied by ±10% due to space constraints.

4.2.5 Summary of HOM coupler optimization results

The S-parameters of the three investigated coupler designs have been optimized to provide high transmission at frequencies corresponding to the high-impedance HOMs of the 5-cell PERLE cavity while maintaining FM efficiency. Figures 4.20 (a) and (b) show the monopole and dipole transmissions of the optimized coupler designs, respectively.

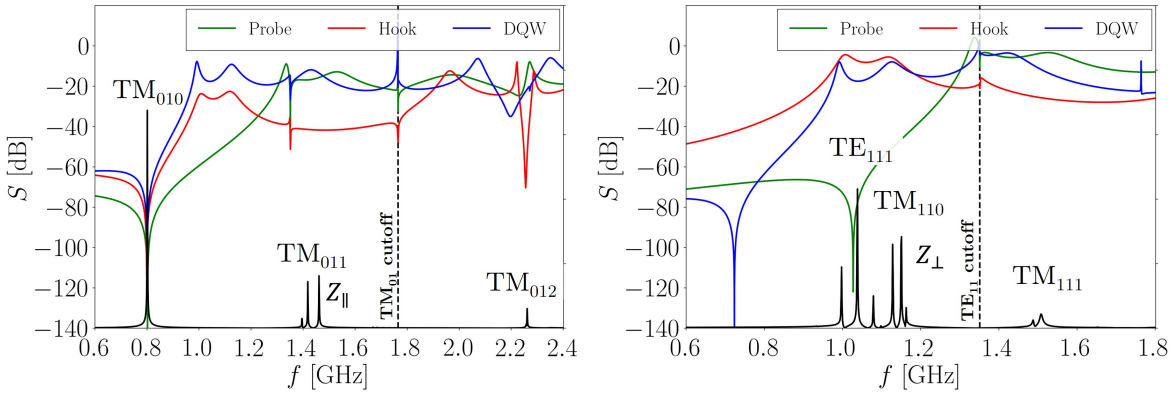

(a) Monopole transmission **(b)** Dipole transmission

Figure 4.20: Monopole (a) and dipole (b) transmissions of the optimized hook-type (red), probe-type (green), and DQW-type (blue) HOM couplers for the PERLE cavity. The longitudinal impedance $Z_{\parallel}$ and transversal impedance $Z_{\perp}$ of the 5-cell PERLE cavity are depicted as black curves in (a) and (b) for reference, respectively. The black vertical lines in (a) and (b) represent the cutoff frequency of the TM_{01} and TE_{11} beam pipe modes, respectively. The mode passband nomenclature is given.

The initial requirements for the high-impedance HOMs and the FM notch filter have been satisfied for certain selected designs. The DQW coupler provides higher transmission at the TM_{011} monopole passband than the probe-type coupler. Due to its design, the hook-type coupler is intrinsically unsuitable for damping the first monopole passband. Conversely, the hook-type coupler yields higher damping for the TE_{111} and TM_{110} dipole passbands than the DQW coupler. Due to its inherent design, the probe-type coupler remains inadequate for damping the first two dipole passbands. The DQW-type coupler emerges as the most advantageous solution for simultaneously damping both the first monopole and the first two dipole passbands, while a combination of the probe-type and hook-type couplers is required for efficiently damping them separately. The proposed HOM-damping schemes for the 5-cell PERLE cavity are analyzed in Chapter 5.

4.3 HOM coupler prototyping

After optimizing the RF transmission of the three HOM coupler designs, simulations were conducted using CST to evaluate their damping performance. The analyzed coupler schemes lowered impedance levels below the BBU instability limits. These results were partially published in [49, 90]. The complete survey on HOM-damping and RF-heating simulations for two different damping schemes is presented in Chapter 5. These findings have led to the fabrication of prototypes of each coupler to test them in two-cell and five-cell 801.58 MHz PERLE-type cavities. The survey of the HOM measurements conducted on the PERLE cavities using the fabricated coupler prototypes is presented in Chapter 7. This section first introduces the mechanical design of each produced coupler. Subsequently, the 3D printing procedure and the surface copper-coating technique used for fabricating the HOM couplers are described. Finally, metrological measurements for three of the produced HOM couplers are provided.

4.3.1 Mechanical design for coaxial HOM couplers

Following the optimization of the RF transmission for the three coaxial HOM coupler designs, the subsequent prototyping phase involves developing their mechanical design. Figure 4.21 depicts the mechanical design of the HOM coupler prototypes for the PERLE cavities. These couplers have been used for conducting HOM-damping measurements on the 2-cell and 5-cell 801.58 MHz Cu PERLE cavities (see Section 7.2).

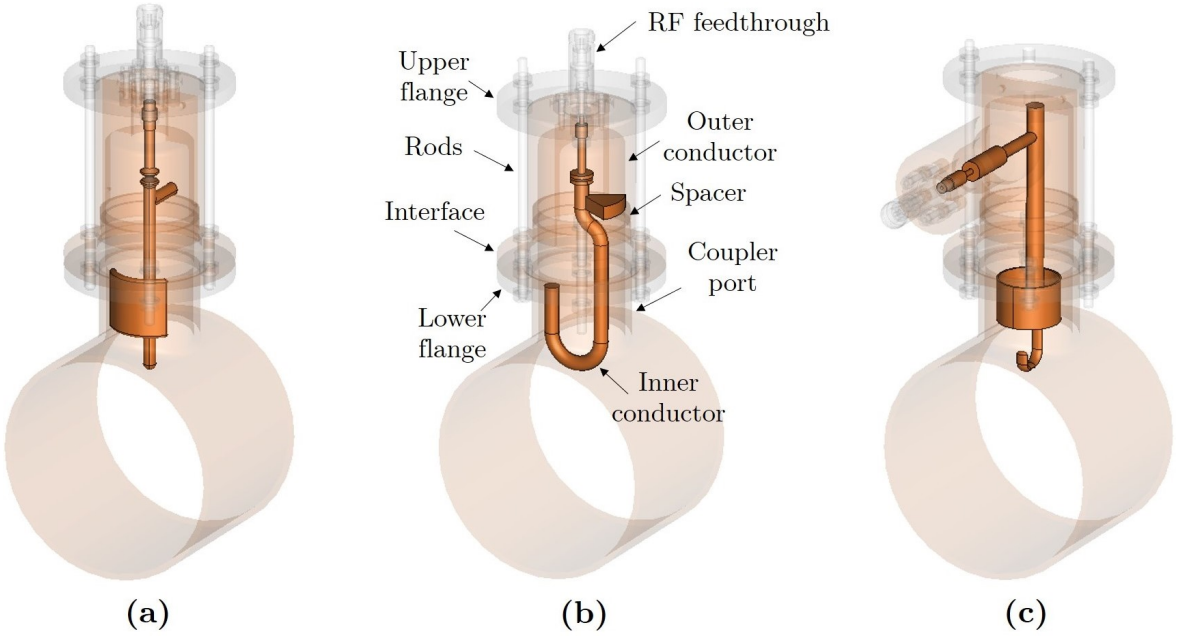

Figure 4.21: Mechanical design of the optimized HOM coupler prototypes: probe-type (a), hook-type (b), and DQW-type PERLE coupler (c).

The three mechanical designs were built based on a fully demountable concept, allowing for the interchangeability of several pieces, such as flanges, spacers, interfaces, and HOM coupler ports, between these three designs. Building pieces separately also facilitates the 3D printing fabrication and the subsequent Cu coating of the surfaces (see Subsection 4.3.2). The inner conductor, the outer conductor, and the hollow-cylindrical interface between the outer conductor and the stainless steel lower flange are 3D printed in epoxy resin and then copper-coated. An 8 mm thick Cu ring-shaped spacer is placed between the coupler interface and its outer conductor. This ring is used to adjust the penetration depth of the inner conductor to 20 mm into the beam pipe. Reducing the thickness of the spacer moves the ensemble of the inner and outer conductor downward, resulting in a greater penetration of the inner conductor into the beam tube. This feature could be advantageous in the event of conducting sensitivity analysis on the penetration depth for HOM-damping measurements. Two stainless steel flanges are used to secure the assembly through six threaded rods. The lower flange is located between the coupler interface and the Cu 3D-printed coupler port. Additional details on the HOM coupler port, which connects the HOM coupler to the cavity beam pipe, are provided in Section 6.3. The upper flange accommodates the RF feedthrough, which connects the inner conductor's upper part to the RF measurement cable (refer to Section 7.2). The drawings containing the technical details of the three mechanical designs are given in Figures A.1, A.2, and A.3 of the Annex A.

4.3.2 3D printing for HOM coupler fabrication

The installation of coaxial Nb HOM couplers on the cutoff tubes of SRF 5-cell PERLE cavities is foreseen to damp the cavity's HOMs. The initial validation of the design and RF transmission behavior of a HOM coupler prototype can be performed through low-power RF measurements on a cavity at room temperature (refer to Section 7.2). This approach avoids an expensive Nb coupler fabrication in the initial design phase. A promising, time-efficient, and cost-saving technique currently under study at CERN involves using epoxy for 3D-printing HOM couplers. The surfaces of the coupler are then electroplated with Copper to impart necessary electrical characteristics. Some of the results from the initial production of these couplers have been presented in [123].

The HOM coupler prototypes have been manufactured employing the stereolithography (SLA©) technique with epoxy at the CERN Polymer Laboratory.[1] The Viper Si2 SLA© rapid prototyping machine (see Figure 4.22 (a)) was utilized for 3D printing HOM couplers with both Accura© 25 [124] and Accura© 48 HTR (High-Heat Resistant) [125] epoxy resins. The build volume of the used printer is $250 \times 250 \times 250$ mm^3. The Viper Si2 can print parts in subsequent layers with a $\pm$ 0.1 mm precision. The printer supports a minimum layer thickness of 0.08 mm and a maximum thickness of

[1]The Polymer Laboratory team at CERN performed the 3D printing of the HOM couplers using the 3D CAD models provided by the author.

0.10 mm. The procedure to manufacture a HOM coupler using SLA 3D printing involves different steps (see Figure 4.22 (b)) [126, 127]. The printing tank contains epoxy resin, which hardens under ultraviolet (UV) rays. A UV laser solidifies a resin layer according to a specific pattern on a platform. Subsequently, the platform is lowered by one layer within the tank, and a blade covers the tank surface with a new resin layer. The procedure is repeated for each layer until the 3D part is completed. Resin supports are also printed to hold specific object parts and removed after printing. Any residual liquid resin is cleaned using a solvent. Finally, the 3D part is cured for 15 minutes in a UV oven to ensure complete resin polymerization and enhance its mechanical properties and durability.

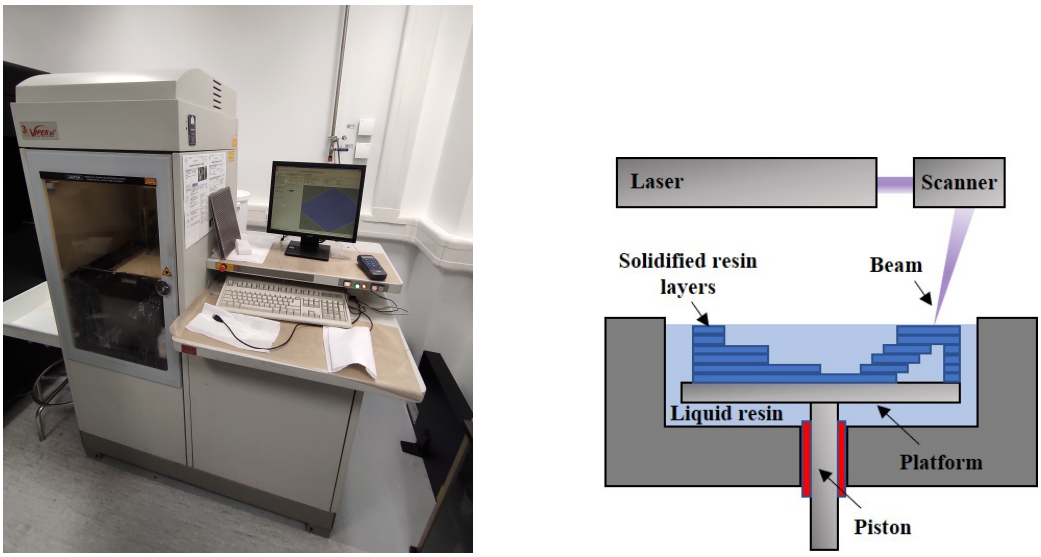

(a) Viper Si2 SLA© printer **(b)** SLA© 3D printing process

Figure 4.22: Viper Si2 SLA© rapid prototyping printer at CERN (a). Scheme of SLA 3D printing process (b).

Figure 4.23 depicts the 3D-printed parts of three produced HOM couplers prototypes. The first probe-type and hook-type PERLE couplers were printed in Accura 25 epoxy (see Figures 4.23 (a) and (b)). The DQW-type PERLE coupler was manufactured in Accura 48 HTR (see Figure 4.23 (c)). The Accura 25 resin, recognizable for its white color, has great flexibility. The Accura 48 HTR, characterized by a transparent color, features higher strength, stiffness, and thermal stability than the Accura 25. Consequently, the Accura 48 HTR is a more robust material for 3D printing and better suited for subsequent electrolytic Cu-plating of the printed parts [123].

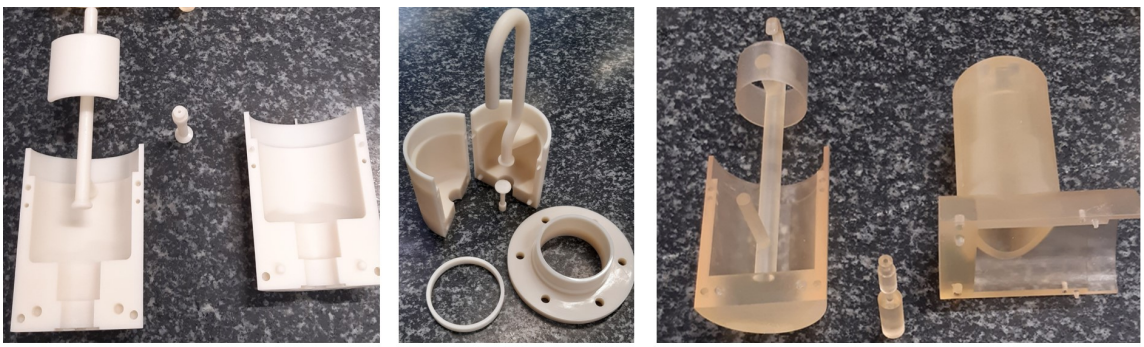

(a) (b) (c)

Figure 4.23: HOM coupler prototypes fabricated using the stereolithography technique. Accura 25 probe (a) and hook couplers (b). Accura 48 HTR DQW coupler (c) [123]. The figures (b) and (c) fall under the Creative Commons Attribution 4.0 (CC BY 4.0) license (https://creativecommons.org/licenses/by/4.0/).

4.3.3 Copper electroplating of epoxy-based HOM couplers

A conductive coating process is necessary to impart electrical conductivity to the epoxy-based HOM coupler. The process involves depositing a layer of conducting material, typically Copper, on the surface of the couplers. In this context, it is crucial to ensure a specific coating thickness to accommodate the skin depth at the operational frequency range of the coupler. The skin depth in a normal conductor is inversely proportional to the square root of the frequency, according to equation (1.80). At a frequency of 0.7 GHz, the skin depth for copper is 2.46 µm, while at 2.5 GHz, it reduces to 1.30 µm. To ensure good electrical conductivity of the coated material, the coated layer has to be thick enough such that the skin depth is small compared to the thickness of the coating. The objective for the produced couplers was to ensure a Cu substrate covering the entire surface with a minimum average thickness of 30 µm. This thickness value was considered sufficient to ensure the desired electrical conductivity properties. Furthermore, it introduces a minimal geometrical variation on the coupler surfaces, with no significant impact on the RF characteristics analyzed in Section 4.2.

The process of Cu-electroplating for epoxy-based HOM couplers at CERN involves several steps [123, 128].[2] Before electroplating, the HOM coupler parts undergo a light corundum-based sandblasting treatment at a pressure of 3 bars. This treatment aims to enhance copper adhesion on the part surface during the coating process. The parts are subsequently degreased using NGL-17-40-type detergent to eliminate any blasting residue. After surface preparation, the components are immersed in a carbon-based bath at 50°C to allow negatively charged carbon particles to create a substrate for the copper coating. Finally, HOM coupler parts are electroplated in a bright acid

[2]Pierre Maurin at CERN Cu-plated the HOM couplers based on the specifications provided by the thesis author.

copper bath. Figure 4.24 depicts one example each of 3D-printed epoxy and Cu-coated hook-type, probe-type, and DQW-type PERLE couplers.

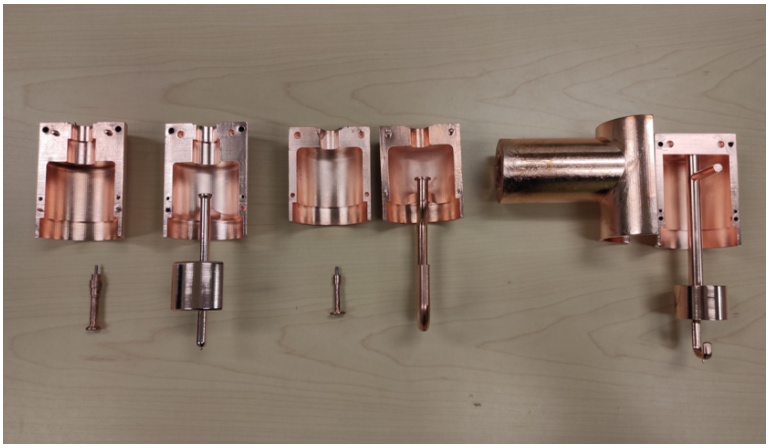

Figure 4.24: 3D-printed epoxy (Accura 48 HTR) and copper-coated HOM coupler prototypes. From the left to the right: probe-type, hook-type, and DQW-type PERLE couplers [123]. The figure falls under the Creative Commons Attribution 4.0 (CC BY 4.0) license (https://creativecommons.org/licenses/by/4.0/).

The results demonstrated the feasibility of Cu-plating for 3D-printed epoxy-based HOM couplers, confirming that the carbon substrate successfully facilitated copper adhesion to the polymer surface. A satisfactory level of coating-surface smoothing has been achieved. A smooth coupler inner surface enhances the overall electric performance of the coupler. However, in the current scenario, the applied technique does not allow full control of homogeneity for the copper deposit throughout the process. Further studies are necessary to enhance understanding and make improvements in this aspect. Moreover, the optimal temperature for the carbon bath is close to the heat deflection temperature of the epoxy Accura 25, which is approximately 58°C at 0.45 MPa, beyond which the polymer undergoes deformation. For this reason, the HOM-couplers fabricated in the second series were made out of Accura 48 HTR epoxy, whose heat deflection temperature at 0.45 MPa is 65°C and can reach values up to 130°C after UV and thermal post-cure. The Accura 48 HTR epoxy HOM coupler series was used to perform the HOM-damping measurements in the 2-cell and 5-cell PERLE cavities presented in Section 7.2.

4.3.4 3D-scanning measurements on HOM couplers

This section presents the results of several 3D-scanning measurements conducted on the fabricated HOM-coupler prototypes to assess the shape deviation between the ideal 3D CAD model and the actual coupler geometry.[3] The measurements were carried out using a HandySCAN BLACK+ Creaform® 3D scanner, which has an accuracy of 25 µm and a measurement resolution of 100 µm [129]. A minimum feasible tolerance of ± 0.5 mm was set for the entire coupler surface. This guarantees that any geometrical variation due to the fabrication process within this tolerance range does not significantly affect the HOM coupler transmission (refer to Section 4.2). The results of the metrological analyses on three of the produced HOM couplers are reported in the following subsections.

4.3.4.1 3D-scanning of the hook-type coupler prototype

3D measurements were conducted on one of the produced Accura 25 hook-type PERLE couplers. The 3D scans were carried out after the surface-coating process on both antenna and shell blocks, which were secured together during the scan by a cable tie. The metrological analysis aimed to evaluate the geometrical deviation of the resulting coupler surface from the designed shape and, to some extent, the thickness of the copper deposit in specific areas. Figure 4.25 depicts three different views of the 3D scans of the Cu-coated hook-type coupler.

The color map represents the normal surface deviation between the actual and ideal shape. Positive and negative deviations signify excess or lack of material with respect to the CAD model, respectively. Figure 4.26 depicts the normal surface deviation values for each inspected point. Results indicate that the majority of studied points fall within the tolerance range of ± 0.5 mm. However, some regions of the coupler exhibit a slightly higher lack (such as at points (13), (24), and (27)) or excess of material (at points (10), (33), and (34)). The lack of material, ranging from 2 µm to 1.197 mm, may be attributed to different factors, such as epoxy shrinkage, the non-uniformity of 3D printing, and limitations of the used electroplating process. The average lack of material on the analyzed points of the coupler surface is 251 µm. The material deficit detected at points (13) and (27) may reduce the magnetic coupling to the HOMs, while at point (24) region, it can alter the electric coupling to the HOMs and change the notch at the FM. The excess of material in the coated surface, which spans from 7 µm to 1.28 mm, can be due to the deposition accuracy of the epoxy layer and the limitations in achieving surface uniformity during the coating process. The average material excess on the coupler surface is 484 µm for the inspected points. The extra material at points (10) and (33) may influence the electric coupling to the HOMs, while the excess at point (34) can potentially increase the active area for the magnetic coupling.

[3] Jean-Philippe Rigaud at CERN carried out scans of the 3D-printed HOM couplers based on the specifications provided by the author.

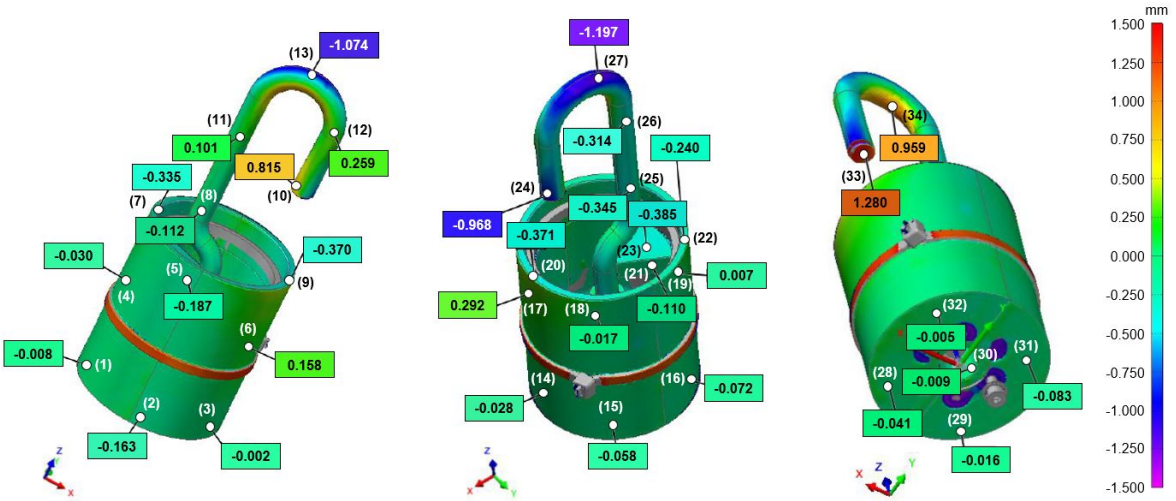

Figure 4.25: 3D scans of the analyzed Accura 25 hook-type coupler after surface-coating [123, 130]. Multiple points of interest, labeled from (1) to (34), are analyzed. Each inspected point is associated with the corresponding shape deviation in the normal direction in millimeters. Positive and negative variations represent excess or lack of material with respect to the ideal geometry, respectively. The two parts of the coupler were held together during the scan by a cable tie, which is visible in red. The figure falls under the Creative Commons Attribution 4.0 (CC BY 4.0) license (https://creativecommons.org/licenses/by/4.0/).

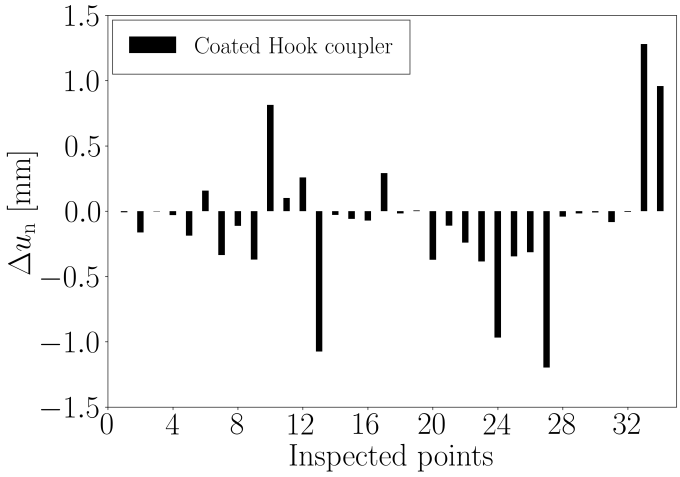

Figure 4.26: Measured shape deviation in the normal direction of the copper-coated hook-type coupler with respect to the CAD model. Thirty-four points of interest have been inspected. The indexes associated with the studied points correspond to the labels shown in Figure 4.25. Positive values represent an excess of material, while negative values indicate a deficit of material with respect to the ideal model.

4.3.4.2 3D-scanning of the probe-type coupler prototype

This subsection presents the 3D-scanning measurements performed on one of the manufactured Accura 48 HTR probe-type PERLE couplers. Both coupler antenna and shell blocks were scanned before and after the coating process. The aim is to comprehensively explore the resulting thickness change on their surfaces and, consequently, the shape variations throughout the production stages. The local thickness change Δh_c can be estimated as the absolute difference between the local deviation measured before and after the coating process at selected points. Positive values of Δh_c represent the estimated local coating thickness, while negative values indicate a potential local depression of the material after the coating process. This phenomenon might be attributed to thermal deformations during the surface coating. In depressed regions, the estimation of the coating thickness using the current method remains uncertain. By averaging the values found for the inspected points, the average coating thickness and depression could be obtained.

Figure 4.27 depicts the 3D color maps of the probe-type coupler antenna's front, rear, and bottom views before the coating process. The measured quantity represents the geometric deviation between the 3D CAD model and the geometry of the coupler without the coating layer. The shape deviations fall within the tolerance range for most of the coupler surfaces. However, some regions deviate from the ± 0.5 mm tolerance range. The active surfaces of the capacitive plate and the terminal part of the antenna exhibit the most significant deviations, featuring a material surplus spanning from 0.592 mm to 2.138 mm and a material deficit ranging from 0.879 mm to 2.430 mm. The average excess and deficit of material on the antenna surface are 460 µm and 509 µm for the inspected points, respectively. The epoxy shrinkage during the fabrication process may contribute to the observed material lack. Conversely, the material surplus may be due to different factors, such as printer calibration, layer deposition accuracy, and temperature variations during printing.

Figure 4.28 shows the 3D scans on the coupler antenna after the surface coating. The color maps indicate the shape deviations between the CAD model and the copper-coated coupler. The estimated coating thickness ranges from 3.1 µm to 1.261 mm for the inspected points. The average coating thickness for the antenna surface for the inspected points is about 298 µm (see Table 4.4). The coated probe-type coupler antenna meets the tolerance specification, except for the capacitive plate surfaces and the antenna's terminal part. The material surplus varies in these regions from 1.090 mm to 3.399 mm, while the material deficit spans from 1.206 mm to 3.509 mm (see Table 4.4). The identified geometric variations on the surface of the capacitive plate at points (14), (20), and (21) affect the alignment of the plate with the coupler shell. This might modify the distance between the outer surface of the plate and the inner surface of the surrounding coupler shell, altering the FM rejection of the coupler from the design specifications. The geometric deviations at points (15) and (22) may affect the coupling to the HOMs, particularly to monopole modes.

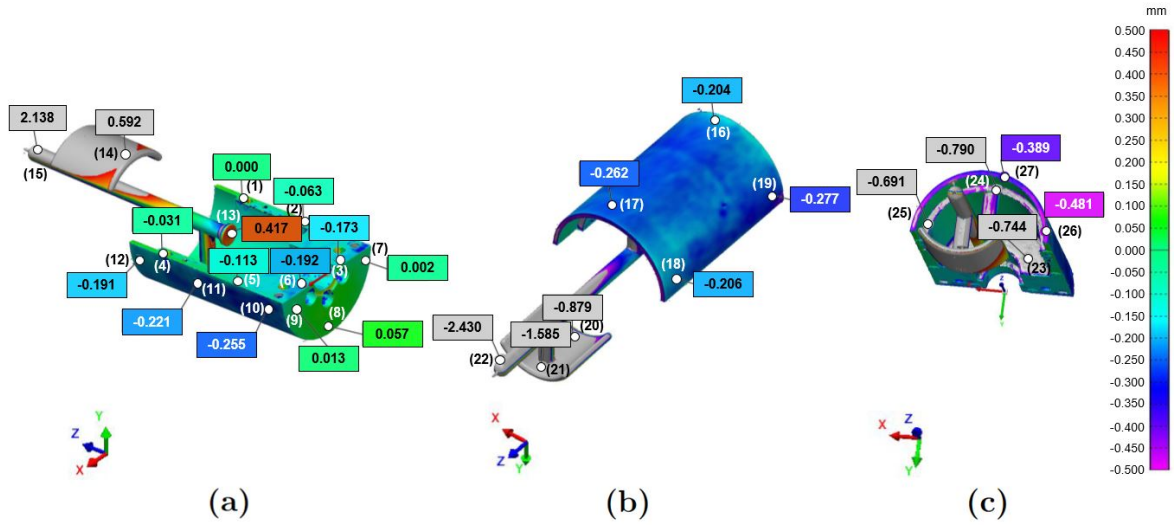

Figure 4.27: 3D scans of the investigated Accura 48 HTR probe-type PERLE coupler before surface-coating [131]. Front (a), rear (b), and bottom (c) views of the coupler antenna block. The indexes from (1) to (27) indicate the inspected points. The normal geometrical deviation for each inspected point is indicated in millimeters. Excess and lack of material are associated with positive and negative variations with respect to the ideal geometry, respectively.

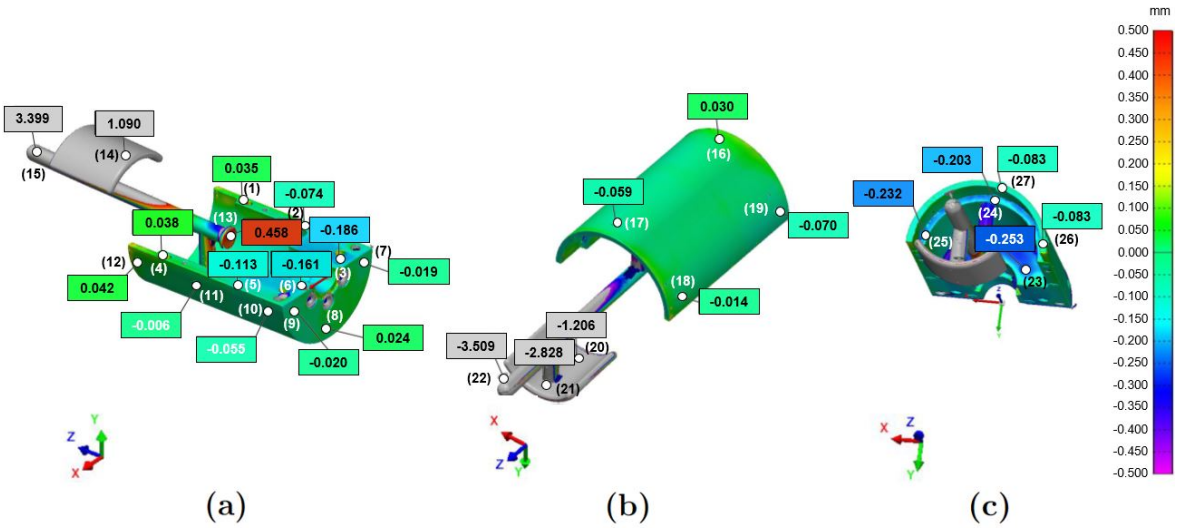

Figure 4.28: 3D scans of the investigated Accura 48 HTR probe-type PERLE coupler after surface-coating [132]. Front (a), rear (b), and bottom (c) views of the coupler antenna block. The indexes from (1) to (27) depict the investigated points. The normal shape deviation for each studied point is shown in millimeters. Excess and lack of material are related to positive and negative variations with respect to the ideal geometry, respectively.

Figure 4.29 (a) depicts the normal surface deviation values for each inspected point for the uncoated and coated probe-type coupler antenna with respect to the ideal geometry. Figure 4.29 (b) illustrates the estimated local thickness variation for the cooper-coated probe-type coupler antenna. The maximum, minimum, and average geometrical deviations before and after coating, along with the estimated local thickness change, of the probe-type coupler antenna block are summarized in Table 4.4.

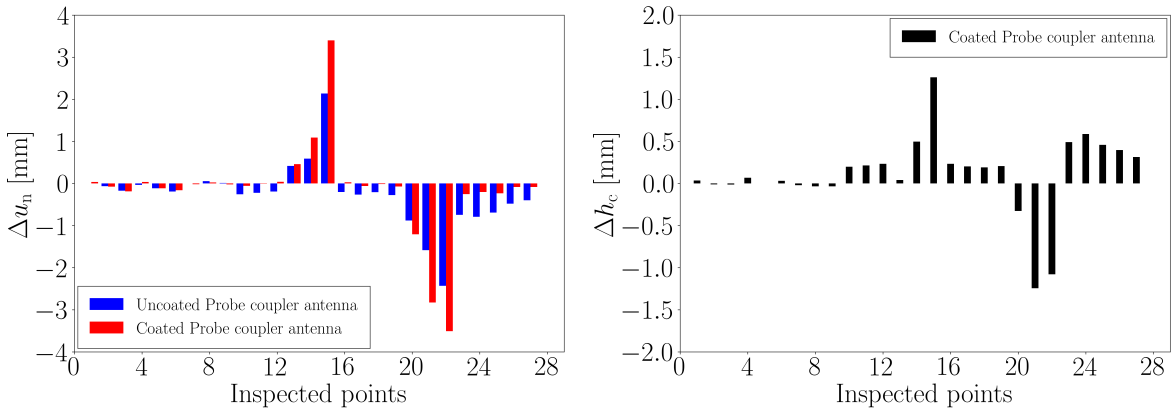

(a) Measured shape deviations **(b)** Estimated local thickness change

Figure 4.29: Measured shape deviation in the normal direction for the uncoated (blue) and coated (red) probe-type coupler antenna with respect to the CAD geometry (a). Twenty-seven points have been investigated. The indexes correspond to the labels depicted in Figures 4.27 and 4.28. Estimated local thickness variation for the Cu-coated probe coupler antenna (b).

Figure 4.30 shows the 3D measurements of the probe-type coupler shell block before the coating process. The material deficit, most likely due to the epoxy shrinkage, ranges from 0.037 mm to 0.646 mm. The geometric deviations in the shell surface are within the set tolerance range, except for points (13) and (15), which exhibit a lack of material slightly outside the acceptable limits. The average lack of material is 245 µm for the analyzed points. Material excess of 0.037 mm is observed in the region surrounding the point (8). Figure 4.31 depicts the 3D scans on the coupler shell block after the surface-coating process. The approximated coating thickness varies from 8 µm to 409 µm for the investigated points. The average coating thickness of the shell surface is about 222 µm. Overall, the coated probe-type coupler shell fulfills the design requirements.

Figure 4.32 (a) displays the surface deviation values of each investigated point for the uncoated and coated probe-type coupler shell with respect to the 3D CAD model. Figure 4.32 (b) illustrates the estimated local thickness change for the cooper-coated probe-type coupler shell. The maximum, minimum, and average geometrical deviations before and after coating, as well as the estimated local thickness change of the probe-type coupler shell, are summarized in Table 4.5.

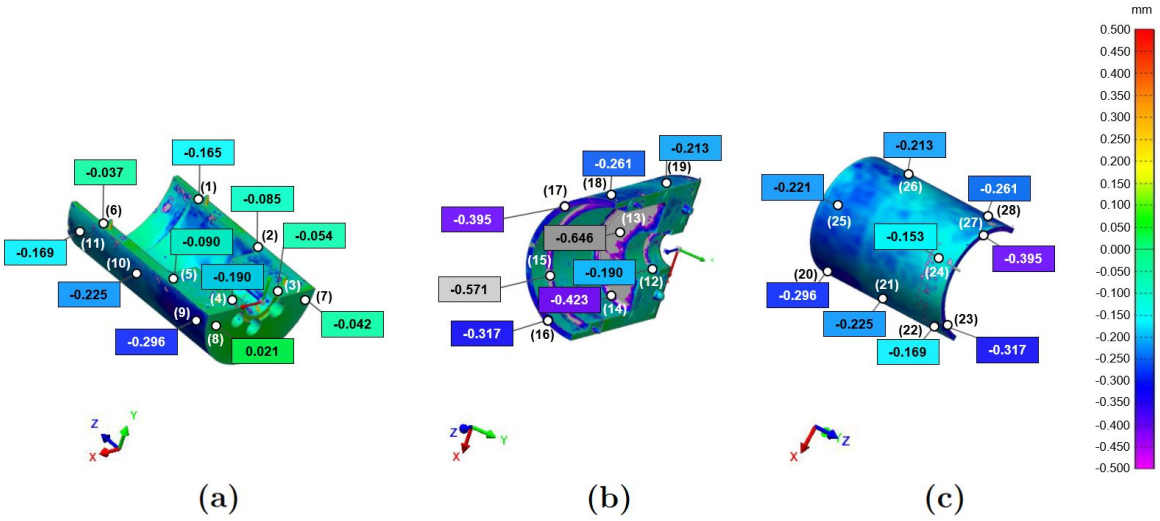

Figure 4.30: 3D scan of the analyzed Accura 48 HTR probe-type coupler shell before surface-coating. Front (a)-(b) and rear (c) views of the coupler shell [133]. Multiple points of interest are labeled from (1) to (28), each showing the corresponding normal geometric deviation in millimeters. Positive and negative variations indicate excess or lack of material with respect to the 3D CAD geometry, respectively.

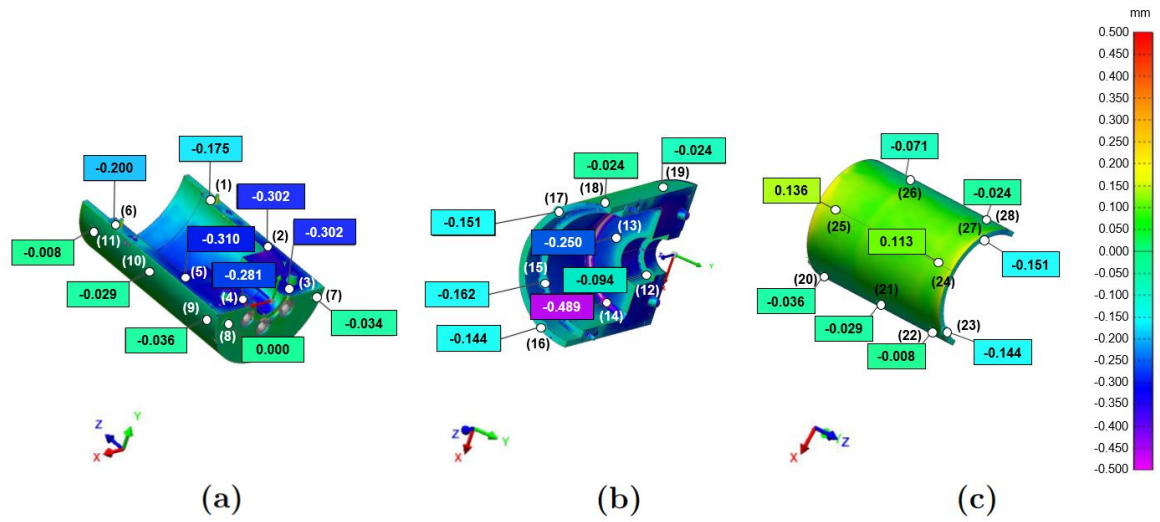

Figure 4.31: 3D scan of the analyzed Accura 48 HTR probe-type coupler shell after surface-coating. Front (a)-(b) and rear (c) views of the coupler shell [134]. Several points of interest are labeled from (1) to (28), each indicating the corresponding normal shape deviation in millimeters. Positive and negative variations indicate excess or lack of material with respect to the ideal geometry, respectively.

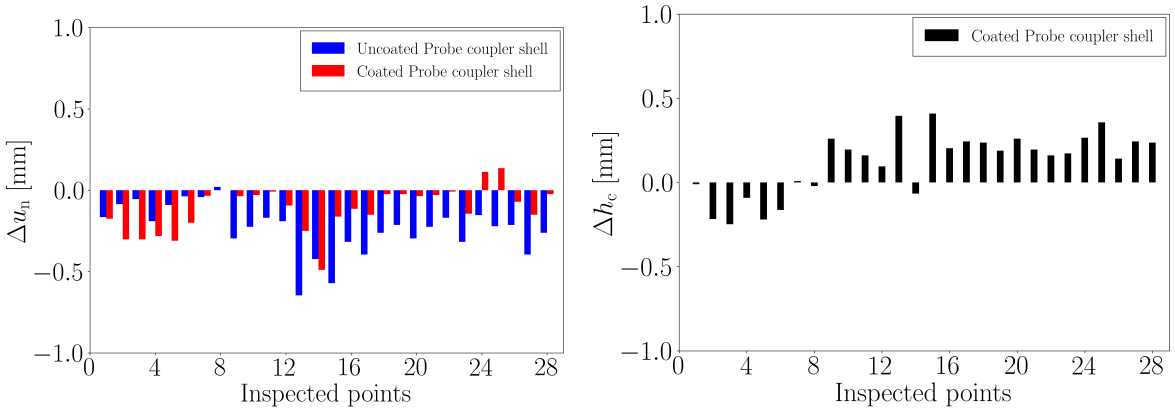

(a) Measured shape deviations **(b)** Estimated local thickness change

Figure 4.32: Measured shape change in the normal direction for the uncoated (blue) and coated (red) probe-type coupler shell with respect to the ideal geometry (a). Twenty-eight points of interest have been inspected. The indexes indicating the studied points are related to the labels depicted in Figures 4.30 and 4.31. Positive and negative quantities represent a surplus or deficit of material with respect to the CAD model, respectively. Estimated local thickness change for the copper-coated probe-type coupler shell (b).

Table 4.4: Measured geometrical deviation for the probe-type coupler antenna before and after the coating process. The maximum, minimum, and average geometrical deviations and the local thickness change are calculated from the deviations observed at the inspected points.

Antenna surface before coating - Probe-type coupler			
	$\lvert\Delta u\rvert_{\mathrm{n,max}}$ [mm]	$\lvert\Delta u\rvert_{\mathrm{n,min}}$ [mm]	$\lvert\Delta u\rvert_{\mathrm{n,ave}}$ [mm]
Material excess	2.138	0.002	0.460
Material deficit	2.430	0.031	0.509
Antenna surface after coating - Probe-type coupler			
	$\lvert\Delta u\rvert_{\mathrm{n,max}}$ [mm]	$\lvert\Delta u\rvert_{\mathrm{n,min}}$ [mm]	$\lvert\Delta u\rvert_{\mathrm{n,ave}}$ [mm]
Material excess	3.399	0.024	0.640
Material deficit	3.509	0.006	0.483
Local thickness change on the antenna surface - Probe-type coupler			
	$\lvert\Delta h_c\rvert_{\mathrm{max}}$ [mm]	$\lvert\Delta h_c\rvert_{\mathrm{min}}$ [mm]	$\lvert\Delta h_c\rvert_{\mathrm{ave}}$ [mm]
Coating layer	1.261	0.031	0.298
Material depression	1.243	0.011	0.345

Table 4.5: Measured geometrical deviation for the probe-type coupler shell before and after the coating process. The calculated maximum, minimum, and average geometrical deviations and the local thickness change are derived from the deviations observed at the inspected points.

Shell surface before coating - Probe coupler			
	$\lvert\Delta u\rvert_{\mathrm{n,max}}$ [mm]	$\lvert\Delta u\rvert_{\mathrm{n,min}}$ [mm]	$\lvert\Delta u\rvert_{\mathrm{n,ave}}$ [mm]
Material excess	0.021	-	0.021
Material deficit	0.646	0.037	0.245
Shell surface after coating - Probe-type coupler			
	$\lvert\Delta u\rvert_{\mathrm{n,max}}$ [mm]	$\lvert\Delta u\rvert_{\mathrm{n,min}}$ [mm]	$\lvert\Delta u\rvert_{\mathrm{n,ave}}$ [mm]
Material excess	0.021	0.113	0.083
Material deficit	0.489	0.008	0.138
Local thickness change on the shell surface - Probe-type coupler			
	$\lvert\Delta h_{\mathrm{c}}\rvert_{\mathrm{max}}$ [mm]	$\lvert\Delta h_{\mathrm{c}}\rvert_{\mathrm{min}}$ [mm]	$\lvert\Delta h_{\mathrm{c}}\rvert_{\mathrm{ave}}$ [mm]
Coating layer	0.409	0.008	0.222
Material depression	0.248	0.010	0.130

4.3.4.3 3D-scanning of the DQW coupler prototype

The DQW-type PERLE coupler presents the most intricate shape among the three produced HOM couplers. 3D-scanning measurements were conducted on one of the manufactured Accura 48 HTR DQW couplers. The antenna and shell components were scanned before and after the coating process to estimate the local thickness change during fabrication.

Figure 4.33 illustrates the 3D scans of the front and rear parts of the DQW antenna before the surface underwent the coating process. The color maps indicate the shape deviation between the 3D CAD model and the printed coupler geometry without the coating layer. The geometry deviations are within the tolerance range of $\pm$ 0.5 mm for most of the antenna surfaces. Some other coupler regions fall outside the set tolerance range, with a lack of material ranging from 0.558 mm to 1.870 mm. The average material deficit on the analyzed points of the antenna surface is 401 µm. A relatively significant material deficit of 1.870 mm was identified at point (1) in the lower part of the antenna loop. This can potentially diminish the strength of the electromagnetic coupling to the cavity HOMs. No extra material was found in the inspected points. Similar considerations concerning the causes of excess and lack of material after 3D printing, as discussed for the other couplers, also apply to the DQW-type coupler.

Figure 4.34 depicts the 3D measurements on the coupler parts after the coating process. The color maps depict the geometry deviations between the CAD model and

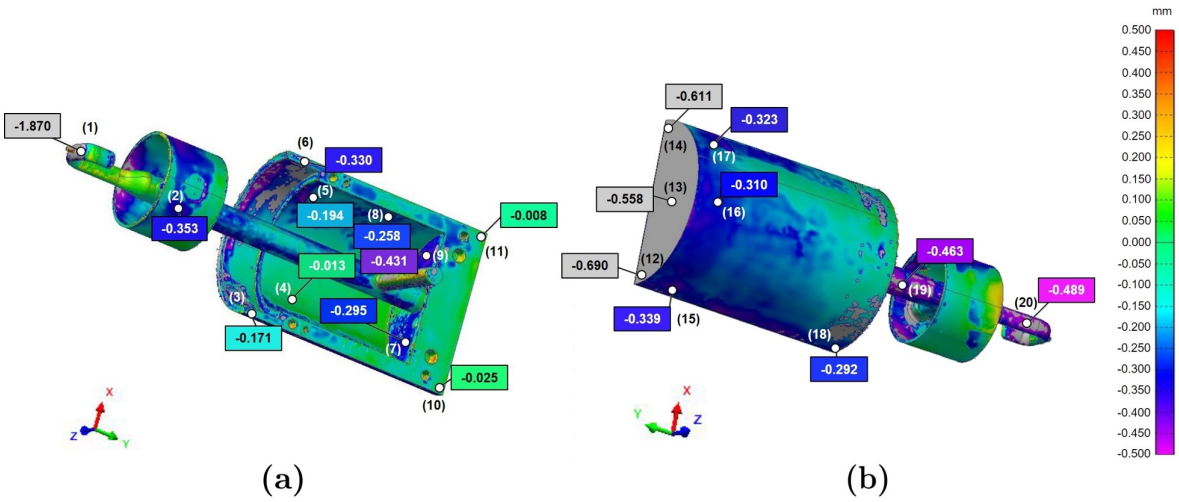

Figure 4.33: 3D scan of the analyzed Accura 48 HTR DQW coupler antenna before surface-coating. Front (a) and rear (b) views of the coupler antenna [135]. Multiple points of interest, labeled from (1) to (20), are highlighted, each displaying the corresponding normal shape deviation in millimeters. Positive and negative variations indicate excess or lack of material with respect to the ideal geometry, respectively.

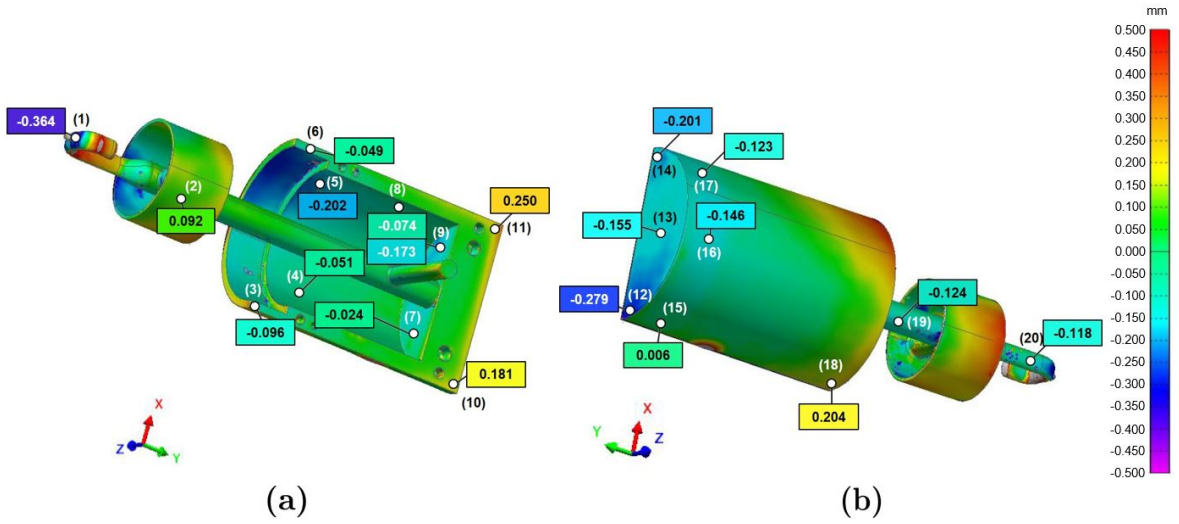

Figure 4.34: 3D scan of the analyzed Accura 48 HTR DQW coupler antenna after surface-coating. Front (a) and rear (b) views of the coupler antenna [136]. Multiple points of interest, labeled from (1) to (20), are depicted, each indicating the corresponding normal shape deviation in millimeters. Positive and negative variations represent excess or lack of material with respect to the ideal geometry, respectively.

the printed and copper-coated HOM coupler. The measured coating thickness spans from 75 µm to 1.506 mm for the investigated points. The antenna surface's average copper coating thickness is about 300 µm. After the surface-coating of the DQW cou-

pler antenna, the measured shape deviations fall within the ± 0.5 mm tolerance range, except for some regions deviating from the average. A relatively large local coating thickness of 1.506 mm was detected at point (1) in the lower part of the loop-shaped section. However, in this case, this relatively large amount of copper is beneficial in recovering the lack of material detected at the same point after the 3D printing process. Finally, a material depression of about 8 µm and 38 µm was detected for points (4) and (5), respectively. The estimated average material deficit in this region is about 23 µm. Figure 4.35 (a) reports the measured deviations in the normal direction to the surface of the DQW coupler antenna before and after surface-coating for the investigated points of the DQW coupler antenna. Figure 4.35 (b) illustrates the resulting estimated local coating thickness for the same points. The maximum, minimum, and average geometrical deviations before and after coating, along with the estimated local thickness change, of the DQW coupler antenna are summarized in Table 4.6

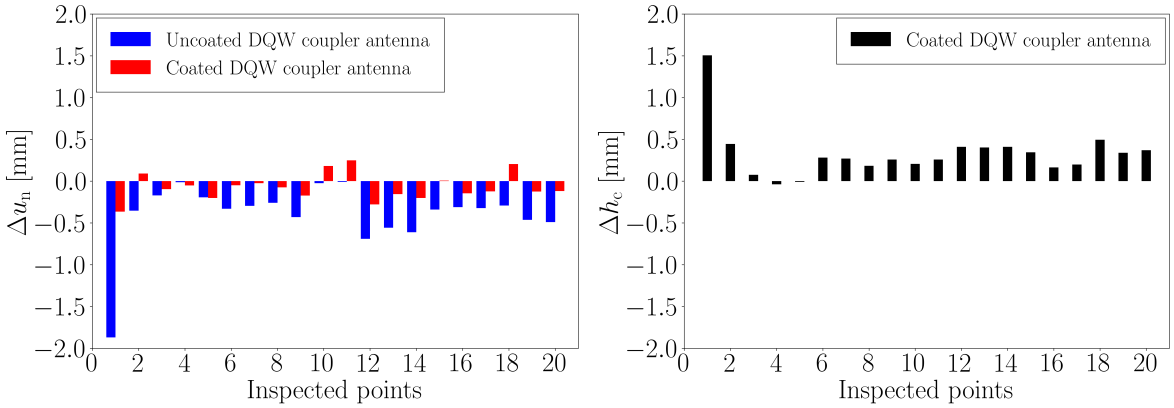

(a) Measured shape deviations **(b)** Estimated local thickness change

Figure 4.35: Measured geometry deviation in the normal direction for the uncoated (blue) and coated (red) DQW coupler antenna with respect to the design geometry (a). Twenty points of interest have been inspected. The indexes associated with the investigated points correspond to the labels depicted in Figures 4.33 and 4.34. Positive and negative values represent an excess or deficit of material with respect to the CAD model, respectively. Estimated local thickness change for the copper-coated DQW coupler antenna (b). Positive values represent the estimated local coating thickness, while negative values depict the possible material depression.

Figures 4.36 and Figures 4.37 illustrate the 3D scans of the coupler shell block before and after the coating process, respectively. Overall, the shape deviations in the shell active surfaces before the coating process are within the set tolerance range. The lack of material, most likely due to the epoxy shrinkage, spans from 0.01 mm to 0.76 mm. The average material deficit on the coupler shell is 291 µm for the inspected points. Some regions present extra material, ranging from 0.032 mm to 0.254 mm. The average excess of material on the surface is 125 µm for the analyzed points.

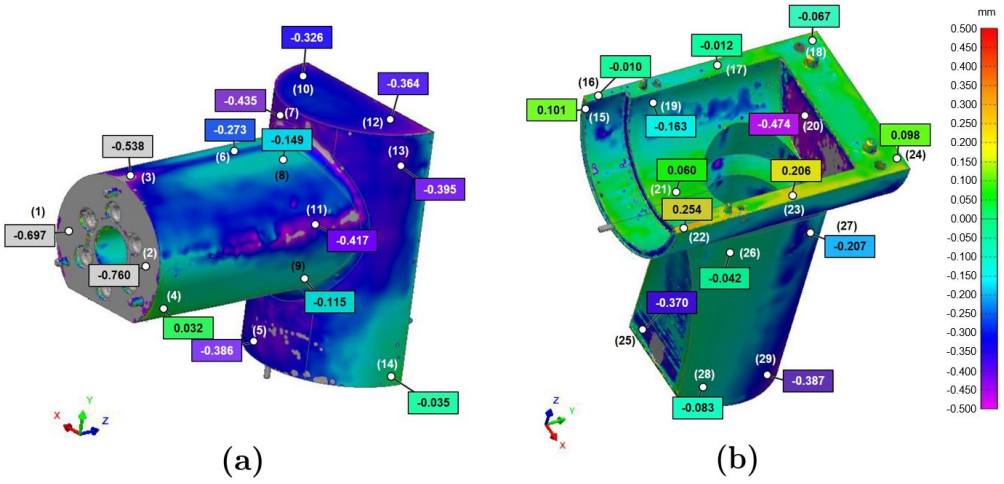

Figure 4.36: 3D scan of the analyzed Accura 48 HTR DQW coupler shell before surface-coating. Front (a) and rear (b) views of the coupler shell [137]. Multiple points of interest, labeled from (1) to (29), are highlighted, each indicating the corresponding normal shape deviation in millimeters. Positive and negative variations indicate excess or lack of material with respect to the ideal geometry, respectively.

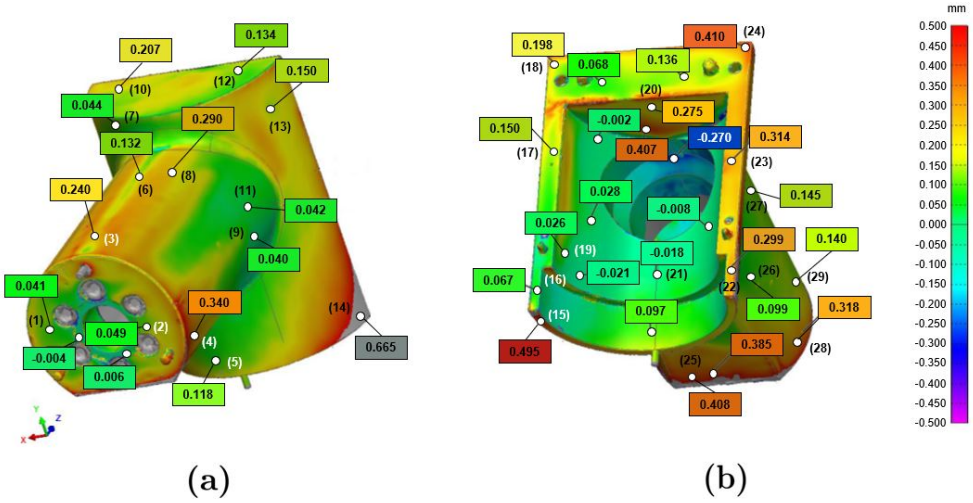

Figure 4.37: 3D scan of the analyzed Accura 48 HTR DQW coupler shell after surface-coating. Front (a) and rear (b) views of the coupler shell [138]. Multiple points of interest, labeled from (1) to (29), are depicted, each indicating the corresponding normal shape deviation in millimeters. Positive and negative variations indicate excess or lack of material with respect to the ideal geometry, respectively.

After the coating process, the measured geometrical deviations are within the ± 0.5 mm tolerance range, except for some points deviating from the average. The measured coating thickness varies from 45 µm to 809 µm. The average copper coating thickness is about 423 µm. Likewise, the factors influencing excess and insufficient material after the coating process, as explored for the other two analyzed couplers, also hold for the DQW-type coupler shell. Figure 4.38 (a) indicates the normal surface deviation values for each investigated point of the coupler shell. Figure 4.38 (b) illustrates the resulting estimated local coating thickness for the same points. The maximum, minimum, and average geometrical deviations before and after coating, as well as the estimated local thickness change of the DQW coupler shell, are summarized in Table 4.7.

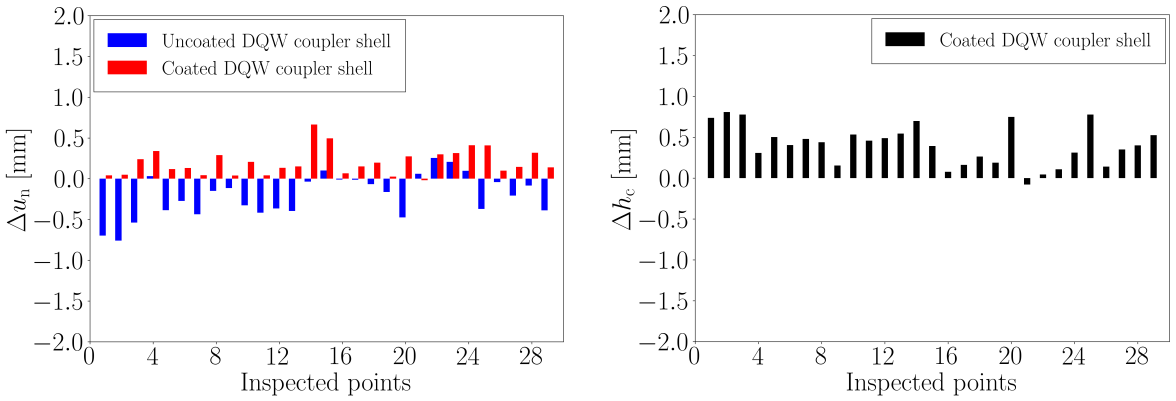

(a) Measured shape deviations **(b)** Estimated local thickness change

Figure 4.38: Measured shape variation in the normal direction for the uncoated (blue) and coated (red) DQW coupler shell with respect to CAD model (a). Twenty-nine points of interest have been investigated. The indexes are related to the labels depicted in Figures 4.36 and 4.37. Estimated local thickness variation for the copper-coated DQW coupler shell (b).

The metrological analyses on the three analyzed HOM couplers suggest that, on average, most of the measured surface regions fall within the set tolerance interval of ± 0.5 mm after undergoing the coating process. The estimated average coating thickness spans from approximately 200 µm to 350 µm. The found coating values exceed the minimum required coating thickness of 30 µm for the frequency range of interest. The subsequent shape deviation remains within the specified tolerance range. Locally, some regions exhibit either a lack or excess of material due to technical limitations in the used 3D-printing and copper-coating processes, which require further improvement. These shape deviations may potentially impact the HOM-damping performance and FM rejection of the HOM couplers. Nevertheless, the analyzed technique demonstrates promise for prototyping HOM couplers intended for low-power RF measurements on Cu cavity prototypes.

Table 4.6: Measured geometrical deviation for the DQW coupler antenna before and after the coating process. The maximum, minimum, and average geometrical deviations and the local thickness change are calculated from the deviations observed at the inspected points.

Antenna surface before coating - DQW coupler			
	$\lvert\Delta u\rvert_{\mathrm{n,max}}$ [mm]	$\lvert\Delta u\rvert_{\mathrm{n,min}}$ [mm]	$\lvert\Delta u\rvert_{\mathrm{n,ave}}$ [mm]
Material excess	-	-	-
Material deficit	1.870	0.008	0.401
Antenna surface after coating - DQW coupler			
	$\lvert\Delta u\rvert_{\mathrm{n,max}}$ [mm]	$\lvert\Delta u\rvert_{\mathrm{n,min}}$ [mm]	$\lvert\Delta u\rvert_{\mathrm{n,ave}}$ [mm]
Material excess	0.250	0.006	0.147
Material deficit	0.364	0.024	0.145
Local thickness change on the antenna surface - DQW coupler			
	$\lvert\Delta h_{\mathrm{c}}\rvert_{\mathrm{max}}$ [mm]	$\lvert\Delta h_{\mathrm{c}}\rvert_{\mathrm{min}}$ [mm]	$\lvert\Delta h_{\mathrm{c}}\rvert_{\mathrm{ave}}$ [mm]
Coating layer	1.506	0.075	0.368
Material depression	0.038	0.008	0.023

Table 4.7: Measured geometrical deviation for the DQW coupler shell before and after the coating process. The maximum, minimum, and average geometrical deviations and the local thickness change are calculated from the deviations observed at the inspected points.

Shell surface before coating - DQW coupler			
	$\lvert\Delta u\rvert_{\mathrm{n,max}}$ [mm]	$\lvert\Delta u\rvert_{\mathrm{n,min}}$ [mm]	$\lvert\Delta u\rvert_{\mathrm{n,ave}}$ [mm]
Material excess	0.254	0.060	0.144
Material deficit	0.760	0.010	0.292
Shell surface after coating - DQW coupler			
	$\lvert\Delta u\rvert_{\mathrm{n,max}}$ [mm]	$\lvert\Delta u\rvert_{\mathrm{n,min}}$ [mm]	$\lvert\Delta u\rvert_{\mathrm{n,ave}}$ [mm]
Material excess	0.665	0.026	0.208
Material deficit	0.018	-	0.018
Local thickness change on the shell surface - DQW coupler			
	$\lvert\Delta h_{\mathrm{c}}\rvert_{\mathrm{max}}$ [mm]	$\lvert\Delta h_{\mathrm{c}}\rvert_{\mathrm{min}}$ [mm]	$\lvert\Delta h_{\mathrm{c}}\rvert_{\mathrm{ave}}$ [mm]
Coating layer	0.809	0.045	0.423
Material depression	0.018	-	0.018

4.3.5 Niobium 3D-printed HOM couplers

The previous sections presented an analysis of 3D-printed epoxy and Cu-coated HOM couplers designed for low-power RF measurements on Cu cavity prototypes. Although these coupler prototypes can effectively meet the immediate needs for low-power applications, questions regarding Niobium 3D-printed HOM couplers and their long-term durability and performance under real-world operating conditions remain relevant.

The fabrication of metal 3D-printed HOM couplers employs powder bed fusion techniques, specifically Selective Laser Melting (SLM) and Electron Beam Melting (EBM) [139]. Both techniques enable the creation of complex geometries, making them ideal for manufacturing HOM couplers that require specific performance characteristics in accelerator applications. In the SLM process, a high-powered laser selectively fuses metal powder particles layer by layer. In contrast, the EBM technique uses a focused electron beam in a vacuum to melt metal powder. Recently, CERN has explored the possibility of manufacturing 3D-printed metal HOM couplers, specifically investigating options in titanium (Ti) and Niobium [127]. Titanium was chosen for initial 3D printing tests due to its ease of fabrication. While not a superconductor below 9.2 K like Nb, Ti exhibits similar thermal expansion, making it a practical step toward the fabrication of Nb HOM couplers. Figure 4.39 (a) and (b) show prototypes of 400 MHz DQW couplers 3D-printed in Ti and Nb, respectively [140].

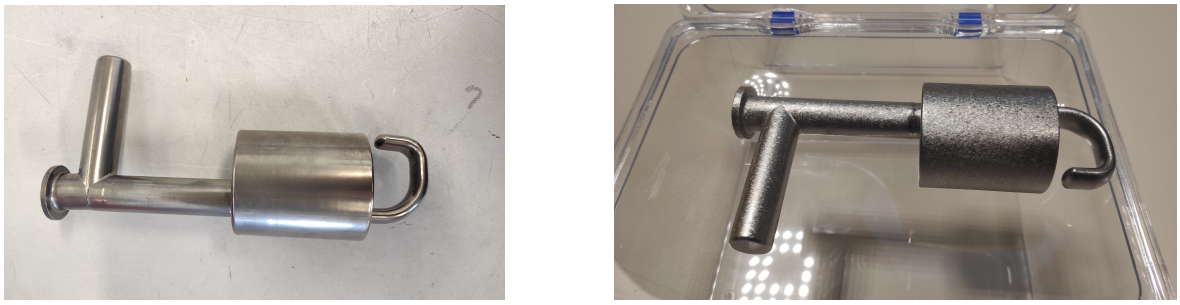

(a) Ti 3D-printed DQW coupler **(b)** Nb 3D-printed DQW coupler

Figure 4.39: Prototypes of 400 MHz DQW HOM couplers 3D-printed in Ti (a) and Nb (b).

One significant challenge in ensuring the performance of Nb 3D-printed HOM couplers in realistic operating conditions is surface polishing. A porous surface can lead to increased surface resistance, raising the risk of a quench of the HOM coupler under operation. Furthermore, in the case of active-cooled HOM couplers, porosity may result in leaks in the liquid helium. Minimizing the surface roughness becomes crucial to mitigate these effects. One potential solution is the employment of the Buffered Chemical Polishing (BCP) [141] technique to reduce surface defects and improve the overall quality of the material. Recent tests at CERN, using Nb powder as raw material and employing titanium gettering with thermal treatment in hydrogen purification, achieved a residual resistivity ratio (RRR) of 260, showing significant improvement in

material quality. Testing and validation will be essential for evaluating the long-term stability of 3D-printed Nb HOM couplers. This would include assessing their performance under mechanical and RF-heating loads. No tests have yet been conducted at CERN on Nb 3D-printed HOM couplers in Nb cavities [140].

5 HOM-damping and RF-heating analyses

This chapter presents the performance analyses conducted on the five-cell 801.58 MHz PERLE cavity equipped with the designed HOM couplers presented in Chapter 4. These studies are relevant due to the relatively high current ($I_{\mathrm{b,op}} = 120$ mA) of the 500 MeV PERLE version, which can lead to high HOM power loss and transverse beam instabilities in its SRF accelerating cavities. The longitudinal and transversal impedances of the analyzed equipped cavity are compared to their respective impedance limits set by the Beam Breakup (BBU) instability phenomenon in an ERL (see Chapter 3). The objective is to determine a suitable HOM damping scheme to reduce the longitudinal and transversal impedances below their limits and ensure ERL stability during its operation. Furthermore, the HOM power deposited by the beam into the cavity is estimated. Finally, the dynamic heat load on the HOM coupler surfaces, along with the resulting increase in temperature, are evaluated to prevent the risk of a quench in both the HOM couplers and the cavity.

5.1 Numerical methods for impedance calculation

This section illustrates the concepts of wakefields and impedance to describe the electromagnetic (EM) interaction of a bunch of charged particles with the surrounding enclosure [142]. This interaction can be described by wakefields in the time domain or by impedances in the frequency domain. Wakefields are self-induced EM fields that arise in a resonant cavity because of the interaction of a traveling beam with the surrounding enclosure [143]. The beam induces surface currents and charges on the cavity walls, which turn into sources of parasitic fields [144]. Wakefields emerge from any geometrical or material change of the cavity along the beam path. They can act back on the traveling charged bunches influencing their motion, leading to beam instabilities or undesired beam power loss [145].

It is convenient to classify wakefields in two different categories, namely short-range wakefields and long-range wakefields [143]. The short-range wakefields influence the single-bunch beam dynamics. The long-range wakefields involve excited EM fields that can remain in the accelerating structure for a longer time until the next bunch arrives,

potentially causing bunch instabilities. This phenomenon generally occurs when a train of bunches repeatedly excites high-Q_{L} resonant modes of the cavity. The long-range wakefields typically correspond to the high impedance peaks in the frequency spectrum of the cavity. The main goal is to mitigate the high impedance peaks by lowering the loaded quality factor of resonant modes below the instability limits using HOM couplers. The numerical methods used for calculating the wake impedance and eigenmode impedance are derived and discussed in the following subsections.

5.1.1 Wakefields and wake impedance

When analyzing the motion of charged particles in an accelerator, the focus typically lies on the integrated interaction of the particles with the wakefield. The wake function is defined as the integrated EM field experienced by a test charge at a transverse offset $\mathbf{r}$ from the beam axis and at a longitudinal distance s behind the exciting charged particle. The wake function is calculated according to the following equation [142, 146]

$$\mathbf{w}(\mathbf{r}, s) = \frac{1}{q} \int_{-\infty}^{\infty} [\mathbf{E}(\mathbf{r}, z, t) + c\hat{\mathbf{z}} \times \mathbf{B}(\mathbf{r}, z, t)]_{t=(s+z)/c} \, \mathrm{d}z, \tag{5.1}$$

where q is a charged particle with delta-function distribution moving in the longitudinal direction z with velocity $\mathbf{v} = c\hat{\mathbf{z}}$ close to the speed of light. The wake function comprises three components, one in the longitudinal and two in the transversal directions. Since $\hat{\mathbf{z}} \times \mathbf{B}$ has no component along the direction of the particle motion, the second term of the equation (5.1) vanishes, and the expression for the longitudinal wake function is reduced to

$$w_{\parallel}(\mathbf{r}, s) = \frac{1}{q} \int_{-\infty}^{\infty} E_z(\mathbf{r}, z, (s+z)/c) \, \mathrm{d}z. \tag{5.2}$$

The wake function can be considered as a Green's function of the problem [144]. If the wakefield is generated by an exciting bunch with an arbitrary shape, the interaction between the bunch and the field is described by the wake potential, which can be derived from the convolution of the wake function with the bunch shape $\xi_{\mathrm{c}}(s)$ as

$$\mathbf{W}(\mathbf{r}, s) = \int_{0}^{\infty} \xi_{\mathrm{c}}(s - s') \mathbf{w}(\mathbf{r}, s') \, \mathrm{d}s'. \tag{5.3}$$

For a Gaussian bunch having a longitudinal bunch length σ_z and centered at s_0, the bunch shape function is defined as

$$\xi_{\mathrm{c}}(s) = \frac{1}{\sigma_z \sqrt{2\pi}} \mathrm{e}^{-\frac{(s-s_0)^2}{2\sigma_z^2}}. \tag{5.4}$$

The impedance spectrum of the cavity is obtained from the Fourier transform of the wake potential in both longitudinal and transverse directions as follows [142]

$$Z_{\parallel}(\mathbf{r},\omega) = \frac{1}{c}\int_{-\infty}^{\infty} W_{\parallel}(\mathbf{r},s)\mathrm{e}^{-\frac{j\omega s}{c}}\,\mathrm{d}s, \tag{5.5}$$

$$\mathbf{Z}_{\perp}(\mathbf{r},\omega) = \frac{-j}{c}\int_{-\infty}^{\infty} \mathbf{W}_{\perp}(\mathbf{r},s)\mathrm{e}^{-\frac{j\omega s}{c}}\,\mathrm{d}s. \tag{5.6}$$

The longitudinal and transverse impedance defined above are both expressed in units of Ω. The deflecting dipole field strength increases proportionally to the transverse offset of the beam from the cavity axis. Equation (5.6) can be divided by the beam offset to obtain a definition that is independent of the beam transverse displacement from the cavity axis, resulting in a unit change of the transversal impedance in Ω/m [147]. Finally, the transversal impedance is related to the longitudinal impedance via the Panofsky-Wenzel theorem [35, 142] as follows

$$\mathbf{Z}_{\perp}(\mathbf{r},\omega) = \frac{c}{\omega}\nabla_{\perp} Z_{\parallel}(\mathbf{r},\omega), \tag{5.7}$$

where $\nabla_{\perp}$ is the transverse gradient operator.

Wakefields can be computed using time domain solvers such as ABCI [148] for 2D axisymmetric structures or CST Studio Suite® for 3D geometries. In these solvers, the wake potential, the wake impedance, and loss factors are calculated considering a single exciting Gaussian-shaped bunch that traverses the structure under study. The wake impedance is calculated in CST by normalizing the Fourier transform of the wake potential to the charge distribution [21]. The excitation of different HOMs within the structure depends on the position of the beam relative to the geometry axis. A beam traversing a cavity with axisymmetric geometry on-axis can excite only TM-type monopole modes. Conversely, an off-axis beam can excite modes with higher polar orders, such as dipole modes. The monopole and dipole modes significantly impact beam motion in an accelerating cavity due to their strong EM field near its longitudinal axis.

In HOM-damped multi-cell cavities, identifying modes can be challenging due to the overlap of modes in the frequency spectrum. For this reason, different excitation schemes can be employed in 3D wakefield solvers to separately excite modes of a certain polar order and polarization and suppress the other cavity modes. Figure 5.1 illustrates the beam excitation schemes applied in this thesis to compute the impedance of monopole and dipole modes [149]. The wake impedance calculation for the TM-type monopole modes is carried out using a beam with charge q passing along the cavity axis. If the cavity is symmetric relative to a symmetry plane, a PMC symmetry plane can be used to reduce the simulation domain size and, consequently, the computation time of monopole impedance (see Figure 5.1 (a)). The impedance of the dipole modes is computed using a multi-beam wake excitation method: two beams with an opposite charge and equal offsets from the beam axis move through the cavity to simultaneously excite dipole modes. The superposition of the fields from the two beams preserves dipole

modes while suppressing modes with different polar orders. The bunch charge of each beam is set to $q/2$ to ensure that the combined effect corresponds to a particle beam with charge q. Furthermore, in a two-beam wake excitation scheme, normalization to two charges is necessary for calculating the wake impedance, as the wake potential arises from the superposition of the fields of two co-moving beams [115, 149, 150]. Figures 5.1 (b) and (c) illustrate the two-beam schemes for exciting dipole modes with horizontal and vertical polarizations, respectively. Dipole modes with horizontal polarization are excited by two beams with a horizontal offset, whereas dipole modes with vertical polarization are excited by two beams with a vertical offset. In axisymmetric structures, the use of PEC and PMC symmetry planes can reduce computation time when using the two-beam scheme to excite dipole modes with horizontal and vertical polarizations, respectively (see Figures 5.1 (b) and (c)).

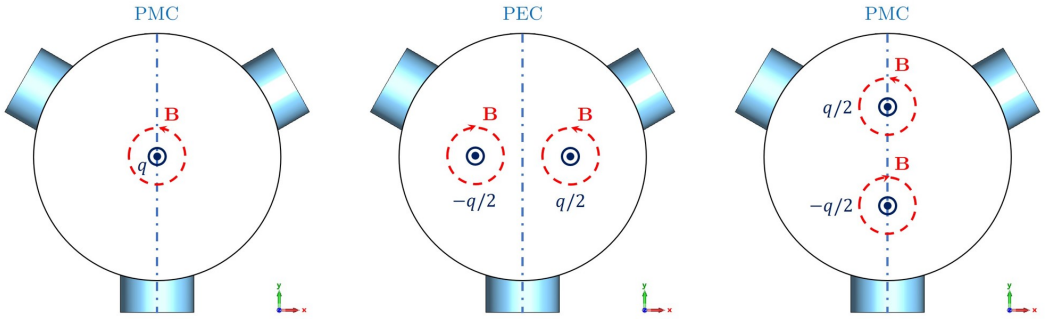

(a) Monopole excitation

(b) Dipole excitation – Horizontal polarization

(c) Dipole excitation – Vertical polarization

Figure 5.1: Monopole and dipole excitation schemes used in 3D wakefield simulations (figures adapted from [115, 149, 150]). In axisymmetric cavities, the indicated boundary conditions can be employed to effectively reduce the simulation time.

The wake impedance spectra obtained from the Fourier transform of the wake potential exhibit impedance peaks that correspond to the high-Q modes [21]. Typically, these high-impedance modes reside below the cutoff frequency of the TM_{01} beam pipe mode and are trapped in the cavity. Because of their high Q-values, once excited by the traversing beam, the energy of these modes remains in the cavity for a long time. Their field amplitude decays according to $\mathrm{e}^{-\frac{2t}{\tau_n}}$, with τ_n being the mode-dependent time constant defined as [17, p. 335]

$$\tau_n = \frac{2Q_{\mathrm{L},n}}{\omega_n}, \tag{5.8}$$

where ω_n and $Q_{\mathrm{L},n}$ are the angular frequency and the loaded quality factor of the considered mode n, respectively. The wake length is the distance behind the driving bunch needed to decrease the energy of a mode to 1/e of its initial value [21]. A large value of the wake length is required to solve the impedance peaks of the high-Q modes.

For example, a mode at 1.5 GHz with a $Q_{\mathrm{L}} = 1 \times 10^5$ needs a simulated wake length of $c\tau = 6.37$ km. This wake length is prohibitively large to be simulated. The required computation time would be very long, depending on the number of mesh cells and the simulated bunch length. In wakefield simulations, the simulated wake potential is usually truncated after a few hundred meters. However, this would not allow the impedance peaks of such high-Q modes to be fully resolved. Therefore, the impedance extrapolation scheme method, proposed in [151], has been utilized throughout this thesis to solve the impedance peaks of high-Q modes. The impedance extrapolation method has been implemented in a Python® [152] script. The calculation consists of simulating two wake potentials truncated at different wake lengths. For example, the first wake is truncated after ct_1 and the second after ct_2, where t_1 and t_2 represent two time instants. It is advantageous to set $t_2 = 2t_1$ to simplify the calculation. This method allows us to extrapolate the truncated wake impedance to its value at an infinite wake length, and it is applicable to the full impedance spectrum at once [21]. Ultimately, it permits a considerable reduction in the total computation time. More details on the above-mentioned method can be found in [151].

5.1.2 Eigenmode impedance

Eigenmode simulations in 3D EM solvers are required to calculate the main figures of merit of a cavity mode, such as the resonant frequency, the integrated voltage, the R/Q, and the Q-value. The modal quantities of a cavity are obtained by solving the eigenvalue problem derived from the discretization of the Helmholtz equations (1.40) and (1.41) by numerical methods such as FEM. The eigenvalues of the eigenvalue problem represent the resonant frequencies of the modes, while the eigenvectors correspond to the field patterns of the resonant modes, as detailed in Section 1.2. The solutions of the eigenvalue problem are also denoted as eigenmodes of the cavity [153]. The other figure of merit, described in Chapter 1, can be calculated from the results of eigenmode simulations. The fully resolved impedance of a mode, i.e., $(R/Q)Q_{\mathrm{L}}$, can be calculated via eigenmode simulations. For this reason, they are also used to complete 3D wakefield computations and verify the accuracy of the wake-impedance peaks of the excited HOMs [21].

The simulation of a lossless cavity consists of applying PEC boundary conditions to the external boundaries of the cavity vacuum, resulting in a linear eigenvalue problem. For the computation of external losses in a cavity, surface impedance boundary conditions can be applied to the vacuum boundaries to simulate the energy deposited on the walls. An important parameter computed in eigenmode simulations is the external quality factor Q_{ext} of a resonant mode (see Section 1.3.7). The external quality factor describes the energy loss of a mode through a port. The standard method for the Q_{ext} calculation consists of terminating HOM couplers or beam pipe openings with waveguide ports featuring matched impedance boundary conditions. The termination impedance, which is the ratio between the modal voltage and the current, for each mode

must be the wave impedance of the considered mode [153]. This condition represents a reflection-free boundary condition, i.e., no energy is reflected back into the simulated cavity or coupler. The termination impedances typically vary with frequency, resulting in a complex-valued, nonlinear eigenvalue problem. The 3D eigenmode solver of CST permits the evaluation of the Q_{ext} of a mode through two different solvers: the lossless and lossy solvers. The first employs the perturbation method, which yields the unloaded quality factor Q_0 given the surface conductivity of the material. The lossy solver calculates the Q_{ext} based on the complex-valued, nonlinear eigenvalue problem [154]. The lossy eigenmode solver of CST also provides the Q_{ext} of each port of a multi-port structure. This permits the evaluation of the resonant mode coupling and, consequently, the HOM power flux through each waveguide port. In this thesis, the lossy eigenmode solver of CST has been employed to solve the eigenvalue problem exclusively when external losses are included in the numerical model. Otherwise, the lossless solver has been used for all cases that involve only PEC boundary conditions.

5.2 Beam-induced HOM power calculation

A particle beam traversing a cavity excites HOMs, resulting in a deposit of EM energy into the cavity [17, p. 331]. The deposition of beam-induced HOM power in the accelerating structures can lead to significant performance limitations for the accelerator [155]. Extracting HOM power from the SRF cavities is a significant challenge, as the power has to be removed at cryogenic temperatures. Typically, HOM couplers must extract between 10 W to 100 W of beam-induced HOM power [17, p. 28]. Additionally, the power lost by the beam to the HOMs must be compensated by a corresponding increase in the accelerating voltage [17, p. 336]. Consequently, accurate estimations of the power losses are required. The subject of the following subsections is the evaluation of the HOM power losses in the SRF 5-cell cavity for PERLE for different damping scenarios.

5.2.1 HOM power in damped RF cavities

In the case of resonant excitation of a mode n by a bunch with charge Q_{b} traversing an RF cavity, the average HOM power loss can be determined as the energy left by the single bunch in a steady-state regime during the time interval t_{b} between consecutive bunches, as follows [156]

$$P_{\text{HOM},n} = \frac{1}{t_{\text{b}}} \left(Q_{\text{b}} \left| \underline{V}_{\parallel,n} \right| \mathrm{e}^{-t_{\text{b}}/\tau_n} + k_{\parallel,n} Q_{\text{b}}^2 \right) . \tag{5.9}$$

Here, $\left| \underline{V}_{\parallel,n} \right| \mathrm{e}^{-t_{\text{b}}/\tau_n}$ is the voltage experienced by the bunch associated to the HOM n, with τ_n being the decay time of the HOM field, and $k_{\parallel,n} Q_{\text{b}}^2$ is the energy deposited by the bunch into the HOM n. Considering the maximum voltage amplitude of a mode n

in steady-state operation, given by

$$\left|\underline{V}_{\parallel,n}\right|_{\max} = \underbrace{2k_{\parallel,n}Q_\mathrm{b}}_{\left|\underline{V}_{\parallel,n}\right|} \frac{\mathrm{e}^{t_\mathrm{b}/\tau_n}}{\mathrm{e}^{t_\mathrm{b}/\tau_n}-1}, \tag{5.10}$$

the equation (5.9) can be rewritten as

$$P_{\mathrm{HOM},n} = I_{\mathrm{b},0}\frac{2k_{\parallel,n}Q_\mathrm{b}}{\mathrm{e}^{t_\mathrm{b}/\tau_n}-1} + k_{\parallel,n}Q_\mathrm{b}I_{\mathrm{b},0}, \tag{5.11}$$

where $I_{\mathrm{b},0} = Q_\mathrm{b}/t_\mathrm{b}$ is the average beam current. Finally, equation (5.11) can be expressed using the modal longitudinal loss factor definition (1.75) as

$$P_{\mathrm{HOM},n} = \frac{(R/Q)_{\parallel,n}\omega_n Q_\mathrm{b}^2}{4t_\mathrm{b}}\left(\frac{\mathrm{e}^{t_\mathrm{b}/\tau_n}+1}{\mathrm{e}^{t_\mathrm{b}/\tau_n}-1}\right), \tag{5.12}$$

where $(R/Q)_{\parallel,n}$ is the longitudinal geometric shunt impedance of a mode n.

The beam-induced HOM power depends on the interaction between the beam and the surrounding accelerating structure, as well as the position of beam spectral lines with respect to the cavity HOMs (see Figure 2.7) [17, p. 336]. Moreover, the HOM power depends on the relationship between the decay time of the HOM excited by a bunch and the arrival time of the next bunch into the cavity. If the subsequent bunch enters the cavity before the EM field of a HOM n has sufficiently damped down, i.e., $t_\mathrm{b} \ll \tau_n$, a multi-bunch resonant excitation occurs [156]. In this case, the resulting beam-induced HOM power can be approximated from equation (5.12) as

$$P_{\mathrm{HOM},n} \approx \frac{(R/Q)_{\parallel,n}\omega_n Q_\mathrm{b}^2}{4t_\mathrm{b}}\left(\frac{2\tau_n}{t_\mathrm{b}}+1\right), \tag{5.13}$$

where the exponential function $\mathrm{e}^{t_\mathrm{b}/\tau_n}$ is approximated using the first-order Taylor series expansion around zero, i.e., $e^{t_\mathrm{b}/\tau_n} \approx 1 + t_\mathrm{b}/\tau_n$. Utilizing the average beam current and HOM field decay time definitions, the equation (5.13) can be finally simplified as

$$P_{\mathrm{HOM},n} \approx \frac{(R/Q)_{\parallel,n}\omega_n Q_\mathrm{b}^2}{4t_\mathrm{b}}\left(\frac{2\tau_n}{t_\mathrm{b}}\right) = (R/Q)_{\parallel,n}Q_{\mathrm{L},n}I_{\mathrm{b},0}^2. \tag{5.14}$$

While the event of a multi-bunch resonant excitation in an accelerating structure is low, if it occurs, the consequent mode excitation can be severe [17, p. 336]. Conversely, if the field of a HOM n has effectively decayed before the next bunch enters the cavity, i.e., $t_\mathrm{b} \gg \tau_n$, a non-resonant single-bunch interaction occurs [156]. In this case, the approximated beam-induced HOM power, given by equation (5.12), is simplified to

$$P_{\mathrm{HOM},n} \approx k_{\parallel,n}Q_\mathrm{b}I_{\mathrm{b},0}. \tag{5.15}$$

Since the cavity modes are orthogonal, the power loss contribution of each HOM n can

be summed to obtain the total HOM power deposited by the beam as [17, p. 336]

$$P_{\mathrm{HOM}} = \sum_n P_{\mathrm{HOM},n}. \tag{5.16}$$

This equation takes into account the modal power contribution of each single excited mode up to a certain frequency. It can be used to approximate the power evaluation for modes confined within the cavity [157]. Bunches with a short longitudinal RMS length can excite frequencies up to tens of GHz, making the computation of each mode power contribution time-consuming. The HOM power deposition in a cavity is larger at high frequencies because longitudinal and transverse wake losses scale with the second and third power of frequency [158]. Hence, extending the analyses to higher frequencies is crucial. In such cases, the calculation of the HOM power requires the use of wakefield solvers.

The average HOM power deposited into a cavity by the beam in a single pass can be calculated as [159]

$$P_{\mathrm{HOM,ave}} = k_{\parallel,\mathrm{HOM}} Q_{\mathrm{b}} I_{\mathrm{b},0}. \tag{5.17}$$

Here, the term $k_{\parallel,\mathrm{HOM}}$ represents the longitudinal loss factor of the excited HOMs, which is given by [142]

$$k_{\parallel,\mathrm{HOM}} = k_{\parallel} - k_{\parallel,0}, \tag{5.18}$$

where $k_{\parallel,0}$ is the longitudinal loss factor of the FM and $k_{\parallel}$ the total longitudinal loss factor. The bunch-length dependent loss factor $k_{\parallel,0}$ of the FM is expressed as

$$k_{\parallel,0} = \frac{\omega_0}{4}(R/Q)_{\parallel,0}\mathrm{e}^{-(\omega_0\sigma_z/c)^2}, \tag{5.19}$$

where ω_0 is the angular frequency of the FM, and c is the speed of light. The total longitudinal loss factor $k_{\parallel}$ for a Gaussian bunch is given by [142, 160]

$$k_{\parallel}(\sigma_z) = \frac{1}{2\pi}\int_{-\infty}^{\infty} Z_{\parallel}(\omega)\mathrm{e}^{-(\omega\sigma_z/c)^2}\mathrm{d}\omega, \tag{5.20}$$

where $Z_{\parallel}(\omega)$ is the longitudinal impedance of the cavity. Numerical wakefield solvers, such as ABCI and CST, can calculate the integrated loss factor spectrum and the total longitudinal loss factor of a bare cavity (see Subsection 5.3.2).

The beam-filling pattern and the position of high-impedance peaks in the cavity spectrum are critical factors when evaluating HOM power deposition [159]. When HOM frequencies are near the main beam spectral lines (refer to Subsection 2.2.2), the beam-induced voltage could potentially build up, leading to a corresponding increase in HOM power. To account for the beam-filling pattern dependency, the HOM power deposited by the beam into the cavity can be calculated from the longitudinal wake impedance according to the following equation [155]

$$P_{\mathrm{HOM}} = I_{\mathrm{b},0}^2 \sum_{n=-\infty}^{\infty} \Re\big[Z_{\parallel}(nf_{\mathrm{b}})\big] \big|\hat{I}_n\big|^2, \tag{5.21}$$

where $I_{\mathrm{b},0}$ is the average beam current, $Z_{\parallel}$ the longitudinal impedance of the cavity, n the revolution harmonic number, $\hat{I}_n$ the normalized Fourier spectrum of the beam current at the nth revolution harmonic, and f_{b} the revolution frequency. The term $\hat{I}_n$ depends on the beam-filling pattern of the accelerator. Depending on the chosen filling pattern, different modes could be excited by the beam, leading to a different HOM power deposition into the cavity. In this thesis, the beam current spectrum of PERLE, as illustrated in Figure 5.2 (a), is used for evaluating the beam-induced HOM power. The current spectrum is calculated from the main beam parameters listed in Table 2.1 and considering the beam filling pattern and bunch timing illustrated in Figure 3.8.

Because of the relatively short bunch length ($\sigma_z = 3$ mm) foreseen for the 500 MeV version of PERLE, the beam exhibits significant spectral contributions up to approximately 39 GHz. The numerical determination of the impedance of the cavity and HOM power up to this high frequency is computationally prohibitive in a wakefield solver. S. Gorgi Zadeh *et al.* proposed in [161] a method to approximate the HOM power up to high frequencies. This method is used here to estimate the HOM power deposited by the beam for the different PERLE damping options. As the HOM power is directly proportional to the square of the beam current, according to the equation (5.21), it can be computed up to a certain frequency and approximated for higher frequencies. The beam current spectrum is initially analyzed and divided into three parts: low (l), middle (m), and high (h) frequency ranges. This division is based on the impedance behavior of the analyzed cavity. The low-frequency range is characterized by the presence of trapped modes exhibiting high narrow-band impedance. Typically, this region extends to frequencies approximately three times the frequency of the FM. The middle-frequency range corresponds to the region where the impedance has broadband behavior. For higher frequencies, the impedance spectrum of a cavity exhibits a predominantly broadband behavior. Therefore, the HOM power computed in the middle-frequency region can be used to reasonably approximate the power of the high-frequency region. According to the most recent spectrum of the PERLE beam current squared $|I_{\mathrm{b}}|^2$, as shown in Figure 5.2, 18.58% of $|I_{\mathrm{b}}|^2$ is located between 0 GHz and 2.5 GHz (low-frequency region), 7.70% between 2.5 GHz and 4 GHz (medium-frequency region), 73.71% between 4 GHz and 39 GHz. Therefore, the total HOM power for the 500 MeV version of PERLE can be approximated by

$$P_{\mathrm{tot}} \approx P_{\mathrm{l}} + P_{\mathrm{m}} + \frac{73.71}{7.70} P_{\mathrm{m}}, \tag{5.22}$$

where P_{l} and P_{m} represent the HOM power calculated in the low and medium-frequency regions, respectively.

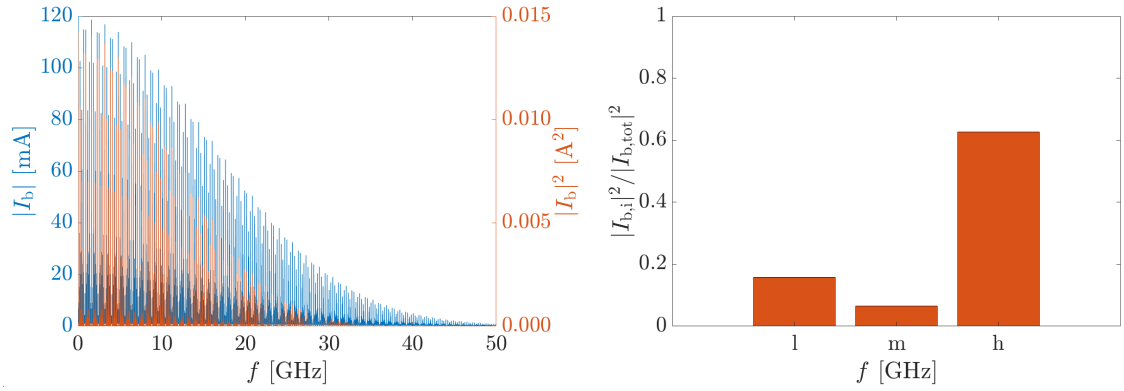

(a) Beam spectrum of PERLE **(b)** Percentage of $|I_b|^2$

Figure 5.2: Beam spectrum of PERLE (a). The spectrum corresponds to the PERLE filling pattern shown in Figure 3.8. The beam spectrum exhibits symmetry around f=0, and for illustration purposes, only the positive frequency range is shown here. The percentage of $|I_b|^2$ within each i-frequency region is shown in (b). The low-frequency region (i = l) goes from 0 GHz to 2.5 GHz, the medium-frequency region (i = m) from 2.5 GHz to 4 GHz, and the high-frequency region (i = h) from 4 GHz to 39 GHz.

5.2.2 Propagation of HOM power through the cavity ports

The previous section discussed the numerical methods for estimating the HOM power deposition by a traversing beam into a cavity. The HOM power must be extracted through external coupling mechanisms installed in the cavity, notably the HOM couplers. HOM coupler performance can be evaluated by determining the contribution of each coupler to HOM power extraction. The following method, introduced by S. Gorgi Zadeh in [115], is used to approximate the HOM power propagating into the waveguide ports connected to the output of HOM couplers using time-domain calculations.

The wakefield solver of CST is used to excite the cavity under test in the time domain with a single Gaussian bunch. The HOM couplers, the FPC, and the beam pipe entries are terminated with multi-mode ports to simulate the HOM energy leaving the cavity. The signals scattered into different modes k of each defined port i are calculated from the single bunch excitation. The spectral weighting method is used to account for the beam filling pattern [162, 163]. This post-processing technique is applied to the results of CST wakefield simulations and implemented in a MATLAB script. First, the complex-valued weighting transfer function $\underline{F}_{i,k}$ of mode k of port i is calculated as the ratio between the Fourier transform of the signal excited in the port and the Fourier transform of the current of the single Gaussian bunch as follows

$$\underline{F}_{i,k}(\omega_n) = \frac{\mathrm{FFT}[b_{i,k}(t)]}{\mathrm{FFT}[i_b(t)]}, \tag{5.23}$$

where $b_{i,k}(t)$ is the time-dependent signal excited into the mode k of port i, $i_b(t)$

the current of the exciting beam, and ω_n the angular frequency of the nth revolution harmonic. Then, the scattered signal for a beam-filling pattern is determined in the frequency domain as

$$\underline{b}_{i,k}(\omega_n) = \underline{F}_{i,k}(\omega_n)\underline{I}_b(\omega_n), \tag{5.24}$$

where $\underline{I}_b(\omega_n)$ is the PERLE beam current spectrum, as illustrated in Figure 5.2 (a). Finally, the HOM power propagating through a port i can be obtained by summing over all the harmonics n and modes k as follows [115]

$$P_i = \sum_{n=1}^{N_h} \sum_{k=1}^{K_i} |\underline{b}_{i,k}(\omega_n)|^2, \tag{5.25}$$

where K_i is the total number of modes defined at port i, and N_h is the maximum considered harmonic number.

5.3 Five-cell cavity at 801.58 MHz for PERLE

In this section, the HOM couplers optimized in Chapter 4 are integrated and simulated with the 5-cell cavity at 801.58 MHz for PERLE. The focus is on the damping of the monopole (longitudinal) and dipole (transverse deflecting) HOMs, as they are the most parasitic modes [21]. Two HOM-damping schemes are investigated: the 2 Probe-type and 2 Hook-type couplers (2P2H scheme) and 4 DQW-type couplers (4DQW scheme). Figure 5.3 illustrates the two HOM-damping schemes simulated using CST. In the following, the term "HOM-endgroup" is employed to refer to the ensemble of the HOM couplers installed on one cavity side, potentially including the FPC.

In both damping schemes, the HOM-endgroup on the FPC side includes two HOM couplers and the FPC. Coaxial HOM couplers, FPC, and beam pipe (BP) entries are terminated with waveguide ports to avoid undesired field reflections. The two HOM couplers are located 69 mm away from the straight wall of the adjacent end-cell, while the FPC is at a distance of 103 mm. The endgroup on the opposite side features two HOM couplers positioned 78 mm from the neighboring end-cell. This endgroup will host the cavity tuner in the final configuration [164]. A small vacuum volume is also included to accommodate a probe for diagnostic measurements (not represented in the model). The above-mentioned quantities refer to the distance between the coupler axis and the adjacent end-cell wall. The penetration of the antenna into the beam pipe was set at 20 mm for all HOM couplers (refer to Section (4.2)), while the FPC penetrates the beam tube by 2.5 mm. The HOM couplers on each beam pipe are positioned to form an angle of 120° between their axes. Figure 5.4 illustrates the 5-cell PERLE cavity equipped with HOM couplers, the FPC, and the tuner with the He vessel (see also Figure A.4 in the Annex A).

These technical specifications were determined based on the following factors:

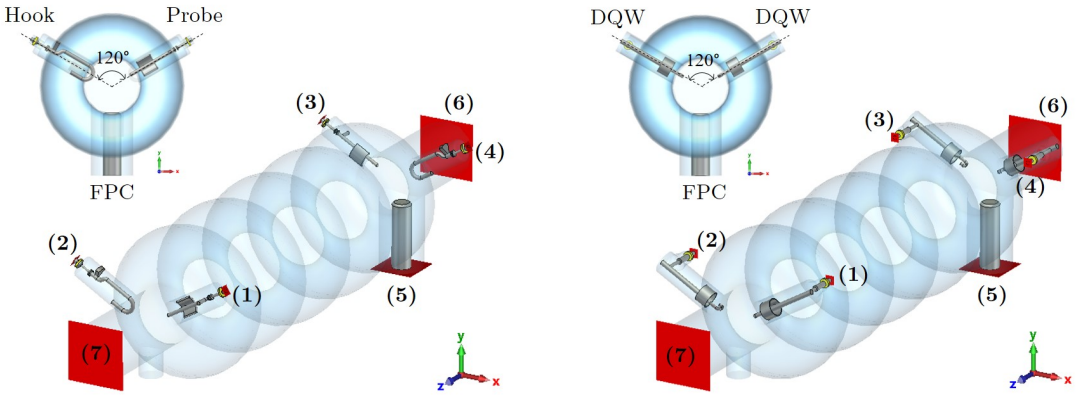

(a) 5-cell cavity with 2P2H scheme **(b)** 5-cell cavity with 4DQW scheme

Figure 5.3: 5-cell 801.58 MHz cavity equipped with HOM couplers simulated in CST: (a) 2P2H scheme, (b) 4DQW scheme. Two HOM couplers are located on each side of the cavity and are positioned to form an angle of 120° between their axes. Waveguide ports are indicated in red. HOM coupler ports are numbered from (1) to (4), FPC port as (5), and beam pipe ports on FPC and tuner sides as (6) and (7), respectively.

(i) **Number of couplers**. The number of HOM couplers is not strictly limited [21]. The decision regarding the number of HOM couplers per endgroup comes with a trade-off between the HOM-damping level needed to meet the BBU requirements and costs. It also considers engineering requirements for integration with the He vessel and cryomodule design. Coaxial HOM couplers can be positioned either inside or outside the He vessel. The first solution allows for better coupling with the evanescent cavity fields. The latter solution is typically employed to have direct access to HOM couplers in case their tuning for the FM rejection is needed. Most existing cavities typically utilize a minimal set of two HOM couplers per cavity. Typically, HOM couplers are employed on both sides of the cavity to ensure efficient damping of tilted fields on both sides [21]. The probe-type and hook-type couplers designed in this thesis were conceived to strongly damp trapped monopole and dipole modes of the PERLE cavity, respectively. The 2P2H damping scheme features two probe-type and two hook-type couplers to lower the impedance of both monopole and dipole modes below the BBU instability limits. The decision to incorporate four HOM couplers is compatible with engineering requirements for the cryomodule design of the PERLE cavity. It is based on the following considerations: two hook-type couplers are needed to damp both polarizations of confined dipole modes, lowering their external quality factor by at least a factor 10 than the critical Q_{ext} predicted by the Equation (3.9), as demonstrated in our previous work [90]. However, the two-hook damping scheme does not provide sufficient stability margin for monopole mode mitigation. Two probe-type couplers have been demonstrated to mitigate monopole modes

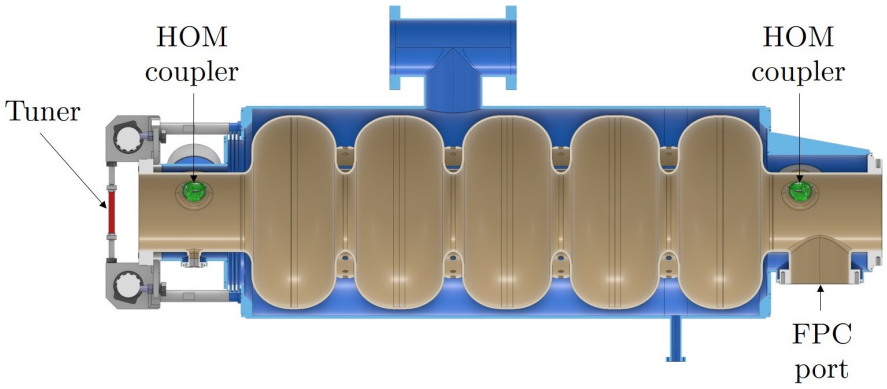

Figure 5.4: Cross-section rendering of the 5-cell PERLE cavity illustrating the integration of DQW HOM couplers (green), the FPC port, and the tuner with the helium vessel [165].

below BBU instability limits [90]. Consequently, an HOM-damping scheme with four couplers (two probe-type and two hook-type) was chosen to address the damping of both types of modes and ensure symmetry in the HOM-damping scheme. The DQW coupler was conceived to damp both confined monopole and dipole modes. To ensure a fair comparison with the 2P2H damping scheme in terms of the number of couplers and endgroup symmetry, the 4DQW damping scheme was also considered to strongly damp HOMs of the PERLE cavity.

(ii) **Coupler position**. Increasing the penetration of the HOM couplers into the beam pipe results in stronger damping [96]. The same applies if the HOM couplers are positioned closer to the cavity end-cells. However, the HOM couplers may incur excessive coupling to the FM and higher RF heating, which can trigger a quench in the endgroup. Our previous works [49, 90, 166], which partially report results on similar HOM-damping schemes, have demonstrated that the positioning of HOM couplers within the above-mentioned distance range effectively mitigates HOMs below the BBU instability limits. The chosen geometrical specifications also met the mechanical requirements for the integration of the cavity into the cryomodule studied at IJCLab [164].

(iii) **Angle between couplers**. The angular position of the coupler with respect to the beam axis influences the damping of HOMs. The couplers on the FPC side are spaced symmetrically around the beam pipe (120° between their axes). This angular disposition is called "Y-endgroup" [167]. This coupler arrangement can preserve dipole HOM symmetry, minimizing the dependency on transverse mode polarization and the transverse kicks to the beam [21]. In this way, any orientation of dipole mode is quasi-equally damped. Furthermore, the monopole power deposition to each coupler is quasi-identical if the damping structure considers the same type of couplers [167]. The HOM couplers on the tuner side have the same angular configuration to maintain symmetry in the damping structure.

(iv) **FPC position**. The FPC integrated with the cavity beam pipe is an adapted version of the one utilized in the SPL cavities [168]. The characteristic impedance of the coaxial line is kept at 50 Ω. The position of the FPC was chosen to meet the specification of the required operational loaded quality factor of 2.5×10^6 for the FM, in accordance with the input RF power studies presented in Section 2.4. The FPC was included in the simulated HOM-damping schemes solely to determine to what extent it can provide additional mode damping.

The results of HOM-damping, HOM power, and RF-heating simulations for the 2P2H and the 4DQW damping schemes are reported in the next subsections.

5.3.1 Longitudinal and transversal impedance

Figures 5.5 (a) and (b) illustrate the longitudinal and transversal impedance spectra of the 5-cell 801.58 MHz cavity for the two analyzed HOM damping schemes, respectively. The analyzed frequency range covers the HOMs with the highest impedances. The comparison between 3D wakefield and lossy eigenmode solutions is also depicted.

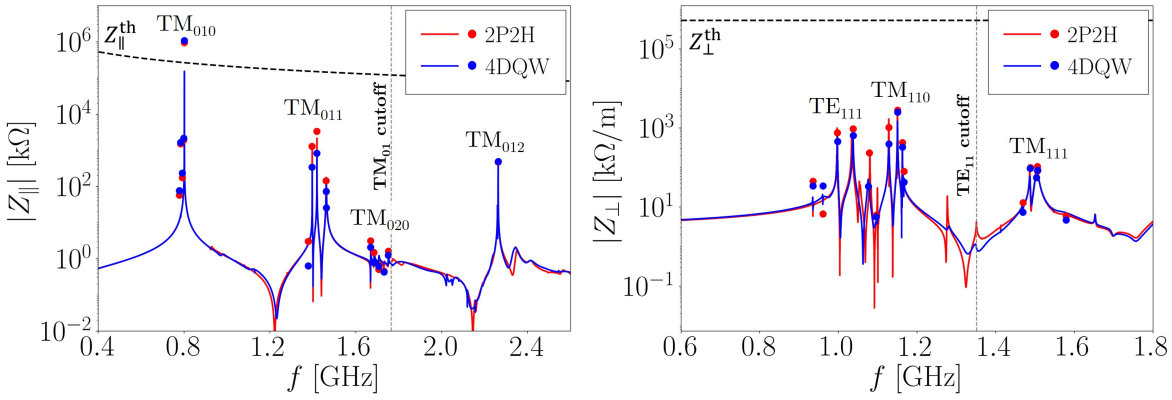

(a) Longitudinal impedance **(b)** Transversal impedance

Figure 5.5: Longitudinal (a) and transversal (b) impedance spectra of the 5-cell 801.58 MHz cavity with two different HOM damping schemes. The wake impedances (solid lines) are calculated and extrapolated from the wake potentials with a wakelength of 1000 m. The dots denote the impedance $(R/Q)Q_{\text{L}}$ calculated with lossy eigenmode simulations. The black-dotted lines represent the BBU instability thresholds for the 500 MeV PERLE version. The grey dashed vertical lines are the cutoff frequencies of the TM_{01} and TE_{11} beam pipe modes.

The results demonstrate excellent agreement between the wakefield and eigenmode computational methods. The transverse wakefield calculation has been performed for one dipole mode polarization only. The results for the remaining dipole polarization exhibit minimal deviation, primarily due to the use of quasi-symmetrical endgroups that guarantee dipole HOM symmetry. This is validated by the eigenmode computation that typically covers both polarization directions. The monopole modes TM_{011}

and TM_{020} and the dipole modes TE_{111}, TM_{110} and TM_{111} are trapped in the cavity. In particular, the TM_{011}, TE_{111}, and TM_{110} mode passbands exhibit the highest impedance among the trapped mode passbands. These modes can limit the stable beam current achievable in the ERL. Consequently, they require strong damping to reduce their impedance below the BBU instability limits. In both analyzed HOM-damping schemes, cavity HOMs are effectively damped below the impedance thresholds. The 4DQW damping scheme permits a reduction in the impedance of the TM_{011}-$4\pi/5$ and TM_{011}-$3\pi/5$ modes by a factor of four, and that of the TM_{011}-$2\pi/5$ and TM_{011}-$\pi/5$ by a factor of 2.5, compared to the 2P2H damping scheme. It also yields a better absorption than the 2P2H scheme for the first two dipole mode passbands (TE_{111} and the TM_{110}), i.e., on average, more than a factor of 1.5 for the highest transverse impedance modes. The TM_{012}-π mode at around 2.26 GHz appears relatively trapped within the middle cells of the five-cell cavity (see Figure 2.8 (b)). Its impedance is mostly unaffected by the used HOM-damping scheme since it resonates considerably above the TM_{01} beam tube mode cutoff. Modifying the shape of the cavity end-cells could enhance the coupling of this mode to the beam tubes, consequently lowering its impedance [21]. Table 5.1 lists the monopole and dipole HOMs with the highest eigenmode and wake impedances in the two analyzed damping options and the corresponding BBU impedance thresholds.

Table 5.1: Eigenmode $(R/Q)Q_{\mathrm{L}}$ and wake impedance Z of relevant monopole and dipole modes for the 801.58 MHz 5-cell cavity with the 2P2H and 4DQW damping schemes.

Monopole modes						
		2P2H scheme		4DQW scheme		
Mode n	f_n [GHz]	$R/Q_{\parallel}Q_{\mathrm{L}}$ [kΩ]	$Z_{\parallel}$ [kΩ]	$R/Q_{\parallel}Q_{\mathrm{L}}$ [kΩ]	$Z_{\parallel}$ [kΩ]	$Z^{\mathrm{th}}_{\parallel,n}$ [kΩ]
TM_{011}-$4\pi/5$	1.397	1275	1268	341	285	1.52×10^5
TM_{011}-$3\pi/5$	1.419	3325	2154	827	697	1.49×10^5
TM_{012}-π	2.263	474	370	485	453	9.37×10^4
Dipole modes						
		2P2H scheme		4DQW scheme		
Mode n	f_n [GHz]	$R/Q_{\perp}Q_{\mathrm{L}}$ [kΩ/m]	$Z_{\perp}$ [kΩ/m]	$R/Q_{\perp}Q_{\mathrm{L}}$ [kΩ/m]	$Z_{\perp}$ [kΩ/m]	$Z^{\mathrm{th}}_{\perp,n}$ [kΩ/m]
TE_{111}-$3\pi/5$	0.997	753	992	455	628	5.23×10^5
TE_{111}-$4\pi/5$	1.038	945	883	642	610	5.23×10^5
TM_{110}-$4\pi/5$	1.129	1038	1670	392	389	5.23×10^5
TM_{110}-$3\pi/5$	1.151	2797	2247	2476	1476	5.23×10^5

Simulated results show that the most efficient damping option for the PERLE 5-cell cavity is the 4DQW scheme. This damping configuration features a symmetrical design, which is achieved by mirroring two pairs of DQW couplers on opposite sides of the cavity. The symmetry of the 4DQW HOM-endgroup ensures the preservation of dipole HOM symmetry and quasi-identical HOM power deposition to each coupler.

5.3.2 Average HOM power

The average HOM power of the 5-cell cavity at 801.58 MHz in the 500 MeV PERLE version is approximately 102.65 W for a Gaussian bunch with a 3 mm RMS bunch length. The evaluated HOM power refers to the non-resonant excitation scenario. It is calculated using the equation (5.15) along with the main beam parameters and loss factors reported in Table 5.2. The total longitudinal loss factor is calculated in ABCI for the 2D axisymmetric bare cavity. Figure 5.6 (a) displays the integrated loss factor spectrum. Figure 5.6 (b) illustrates the dependency of the total longitudinal loss factor on the bunch length for the same cavity. The total longitudinal loss factor is inversely proportional to the square root of the bunch length, i.e., $k_{\parallel} \propto \sigma_z^{-1/2}$ [160, p. 250].

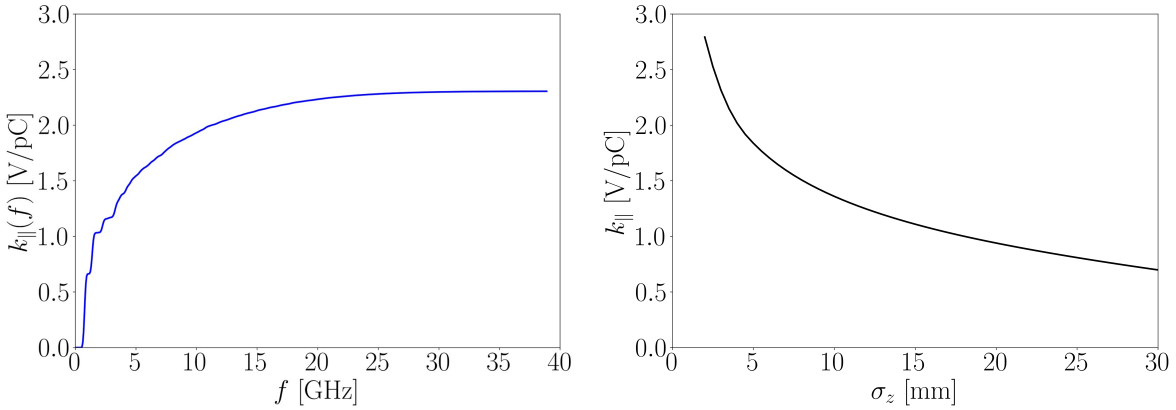

(a) Integrated loss factor spectrum **(b)** Bunch length vs. loss factor

Figure 5.6: Integrated loss factor spectrum for a bunch with a 3 mm bunch length for the 5-cell 801.58 MHz PERLE cavity computed using the 2D wakefield solver in ABCI. Dependency of the total longitudinal loss factor on the bunch length ($k_{\parallel} \propto \sigma_z^{-1/2}$) for the same cavity (b).

Table 5.2: Main beam parameters, loss factors, and average HOM power deposited by the beam in the 5-cell 801.58 MHz bare cavity for the 500 MeV version of PERLE.

Parameter	Symbol	Unit	Value
Longitudinal bunch length	σ_z	mm	3
Bunch charge	Q_{b}	pC	500
Operating beam current	$I_{\mathrm{b,op}}$	mA	120
Total longitudinal loss factor	$k_{\parallel}$	V/pC	2.304
Loss factor of Fundamental Mode (FM)	$k_{\parallel,0}$	V/pC	0.594
Total longitudinal loss factor of HOMs	$k_{\parallel,\mathrm{HOM}}$	V/pC	1.711
Average HOM power	$P_{\mathrm{HOM,ave}}$	W	102.65

For the sake of clarity, the total longitudinal loss factor for a dressed cavity, i.e., a cavity including HOM damping mechanisms, slightly differs from the loss factor of a

bare cavity. The wakefield solver in CST can calculate the longitudinal loss factor for a 3D dressed cavity. However, the very short longitudinal bunch length (3 mm) makes the calculation for a 3D structure computationally prohibitive due to the high mesh density requirements. Therefore, this thesis assumes the same total longitudinal loss factor for the bare and HOM-damped cavities.

5.3.3 HOM power

5.3.3.1 Five-cell cavity with coaxial HOM-couplers

Wakefield simulations were conducted to evaluate the HOM power for the 5-cell cavity equipped with the 2P2H and 4DQW endgroups (see Figure 5.3). The total beam-induced HOM power up to 39 GHz is approximately 129.11 W for the 2P2H scheme and 98.56 W for the 4DQW scheme. This highlights a dependency of the beam-excited HOM power on the employed damping scheme. Indeed, the traversing beam can interact with EM fields differently within the same cavity when different damping schemes are used. Figure 5.7 depicts the total HOM power deposited by the beam in the 5-cell PERLE cavity with the 2P2H or 4DQW damping schemes up to 4 GHz.

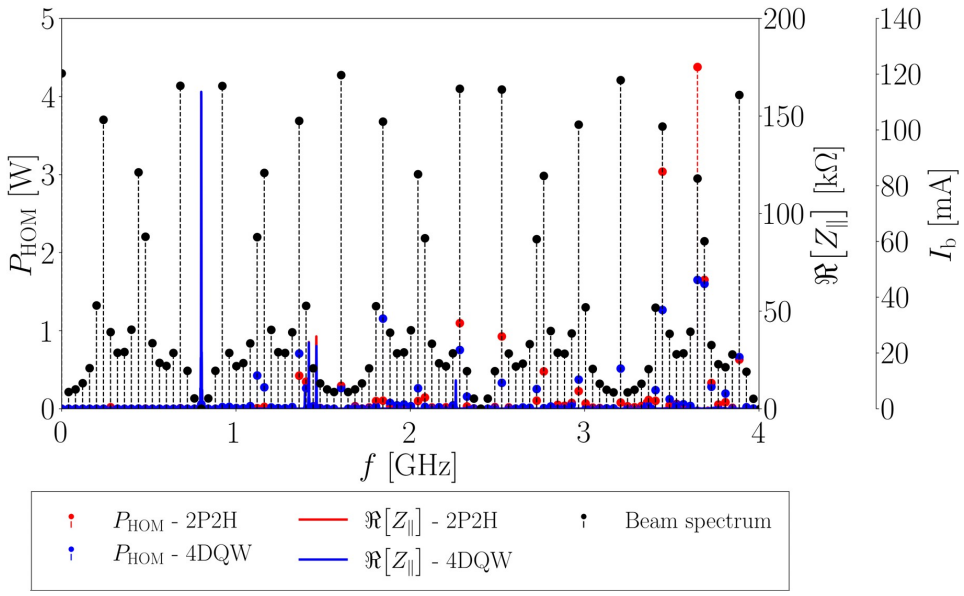

Figure 5.7: Total beam-induced HOM power deposited into the 5-cell cavity equipped with the 2P2H (red-dashed lollipops) or 4DQW (blue-dashed lollipops) schemes up to 4 GHz. The power is computed from the equation (5.21), considering the PERLE beam current spectrum on the third vertical axis (black-dashed lollipops). The final result is multiplied by two to account for the negative side of the beam spectrum. The real part of the longitudinal wake impedance for the 2P2H (red solid line) and 4DQW (blue solid line) damping schemes is shown in the secondary axis. The wake impedance is calculated from a wavelength of 100 m excited by a beam with a bunch length of 30 mm and centered on the cavity axis.

The HOMs with large impedance, which reside below the TM_{01} beam pipe cutoff frequency (1.765 GHz), do not hit any main beam spectral line of the considered beam-filling scheme. The HOM power deposited by the beam below the TM_{01} cutoff frequency is around 1.16 W in the 2P2H damping scheme, while in the 4DQW is around 2.15 W. Some higher contribution of beam-induced HOM power is detected between the TM_{01} beam pipe cutoff frequency and the end of the defined medium-frequency region, ranging from 1.2 W to 4.4 W. Table 5.3 reports the total HOM power propagating through the couplers and beam pipe ports in the two studied damping schemes.

Table 5.3: HOM power propagating through couplers and beam pipe ports in the two analyzed HOM damping schemes shown in Figure 5.3. The power is calculated using the beam spectrum shown in Figure 5.2 (a). P_{l} is the HOM power deposited by the beam up to 2.5 GHz, P_{m} is the power between 2.5 GHz and 4.0 GHz, and P_{h} the power between 4.0 GHz and 39 GHz. P_{tot} is the total HOM power for the whole spectrum. $P_{\mathrm{P},(i)}$, $P_{\mathrm{H},(i)}$, $P_{\mathrm{D},(i)}$, $P_{\mathrm{FPC},(i)}$, and $P_{\mathrm{bp},(i)}$ represent the HOM power extracted from the probe-type, hook-type and DQW couplers, the FPC, and beam pipes at their corresponding port i up to 39 GHz, respectively. The port indexes correspond to the convention used in Figure 5.3. The HOM power is computed from wakefield simulations in CST considering a wake length of 100 m.

Five-cell cavity at 801.58 MHz - 2P2H damping scheme											
	P_{l}	P_{m}	P_{h}	P_{tot}	$P_{\mathrm{P},(1)}$	$P_{\mathrm{H},(2)}$	$P_{\mathrm{P},(3)}$	$P_{\mathrm{H},(4)}$	$P_{\mathrm{FPC},(5)}$	$P_{\mathrm{bp},(6)}$	$P_{\mathrm{bp},(7)}$
[W]	3.53	11.88	113.70	129.11	1.07	0.56	1.38	0.29	13.35	47.35	65.11
[%]	2.73	9.20	88.07		0.83	0.44	1.07	0.22	10.34	36.67	50.43
Five-cell cavity at 801.58 MHz - 4DQW damping scheme											
	P_{l}	P_{m}	P_{h}	P_{tot}	$P_{\mathrm{D},(1)}$	$P_{\mathrm{D},(2)}$	$P_{\mathrm{D},(3)}$	$P_{\mathrm{D},(4)}$	$P_{\mathrm{FPC},(5)}$	$P_{\mathrm{bp},(6)}$	$P_{\mathrm{bp},(7)}$
[W]	4.29	8.92	83.35	98.56	1.30	1.30	2.11	2.11	11.87	34.46	45.41
[%]	4.35	9.05	86.60	-	1.32	1.32	2.14	2.14	12.05	34.97	46.06

In the 2P2H scheme, the probe-type couplers exhibit higher power extraction efficiency compared to the hook-type couplers. This disparity aligns with the fact that probe-type couplers were optimized to damp monopole modes, while hook-type couplers were designed to mainly mitigate dipole modes. The couplers of the 4DQW damping scheme exhibit a higher percentage of HOM power extraction across each port compared to the probe-type and hook-type couplers. This observation remarks on the superior efficiency of the DQW coupler in damping cavity monopole modes compared to the other two analyzed coupler types. Furthermore, the HOM power extraction is quasi-identical for the DQW couplers belonging to one of the two cavity sides due to the symmetrical design of the 4DQW damping scheme. The FPC absorbs more power in the 2P2H damping scheme than in the 4DQW scheme. This excess of HOM power may be due to the lower extraction capacity of the two hook-type couplers compared to

the DQW couplers. The amount of HOM power propagating into the beam pipe ports is 87.10% in the 2P2H scheme and 81.03% in the 4DQW scheme, which constitutes a significant amount of HOM power compared to the quantity extracted from the HOM couplers. Therefore, beamline absorbers (BLAs) placed at the cavity beam pipes are needed to extract the HOM power propagating through the beam pipe ports.

5.3.3.2 Five-cell cavity with coaxial HOM-couplers and BLAs

To address the extraction of the HOM power propagating through the cavity beam pipes, CST eigenmode and wakefield simulations were conducted on the 5-cell cavity equipped with coaxial HOM-coupler endgroups (2P2H or 4DQW scheme) and two BLAs installed on the cavity beam pipe (see Figure 5.8).

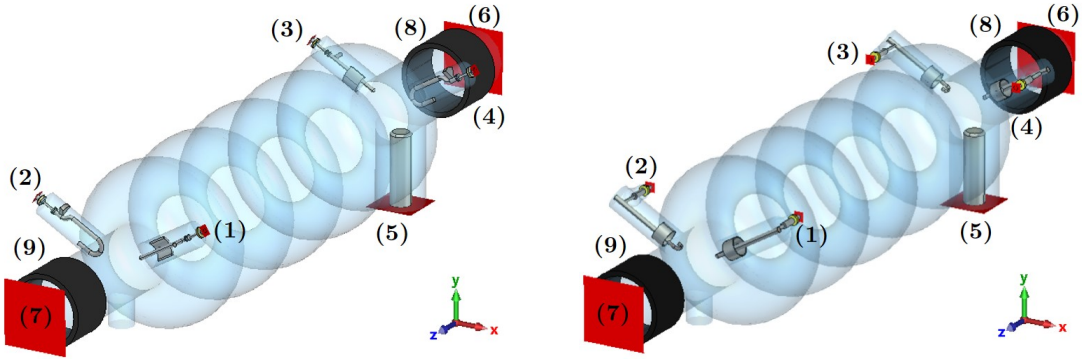

(a) 2P2H HOM-endgroup and BLAs **(b)** 4DQW HOM-endgroup and BLAs

Figure 5.8: 5-cell 801.58 MHz cavity with HOM couplers and BLAs simulated in CST: (a) 2P2H scheme, (b) 4DQW scheme. Waveguide ports are indicated in red. HOM coupler ports are numbered from (1) to (4), FPC port as (5), and BP ports on FPC and tuner sides as (6) and (7), respectively. BLAs are depicted in black and numbered with indexes (8) and (9). The upstream and downstream sections of the cavity are on the right and left sides, respectively.

BLAs can be considered rings made of lossy dielectric materials (refer to Subsection 4.1.3). The introduction of losses in the model leads to a complex-valued, nonlinear numerical problem. The complex and frequency-dependent permittivity characterizes the response of the BLA material to the alternating EM fields, defined as [23, pp. 72-79]

$$\varepsilon(\omega) = \varepsilon'(\omega) - j\varepsilon''(\omega). \tag{5.26}$$

Here, ε' represents the real part of the complex permittivity, and ε'' is the imaginary part of the complex permittivity associated with the dielectric loss. The ratio between the imaginary and real parts of the complex permittivity is the electric loss tangent

$$\tan(\delta_e) = \frac{\varepsilon''}{\varepsilon'}, \tag{5.27}$$

which is typically specified by the manufacturer for any given material. Dividing the equation (5.26) by the vacuum permittivity ε_0 yields the complex relative permittivity

$$\varepsilon_{\mathrm{r}}(\omega) = \varepsilon'_{\mathrm{r}}(\omega) - j\varepsilon''_{\mathrm{r}}(\omega), \tag{5.28}$$

where $\varepsilon'_{\mathrm{r}}(\omega)$ and $\varepsilon''_{\mathrm{r}}(\omega)$ are its real and complex parts, respectively. For many dielectric materials, the real and imaginary parts of the complex relative permittivity can be calculated as a function of the frequency via the Debye equation as

$$\varepsilon_{\mathrm{r}}(\omega) = \varepsilon'_{\mathrm{r}\infty} + \frac{\varepsilon'_{\mathrm{r}0} - \varepsilon'_{\mathrm{r}\infty}}{1 + j\omega\tau_{\mathrm{e}}}, \tag{5.29}$$

where $\varepsilon'_{\mathrm{r}0}$ and $\varepsilon'_{\mathrm{r}\infty}$ represent the real part of the complex permittivity at zero and very high (ideally infinity) frequencies, respectively, and τ_{e} is the relaxation time constant of the material. The simulated BLAs are made of CERASIC-B© [169], a commercial SiC material for HOM absorbers with dielectric constants suitable for the investigated HOM frequency range. The response of $\varepsilon'_{\mathrm{r}}(\omega)$ and $\varepsilon''_{\mathrm{r}}(\omega)$ for the CERASIC-B exhibits the typical dielectric relaxation below 10 GHz [170]. Therefore, its relaxation process can be considered Debye-type and expressed through the equation (5.29). Figure 5.9 (a) depicts the $\varepsilon'_{\mathrm{r}}$ and $\varepsilon''_{\mathrm{r}}$ curves as a function of the frequency for CERASIC-B, obtained from Y. Takeuchi *et al.* in [170] by fitting the measured data with the dielectric relaxation curves based on the Debye model. The three parameters that determine the Debye model of the studied CERASIC-B are $\varepsilon'_{\mathrm{r}0} = 85.7$, $\varepsilon'_{\mathrm{r}\infty} = 13.6$ and $\tau_{\mathrm{e}} = 2.55 \times 10^{-10}$ s. At the FM frequency of the studied cavity (801.58 MHz), CERASIC-B exhibits an electric loss tangent approximately equal to 0.856.

The failure limit of a HOM absorber is driven by the maximum tolerable absorbed power before experiencing cracking in the material. Therefore, the FM and HOM absorbing power fluxes could be used to determine the maximum power handling capability of the SiC BLA [171]. Considering a BLA of inner radius R_{BLA} and length L_{BLA}, the amount of RF power $P_{\mathrm{BLA,tot}}$ dissipated on the SiC absorber's surface A_{BLA} can be defined as

$$\frac{P_{\mathrm{BLA,tot}}}{A_{\mathrm{BLA}}} = \frac{P_{\mathrm{BLA,0}} + P_{\mathrm{BLA,HOM}}}{2\pi R_{\mathrm{BLA}} L_{\mathrm{BLA}}}, \tag{5.30}$$

where $P_{\mathrm{BLA,0}}$ represents the power absorption from the FM and $P_{\mathrm{BLA,HOM}}$ the HOM absorbed power. Estimating the power flux serves as design guidance for the analysis of an HOM-damping structure with BLAs. The FM power absorption into the BLA is of secondary concern, as its EM field decays along the beam pipe. When a beam passes through the cavity, the generated HOM power propagates in the upstream and downstream directions. The coaxial HOM couplers and the BLAs partially absorb the HOM power. Since a HOM absorber introduces an impedance discontinuity, the traveling bunches generate RF modes inside it, inducing a self-generated HOM power within the dielectric material. This self-generated HOM power is mostly absorbed

immediately by the beamline absorber. However, since a BLA is not an ideal absorber, part of the power leaks through it and is reflected back when it reaches the next cavity, eventually being re-absorbed by the BLA itself.

Lossy eigenmode simulations were initially conducted on the 5-cell cavity to assess the optimal axial position of the BLA relative to the cavity axis. The objective was to ensure that the RF power dissipation in the absorber volume from the FM ($P_{\mathrm{BLA},0}$) remains within acceptable limits to mitigate the resulting heating. The goal for the PERLE 500 MeV version is to limit the power absorption from the FM to below 10% of the average HOM power, i.e., $P_{\mathrm{BLA},0}$ should not exceed 10 W. The simulated BLAs have an inner radius $R_{\mathrm{BLA}} = 65$ mm, a length $L_{\mathrm{BLA}} = 100$ mm, and a thickness of 10 mm. Figure 5.9 (b) illustrates the variation of both the FM dissipated power on the BLA surface and the BLA quality factor at FM frequency as a function of the incremental axial distance of the BLA relative to the cavity iris. The allowable range for positioning the BLA between two cavities spans from 190.66 mm to 290.66 mm from the center of the BLA to the cavity iris. Mechanical constraints determine these two extreme values for the studied cavity. They correspond to the incremental axial displacements from the center of the BLA to the cavity iris, $dz_{\mathrm{BLA},i} = 0$ mm and $dz_{\mathrm{BLA},i} = 100$ mm in Figure 5.9 (b), respectively. Positioning the BLA at 290.66 mm from the cavity iris results in a BLA quality factor at FM of $Q_{\mathrm{BLA},0} = 5.04 \times 10^{10}$ and, consequently, in a power dissipated in the absorber by the FM of $P_{\mathrm{BLA},0} = 8.04$ W.

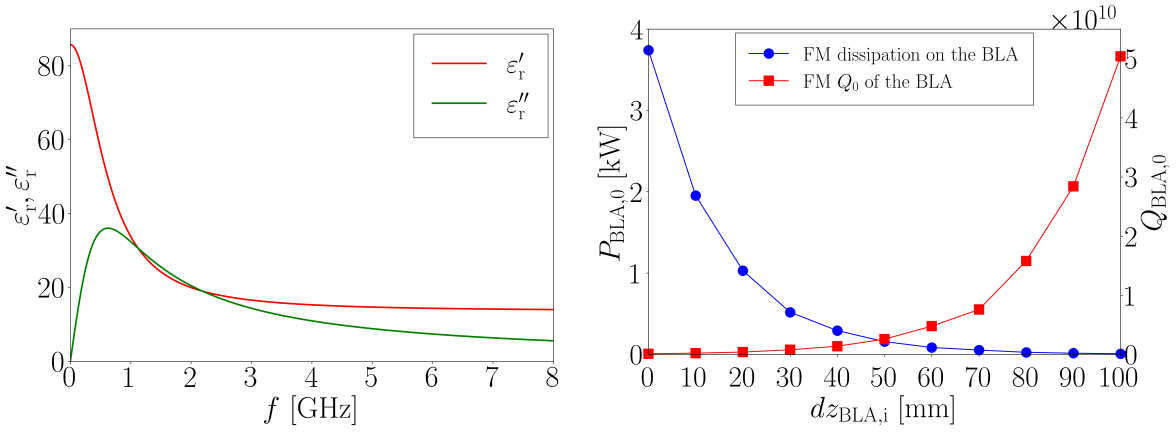

(a) Dielectric relaxation curves

(b) Dissipated power and Q for the BLA

Figure 5.9: Relaxation curves of CERASIC-B based on the Debye model (a). BLA's quality factor at FM and dissipated power on the absorber by the FM with the incremental axial displacement from the center of the BLA to the cavity iris (b).

Subsequently, wakefield simulations were performed on the 5-cell cavity to estimate the HOM power absorbed by the BLAs in the two studied cavity endgroups (2P2H and 4DQW). The total beam-induced HOM power up to 39 GHz is approximately 141.09 W for the 2P2H endgroup and 107.7 W for the 4DQW endgroup. The HOM

power dissipated in the BLAs can be estimated using the following formula [172]

$$P_{\mathrm{BLA,HOM}} \approx P_{\mathrm{wake,HOM}} - P_{\mathrm{ports,HOM}}, \tag{5.31}$$

where $P_{\mathrm{wake,HOM}}$ is the beam-induced HOM power calculated from the wake impedance and $P_{\mathrm{ports,HOM}}$ is the HOM power going out from the cavity through the coupler and beam pipe ports. BLAs at the cavity beam tubes increased the generated HOM power by approximately 9.3% in both the 2P2H and 4DQW damping schemes. Table 5.4 reports the total HOM power propagating through the coaxial couplers, BLAs, and beam pipe ports for the two analyzed damping scenarios.

Table 5.4: HOM power propagating through couplers, BLAs, and beam pipe ports in two different analyzed HOM damping schemes shown in Figure 5.8. The power is calculated using the beam spectrum shown in Figure 5.2 (a). P_{l}, P_{m}, P_{h} are the HOM power extracted in the low-frequency, medium-frequency, and high-frequency regions, respectively. P_{tot} is the total HOM power for the whole spectrum. $P_{\mathrm{P},(i)}$, $P_{\mathrm{H},(i)}$, $P_{\mathrm{D},(i)}$, $P_{\mathrm{FPC},(i)}$, $P_{\mathrm{bp},(i)}$, and $P_{\mathrm{BLA},(i)}$ represent the HOM power extracted from the probe-type, hook-type and DQW couplers, the FPC, beam pipes at their corresponding port i, and from the ith BLA up to 39 GHz, respectively. The indexes correspond to the convention used in Figure 5.8. The HOM power is computed from wakefield simulations in CST with a simulated wake length of 100 m.

Five-cell cavity at 801.58 MHz - 2P2H damping scheme with BLAs										
	P_{tot}	$P_{\mathrm{P},(1)}$	$P_{\mathrm{H},(2)}$	$P_{\mathrm{P},(3)}$	$P_{\mathrm{H},(4)}$	$P_{\mathrm{FPC},(5)}$	$P_{\mathrm{bp},(6)}$	$P_{\mathrm{bp},(7)}$	$P_{\mathrm{BLA},(8)}$	$P_{\mathrm{BLA},(9)}$
[W]	141.09	1.47	0.93	1.58	0.31	18.83	23.74	46.65	16.05	31.53
[%]		1.04	0.66	1.12	0.22	13.35	16.83	33.06	11.37	22.35
Five-cell cavity at 801.58 MHz - 4DQW damping scheme with BLAs										
	P_{tot}	$P_{\mathrm{D},(1)}$	$P_{\mathrm{D},(2)}$	$P_{\mathrm{D},(3)}$	$P_{\mathrm{D},(4)}$	$P_{\mathrm{FPC},(5)}$	$P_{\mathrm{bp},(6)}$	$P_{\mathrm{bp},(7)}$	$P_{\mathrm{BLA},(8)}$	$P_{\mathrm{BLA},(9)}$
[W]	107.7	2.43	2.43	2.62	2.62	17.10	22.65	32.99	10.12	14.74
[%]		2.25	2.25	2.43	2.43	15.88	21.03	30.64	9.40	13.69

In the 2P2H damping scheme, the BLAs absorb slightly more power than in the 4DQW scheme. The inclusions of BLAs in the 2P2H damping scenario reduced the power going through the upstream beam pipe by 49.8% (port 6), while the power flowing through the downstream beam pipe by 28.3% (port 7). In the 4DQW damping scenario with BLAs, reductions of 34.3% and 27.3% were observed for the upstream and downstream beam pipes with respect to the same HOM-coupler damping scheme without BLAs, respectively. Furthermore, HOM couplers and FPC extract a few percent more HOM power in the scenarios with BLAs.

The evaluation of the total RF power absorbed by a single BLA also depends on its position in the cryomodule. Positioning a BLA between two cavities provides better HOM damping but involves several engineering constraints related to space and He

cooling for power extraction [21]. Conversely, placing BLAs at the ends of the cryomodule allows for increasing their distance from the cavity iris with fewer mechanical restrictions. In this case, the extraction of HOM power is done at warm temperatures using water cooling channels. Considering that the total expected absorbed power per BLA is lower than 200 W, a possible technical choice could involve installing a BLA in the cryomodule between two adjacent cavities. Figure 5.10 illustrates the integration of a BLA within the cavity cryomodule. A similar option has been chosen for Cornell's ERL main linac for similar HOM power levels [108] (see Section 4.1.3).

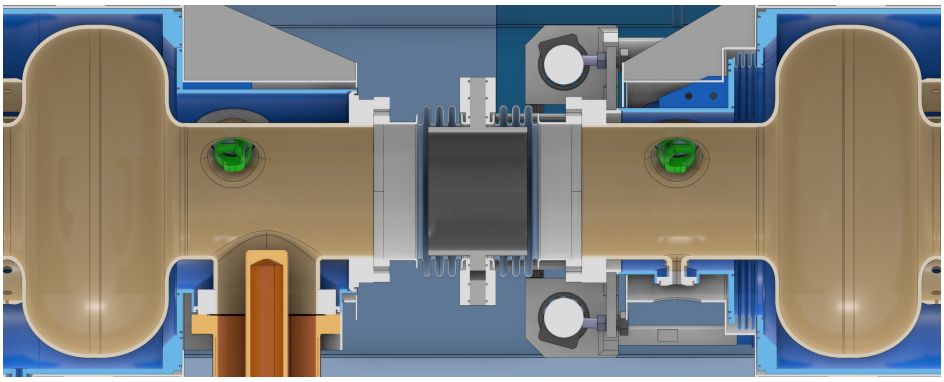

Figure 5.10: Cross-section detail illustrating the integration of a BLA placed between two adjacent 5-cell PERLE cavities (only cavity end-cells are shown) with the cryomodule [165].

In this scenario, the BLA absorbs HOM power from both cavities. Let the BLA on the upstream cavity section be the one shared between two adjacent cavities. Cavity 1 and cavity 2 are the cavities on the left side and right side of the BLA, respectively (see Figure 5.10). Assuming that the HOM endgroups of the two adjacent cavities have similar power absorption characteristics, the HOM power absorbed by the common BLA could be approximated by employing a superposition approach as

$$P_{\mathrm{BLA,HOM}} \approx P_{\mathrm{BLA,(8)}} + P_{\mathrm{BLA,(9)}} + P_{\mathrm{bp,(6)}} + P_{\mathrm{bp,(7)}}. \tag{5.32}$$

Here, $P_{\mathrm{BLA,(8)}}$ represents the HOM power absorbed by the BLA in the upstream section of cavity 1, and $P_{\mathrm{bp,(6)}}$ the traveling power from cavity 1 which leaks from the BLA and is re-absorbed by the BLA once reflected back from the adjacent cavity. Similarly, $P_{\mathrm{BLA,(9)}}$ is the HOM power absorbed by the BLA in the downstream section of cavity 2, and $P_{\mathrm{bp,(7)}}$ the power leaking from cavity 2 which is absorbed once reflected by the BLA. The HOM power absorbed by the BLA is approximately 117.97 W and 80.5 W for the 2P2H and 4DQW scenarios, respectively. In addition, the BLA absorbs the FM power contribution $P_{\mathrm{BLA,0}} = 8.04$ W from each cavity. Therefore, the total RF power dissipated on the common BLA is approximately $P_{\mathrm{BLA,tot}} = 134.05$ W for the 2P2H scheme and $P_{\mathrm{BLA,tot}} = 96.58$ W for the 4DQW scheme, resulting in a power flux of 3.28×10^{-3} W/mm^2 and 2.36×10^{-3} W/mm^2 for the considered BLA, respectively. Recent high-power tests on water-cooled SiC beamline HOM absorbers [171] found a

power flux of up to 0.44 W/mm^2 to be tolerable. The obtained power flux values are lower than this benchmark value, which is currently considered a design guideline for future BLAs. The potential choice to install a BLA between the cavities will require comprehensive thermal studies on the BLAs in the future, which exceeds the scope of this thesis. These would include modeling the cooling of the BLA using a 40 K or 80 K forced Helium stream flowing within cooling channels. Additionally, they would necessitate the design of 5 K intercept stations and a bellow to guarantee a connection between either 40 K and 5 K or 80 K and 5 K temperature, as depicted in Figure 4.5.

5.4 RF-heating analyses on coaxial HOM coupler

In the context of accelerators employing HOM-damped SRF cavities, evaluating the peak temperature of the operating HOM couplers is a crucial aspect [173]. In CW particle accelerators, like high-current ERLs, the power deposition associated with the beam-excited HOMs is a major concern compared to pulsed machines [174]. The beam-induced wakefields absorbed by the HOM couplers result in power deposition on the coupler surfaces, necessitating the implementation of cooling techniques to ensure the couplers remain superconducting. If the coupler experiences a quench, the dissipated power on its surfaces can increase by several orders of magnitude, potentially damaging and melting coupler parts. The thermal quench can occur in the high-magnetic field area of the coupler. It may expand to the cavity endgroups if efficient cooling measures are not implemented, posing a risk of a loss of the cavity superconducting state.

Aside from the heat transferred to the helium bath at 2 K, two different heat sources contribute to the RF-heating of a HOM coupler [96]:

(i) Dynamic heat load by surface currents on the coupler surface. The power deposition on its surface occurs due to the absorption of EM fields of the modes extracted from the cavity.

(ii) Static heat load by thermal conduction through the coaxial cable used to transmit the extracted HOM power to a load outside the cryomodule.

In the following subsections, the fundamental heat transfer equations, as applied to the specific thermal behavior of SRF cavities and HOM couplers, are briefly introduced. Subsequently, the dynamic thermal load is analyzed for the 2P2H and 4DQW damping schemes, presented in Section 5.3. The coupled RF-thermal simulations were conducted in COMSOL Multiphysics® [175]. Furthermore, different cooling solutions are investigated to ensure the stable superconducting state of the HOM couplers during the PERLE ERL operation. The evaluation of the static heat load would necessitate further engineering studies to incorporate several thermal intercepts to the outer conductor to mitigate the total thermal load on the couplers. Therefore, the static heat load study is not addressed as it falls outside the scope of this thesis.

5.4.1 Heat transfer in cavities and couplers

The temperature distribution inside solid structures, such as the cavity walls or the surfaces of an HOM coupler, is governed by the heat conduction equation according to [176]

$$\nabla \cdot (\kappa \nabla T) + Q_v = \varrho c_p \frac{\partial T}{\partial t} \text{ on } \mathbf{\Omega}_\mathrm{s}, \tag{5.33}$$

where κ, ϱ, and c_p are the material thermal conductivity, the volumetric mass density, and the specific heat capacity at constant pressure, respectively. The term Q_v represents a volumetric heat source. The heat equation is solved within the solid domain $\mathbf{\Omega}_\mathrm{s}$. Considering temperature-dependent material properties leads to the nonlinearity of the heat conduction equation. The thermal conductivity κ also varies with the purity of the material, which is described by the Residual Resistance Ratio (RRR) (refer to Subsection 1.3.6). The thermal analyses presented in this section consider temperature-dependent material properties. Furthermore, they refer to the stationary case where the right-hand side of the equation (5.33) vanishes.

In the study of heat conduction, the boundary conditions play a fundamental role in determining the thermal behavior within a given domain. The inner surfaces of the cavity and HOM couplers exposed to the EM fields receive a net heat flux, which is described by the following Robin boundary condition

$$\mathbf{n} \cdot (\kappa \nabla T) = \frac{1}{2} \Re\{\underline{Z}_\mathrm{s}\} \underline{\mathbf{H}} \cdot \underline{\mathbf{H}}^* \text{ on } \partial\mathbf{\Omega}_\mathrm{s} \cap \partial\mathbf{\Omega}_\mathrm{v}, \tag{5.34}$$

where $\underline{Z}_\mathrm{s}$ represents the frequency-dependent surface impedance, and $\underline{\mathbf{H}}^*$ the complex conjugate of the magnetic field strength [177]. Equation (5.34) is applied on $\partial\mathbf{\Omega}_\mathrm{s} \cap \partial\mathbf{\Omega}_\mathrm{v}$, which represents to the common boundary between the vacuum filled domain $\mathbf{\Omega}_\mathrm{v}$ and the surrounding solid domain $\mathbf{\Omega}_\mathrm{s}$.

In the context of the SRF cavities, the surfaces of the solid domain $\mathbf{\Omega}_\mathrm{s}$ in contact with the 2 K He bath, such as the exterior surfaces of the cavity, can be described by the following Dirichlet boundary condition

$$T = T_\mathrm{bath} \text{ on } \partial\mathbf{\Omega}_\mathrm{s} \setminus \partial\mathbf{\Omega}_\mathrm{v}, \tag{5.35}$$

where T_bath represents the prescribed bath temperature. Generally, the heat transfer to the exterior surfaces of $\mathbf{\Omega}_\mathrm{s}$ can be also described by the following condition

$$\mathbf{n} \cdot (\kappa \nabla T) = h_\mathrm{Kap}(T - T_\mathrm{bath}) \text{ on } \partial\mathbf{\Omega}_\mathrm{s} \setminus \partial\mathbf{\Omega}_\mathrm{v}, \tag{5.36}$$

where $\mathbf{n}$ is the outward unit normal vector to the considered surface. The term h_Kap represents the temperature-dependent Kapitza conductance, measured and described in [178, 179]. The Kapitza conductance can be used to approximate the convection heat transfer from Nb to superfluid or liquid He. The additional heat transfer contribution

due to radiation, denoted as $\mathbf{q}_{\mathrm{rad}}$, satisfies the following condition [176]

$$\mathbf{n} \cdot \mathbf{q}_{\mathrm{rad}} = \epsilon \sigma_{\mathrm{SB}} (T^4 - T_{\mathrm{bath}}^4) \text{ on } \partial\mathbf{\Omega}_{\mathrm{s}} \setminus \partial\mathbf{\Omega}_{\mathrm{v}}, \tag{5.37}$$

where $\sigma_{\mathrm{SB}} = 5.67 \times 10^{-8}$ W/(m$^2 \cdot$ K^4) is the Stefan–Boltzmann constant and ϵ is the total hemispherical emissivity of the surface. It is worth emphasizing that the impact of heat radiation on the thermal behavior of SRF cavities and HOM couplers remains marginal compared to the net heat flux given in the equation (5.34) [180]. Therefore, it is not considered in this analysis.

5.4.2 Dynamic heat load on the HOM coupler

The dynamic heat load on the HOM coupler surfaces depends on the FM of the cavity and the excitation of cavity HOMs by the circulating beam [96]. The mode excitation is unavoidably linked to the resulting HOM power [181]. If the frequency of a HOM is close to a beam resonance spectral line, i.e., a beam resonant frequency, the beam-induced voltage can be significant (refer to Subsection 2.2.2). The voltage rise, in turn, can lead to a large HOM power that needs to be extracted through the HOM couplers. This causes a significant RF-heating effect on their surfaces. Typically, the FM dominates the total dissipated power [96]. The power deposition due to the HOMs is primarily dominated by TM monopole modes, as dipole, quadrupole, and modes of higher order exhibit lower induced voltage along the axis [181].

Eigenmode simulations have been initially performed using COMSOL Multiphysics to determine the surface currents on the cavity and HOM coupler surfaces related to the FM and the relevant HOMs. The surface current associated with a cavity mode n can be defined as [96]

$$I_{\mathrm{s},n}^2 = \oiint_{\partial\mathbf{\Omega}_{\mathrm{c}}} \underline{\mathbf{H}}_n \cdot \underline{\mathbf{H}}_n^* \, \mathrm{d}A, \tag{5.38}$$

where $\underline{\mathbf{H}}_n^*$ is the complex conjugate of the magnetic field strength of the mode n, and $\partial\mathbf{\Omega}_{\mathrm{c}}$ can be either the cavity wall or the surface of the HOM coupler, including the inner conductor (IC) and the outer conductor (OC). In the equation (5.38), the $n = 0$ corresponds to the FM, while indexes $n > 0$ refer to higher order modes.

Considering the modal surface current according to the equation (5.38) and the frequency dependence of the surface resistance, the total dissipated power density on the superconducting cavity and coupler surfaces due to the ensemble of modes N can be approximated as [96]

$$\frac{\partial}{\partial A} P_{\mathrm{ds}} \approx \frac{R_{\mathrm{s},0}(T)}{2} \sum_{n=0}^{N} \left(\frac{\omega_n}{\omega_0} \right)^2 \underline{\mathbf{H}}_n \cdot \underline{\mathbf{H}}_n^*, \tag{5.39}$$

where $R_{\mathrm{s},0}(T)$ denotes the temperature-dependent surface resistance at FM frequency.

For HOM couplers made of superconducting material, the surface resistance is composed of the R_{BCS} and the residual resistance R_{res} terms, as given by the equation (1.86). The cavity and HOM couplers are assumed to be made out of Nb with RRR = 300. The R_{BCS} resistance of Nb, illustrated in Figure 5.11 (a), is computed up to its critical temperature (T_{c} = 9.2 K) using the code written by Halbritter [182]. The residual resistance of well-prepared Nb surfaces can vary between 10 nΩ and 20 nΩ [17, p. 75]. The record values for the Nb residual resistance are near 1-2 nΩ [183, 184]. A residual resistance of 3.19 nΩ, measured by F. Marhauser *et al.* [58] for the Nb sheets used for manufacturing the 801.58 MHz cavity presented in Figure 2.3, is assumed for the cavity walls. The analyzed Nb HOM couplers are expected to be manufactured using the Selective Laser Melting technique [127]. The porosity level characterizing the 3D-printed surfaces before any surface treatment (refer to Section 6.3) may degrade their surface resistance. Therefore, the HOM coupler surfaces assume a conservative value of R_{res} = 60 nΩ. The Nb thermal conductivity measured by B. Aune [185], shown in Figure (b), is considered for the thermal analysis.

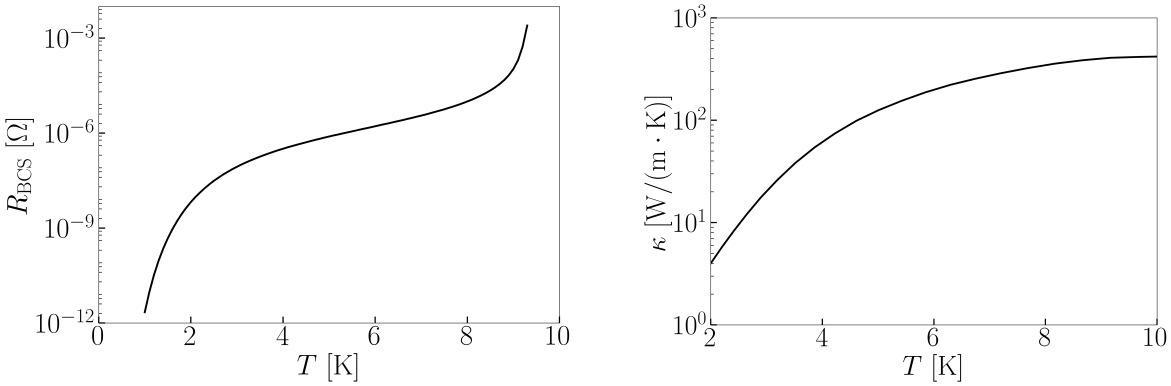

(a) R_{BCS} resistance of Nb

(b) Thermal conductivity of Nb

Figure 5.11: R_{BCS} resistance of Nb with RRR = 300 at 800 MHz as a function of temperature (a). The surface resistance was computed using the Halbritter code up to the critical temperature T_{c} = 9.2 K of Nb. Thermal conductivity of Nb as a function of temperature (b).

Equation (5.39) represents the thermal load for the cavity and HOM coupler surfaces, which is determined by the power deposition due to the presence of EM fields and the temperature-dependent non-zero surface resistance. The numerical model also considers the heat generated by the power absorbed by a ceramic RF window on the coupler feedthrough. This window acts as a vacuum barrier in the coaxial HOM couplers [121]. The total power absorbed by the ceramic window per unit volume due to the ensemble of modes N can be written as [186, p. 52]

$$\frac{\partial}{\partial V} P_{\mathrm{cer}} \approx \frac{\varepsilon_0}{2} \sum_{n=0}^{N} \omega_n \varepsilon_{\mathrm{r}}(\omega_n) \tan \delta_{\mathrm{e}}(\omega_n) \underline{\mathbf{E}}_n \cdot \underline{\mathbf{E}}_n^*, \tag{5.40}$$

where $\underline{\mathbf{E}}_n^*$ is the complex conjugate of the electric field strength of the mode n, and $\varepsilon_\mathrm{r}(\omega_n)$ and $\tan\delta_\mathrm{e}(\omega_n)$ are the modal frequency-dependent relative permittivity and the electric loss tangent of the ceramic window, respectively. The material used for the ceramic window is the single-crystal sapphire [187], which is typically employed in coaxial HOM couplers for high-field CW operation [21].

When evaluating the power deposition on the cavity and coupler surfaces, via the equation (5.39), and the power absorbed by the ceramic window, given by the equation (5.40), it is crucial to choose the appropriate scaling factor to apply to FM and HOM electromagnetic fields. The FM is scaled for the nominal cavity accelerating gradient. When scaling the EM fields of HOMs excited by a bunch, the relationship between their decay time and the arrival time of the next bunch into the cavity should be considered. The time constant τ_n (see the equation (5.8)) of the damped cavity HOMs in the 2P2H and 4DQW damping scheme is in the order of tens of µs to tens of ns. These HOM decay times are much longer than the shortest bunch spacing in the multi-turn PERLE filling pattern. Specifically, the minimum bunch spacing is 3.12 ns between bunch no. 5 and bunch no. 3 (see Figure 3.8). Therefore, the beam-induced voltage in each HOM reaches the equilibrium state for a finite HOM coupling, regardless of the beam peak current value associated with the considered HOM frequency.

For the estimation of HOM power deposition on the cavity and HOM coupler parts, it can be assumed that all HOMs voltages have reached equilibrium states at their loaded-quality factors $Q_{\mathrm{L},n}$ and for a given average beam current $I_{\mathrm{b},0}$. Consequently, the electric and magnetic field strengths of each HOM can be scaled with the time-average beam current, which continuously interacts with all the excited HOMs. This implies that, for each HOM, the cavity sees all bunches as an averaged beam current throughout the interaction. Considering this assumption, the magnetic and electric field strengths of a monopole HOM n, with $1 \leq n \leq N$, could be multiplied in equations (5.39) and (5.40), respectively, by the scaling factor $\xi_{V,n}^{(\mathrm{Mon})}$, which can be approximated as follows

$$\xi_{V,n}^{(\mathrm{Mon})} \approx \frac{(R/Q)_{\parallel,n} Q_{\mathrm{L},n} I_{\mathrm{b},0}}{\left|\underline{V}_{\parallel,n}\right|}, \tag{5.41}$$

where the numerator represents the beam-induced HOM voltage and $\left|\underline{V}_{\parallel,n}\right|$ denotes the magnitude of the longitudinal voltage of the nth HOM. Similarly, using the Panofsky-Wenzel theorem [35], the EM fields of dipole HOMs can be multiplied by the scaling factor $\xi_{V,n}^{(\mathrm{Dip})}$, given by

$$\xi_{V,n}^{(\mathrm{Dip})} \approx \frac{k_n r_\mathrm{p} (R/Q)_{\perp,n} Q_{\mathrm{L},n} I_{\mathrm{b},0}}{\left|\underline{\mathbf{V}}_{\perp,n}\right|}, \tag{5.42}$$

where r_p represents the beam offset from the cavity axis in the predominant mode polarization and $\left|\underline{\mathbf{V}}_{\perp,n}\right|$ denotes the magnitude of the transverse voltage vector of the mode n. In the following study, the first two monopole passbands (TM_{011} and

TM_{020}) and the first three dipole passbands (TE_{111}, TM_{110} and TM_{111}) are considered. These modes are trapped within the cavity and exhibit the highest levels of impedance. The scaling factors given by the equations (5.41) and (5.42) are used to scale their electric and magnetic fields when evaluating the associated surface currents and power deposition on the coupler parts, if not differently stated.

5.4.2.1 Electric and magnetic fields

The peak surface electric and magnetic fields on the cavity walls, calculated using COMSOL, are around 51.5 MV/m and 97.3 mT, respectively. Figures 5.12 (a) and (b) illustrate the magnetic field strength maps of the FM on the IC surface of probe-type, hook-type couplers and DQW PERLE couplers positioned on the FPC side of 2P2H and 4DQW damping schemes of the 5-cell 801.58 MHz cavity, respectively.

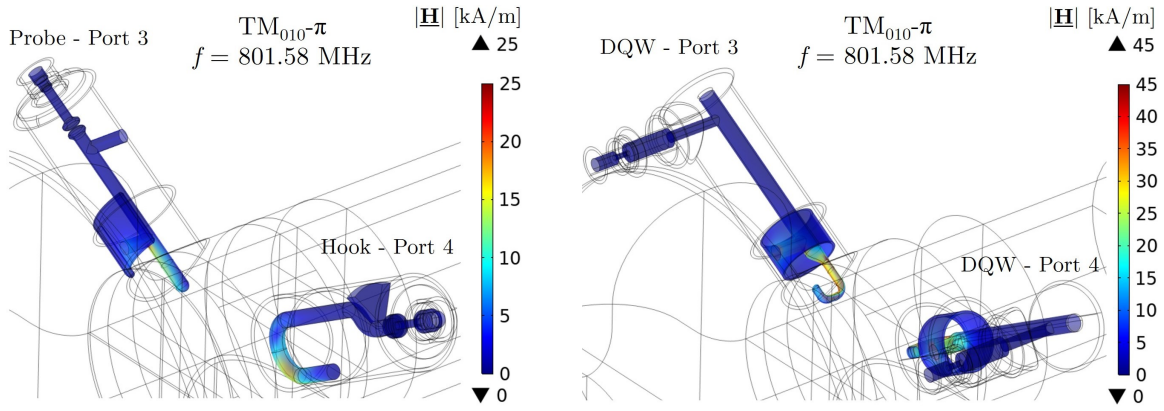

(a) Probe-type and hook-type couplers **(b)** DQW couplers

Figure 5.12: Magnetic field strength of the FM (f_0 = 801.58 MHz) on the IC surface of probe-type and hook-type PERLE couplers (a) and DQW couplers (b) calculated using COMSOL. The couplers shown in (a) and (b) are positioned on the FPC side of the 5-cell PERLE cavity and belong to the 2P2H and 4DQW damping schemes, respectively. Fields are scaled for the cavity nominal accelerating gradient of 22.4 MV/m.

The FM magnetic field is primarily concentrated in the three types of couplers at the lower part of their inner conductor penetrating into the cutoff beam pipe. The penetration depth of the pick-up antenna into the cavity beam pipe is set at 20 mm for all the studied couplers. The peak values of the electric field strength, magnetic field flux density, and surface current at FM frequency on the coupler surfaces are depicted in Table 5.5. These values are calculated for the cavity nominal gradient of 22.4 MV/m. The same table reports the peak values of the electric field strength on the ceramic window surfaces. Moreover, the calculated external quality factor at each port is indicated. For the same type of coupler, a higher quality factor denotes a lower rate of EM absorption, and vice versa. For the same penetration depth of the pick-up antenna, a coupler closer to the cavity iris will exhibit a lower external quality factor.

The probe-type and hook-type designs reveal comparable surface current values, ranging from 226.8 A to 326.4 A. The DQW couplers exhibit a significantly higher surface current, approximately 2.7 times greater than the other two coupler designs. This is due to the higher magnetic field absorbed by the DQW coupler surfaces. It is worth noting that the peak magnetic field on the DQW pick-up loop antenna, which faces the cavity iris, is roughly a factor of two lower than the peak magnetic field on the cavity surface. Therefore, employing cooling channels for the DQW coupler is strongly recommended to avoid the possibility of a quench due to the high magnetic field on its inner conductor (see Subsection 5.4.2.2). The electric field of FM on ceramic windows is significantly smaller compared to that seen by the HOM coupler surfaces. The maximum EM field and surface current values are higher for the HOM couplers on the FPC side (ports 3 and 4) as they are positioned closer to the cavity iris than the couplers on the opposite cavity side. Therefore, our analysis will be mainly focused on the HOM couplers on the FPC side since they are more heavily loaded.

Table 5.5: Peak values of the electric field, magnetic field, and surface current at FM frequency on the HOM couplers' IC and OC surfaces in the two analyzed damping schemes: 2P2H and 4DQW. The electric field strength magnitude for the ceramic window is also reported. The same port number convention used in Figure 5.3 is employed. Furthermore, the external quality factor for each coupler port is depicted.

2P2H damping scheme									
			Inner conductor			Outer conductor			Ceramic
Coupler	Port i	Q_{ext} [1]	$\lvert\underline{\mathbf{E}}_0\rvert$ [MV/m]	$\lvert\underline{\mathbf{B}}_0\rvert$ [mT]	$I_{\text{s},0}$ [A]	$\lvert\underline{\mathbf{E}}_0\rvert$ [MV/m]	$\lvert\underline{\mathbf{B}}_0\rvert$ [mT]	$I_{\text{s},0}$ [A]	$\lvert\underline{\mathbf{E}}_0\rvert$ [MV/m]
Probe	1	7.5×10^{9}	20.1	23.7	226.8	5.1	8.8	111.7	3.9×10^{-3}
Hook	2	9.6×10^{11}	14.7	15.8	240.9	12.0	15.5	168.9	2.8×10^{-3}
Probe	3	3.9×10^{9}	25.7	31.3	308.4	7.4	12.8	152.3	2.8×10^{-2}
Hook	4	2.8×10^{11}	21.7	22.5	326.4	16.2	21.2	228.8	2.0×10^{-2}
4DQW damping scheme									
			Inner conductor			Outer conductor			Ceramic
Coupler	Port i	Q_{ext} [1]	$\lvert\underline{\mathbf{E}}_0\rvert$ [MV/m]	$\lvert\underline{\mathbf{B}}_0\rvert$ [mT]	$I_{\text{s},0}$ [A]	$\lvert\underline{\mathbf{E}}_0\rvert$ [MV/m]	$\lvert\underline{\mathbf{B}}_0\rvert$ [mT]	$I_{\text{s},0}$ [A]	$\lvert\underline{\mathbf{E}}_0\rvert$ [MV/m]
DQW	1	1.9×10^{11}	36.7	41.8	647.7	3.6	10.9	154.3	5.5×10^{-3}
DQW	2	1.9×10^{11}	31.6	41.1	647.1	3.9	10.6	154.5	5.0×10^{-3}
DQW	3	9.9×10^{10}	35.7	56.7	878.7	5.5	14.5	210.5	7.2×10^{-3}
DQW	4	9.9×10^{10}	40.6	52.7	878.6	5.2	15.4	210.6	7.4×10^{-3}

Figures 5.13 (a) and (b) illustrate the magnetic field strength map of selected high-R/Q monopole and dipole HOMs on the IC surface of the DQW coupler at port 3 on the FPC side, respectively. In these figures, the HOM magnetic fields are scaled to an extracted power of 1 W at the output port for comparison. Given this normalization,

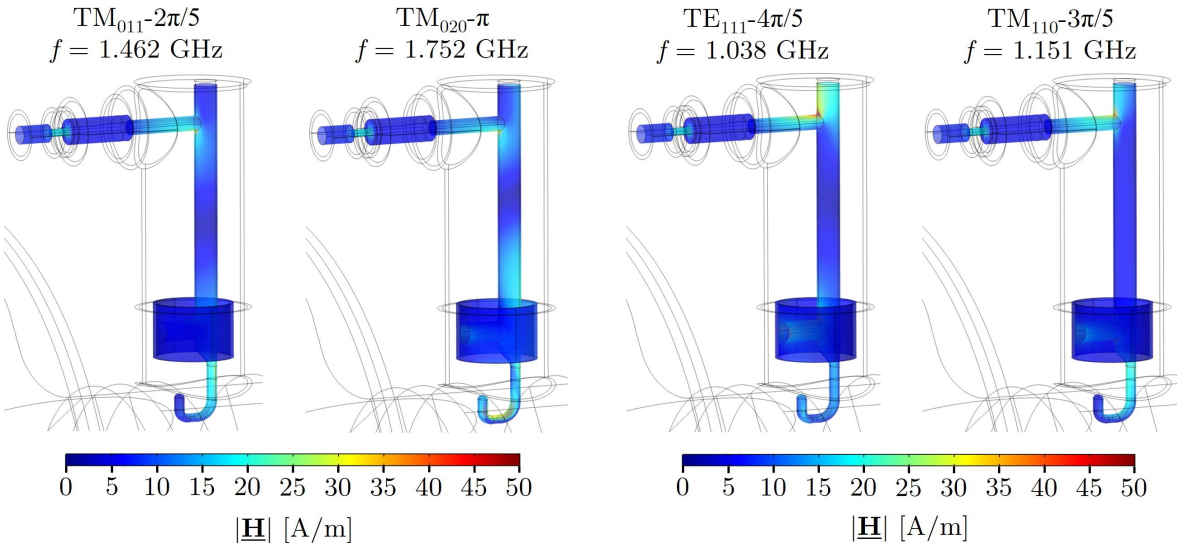

(a) Monopole HOMs **(b)** Dipole HOMs

Figure 5.13: Magnetic field strength magnitude of different high-R/Q monopole (a) and dipole (b) HOMs on the IC surface of the DQW coupler at port 3 (FPC side). Fields are scaled to an extracted power of 1 W at the output port.

the corresponding HOM magnetic field strength magnitudes on the IC are significantly lower (in the order of tens of A/m) than the surface magnetic field of the FM (in the order of tens of kA/m). Figure 5.14 (a) and (b) depict the surface currents associated with the considered monopole and dipole HOMs on the IC surface of the three analyzed coupler designs located on the FPC side, respectively.

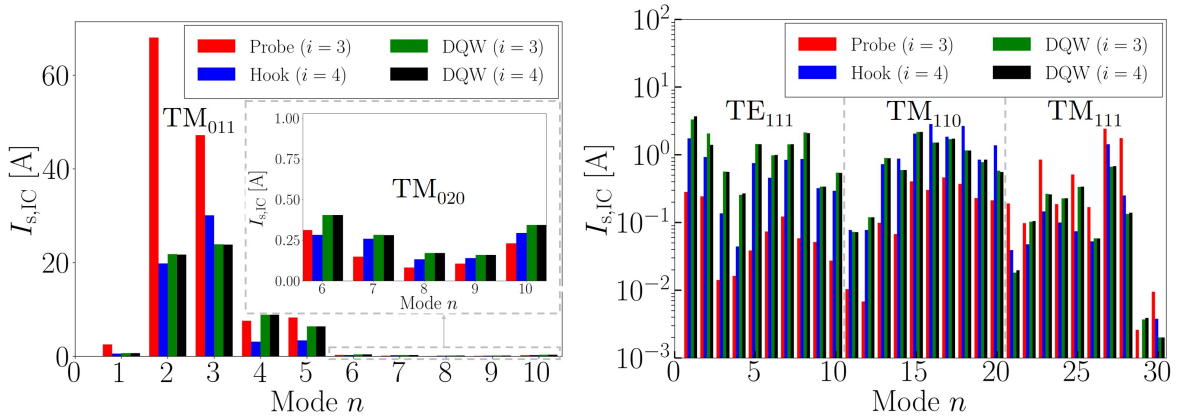

(a) Monopole HOMs **(b)** Dipole HOMs

Figure 5.14: Monopole (a) and dipole (b) surface currents for the IC of HOM couplers on the FPC side, calculated using the equation (5.38). Monopole and dipole HOM magnetic strength fields are scaled using $\xi_{V,n}^{(\mathrm{Mon})}$ and $\xi_{V,n}^{(\mathrm{Dip})}$ factors, respectively.

The HOM surface currents are calculated using the equation (5.38), where the magnetic field strengths of monopole and dipole HOMs are scaled using $\xi_{V,n}^{(\mathrm{Mon})}$ and $\xi_{V,n}^{(\mathrm{Dip})}$ factors, respectively. The surface currents of monopole HOMs span from 75 mA to 68 A for the probe and hook coupler designs and from 159 mA to 26 A for the DQW couplers. For the dipole HOMs, the surface currents range from 1 mA to 3 A for the probe and hook coupler and from 2 mA to 6 A for the DQW couplers. The calculated fields and surface currents indicate that the FM contributes the most to the RF heating on the HOM coupler surfaces. Monopole HOMs deposit more power than dipole HOMs due to their higher surface currents. Therefore, dipole HOMs are considered a second-order concern for the RF heating on the coupler surfaces.

5.4.2.2 Power deposition and maximum temperature

Based on the scaled EM fields, the heat flux provided by the equation (5.39) and the absorbed power given by the equation (5.40) constitute the total thermal load of the steady-state thermal analysis on the 5-cell cavity with the 2P2H or 4DQW HOM endgroups. Two cooling options are explored to counteract the RF overheating of the HOM coupler parts, referred to as "conduction cooling" and "convective cooling".

The conduction cooling technique consists of cooling the HOM coupler parts via direct contact between the stainless steel flange, in contact with the lower part of the HOM coupler OC, and the He-bath at 2 K. The He-vessel is extended to wrap around the HOM coupler stainless steel flange. This cooling condition is modeled by applying the equation (5.35) to the OC surfaces from the interface with the cavity up to the flange location (see Figure 5.15). The flange itself is not included in the numerical model for simplicity. Equation (5.35) is also applied to the cavity walls in contact with the He-bath, i.e., the convective heat transfer between the cavity walls and the helium is neglected. Figure 5.15 depicts the peak temperature resulting from the FM RF heating on the cavity walls and the probe-type and hook-type coupler surfaces.

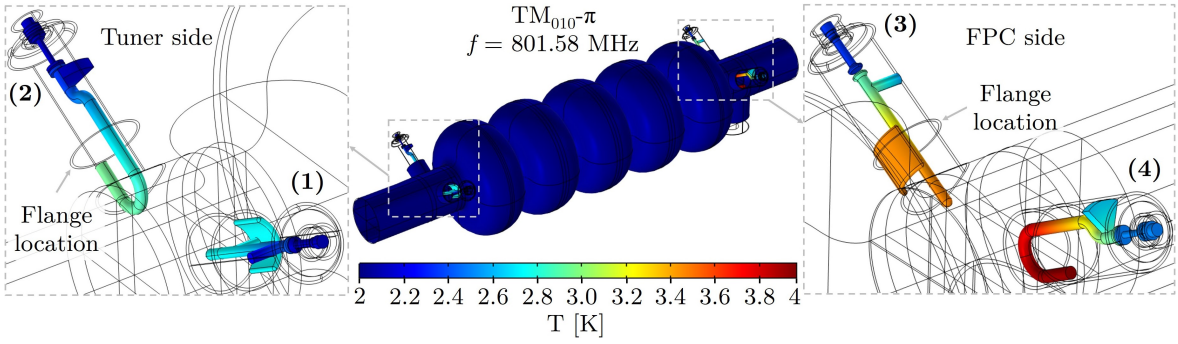

Figure 5.15: Maximum temperature resulting from the FM RF heating on the 5-cell cavity with 2P2H endgroup. The temperature maps of the inner conductors of the hook and probe HOM couplers located on the tuner and FPC sides are depicted on the left and right-hand sides of the figure, respectively. The port number for each HOM coupler is also reported.

Table 5.6 reports the dissipated power values due to FM and peak temperatures for the HOM coupler parts of the two analyzed damping schemes in the case of conduction cooling. Due to their proximity to the cavity iris, the HOM couplers on the FPC side exhibit larger power dissipation, resulting in higher temperatures. In the 2P2H damping scheme, the maximum temperature of 4 K is reached at the pick-up loop of the hook coupler located at port 4 on the FPC side (see Figure 5.15). The power absorbed by the ceramic windows at FM frequency is significantly smaller compared to the power dissipated in the HOM coupler surface. For the chosen conductive cooling technique, the DQW couplers experience a quench on the IC surfaces due to the higher absorbed magnetic field at FM frequency (see Table 5.5). The DQW couplers on the FPC side lose the superconducting state earlier than the couplers on the opposite side due to their proximity to the cavity iris.

Table 5.6: Dissipated power and peak temperature values at FM frequency on the HOM coupler parts in the 2P2H and 4DQW damping schemes in case of conduction cooling. The values for the 4DQW damping scheme refer to the last stable temperature found by the stationary solver before the couplers undergo unstable temperatures.

2P2H damping scheme							
		Inner conductor		Outer conductor		Ceramic	
Coupler	Port i	$P_{\mathrm{ds},0}$ [mW]	$T_{\max}$ [K]	$P_{\mathrm{ds},0}$ [mW]	$T_{\max}$ [K]	$P_{\mathrm{cer},0}$ [mW]	$T_{\max}$ [K]
Probe	1	2.7	2.8	0.4	2.2	2.0×10^{-1}	2.1
Hook	2	3.9	3.0	0.9	2.2	7.8×10^{-3}	2.1
Probe	3	11.2	3.5	0.8	2.3	3.8×10^{-1}	2.3
Hook	4	19.0	4.0	1.7	2.6	1.5×10^{-2}	2.5
4DQW damping scheme*							
		Inner conductor		Outer conductor		Ceramic	
Coupler	Port i	$P_{\mathrm{ds},0}$ [mW]	$T_{\max}$ [K]	$P_{\mathrm{ds},0}$ [mW]	$T_{\max}$ [K]	$P_{\mathrm{cer},0}$ [mW]	$T_{\max}$ [K]
DQW	1	130.3	5.9	0.4	4.1	3.0×10^{-3}	3.7
DQW	2	138.6	6.0	0.4	4.2	3.1×10^{-3}	3.7
DQW	3	150.2	6.1	0.4	4.3	3.3×10^{-3}	3.8
DQW	4	126.4	5.8	0.4	4.1	3.2×10^{-3}	3.7

*Values before DQW couplers undergo unstable temperatures.

Additional stationary analyses were conducted to assess the maximum stable temperature achievable in the numerical model before DQW couplers experience a quench under the described conductive cooling conditions. To ensure model convergence, the total heat load is incrementally assigned to each HOM coupler through subsequent solver iterations until the last stable temperature on each coupler is reached. Figure 5.16 (a) shows the maximum temperature on the IC surface of the DQW couplers

as a function of the ratio between the magnetic field at the kth solver iteration and the peak magnetic field on the coupler surface at FM frequency. The maximum temperature found for the DQW couplers at the last solver iteration is around 6 K. This temperature is reached for the DQW couplers on the FPC side at about 26 mT, corresponding to roughly 50% of the coupler peak magnetic field at FM frequency. Conversely, a similar temperature is reached at about 28 mT for the DQW couplers on the tuner side, corresponding to roughly 67% of their peak magnetic field. Figure 5.16 (b) depicts the maximum temperature on the IC surface of the DQW couplers as a function of the dissipated power at the kth solver iteration. The maximum dissipated power values found at the last stable temperature are about 138.6 mW and 150.2 mW for the DQW couplers on the tuner side (ports 1 and 2) and the FPC side (ports 3 and 4), respectively. The dissipated power values and peak stable temperatures for the IC, OC, and windows of the DQW couplers are reported in Table 5.6. Similar analyses were performed on the couplers of the 2P2H endgroup for comparison. The corresponding maximum temperature curves as a function of the incremental magnetic field and dissipated power at FM are reported in Figures 5.17 (a) and (b), respectively.

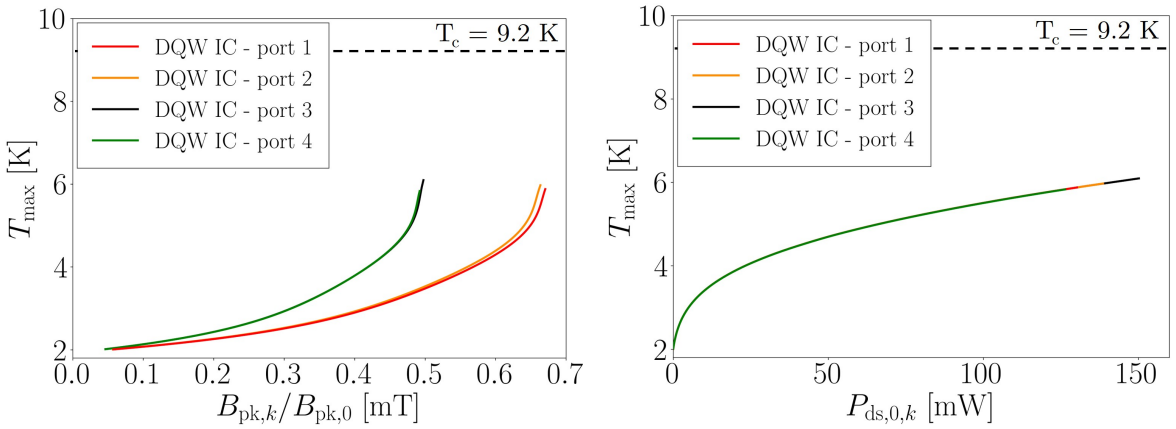

(a) Maximum T vs. Incremental FM B-field **(b)** Maximum T vs. FM dissipated power

Figure 5.16: Maximum temperature on the IC surface of the DQW couplers as a function of the incremental surface magnetic field (a) and the peak dissipated power at FM frequency (b) in the case of conduction cooling. The temperature is recorded during subsequent stationary solver iterations until the last stable temperature is found. The critical temperature $T_c = 9.2$ K of Nb is reported for reference.

The probe-type and hook-type couplers do not experience any thermal quench at the nominal field under conduction cooling. The maximum temperature of 4 K reached at the hook-type coupler at port 4 provides sufficient margin to the Nb critical temperature. Referring to the 4DQW damping schemes and Figure 5.16 (a), the temperature sharply increases at a certain B-field level. Above this limit, the stationary solver was not able to find any stable temperature above 6 K due to the strong non-linear behavior of the material properties in the explored temperature regime and the high dissipated

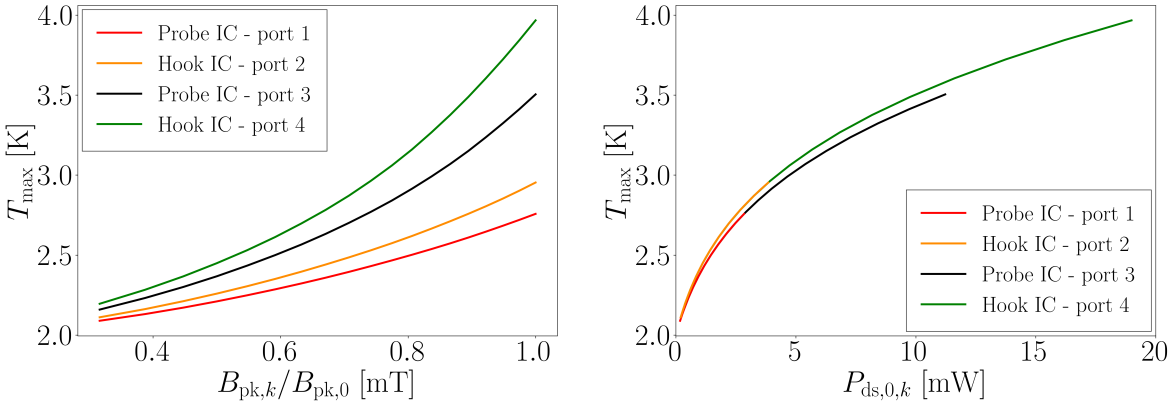

(a) Maximum T vs. Incremental FM B-field **(b)** Maximum T vs. FM dissipated power

Figure 5.17: Maximum temperature on the IC surface of the probe-type and hook-type couplers as a function of the incremental surface magnetic field (a) and the peak dissipated power at FM frequency (b) in the case of conduction cooling. The temperature is recorded during subsequent stationary solver iterations.

power on the coupler surfaces. This lack of convergence can be associated with the field at which the thermal quench is most likely to occur [188]. The RF heating due to the FM depends on the FM notch tuning and the strength of the EM field coupling to the pick-up antenna. Results from RF-heating simulations demonstrate that the probe-type and hook-type coupler designs could operate within a safety margin to quench by employing conduction cooling. The DQW PERLE couplers necessitate the use of an active cooling technique to maintain the superconducting state due to the high magnetic field on their IC surfaces. Reducing the coupler penetration into the beam pipe tube can lower the thermal load on the coupler antenna. However, this comes with the drawback of reducing the damping to the HOMs.

To counteract the RF heating from FM and excited HOMs, the rods composing the IC of the DQW PERLE coupler can be manufactured as hollow cylinders, allowing for active cooling of their Nb surfaces via liquid He. This technique has been proposed at CERN for the DQW coupler of the 400 MHz DQW cavities [189]. The coupler is equipped with its own He jacket and two cooling channels on the inner conductor: one on the central shaft and one on the top perpendicular coaxial line (refer to Figure 4.3 (a)). The loop-shaped antenna is passively cooled. An upgraded Nb 3D-printed version of the DQW coupler, currently under development at CERN, could feature an extension of the central shaft cooling channel to the pickup loop antenna, which is the part most exposed to the EM fields. In addition, another cooling channel can be manufactured for the road connecting the central shaft to the capacitive jacket [140].

A similar solution is employed for the proposed DQW PERLE coupler to avoid thermal quench. The inner conductor surfaces exposed to Helium could be modeled as cooling channels with an artificial thick layer. The layer thickness could be chosen as

1 mm, which is approximately half of the average thickness foreseen for the channels of 400 MHz DQW coupler [140]. The cooling channel surfaces are those of the central shaft, its two perpendicular roads, and the loop-shaped antenna (see Figure 5.19 (b)). However, since the Kapitza resistance occurs at the interface between the solid and the He, the convective cooling modeling is simplified by assigning the boundary condition (5.36), together with the temperature-dependent Kapitza conductance given in Figure 5.18, to the IC surfaces in contact with the Helium, without modeling the channel thickness. The Kapitza conductance fit proposed by Mittag [178], valid for $T - T_{\mathrm{bath}} < 1.4$ K with $T_{\mathrm{bath}} = 2$ K, is considered for the heat transfer between Helium and Nb surfaces as follows

$$h_{\mathrm{Kap}}(T) = 200\, T^{4.65} \left[1 + 1.5 \left(\frac{T - T_{\mathrm{bath}}}{T_{\mathrm{bath}}} \right) + \left(\frac{T - T_{\mathrm{bath}}}{T_{\mathrm{bath}}} \right)^2 + 0.25 \left(\frac{T - T_{\mathrm{bath}}}{T_{\mathrm{bath}}} \right)^3 \right]. \tag{5.43}$$

This condition also takes into account the interface resistance of the coupler walls to the He thermal flow [188].

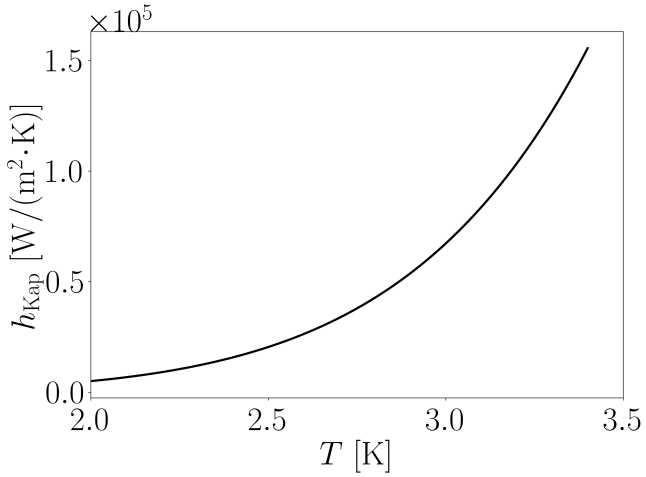

Figure 5.18: Kapitza conductance of Nb (RRR = 300) according to Mittag fit [178] used in the thermal simulations to model the heat transfer between the Nb cooling channels and He.

Figure 5.19 (a) and (b) depict the temperature maps of the DQW couplers at port 3 on the FPC side, resulting from RF-heating due to FM. These maps illustrate the conduction and additional convective cooling cases through He channels, respectively. In both cases, the outer conductor is cooled down via direct contact with the cavity He bath, allowing the outer conductor to remain at a temperature slightly higher than 2 K. The temperature of IC surfaces, which experience a thermal quench at the nominal field in the case of conduction cooling, is successfully lowered below the critical temperature of Nb when convective cooling through He channels is simulated. Specifically, the inner

conductor exhibits a maximum temperature increase of only 5.13 mK at the pick-up antenna. The peak extracted power from the He flowing into the channel is 42.1 W/m^2. The maximum temperature of 2.3 K occurs at the capacitive jacket, which is passively cooled by the He channel connecting the jacket to the central shaft. Under these conditions, the DQW coupler could safely operate with sufficient margin to prevent a thermal quench. A similar solution can also be employed for the hook-type and probe-type couplers to lower their peak temperatures, which still remain to be studied.

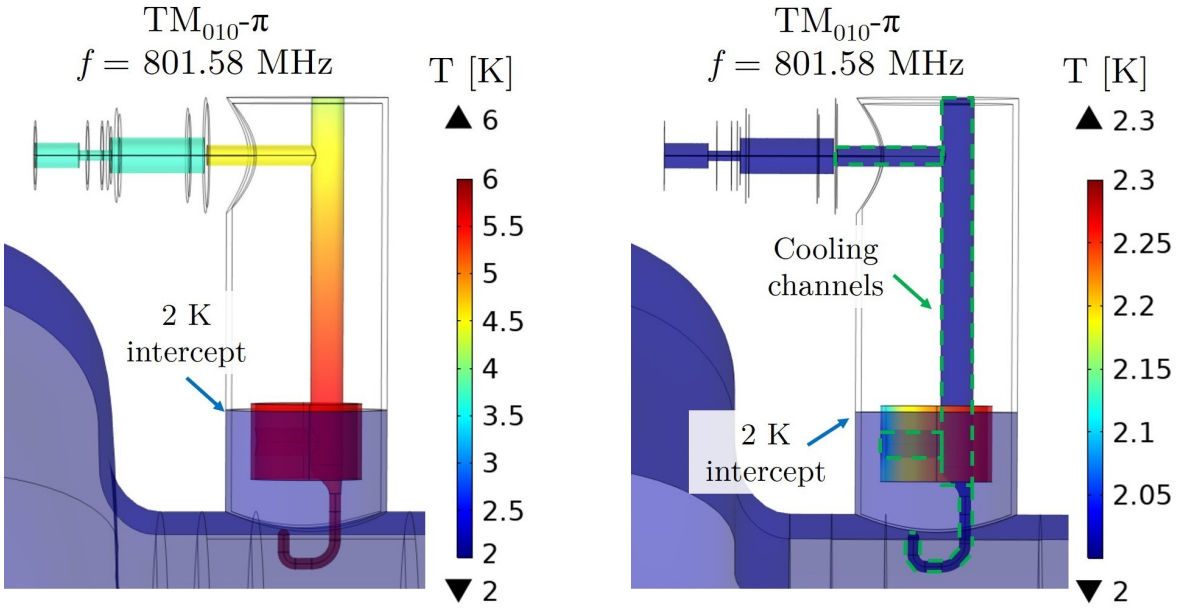

(a) DQW (port 3) - Conduction cooling

(b) DQW (port 3) - Convective cooling

Figure 5.19: Temperature map resulting from FM RF heating of the DQW coupler at the FPC side (port 3) of the 5-cell cavity. In the conduction cooling case (a), the temperature refers to the maximum stable temperature found in the simulation before the coupler undergoes quenching. Maximum temperature when adding convective cooling through IC channels (highlighted in green) (b). The 2 K intercept with the cavity He-bath is also depicted.

Finally, the impact of HOM power deposition on the peak temperature of the HOM couplers is studied. The analysis has been limited to the 2P2H damping scheme under conduction cooling conditions, as the 4DQW endgroup undergoes a thermal quench under similar cooling conditions due to the heating effect of the FM. When including convective cooling in the 4DQW damping scheme, He-cooling strongly mitigates the RF heating due to the FM, which is greater than the HOM power deposition under the assumed interaction between the passing bunch and cavity HOMs (refer to Subsection 5.4.2). Therefore, it was assumed that, under these conditions, the temperature increase due to HOMs in the 4DQW damping scheme would not be significant enough to compromise the operation of the couplers. Table 5.7 summarizes the dissipated power on IC and OC, the absorbed power on ceramic windows, and the peak tempera-

tures due to FM and trapped monopole and dipole HOMs for the couplers belonging to the 2P2H damping scheme operating under conduction cooling conditions. The total HOM power deposition on IC and OC surfaces is at least one order of magnitude lower compared to the power dissipated by the FM (see Table 5.6). However, the HOM power absorbed by the ceramic windows is higher than that due to FM, ranging from 2.7 mW to 17.1 mW. This is due to the proximity of the ceramic window to the HOM coupler output port, where HOM power is extracted. The highest temperatures are observed at the couplers on the FPC side due to their higher damping rate. The maximum temperature of 4.2 K is reached at the pick-up antenna of the probe coupler located at port 3. HOM power deposition contributes to increasing the peak temperature of the IC and OC coupler surface in a range from 78 mK to 240 mK compared to the case when only FM RF heating is considered. However, for the probe-type coupler at port 3, the peak temperature increases by 655 mK on the IC surface and 1.3 K on the OC surface. The contribution to the RF-heating from dipole modes can be neglected since the highest dipole mode deposition contribution is in the order of tens of µW.

Table 5.7: FM and HOM dissipated power on IC and OC, absorbed power on ceramic windows, and resulting peak temperatures for the 2P2H damping scheme under conduction cooling conditions.

2P2H damping scheme - FM and trapped HOMs							
		Inner conductor		Outer conductor		Ceramic	
Coupler	Port i	P_{ds} [mW]	T_{max} [K]	P_{ds} [mW]	T_{max} [K]	P_{cer} [mW]	T_{max} [K]
Probe	1	3.0	2.9	0.5	2.4	4.9	2.4
Hook	2	4.2	3.1	1.0	2.4	5.4	2.4
Probe	3	14.8	4.2	1.2	3.6	17.1	3.6
Hook	4	19.7	4.1	1.8	2.7	2.7	2.6

Under the simulated conduction cooling conditions, the 2P2H damping scheme provides sufficient FM rejection and enough damping to mitigate FM and HOM power deposition on the coupler parts and consequently lower the resulting maximum temperature below the quench limit. Due to the high rate of EM absorption, the 4DQW damping scheme requires additional convective cooling through He-channels to operate safely in the superconducting state. These findings will serve as the foundation for exploring additional phenomena, like multipacting and notch detuning during thermal contraction, in future studies concerning Nb HOM coupler design, which exceed the scope of this thesis. The impact of the heat transfer through the RF cable required for HOM power extraction still needs to be investigated. This additional heat contribution will likely dominate the thermal behavior of all HOM couplers [96]. In this case, additional thermalization at 2 K on the coupler OC and heat intercepts on the RF cable will be required to further reduce the total thermal load.

6 RF cavity fabrication

This chapter outlines the different steps of the process used for manufacturing the first OFHC (Oxygen-Free High Thermal Conductivity) Cu 5-cell 801.58 MHz cavity for the PERLE project. This cavity prototype has been fabricated at JLab for performing R&D RF bench measurements. The aim is to validate the HOM-damping performance of the two endgroups (2P2H and 4DQW) presented and simulated in Chapter 5. HOM measurements conducted on the Cu 5-cell PERLE cavity with the fabricated HOM coupler prototypes (refer to Chapter 4) are presented in Chapter 7. The deep-drawing fabrication process of elliptical cells from copper sheets is initially described. Then, the geometrical deviations of the cell shape due to the springback effect and manufacturing tolerances are addressed. Subsequently, the dumbbell measurements and the trimming procedure on cavity cells are discussed. The chapter concludes by presenting the bead-pull measurements and the study of the field flatness on the cavity assembly.

6.1 Elliptical cavity manufacturing

The fabrication of an elliptical RF cavity can be divided into three main steps [17, pp. 108-118]. The first stage involves forming material sheets into half-cells, typically called "cups", by the deep-drawing process. This phase is followed by the welding or clamping of the cups in pairs to create "dumbbells" [190]. Cavity beam pipes are fabricated by rolling metal sheets into cylindrical shapes welded at their joints. The two extreme cavity half-cells are assembled with beam pipes to form the cavity end-groups. Finally, the different components are welded or clamped into a completed cavity.

6.1.1 Deep-drawing

The deep-drawing fabrication process was used to manufacture the cavity cells [17, p. 108]. The basic stamping setup, shown in Figure 6.1, includes a set of half-cell male and female dies, a metal sheet (or "blank") clamped by a "blank holder", and one or more ejectors [191]. The metal sheet is formed through the mechanical action of the punch (male die) against the female die, applying the punch force F_{p} [192]. This force is a fundamental parameter of the entire process and is typically calculated using simulation software. During the fabrication, the blank holder anchors the metal sheet

with the clamping force F_h. Finally, the ejectors are used to facilitate the extraction of the stamped cup from the dies, applying the force F_e.

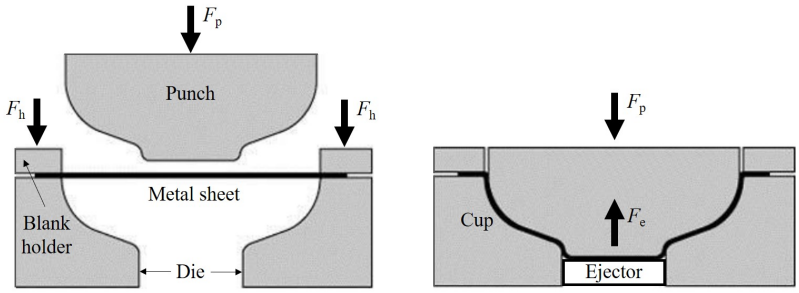

Figure 6.1: Basic scheme of half-cell deep-drawing. Figure adapted from [17, p. 108].

The production of the Cu half-cells for the 801.58 MHz PERLE cavity was performed at JLab.[1] Copper sheets, with a thickness of 4 mm, were transformed into ten half-cells using a deep-drawing process. The geometrical parameters of the produced cavity are depicted in Figure 2.4. During fabrication, a longer excess length on the equator cups than the designed one is left for subsequent frequency tuning. Before pressing Cu sheets, the stamping process can be simulated using FEM software. These simulations predict the stress and force applied to the die set, along with the final shape and thickness of the half-cells. In our case, the punch force to press the Cu blanks with the used die-set was 100 tons. This value has been typically used at JLab for stamping Nb half-cells with the same die set [193]. The stamping setup, the half-cell into the die after deep-drawing, and one of the produced Cu half-cells are shown in Figure 6.2.

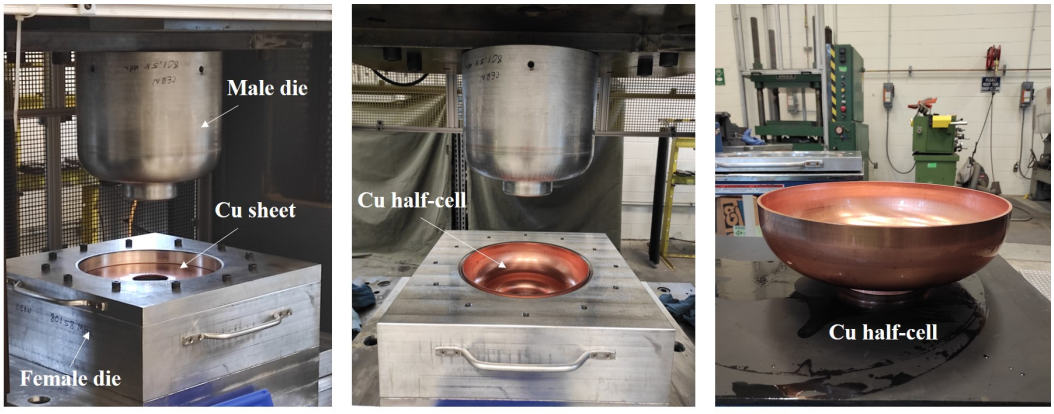

Figure 6.2: Deep-drawing of a copper half-cell. Stamping setup (a). Copper half-cell after pressing (b). Produced copper half-cell (c).

[1]The author, during one of his visits at JLab, witnessed the pressing of cavity cells by Steve Castagnola and Gregory Grose.

6.1.2 Springback effect and coining

The springback is a phenomenon that occurs after forming the material sheets into half-cells through the deep-drawing process. This effect is caused by internal stresses in the material when the dies are released after the forming process. The springback can lead to a shape deviation from the ideal cup geometry, ultimately resulting in fluctuations in the resonant frequency. Typically, the frequency change in a cavity due to springback can range from a few MHz for the FM to several MHz for the HOMs [64, 194]. This frequency variation is influenced by both the half-cell material and the precision of the fabrication process. The cell iris and equator experience the most significant springback.

To quantify the residual springback-induced geometry deviation after deep-drawing, laser scanning was performed on one of the produced Cu cups using the FARO® 8-axis edge system [195].[2] The scanned cell shape was then converted into a CAD model, shown in Figure 6.3 (a), for comparison with the actual geometry. Figure 6.3 (b) depicts the scanned half-cell shape compared to the design shape. The maximum springback at the cell iris measures approximately 2.2 mm in the radial direction, while the cell equator was pushed inward by about 0.2 mm.

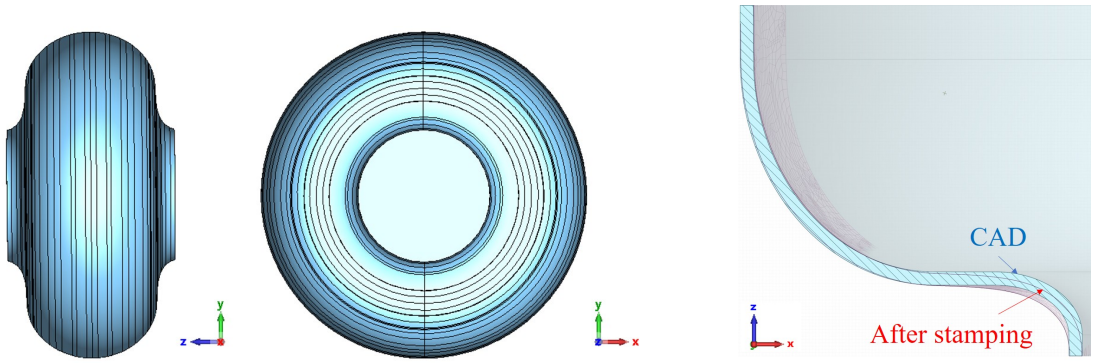

(a) 3D CAD after stamping **(b)** FARO scan

Figure 6.3: Front and side view of the 3D cell model after stamping reconstructed from the FARO scan (a). Quadrant view of the cavity cell (b). The blue line represents the CAD geometry profile, while the red line depicts the FARO scan profile of the inner cell surface after stamping [196].

The coining of the stamped half-cells is a manufacturing process aimed at correcting the shape deviation at the iris caused by the springback effect [17, p. 108]. This procedure, typically performed after deep-drawing on each half-cell, improves the cell curvature at the iris to bring it closer to the nominal geometry specified by the designed die. The coining process for the produced Cu cups required 25 tons of force [193].

[2]Eduard Drachuk at JLab carried out FARO scanning of the copper cups based on the specifications provided by the author.

Figures 6.4 (a) and (b) depict the setup used for the half-cell coining process and the resulting cavity half-cell, respectively. After the coining process, a second scan was conducted on the analyzed cup to assess the residual geometry deviation. Figure 6.5 compares the design shape of the cavity cell to the actual geometry obtained through scanning. The coining process reduced the initial deviation on the analyzed cup due to the springback by 0.5 mm in the radial direction at the iris.

(a) Half-cell coining **(b)** Half-cell after coining

Figure 6.4: Half-cell and used coining ring (a). Half-cell after the coining process (b).

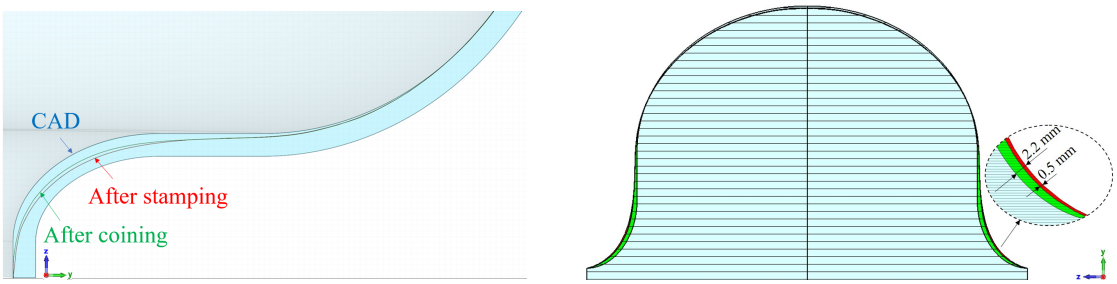

(a) FARO scan **(b)** CAD vs. Scanned geometry

Figure 6.5: Design and actual shape of the cavity half-cell (a). The blue shape represents the CAD geometry. The red line depicts the FARO scan of the inner cell surface after stamping, while the green line illustrates the scan of the same surface after coining [196]. Symmetric front view of reconstructed cavity cell with details of the cell iris (b). The red and green areas represent the springback-induced geometry deviation on the cavity cell after stamping and coining, respectively.

The reconstructed single-cell scanned geometry, shown in Figure 6.3, was used as input for eigenmode simulations performed using CST to assess the frequency shifts on the FM and trapped modes due to the springback. PEC boundary conditions are applied to the external surfaces and both ends of the simulated single-cell vacuum model. Figure 6.6 compares the frequency deviation from the ideal cell shape for

the scanned geometry after stamping (uncoined cell) and after coining (coined cell). The frequency shifts for the studied modes vary from -16.1 MHz for the TE_{111} mode to 5.5 MHz for the TM_{010} mode. The most affected TM and TE modes are those with radial (n) and longitudinal (p) indexes equal to or higher than 1. These indexes represent the predominant direction in which springback affects the cavity cells. For these modes, assessing their proximity to the harmonics of the circulating beam (refer to Subsection 7.2.3.1), as well as their frequency tolerance for the HOM damping performance, is crucial for future 801.58 MHz Nb cavity production. Simulation results show that the coining process can recover approximately 1 MHz for the TM_{010} mode and up to 3 MHz for the most impacted HOMs, such as the TE_{111} mode. Conversely, the frequency deviation slightly increases for a few modes, for example, the TM_{011} mode. Further studies are needed to determine if the springback could be further reduced by using a different coining ring to enhance the plastic deformation of the cell iris to the desired shape or by increasing the coining force. This analysis was limited to one of the produced Cu cups. In our observations, the geometric deviation between one of the scanned cups and the CAD model was approximately 0.8%. In the following, we will assume that all the other produced cups were affected by a similar amount of deformation and frequency deviations.

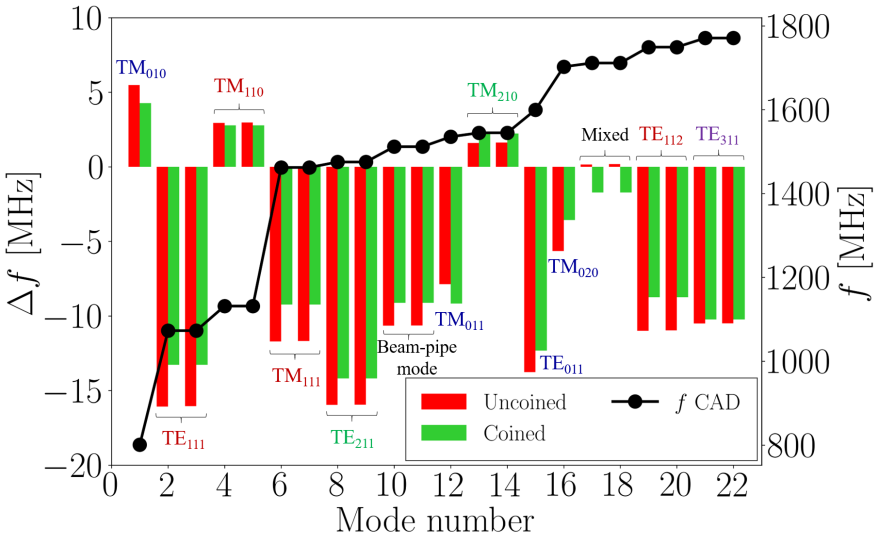

Figure 6.6: Simulated frequency deviation of resonant modes from the ideal shape of a single-cell cavity due to the springback. Monopole HOMs are indicated in blue, while dipole, quadrupole, and sextupole HOMs are depicted in red, green, and purple in the order. The red and green bars represent the frequency shifts in the uncoined and coined single-cell cavities, respectively. The black dotted line depicts the HOM frequencies of the CAD cavity model.

6.2 Dumbbell measurements

During the fabrication phases of an elliptical cavity, monitoring the frequency and field flatness of the FM is crucial. Dumbbell measurements represent a technique for controlling the FM frequency during multi-cell cavity production [197]. The half-cells are intentionally fabricated with an extra length along the equator to compensate for manufacturing errors [190]. Dumbbell measurements permit the determination of the required equator trimming for each produced cup, which allows the tuning of the cavity to the target frequency and achieving the field flatness of the accelerating mode, i.e., the TM_{010}-π mode. To obtain a flat field at the FM, the mid-cells and the end-cells with beam pipes must resonate at the same fundamental frequency [21]. The dumbbell measurements conducted at JLab on the produced cups are presented in this section.

6.2.1 Dumbbell measuring setup

After forming the half-cells, their irises are trimmed [64]. The middle-half-cells are either joined on the irises by Electron Beam Welding (EBW) or clamped together in pairs to create an assembly called middle-cell dumbbell. The end-half cells are connected to beam pipe tubes to form an end-cell dumbbell. The setup used for conducting dumbbell measurements on the produced Cu half-cells is depicted in Figure 6.7.

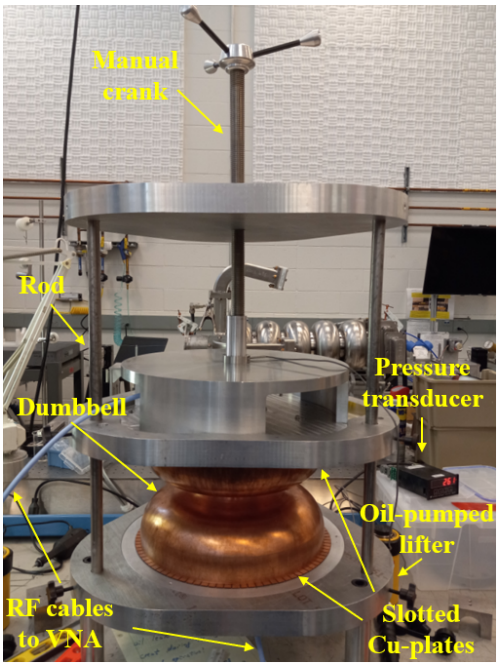

(a) Dumbbell measuring setup

(b) Middle-cell dumbbell

(c) End-cell dumbbell

Figure 6.7: Setup for dumbbell measurements. Middle-half-cell pair and measuring setup components (a). Middle-half-cell pair (b). End-half-cell and beam pipe (c) [198, 199].

Each middle-half-cell pair is sandwiched between two aluminum plates with slotted Cu plates, secured with threaded rods, and balanced with weights, creating an assembly close to a two-cell oscillator that resonates in the $\pi/2$ mode (also called "0-mode"[3]) and π mode (see Figure 6.7 (a)) [64, 197]. On the other hand, the end-cell dumbbell could be considered a half-cell resonator vibrating in the π mode only (see Figure 6.7 (b)) [190]. A manual crank exerts a force on the aluminum plates to ensure good RF contact between the dumbbell and the slotted Cu plates [64]. The applied pressure is monitored by a pressure transducer during measurements. Based on previous measurements of dumbbells performed at JLab, a pressure limit of 200 lbs is recommended for dumbbells with a loaded quality factor lower than 7×10^3 to prevent any inelastic deformation of the cups [198]. Two feedthroughs with antennas are installed in the upper and lower aluminum plates and connected to a Vector Network Analyzer (VNA) for measuring the S_{21} transmission between the two antennas. The amplitude of measured S_{21} signal is fit using a MATLAB interface [200], implemented by Mingqi Ge from JLab, connected to the VNA to determine the dumbbell frequencies and their loaded quality factors. The script allows for evaluating required equator trimming for each produced cup based on the theoretical framework described in the following.

6.2.2 Theoretical framework for dumbbell measurements

The evaluation of the lengths to be trimmed on each cup relies on the measurement of the π-mode frequency of each half cell. The formulas for calculating the individual frequencies of two coupled oscillators and used for dumbbell measurements are given by [197, 201]

$$f_{\pi,\mathrm{U}} = \sqrt{\frac{f_\pi^2 + f_{\pi/2}^2}{2} + \frac{(f_\pi^2 - f_{\pi/2}^2)(2+R)}{2\sqrt{R+4}}}, \tag{6.1}$$

$$f_{\pi,\mathrm{D}} = \sqrt{\frac{f_\pi^2 + f_{\pi/2}^2}{2} + \frac{(f_\pi^2 - f_{\pi/2}^2)(2-R)}{2\sqrt{R+4}}}, \tag{6.2}$$

with the substitution

$$R = \sqrt{\frac{f_\pi^2 - f_{\pi,\mathrm{P,U}}^2}{f_\pi^2 - f_{\pi,\mathrm{P,D}}^2}} - \sqrt{\frac{f_{\pi/2}^2 - f_{\pi/2,\mathrm{P,U}}^2}{f_{\pi/2}^2 - f_{\pi/2,\mathrm{P,D}}^2}}. \tag{6.3}$$

Here, the terms f_π and $f_{\pi/2}$ represent the π mode and $\pi/2$-mode measured frequencies of the considered dumbbell, respectively. Half-cells are identified based on their location in the dumbbell assembly, using indices "U" for the upper half-cell and "D" for the lower half-cell (see Figure 6.7). Mode frequencies measured with a perturbation tip

[3]The term 0-mode refers to the zero-phase difference between cells.

placed on the upper or lower cell side are denoted by the subscripts "P, U" and "P, D", respectively. Both equations (6.1), (6.2) and the equation (6.3) are asymmetric relative to the interchange of indices "U" and "D". Shemelin *et al.* in [190] proposed a correction to equations (6.1) and (6.2) as follows

$$f^*_{\pi,\mathrm{U}} = \sqrt{\frac{f^2_\pi + f^2_{\pi/2}}{2} + \frac{(f^2_\pi - f^2_{\pi/2})(2+R)}{2\sqrt{R^2+4}}}, \tag{6.4}$$

$$f^*_{\pi,\mathrm{D}} = \sqrt{\frac{f^2_\pi + f^2_{\pi/2}}{2} + \frac{(f^2_\pi - f^2_{\pi/2})(2-R)}{2\sqrt{R^2+4}}}. \tag{6.5}$$

Including R^2 in the denominators, equations (6.4) and (6.5) are symmetric if the sign of R in the equation (6.3) changes when the dumbbell is inverted. However, this can only occur if both right components in equation (6.3) are close to unity, which implies

$$R = \sqrt{\frac{f^2_\pi - f^2_{\pi,\mathrm{P,U}}}{f^2_\pi - f^2_{\pi,\mathrm{P,D}}}} - \sqrt{\frac{f^2_{\pi/2} - f^2_{\pi/2,\mathrm{P,U}}}{f^2_{\pi/2} - f^2_{\pi/2,\mathrm{P,D}}}} \approx (1+\tilde{\alpha}) - (1+\tilde{\beta}) = \tilde{\alpha} - \tilde{\beta}, \tag{6.6}$$

$$R' = \sqrt{\frac{f^2_\pi - f^2_{\pi,\mathrm{P,D}}}{f^2_\pi - f^2_{\pi,\mathrm{P,U}}}} - \sqrt{\frac{f^2_{\pi/2} - f^2_{\pi/2,\mathrm{P,D}}}{f^2_{\pi/2} - f^2_{\pi/2,\mathrm{P,U}}}} \approx \frac{1}{1+\tilde{\alpha}} - \frac{1}{1+\tilde{\beta}} \approx \tilde{\beta} - \tilde{\alpha} \approx -R, \tag{6.7}$$

where $\tilde{\alpha}$ and $\tilde{\beta}$ are introduced variables, defined in terms of the quantities above, used to simplify the expressions for R and R'. As a result, this condition is verified if the shift induced by the perturbation exceeds the shift caused by the additional length on the cell equator. The formula for R can thus become symmetrical using the arithmetic mean of R and $-R'$.

Using the measured π-mode frequencies obtained from the equations (6.4) and (6.5), the additional lengths to be trimmed on the equator of each upper and lower cup to achieve the desired target frequency can be calculated, respectively, as follows

$$\Delta L_{\mathrm{t,U}} = \frac{f_{\mathrm{target}} - f^*_{\pi,\mathrm{U}}}{S_{\mathrm{t}}}, \tag{6.8}$$

$$\Delta L_{\mathrm{t,D}} = \frac{f_{\mathrm{target}} - f^*_{\pi,\mathrm{D}}}{S_{\mathrm{t}}}. \tag{6.9}$$

Here, f_{target} is the target frequency of an "ideal" half-cell, and S_{t} is the trimming parameter that indicates the sensitivity of the π-mode frequency of a half-cell to the extra length on its equator. These two parameters may differ between the half-middle and

half-end cells joined with the beam pipes. The target frequencies and trimming parameters for middle-cell and end-cell dumbbells are simulated using CST, as described in the next section, and then entered into the used MATLAB interface to derive the lengths to be trimmed for each half-cell.[4]

6.2.3 Target frequency and trimming coefficient simulations

The 5-cell cavity built from the geometrical parameters shown in Figure 2.4 resonates at the "warm frequency" of 798.45 MHz. To test HOM coupler performance at room temperature (refer to Chapter 7), the cavity geometry must be tuned to the operating cold frequency of 801.58 MHz. The notch filter of HOM couplers is designed to reject the FM transmission at the same operating frequency (refer to Section 4.2). Each middle cell and endgroup (end-cell plus beam pipe) must resonate at the same frequency to achieve the cavity target frequency and obtain a flat field [21].

For this purpose, the frequency tuning of the warm frequency cavity involves a series of CST eigenmode simulations on the middle-cell and end-cell dumbbells. The extra length of each cup is varied to achieve the dumbbell target frequency, while all other geometrical parameters determining the cup's elliptical shape remain unchanged. As a result, the trimming rates of TM_{010}-π mode, i.e., the trimming parameters, for the middle-cell and end-cell dumbbells are determined. Figure 6.8 depicts the electric field distribution of the investigated modes of the simulated vacuum dumbbell models. The TM_{010}-$\pi/2$ and TM_{010}-π modes of the middle-cell dumbbell model must satisfy PEC boundary conditions at the cell equators. Conversely, PMC and PEC boundary conditions are set on the iris and equator of the end-cell dumbbell, respectively, to excite the TM_{010}-π mode.

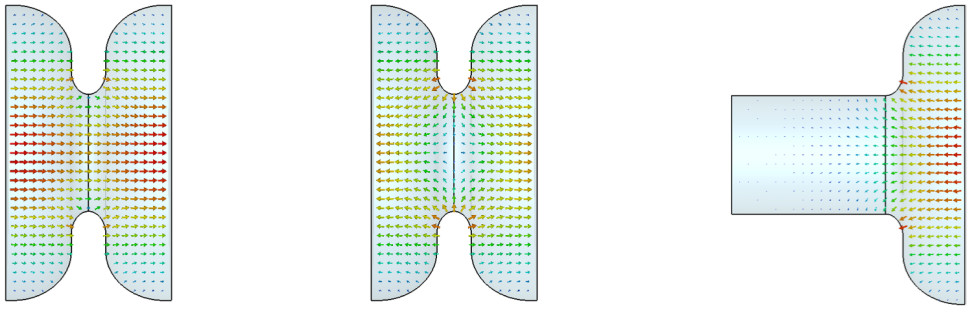

(a) Middle-cell dumbbell TM_{010}-$\pi/2$ mode

(b) Middle-cell dumbbell TM_{010}-π mode

(c) End-cell dumbbell TM_{010}-π mode

Figure 6.8: Electric field distribution of the TM_{010}-$\pi/2$ (a) and TM_{010}-π (b) modes for the middle-cell dumbbell. Electric field of the TM_{010}-π mode for the end-cell dumbbell (c).

[4]Dumbbell measurements were conducted by Gunn-Tae Park at JLab. The thesis author participated remotely and provided simulation results.

The simulation records the frequency change of the FM for the middle-cell and end-cell dumbbells as the trimmed equator lengths are varied. The trimmed length on the middle-cell dumbbell equator is denoted as $\Delta L_{\mathrm{t,m}}$, while the one on the end-cell dumbbell is indicated as $\Delta L_{\mathrm{t,e}}$. The initial simulated excess length on the equator is 18 mm, matching the actual length value for each cup after stamping. Including short flat sections on the equators avoids cutting the elliptical portion of the half-cell contour during trimming. The results of the trimming simulations are presented in Figures 6.9 (a) and (b) for the middle-cell and end-cell dumbbells, respectively. A linear regression analysis was conducted to relate the trimmed lengths and recorded frequency in the two dumbbell models. The slope of the linear equation gives the trimming rate. Results were also fitted with a second-degree polynomial to obtain a more accurate evaluation of the trimmed length required to reach the desired target frequency in each dumbbell.

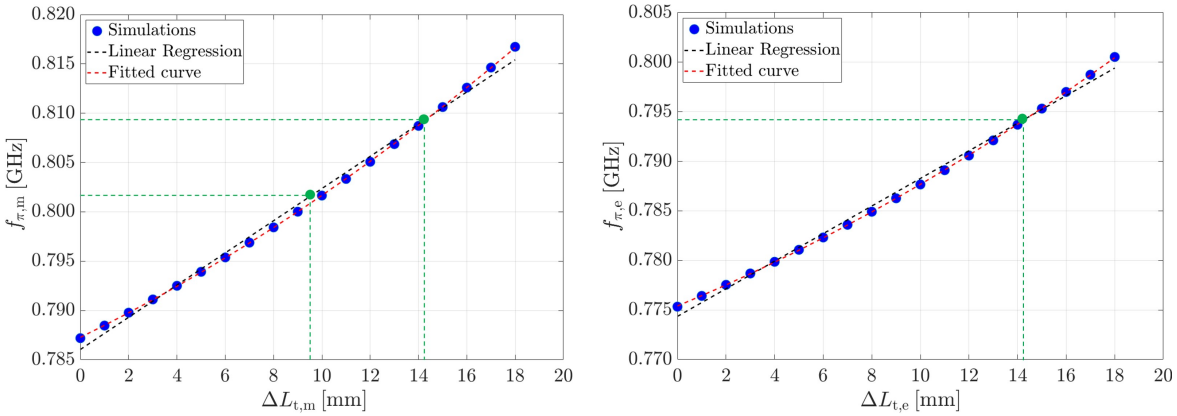

(a) Middle-cell dumbbell **(b)** End-cell dumbbell

Figure 6.9: Trimming simulations on the middle-cell (a) and end-cell (b) dumbbells. The black dashed line represents the linear regression on the simulated TM_{010}-π mode frequency (blue dots). The red dashed lines correspond to the fitted quadratic curve. The green dots depict the target frequency points for tuning the middle-cell and end-cell dumbbells.

The obtained linear regression equations for the simulated TM_{010}-π mode frequency of middle-cell and end-cell dumbbells are the following

$$f_{\pi,\mathrm{m}} = 1.63 \times 10^{-3} \Delta L_{\mathrm{t,m}} + 0.786 \text{ with } R^2 = 0.995, \tag{6.10}$$

$$f_{\pi,\mathrm{e}} = 1.39 \times 10^{-3} \Delta L_{\mathrm{t,e}} + 0.774 \text{ with } R^2 = 0.995. \tag{6.11}$$

The corresponding second-degree polynomial equations are

$$f_{\pi,\mathrm{m}} = 2 \times 10^{-5} \Delta L_{\mathrm{t,m}}^2 + 1.2 \times 10^{-3} \Delta L_{\mathrm{t,m}} + 0.787 \text{ with } R^2 = 1, \tag{6.12}$$

$$f_{\pi,\mathrm{e}} = 2 \times 10^{-5} \Delta L_{\mathrm{t,e}}^2 + 1.0 \times 10^{-3} \Delta L_{\mathrm{t,e}} + 0.775 \text{ with } R^2 = 1. \tag{6.13}$$

The calculated trimming parameters for the middle-cell and end-cell dumbbells are $S_{\mathrm{t,m}} = 1.63$ MHz/mm and $S_{\mathrm{t,e}} = 1.39$ MHz/mm, respectively. The simulated length to be trimmed on each equator of the middle-cell dumbbells to reach the 801.58 MHz frequency is $\Delta L_{\mathrm{t}} = 9.96$ mm. Removing the entire excess length of 18 mm is necessary to closely match the target cold frequency on the two end-cell dumbbells. This would limit the possibility of further trimming on the equator of end cells to compensate for frequency shifts due to fabrication errors. For this reason, it was decided to tune each endgroup to 801.58 MHz considering an equal trimmed length $\Delta L_{\mathrm{t}} = 14.25$ mm for the four half-cells composing the two cavity end-cells. This approach results in an end-cell dumbbell resonating in its π mode at 794.11 MHz while the adjacent half-cell at 809.18 MHz (see Figure 6.10 (a)). When combined, the entire endgroup resonates at the target frequency of 801.58 MHz (see Figure 6.10 (b)). This ensured a longer remaining length for future tuning on the end-cell cups. A scheme illustrating the described approach and the electric field distribution of TM_{010}-π mode for the simulated endgroup is depicted in Figure 6.10.

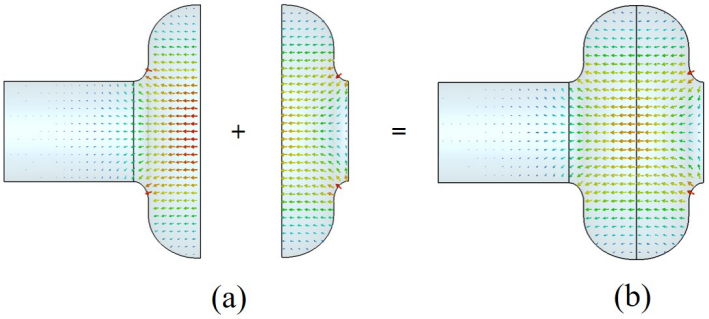

Figure 6.10: (a) Electric field distribution of the TM_{010}-π mode for the tuned 794.11 MHz end-cell dumbbell (left) and 809.18 MHz adjacent half-cell (right). The combination of these two components results in an end-cell and beam pipe jointly resonating at 801.58 MHz (b). PEC boundary conditions are applied at the cell equators, while PMC boundary conditions are set at the beam pipe aperture and cell iris.

Table 6.1 reports for each simulated cup the resulting trimmed (ΔL_{t}) and remaining excess lengths (L_{eq}) on the equator and the obtained target frequencies (f_{target}). The obtained trimmed lengths collectively enable tuning the 5-cell cavity to 801.58 MHz. Figure 6.11 illustrates the computed electric field distribution of the TM_{010}-π mode for the simulated tuned cavity and the electric field along its longitudinal axis. Additionally, it reports the cup ID convention used in this thesis to label each of the ten cavity half-cells. The simulated cavity design features a field flatness of 99%. The TM_{010}-π mode has a frequency of 801.58 MHz, and its R/Q value is 517.54 Ω.

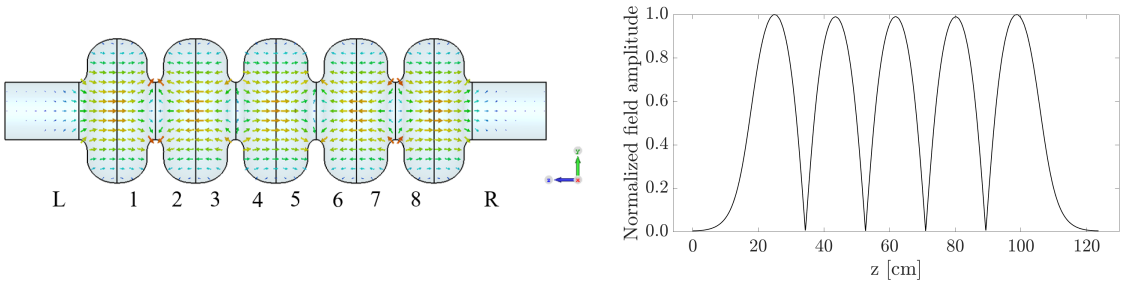

(a) E-field TM_{010}-π mode **(b)** Field flatness TM_{010}-π mode

Figure 6.11: Electric field distribution (a) and field flatness (b) of the TM_{010}-π mode for the tuned 801.58 MHz 5-cell cavity. In (a), "L" indicates the combination of the left beam pipe and the adjacent half cell, while "R" represents the right beam pipe and the contiguous half cell. The half-cells in between are labeled from "1" to "8".

Table 6.1: Simulated trimmed and corresponding excess lengths required to tune the cavity at 801.58 MHz. The used cup ID refers to the convention used in Figure 6.11 (a).

Cup ID	ΔL_t [mm]	L_eq [mm]	f_target [MHz]
L	14.25	3.75	794.11
1	14.25	3.75	809.18
2-7	9.96	8.04	801.58
8	14.25	3.75	809.18
R	14.25	3.75	794.11

6.2.4 Trimming measurement summary

The trimming of the half-cells consisted of an iterative approach involving several exchanges between the dumbbell measurement station and the JLab machine shop, which performed the equator trimming on the produced cups. Three dumbbell measurements were conducted to gradually assess each cell's desired frequency. Performing multiple dumbbell measurements ensured the accuracy of the experimental procedure and obtained trimming rates. This also allowed for maintaining a safety margin for subsequent frequency fine-tuning operations. The measured lengths to be trimmed $\Delta L_{\mathrm{t},i}$ in each measurement round i were evaluated for the upper and lower cups via equations (6.8) and (6.9), which were implemented in the used MATLAB interface. The trimmed length $\Delta L_{\mathrm{t},i}$ in each measurement round, the total removed length ΔL_tot, and the remaining equator extra length per cup L_eq are reported in Table 6.2. The total trimmed length in each half-cell ΔL_tot slightly differs from the simulated length ΔL_t (see Table 6.1) due to fabrication errors, primarily due to the springback effect in the cells.

Table 6.2: Trimmed length summary for each cup from dumbbell measurements [198].

Cup ID	$\Delta L_{t,1}$ [mm]	$\Delta L_{t,2}$ [mm]	$\Delta L_{t,3}$ [mm]	$\Delta L_{t,tot}$ [mm]	L_{eq} [mm]
L	-	-	12.087	12.087	5.913
1	0.705	10.840	0.931	12.476	5.524
2	0.705	6.280	1.124	8.109	9.891
3	0.730	6.140	1.426	8.296	9.704
4	0.730	6.140	1.289	8.159	9.841
5	0.691	5.940	0.205	6.836	11.164
6	0.691	5.940	1.310	7.941	10.059
7	0.721	6.380	0.599	7.700	10.300
8	0.721	10.940	0.642	12.303	5.697
R	-	-	11.908	11.908	6.092

6.3 Cavity assembly

After finalizing the dumbbell measurements, the produced Cu half-cells and two beam pipes were assembled to form the 5-cell 801.58 MHz Cu cavity for low-power RF bench measurements, as depicted in Figure 6.12.

Figure 6.12: Cu prototype of 801.58 MHz PERLE cavity fabricated at JLab.

Electron beam welding was used only for the fabrication of the beam pipes. The cavity cells and beam pipes are clamped together at the irises and equators. The assembly clamping is achieved using carbon steel threaded rods passing through holes in specifically designed aluminum plates in contact with the stainless steel beam pipe flanges. The half-cell and beam pipes were machined with male and female step joints at irises and equators to enhance circumferential RF contacts compared to flat surfaces. Metal holders provide structural support to the cavity.

The developed cavity design allows for the installation of two Cu ports on each beam pipe, designed to accommodate the four 3D-printed epoxy and copper-coated HOM couplers (refer to Chapter 4). The RF measurement setup was utilized for the HOM-damping measurements (refer to Subsection 7.2.3.4). The Cu ports were 3D-printed using a laser micro-fusion technique on a bed of Cu-c2 powder. The ports were manufactured using a TRUMPF TruPrint 1000© machine at the Carnot de Bourgogne Interdisciplinary Laboratory (ICB). The produced Cu ports feature a saddle-shaped contour in the lower part to align with the curvature of the holes in the beam pipes where they are installed. This ensures good mechanical stability and RF contact between the ports and the beam pipes. The 3D-printed ports underwent polishing, particularly on the inner surface, to reduce surface irregularities that could interfere with low-power RF measurements. The surface polishing was carried out after a successful leak test was conducted to assess the surface porosity level at JLab. Figures 6.13 (a) and (b) depict one of the machined Cu ports before and after polishing, respectively.

(a) 3D-printed Cu port **(b)** 3D-printed Cu port after polishing

Figure 6.13: 3D-printed HOM coupler Cu port before (a) and after polishing (b) [199].

6.4 Bead-pull measurements

After finalizing the assembly of the produced 5-cell Cu cavity, the subsequent phase involved the measurement of the frequency, the field profile along the beam axis, and the geometric shunt impedance (R/Q) of the fundamental mode. The cavity was successfully tuned to the target frequency of 801.58 MHz. The details of the measured frequency spectrum and deviation of the produced 5-cell Cu cavity are reported in Subsection 7.2.3.1. This section reports the theoretical framework of bead-pull measurements and the recorded field profile and R/Q of the FM.

Hansen and Post proposed a technique for conducting bead-pull measurements in [202]. These measurements also permit determining the identity of HOMs from the measured field profile (refer to Subsection 7.2.3.2). The measurement procedure consists of recording the field by pulling a bead attached to a nylon wire through the cavity. As the bead traverses the cavity, it introduces a slight perturbation in the surrounding medium that causes a change in the resonant frequency of cavity modes. The entity of the frequency variation depends on the bead shape and composition. The fractional resonant frequency deviation $\delta f_n/f_n$ of mode n due to a small spherical dielectric bead of radius r_b, relative permittivity ε_r, and relative permeability μ_r, is given by [203]

$$\frac{\delta f_n}{f_n} = -\frac{\pi r_\mathrm{b}^3}{U_n}\left(\frac{\varepsilon_\mathrm{r}-1}{\varepsilon_\mathrm{r}+2}\varepsilon_0\left|\underline{\mathbf{E}}_n\right|^2 + \frac{\mu_\mathrm{r}-1}{\mu_\mathrm{r}+2}\mu_0\left|\underline{\mathbf{H}}_n\right|^2\right). \tag{6.14}$$

For a metallic spherical bead ($\varepsilon_\mathrm{r} \to \infty$ and $\mu_\mathrm{r} = 0$ for a perfect conductor), the fractional frequency change of a mode n can be expressed as [63]

$$\frac{\delta f_n}{f_n} = -\frac{\pi r_\mathrm{b}^3}{U_n}\left(\varepsilon_0\left|\underline{\mathbf{E}}_n\right|^2 - \frac{1}{2}\mu_0\left|\underline{\mathbf{H}}_n\right|^2\right). \tag{6.15}$$

The bead-pull measurements discussed in this thesis are conducted using a dielectric bead with a relative permeability of $\mu_\mathrm{r} = 1$. In this case, the variations of the resonant frequency are only related to the perturbation of the electric field, and the equation (6.14) becomes

$$\frac{\delta f_n}{f_n} = -\underbrace{\pi r_\mathrm{b}^3\frac{\varepsilon_\mathrm{r}-1}{\varepsilon_\mathrm{r}+2}}_{F_\mathrm{bead}}\varepsilon_0\frac{\left|\underline{\mathbf{E}}_n\right|^2}{U_n}, \tag{6.16}$$

where F_bead represents the geometrical and material-dependent bead form factor for a dielectric sphere, which accounts for the effect of the field distortion in the vicinity of the bead. The spherical bead can capture all the components of the electric field $\underline{\mathbf{E}}_n$. A comprehensive discussion on the form factor for beads of various shapes and compositions, along with the effects on the electric and magnetic field components, is presented in [63]. Figure 6.14 depicts the bead-pull setup used in our measurements. The used dielectric spherical bead has a radius of $r_\mathrm{b} = 3.175$ mm and is made of Teflon®, with a relative permittivity of $\varepsilon_\mathrm{r} = 2.1$ [204]. The stepper motor system moves the bead across the cavity axis to measure the electric field of the considered mode along the nominal particle bunch trajectory.

In bead-pull measurements, it is common practice to assess the phase variation of the S_{21} signal, denoted as $\delta\phi$, measured between the two reference antennas rather than the frequency variation when moving the bead through the cavity. This approach reduces the measurement time. Consequently, it minimizes the effect of any slight change in environmental conditions like temperature, pressure, and humidity that may

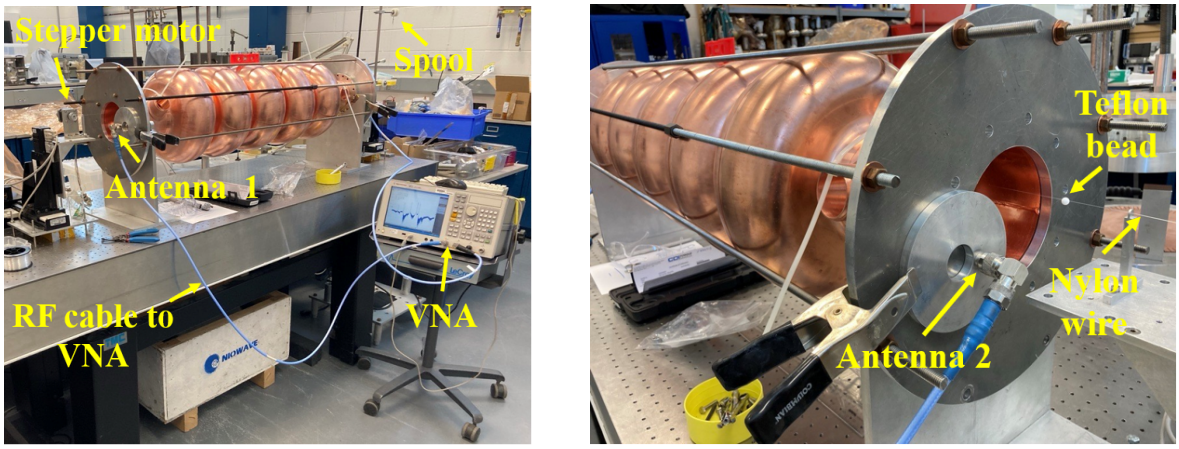

(a) Bead-pull measurement setup **(b)** Detail on the Teflon bead

Figure 6.14: Setup for bead-pull measurement on the 5-cell cavity. The phase of HOMs is recorded from the S_{21} transmission between two reference antennas, denoted as "Antenna 1" in (a) and "Antenna 2" in (b). The two antennas are connected to the VNA via two RF cables. The two stepper motors (only one motor is shown in (a)) allow for the movement of the Teflon bead through the cavity.

impact the results' accuracy. The full capabilities of the used Agilent E5071C VNA enable the synchronization of the bead motion with the frequency shift of the measured mode. While the bead moves, the excitation frequency is kept constant at the resonant center frequency of the mode n. Then, its frequency change δf_n is converted into the phase variation $\delta\phi_n$ of the $S_{21,n}$ signal measured between the two ports, as follows [205]

$$S_{21}(f_n) = |S_{21}(f_n)|\mathrm{e}^{j\delta\phi_n} = \frac{2Q_{\mathrm{L},n}}{\sqrt{Q_{\mathrm{ext},1,n}Q_{\mathrm{ext},2,n}}(1 + jQ_{\mathrm{L},n}\delta_{f_n})}, \tag{6.17}$$

where $\delta_{f_n} = (f/f_n - f_n/f) \approx 2\delta f_n/f_n$, and $Q_{\mathrm{L},n}^{-1} = Q_{0,n}^{-1} + Q_{\mathrm{ext},1,n}^{-1} + Q_{\mathrm{ext},2,n}^{-1}$. Here, $Q_{0,n}$ represents the unloaded quality factor of the mode n, while $Q_{\mathrm{ext},1,n}$ and $Q_{\mathrm{ext},2,n}$ denote the external Q-values of the input and output reference antennas for the considered mode, respectively. It follows that the relationship between the frequency change and the phase variation of a mode n with high loaded quality factor ($Q_{\mathrm{L},n} > 50$) can be approximated as [203, 205]

$$\frac{\delta f_n}{f_n} \approx \frac{1}{2Q_{\mathrm{L},n}} \tan(\delta\phi_n). \tag{6.18}$$

Combining equations (6.16) and (6.18), the following expression is obtained

$$-\frac{|\underline{\mathbf{E}}_n|^2}{\omega_n U_n} = \frac{\tan(\delta\phi_n)}{2\omega_n Q_{\mathrm{L},n}\varepsilon_0 F_{\mathrm{bead}}}, \tag{6.19}$$

where both terms are normalized to the angular frequency ω_n of the mode n. The terms in the equation (6.19) are commonly employed to compare bead-pull measurements and simulations for each mode and to determine the mode identity based on the field profile. The left-hand side can be calculated from CST eigenmode simulations, while the right-hand side is determined from measurements. Using the equation (6.19), the longitudinal shunt impedance of TM monopole modes can be calculated by integrating the longitudinal electric field along the nominal particle's trajectory $\underline{E}_{z,n}(0,0,z)$ (see the equation (1.59)), and using the equation (1.66). Similarly, the transverse shunt impedance for dipole modes could be evaluated by recording both the longitudinal electric field on-axis and off-axis and applying the Panofsky-Wenzel theorem (see Section 1.3.2). In the following, the primary focus will be evaluating the field flatness and R/Q of the FM. The comparison between measured and simulated normalized electric field profiles of several cavity HOMs will be covered in Subsection 7.2.3.2.

The measurements of phase variation while pulling the bead through the cavity permit the evaluation of the cell-to-cell field flatness. For a multi-cell cavity, the field flatness given by the equation (2.4) can be rewritten using the S_{21} phase change as [63]

$$\eta_{\mathrm{ff}} = 1 - \frac{\sqrt{\delta\phi_{\mathrm{p,max}}} - \sqrt{\delta\phi_{\mathrm{p,min}}}}{\frac{1}{N_{\mathrm{cell}}}\sum_{i=1}^{N_{\mathrm{cell}}}\sqrt{\delta\phi_{\mathrm{p},i}}}, \tag{6.20}$$

where N_{cell} is the number of cavity cells, $\delta\phi_{\mathrm{p,max}}$ and $\delta\phi_{\mathrm{p,min}}$ represent the maximum and minimum peak phase variations, respectively, and $\delta\phi_{\mathrm{p},i}$ denotes the peak phase change in the ith cell. Figure 6.15 (a) shows the measured and simulated normalized field amplitude of the TM_{010}-π mode of the produced 5-cell 801.58 MHz Cu bare cavity. Figure 6.15 (b) depicts the two terms of the equation (6.19) for the same mode.

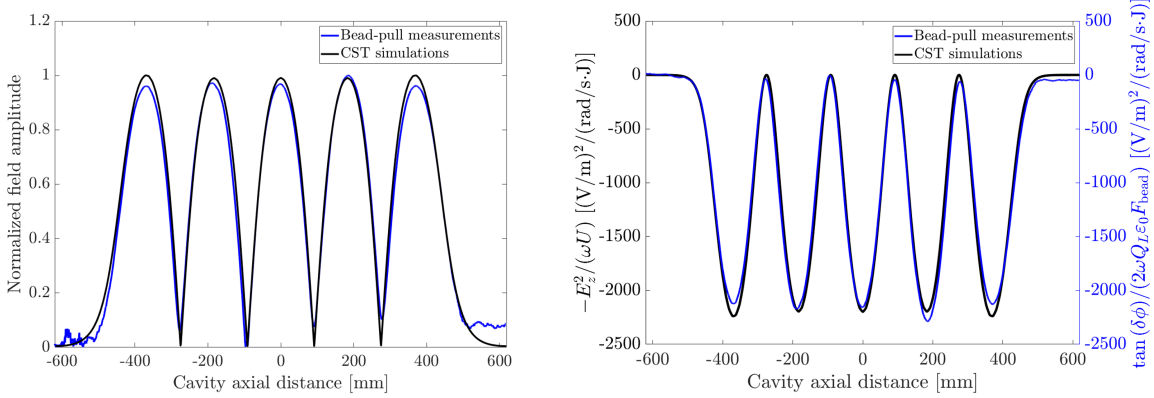

(a) E-field amplitude of TM_{010}-π mode **(b)** $-E_z^2/(\omega U)$ term of TM_{010}-π mode

Figure 6.15: Measured (blue line) and simulated (black line) normalized field profile (a) and the corresponding $-E_z^2/(\omega U)$ term (b) for the TM_{010}-π mode of the 5-cell 801.58 MHz Cu bare cavity.

The results obtained from the CST simulations closely align with the measured data. At room temperature, a field flatness of 96% for the measured π-mode frequency of 801.58 MHz was achieved. The measured field flatness deviates by 3% from the simulated value of 99%. The relative errors in the phase and Q_{L} measurements of the FM are within $\pm 1\%$, each derived from three measurements. The measured R/Q value for the FM is 568.09 Ω, exceeding the simulated CST value by 9.7%. Various factors might contribute to the observed discrepancy in the measurements. In addition to the errors that occur during the different phases of the cavity fabrication process, the main source of uncertainty in measuring the R/Q through the bead-pull technique is the relative permittivity of the bead. This parameter must be measured with good precision to accurately evaluate the R/Q. Aside from the approximation (6.18), the relative error in measuring the R/Q can be estimated from equation (6.19) using the error propagation technique as [63]

$$2\left|\frac{\Delta E_z}{E_z}\right| = \left|\frac{\Delta\phi}{\phi}\right| + \left|\frac{\Delta Q_{\mathrm{L}}}{Q_{\mathrm{L}}}\right| + 3\left|\frac{\Delta r_{\mathrm{b}}}{r_{\mathrm{b}}}\right| + 3\left|\frac{\Delta\varepsilon_{\mathrm{r}}}{(\varepsilon_{\mathrm{r}}-1)(\varepsilon_{\mathrm{r}}+2)}\right|. \tag{6.21}$$

Considering a relative error of 1% for the phase, the loaded Q and the relative permittivity, and 0.2% for the bead radius, the estimated relative error of the R/Q is approximately 5.6% when using a Teflon sphere. It would be reasonable to attribute the remaining error to additional factors omitted in our investigation. Specifically, the effect of the non-ideal shape of the bead and the presence of the center hole where the wire passes through were not considered. Finally, the impact of bead vibration and slipping during the measurements was not included.

7 RF measurements on PERLE HOM couplers and cavities

RF measurements are crucial for qualifying any RF cavity. They are used, for instance, to quantify the interaction between the electromagnetic field of resonant modes and external coupling mechanisms connected to the cavity, such as HOM couplers. Additional measurements are conducted throughout the fabrication process of a cavity, involving the evaluation of the frequency spectrum and the field distribution of resonant modes. First, this chapter addresses the RF engineering concepts employed in this thesis for conducting RF measurements on cavities. Subsequently, it provides a survey of the low-power RF measurements conducted at room temperature on different HOM couplers installed on 801.58 MHz prototype Cu cavities manufactured for the PERLE project and CERN FCC R&D studies.

7.1 Theoretical background for RF measurements of cavity modes

The excitation of a resonant mode within a cavity involves establishing a connection between the cavity and an RF source [17, pp. 145-146]. Figure 7.1 shows a setup of a cavity equipped with two RF couplers. The power from the RF source is delivered to the cavity via an input coupler (or transmitted coupler) operating in a transverse electromagnetic (TEM) mode. The coupling strength is determined by the overlap between the cavity fields and the fields that leak into the cutoff region from the input coupler. The desired coupling strength of the input coupler is modified by adjusting the penetration of its center conductor. Conversely, the role of the output coupler is to either pick up the power transmitted through the cavity, in the case of a Field Probe (FP), or extract it, in the case of a HOM coupler.

The equivalent circuit for a cavity with two couplers is depicted in Figure 7.2 [33, p. 144]. This represents a two-port cavity system. Port 1 is connected to an FPC (or input coupler) driven by an RF generator [17, p. 149]. The combination of the RF generator and isolator is represented by an ideal current source, delivering a current I_{g}, and a shunt admittance G_0 (the reciprocal of impedance). An ideal transmission line with admittance G_0 connects the RF generator with the FPC, modeled as a transformer.

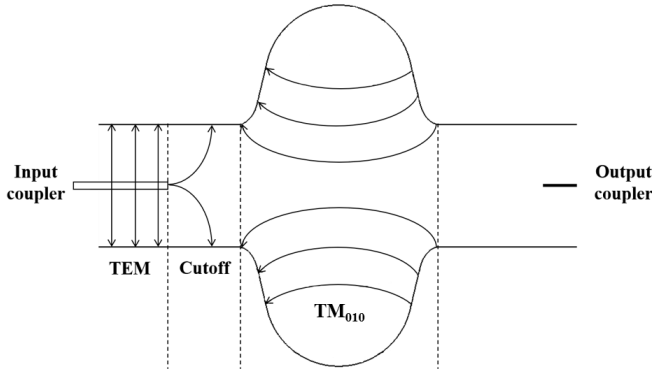

Figure 7.1: RF cavity equipped with two couplers. The input coupler, connected to port 1, delivers the power from an RF source in a TEM mode, while the output coupler, connected to port 2, picks up the power. The electric field lines of the TEM mode, the cutoff region, and the TM_{010} mode in the cavity are depicted (figure adapted from [17, p. 146]).

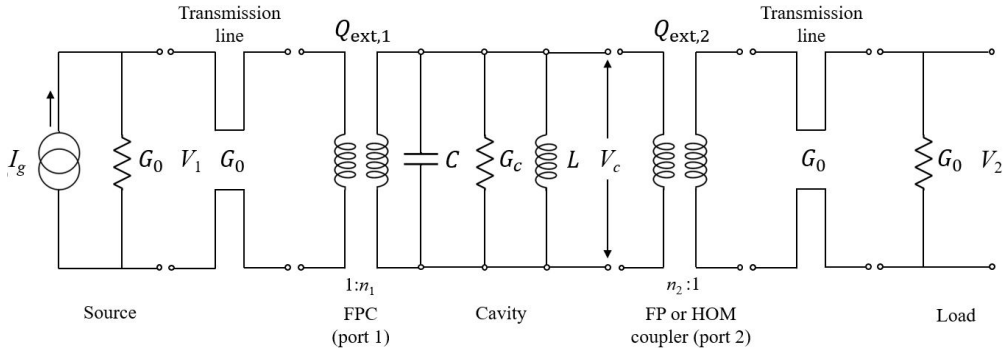

Figure 7.2: Equivalent circuit for a two-port cavity system. The input coupler (FPC) at port 1 is driven by an RF generator. The output coupler (FP or HOM coupler) at port 2 picks up the power propagating along the transmission line toward the cavity (figure adapted from [33, p. 144]).

This configuration permits matching the transmission line to a cavity with an arbitrary impedance. The cavity is represented through an equivalent circuit with admittance G_c, inductance L, capacitance C, and voltage V_c. A circulator, placed between the RF generator and the cavity, is connected to a load acting as an isolator to protect the generator from signal reflections. Port 2 typically hosts an FP or a HOM coupler connected to a load. The presence of a load ensures that signals from the cavity are terminated in a matched load.

7.1.1 Coupler basic parameters

Different figures of merit characterize the RF measurements of cavities and couplers. Some of the parameters used to evaluate the cavity and coupler RF performance are

briefly presented in this section. These quantities are expressed in terms of the cavity parameters whenever possible, with detailed circuit treatise provided in [17, pp. 145-169].

7.1.1.1 Undriven cavity

Consider an undriven RF cavity (RF turned off) with two ports, each connected to a coupler [17, pp. 146-148]. The total losses in the cavity are given by

$$P_{\text{loss}} = P_{\text{c}} + P_{\text{e}} + P_{\text{t}}, \tag{7.1}$$

where P_{c} is the power dissipated in the cavity walls, P_{e} is the emitted power leaking back out of the input coupler, and P_{t} is the power coming out of the fixed output coupler. Under these conditions, the stored energy satisfies the following differential equation

$$\frac{dU}{dt} = -P_{\text{loss}} = -\frac{\omega U}{Q_{\text{L}}}, \tag{7.2}$$

where Q_{L} is the loaded quality factor. The solution of equation (7.2), assuming quadratic losses, is

$$U = U(0)\text{e}^{-\omega t/Q_{\text{L}}}, \tag{7.3}$$

where $U(0)$ is the stored energy at $t = 0$. Hence, the energy in the cavity decays exponentially with a time constant, denoted as the time constant of the loaded cavity, defined as[1]

$$\tau_{\text{L}} = \frac{Q_{\text{L}}}{\omega}. \tag{7.4}$$

In practice, connecting the two ports of a cavity system allows for the measurement of the loaded quality factor, Q_{L}, associated with the total power lost within the cavity. In general, the equation (7.4) enables the determination of Q_{L} for a cavity connected to input and output RF lines. Alternatively, the loaded quality factor can be derived from the equation (1.89) as follows

$$\frac{1}{Q_{\text{L}}} = \frac{1}{Q_0} + \frac{1}{Q_{\text{ext,1}}} + \frac{1}{Q_{\text{ext,2}}} = \frac{P_{\text{c}}}{\omega U} + \frac{P_{\text{e}}}{\omega U} + \frac{P_{\text{t}}}{\omega U}, \tag{7.5}$$

where $Q_{\text{ext,1}}$ and $Q_{\text{ext,2}}$ indicate the external quality factors of the couplers connected at port 1 and port 2, respectively. Equation (7.5) can be rewritten by defining the coupling parameters for port 1 and port 2 as

[1]Note that field decays with a time constant of $2\tau_{\text{L}}$ according to this convention.

$$\beta_1 = \frac{Q_0}{Q_{\text{ext},1}} = \frac{P_\text{e}}{P_\text{c}}, \tag{7.6}$$

$$\beta_2 = \frac{Q_0}{Q_{\text{ext},2}} = \frac{P_\text{t}}{P_\text{c}}, \tag{7.7}$$

which gives

$$\frac{1}{Q_\text{L}} = \frac{1}{Q_0}(1 + \beta_1 + \beta_2), \tag{7.8}$$

and, consequently, the following definition of intrinsic quality factor

$$Q_0 = Q_\text{L}(1 + \beta_1 + \beta_2). \tag{7.9}$$

7.1.1.2 Driven cavity

In general, in case an FP represents the output coupler, it can be assumed that it is very weakly coupled ($\beta_2 \ll 1$) so that, in a first approximation, the output coupler can be neglected in the evaluation of the RF performance of the system [17, pp. 148-154]. For this reason, when considering only one coupler, we will denote the input coupling parameter as simply β. The cavity-coupler system becomes a driven nonlinear harmonic oscillator when the RF is on. From the conservation of energy, the power flowing into a cavity, denoted as P_in, can be expressed as

$$P_\text{in} = P_\text{f} - P_\text{r} = P_\text{f} - |\Gamma|^2 P_\text{f}, \tag{7.10}$$

where P_f represents the power propagating forward along the transmission line toward the cavity, and $P_\text{r} = |\Gamma|^2 P_\text{f}$ the reflected power. The power reflection depends on the reflection coefficient Γ, which in steady-state is defined as

$$\Gamma(f) = \frac{\beta - 1 - jQ_0\delta_{f_0}}{\beta + 1 + jQ_0\delta_{f_0}}, \tag{7.11}$$

where $\delta_{f_0} = (f/f_0 - f_0/f)$, with f_0 being the resonant frequency, β_1 is the coupling parameter of the input coupler and Q_0 the intrinsic quality factor of the cavity. If the cavity is driven exactly on resonance (i.e., $f = f_0$), the reflection coefficient simplifies to the following expression

$$\Gamma(f_0) = \frac{\beta - 1}{\beta + 1}, \tag{7.12}$$

and the ratio between the reflected power and the power coming from the generator can be written from the reflection coefficient as

$$\frac{P_\mathrm{r}}{P_\mathrm{f}} = \left(\frac{\beta - 1}{\beta + 1}\right)^2. \tag{7.13}$$

This quantity can be used to find the coupling strength in steady-state conditions. Taking the square root of both sides of the equation (7.13) and solving for β, the following expression for the coupling parameter is obtained

$$\beta = \frac{1 \pm \sqrt{P_\mathrm{r}/P_\mathrm{f}}}{1 \mp \sqrt{P_\mathrm{r}/P_\mathrm{f}}}. \tag{7.14}$$

This equation permits the experimental determination of β from power measurements in steady-state conditions [17, pp. 157-160]). Here, the upper sign is used for $\beta > 1$ (overcoupled), while the lower sign is employed for $\beta < 1$ (undercoupled). For $\beta = 1$, the cavity acts as a perfectly matched load. It is possible to determine whether the cavity is overcoupled or undercoupled by adjusting the penetration of the input coupler. For instance, the coupling factor can be augmented by increasing the penetration of the coupler antenna. In this scenario, the cavity becomes overcoupled. Conversely, decreasing the penetration of the antenna can make the cavity undercoupled.

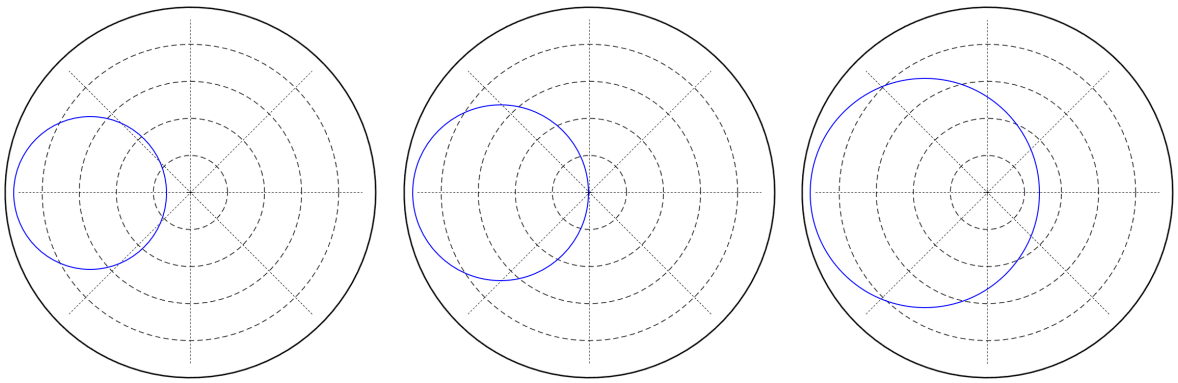

(a) $\beta < 1$ **(b)** $\beta = 1$ **(c)** $\beta > 1$

Figure 7.3: Polar plots of the reflection coefficient at three different cavity couplings: (a) undercoupling, (b) matched condition and overcoupling (c) [17, p. 160]). The obtained loop is depicted in blue. These plots are obtained using equation (7.11).

Figure 7.3 illustrates the polar plots of the reflection coefficient for a cavity under measurement, showing three different coupling scenarios. The cavity is considered overcoupled when the obtained loop encompasses the origin; otherwise, the cavity is undercoupled. If the loop passes through the origin, the reflection diminishes to zero on resonance, and the cavity is considered unity coupled.

7.1.1.3 Scattering matrix

The scattering matrix, usually referred to as S-matrix for brevity, is widely used in microwave engineering to describe a two-port or, more in general, an N-port network [206]. To describe a network at high frequencies, it is more convenient to use wave descriptions rather than dealing with voltage and currents. The reason is that measuring voltages and currents at high frequencies can generally become challenging. The incident and reflected waves, denoted as a_k and b_k respectively, are measures of the incident and reflected power within a microwave structure. They are defined as

$$a_k = \frac{V_k + R_k I_k}{2\sqrt{R_k}}, \tag{7.15}$$

$$b_k = \frac{V_k - R_k I_k}{2\sqrt{R_k}}, \tag{7.16}$$

where V_k and I_k represent the voltage and the current at the terminal pair k, and R_k denotes a reference resistance usually related to a source or a load. The term "port" is used in this thesis instead of "terminal pair" to represent a power flow. For a two-port network, as illustrated in Figure 7.4, which can represent a two-port cavity system (see Figure 7.2), the relationship between a_k (independent variable) and b_k (dependent variable), with k=1, 2, can be written in matrix formulation as

$$\begin{bmatrix} b_1 \\ b_2 \end{bmatrix} = \begin{bmatrix} S_{11} & S_{12} \\ S_{21} & S_{22} \end{bmatrix} \begin{bmatrix} a_1 \\ a_2 \end{bmatrix}, \tag{7.17}$$

where index 1 corresponds to the input port, while index 2 designates the output port. The matrix elements S_{11} and S_{22} are the input and output reflection coefficients, respectively. The elements S_{21} and S_{12} represent the transmission coefficients from port 1 to port 2 and vice versa. In reciprocal networks, the scattering matrix $\mathbf{S}$ is symmetric, hence $S_{12} = S_{21}$.

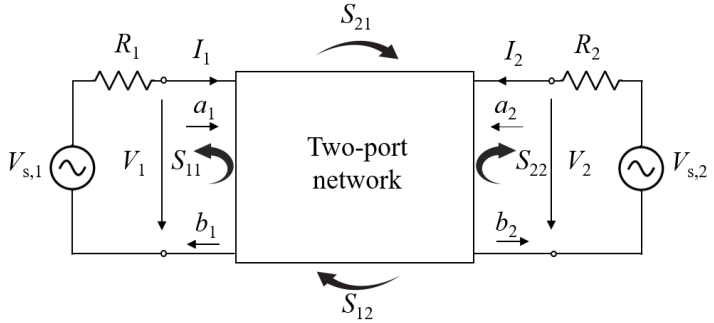

Figure 7.4: Scattering matrix formalism for a two-port network with resistive terminations. V_k and I_k denote the voltage and the current at the terminal pair k. R_k is a reference resistance related to a source or a load.

The scattering parameters can be equivalently defined in power terms as [110]

$$|S_{11}|^2 = \frac{P_{\mathrm{r},1}}{P_{\mathrm{f}}}, \tag{7.18}$$

$$|S_{22}|^2 = \frac{P_{\mathrm{r},2}}{P_{\mathrm{f}}}, \tag{7.19}$$

$$|S_{21}|^2 = \frac{P_{\mathrm{t}}}{P_{\mathrm{f}}}. \tag{7.20}$$

where $P_{\mathrm{r},1}$ and $P_{\mathrm{r},2}$ represent the total reflected powers for ports 1 and 2, respectively. Considering the equations (7.14), (7.18) and (7.19), the coupling parameters β_1 and β_2 can be described in terms of the scattering parameters as [207]

$$\beta_1 = \frac{1 \pm |S_{11}|}{1 \mp |S_{11}|}, \tag{7.21}$$

$$\beta_2 = \frac{1 \pm |S_{22}|}{1 \mp |S_{22}|}. \tag{7.22}$$

For the equations (7.21) and (7.22), the same considerations made for the equation (7.14) about sign convention and coupling cases hold true.

7.1.2 HOM measurements for a cavity with a HOM coupler

The preceding subsection discussed the scenario of a cavity equipped with an input coupler and a field probe. Consider a cavity equipped with a probe antenna, which serves as a reference antenna, connected to the input port (port 1) and a HOM coupler situated at the output port (port 2), as shown in Figure 7.5.

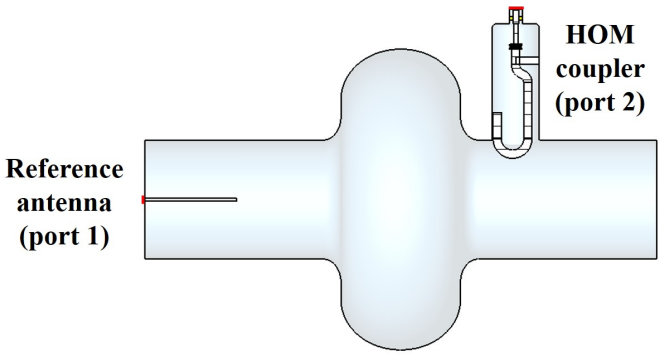

Figure 7.5: Single-cell RF cavity equipped with a reference antenna and a HOM coupler. The reference antenna is connected to port 1, while the HOM coupler is linked to port 2.

Although it remains possible to assume that the HOM coupler weakly couples to the FM (i.e., $\beta_2 \ll 1$) because of its rejection characteristics towards this mode, the same

assumption cannot be extended to the cavity HOMs. Indeed, the primary function of a HOM coupler is to enable the coupling to the EM fields of HOMs to extract the power associated with these parasitic modes. This section presents an approach for measuring the performance of a HOM coupler installed in a cavity, aiming at minimizing the error related to the recorded scattering parameters S_{11} and S_{22} in case of weak coupling of EM fields to the antennas involved in the measurements.

7.1.2.1 Theoretical framework

The damping of HOMs is quantified by the external quality factor Q_{ext}, which characterizes the efficiency of the HOM couplers in a damped cavity. Consider the configuration in Figure 7.5. The scattering parameters between the probe antenna and the HOM coupler are evaluated using a VNA. The standard procedure to measure Q_{ext} of cavity modes for both antennas involves several steps.

First, the loaded quality factor Q_{L} is determined from the resonant frequency and 3 dB bandwidth of the measured S_{21} transmission. The S_{21} parameter formula in a two-port cavity system (see Figure 7.2) can be expressed as follows [63]

$$S_{21}(f) = \frac{2\sqrt{\beta_1\beta_2}}{(1+\beta_1+\beta_2) + jQ_0\delta_{f_0}}, \tag{7.23}$$

where $\delta_{f_0} = (f/f_0 - f_0/f)$ with f_0 being the resonant frequency of the considered mode. Here, the coupling parameters for the input coupler and the HOM coupler are described using the equations (7.6) and (7.7). This derivation is valid regardless of whether $\beta_1 < 1$ or $\beta_1 > 1$, as well as for $\beta_2 < 1$ or $\beta_2 > 1$. Moreover, the equations (7.8) and (7.9) hold true for the studied scenario. In the event that the cavity is driven exactly on resonance (i.e., $f = f_0$), the equation (7.23) becomes

$$S_{21}(f_0) = 10\log\left[\frac{4\beta_1\beta_2}{(1+\beta_1+\beta_2)^2}\right]. \tag{7.24}$$

Subsequently, the coupling factors of the reference antenna (β_1) and HOM coupler (β_2) are derived at resonance from the reflection measurements using the equations (7.21) and (7.22). Finally, the intrinsic quality factor at resonance is obtained from the equation (7.9), enabling the calculation of the external quality factors for the two antennas from the equations (7.6) and (7.7).

In scenarios characterized by very weak coupling between the antennas and resonant modes, such as in room temperature measurements, utilizing S_{11} and S_{22} scattering parameters leads to notable errors. If the reference antenna is severely undercoupled (i.e., $\beta_1 \ll 1$ and $S_{11} \sim 1$), it is possible to approximate its coupling parameter for a specific mode as follows

$$\beta_1 \approx \frac{1 - |S_{11}(f_0)/S_{11}(|f| \gg f_0)|}{1 + |S_{11}(f_0)/S_{11}(|f| \gg f_0)|}, \tag{7.25}$$

with $|f| \gg f_0$ being the off-resonance condition, while $f = f_0$ representing the on-resonance condition. Alternatively, it could be possible to obtain a reliable result by using a longer reference antenna to enhance the coupling. In case the HOM coupler is highly undercoupled for a certain mode (i.e., $\beta_2 \ll 1$ and $S_{22} \sim 1$), rather than using the equation (7.22), it is possible to derive $\beta_2 \ll 1$, and consequently the external quality factor of the HOM coupler, by measuring S_{21} instead of S_{22}. By rearranging the equation (7.24) and employing the equations (7.7) and (7.8) the Q_{ext} of the HOM coupler can be expressed as

$$Q_{\text{ext},2}(f_0) = \frac{4\beta_1}{1+\beta_1+\beta_2} Q_{\text{L}} \cdot 10^{\frac{|S_{21}(f_0)|}{10}}. \tag{7.26}$$

This S_{21} transmission measurement technique requires two-port cable calibration on both the input and output cables.

7.1.2.2 HOM measurement procedure

Based on the theoretical framework described in the previous subsection, the procedure outlined below has been developed for the HOM measurements. This technique has the advantage of being unique, independently of the type of measured mode, and permits the determination of the Q_{ext} for the HOM coupler through an iterative process. The following notation is employed to indicate the two types of coupling parameters, regardless of whether they are associated with the input or the HOM coupler antennas: β_l and β_s denote the coupling parameters of the coupler that exhibits a large coupling ($\beta \sim 1$) or small coupling ($\beta \ll 1$) with the EM field inside the cavity, respectively. The sequence used for measuring cavity modes can be summarized as follows [166]:

(i) The loaded quality factor Q_{L} and the S_{21} values are recorded using a VNA.

(ii) The on-resonance and off-resonance reflection coefficients of both ports are measured. The coupling strength of each port is calculated on the basis of the following two parameters

$$\Delta S_{11}(f_0) = S_{11}(|f| \gg f_0) - S_{11}(f_0), \tag{7.27}$$

$$\Delta S_{22}(f_0) = S_{22}(|f| \gg f_0) - S_{22}(f_0). \tag{7.28}$$

If $\Delta S_{11}(f_0) > \Delta S_{22}(f_0)$, port 1 exhibits stronger coupling to the EM field of the considered mode than port 2, and vice versa. Only the reflected signal to the strongly-coupled antenna, denoted as S_{ll}, is considered, and the large-coupling parameter β_l is approximated, in analogy with the equation (7.25), as

$$\beta_l \approx \frac{1 \pm |S_{ll}(f_0)/S_{ll}(|f| \gg f_0)|}{1 \mp |S_{ll}(f_0)/S_{ll}(|f| \gg f_0)|}. \tag{7.29}$$

The polar plot of the reflection parameter S_{ll} is recorded, allowing the distinction between overcoupling (upper sign is employed) and undercoupling (lower sign is used) scenarios of the antenna. Here, for the sake of clarity, it is important to know that the pair of indices "ll" can be either "11" or "22", depending on whether the strongest coupling is at port 1 or port 2. Consequently, the reflected signal to the weakly-coupled antenna is denoted as S_{ss}. Precise measurements of S_{ss} parameter become challenging in cases of very weak coupling. This can potentially result in an inaccurate evaluation of the coupling parameter for the weakly-coupled antenna, referred to as β_s.

(iii) Assuming that $\beta_s \ll \beta_l$, the external quality factor for the weak-coupled antenna, denoted as $Q_{\mathrm{ext},s}$, can be approximated, in analogy with the equation (7.26), as

$$Q_{\mathrm{ext},s}(f_0) \approx \frac{4\beta_l}{1+\beta_l} Q_{\mathrm{L}} \cdot 10^{\frac{|S_{21}(f_0)|}{10}}. \tag{7.30}$$

Here, the parameter β_s is neglected due to the above-stated considerations on the S_{ss} signal of a weak-coupled antenna.

(iv) Successively, the coupling parameter β_s, the intrinsic quality factor Q_0, and the external quality factor for the strong-coupled antenna, denoted as $Q_{\mathrm{ext},l}$, are determined by using the following relations

$$\beta_s \approx \frac{(1+\beta_l)Q_{\mathrm{L}}}{Q_{\mathrm{ext},s}(f_0)}, \tag{7.31}$$

$$Q_0(f_0) = Q_{\mathrm{L}}(1+\beta_s+\beta_l), \tag{7.32}$$

$$Q_{\mathrm{ext},l}(f_0) = \frac{Q_0(f_0)}{\beta_l}. \tag{7.33}$$

(v) Finally, the second step of the iterative process gives the second-order approximation of the external quality factors for the two couplers, which are given by

$$Q_{\mathrm{ext},l}(f_0) = \frac{Q_0 Q_{\mathrm{L}}}{Q_0 - Q_{\mathrm{L}}}, \tag{7.34}$$

$$Q_{\mathrm{ext},s}(f_0) = \frac{(1+\beta_s+\beta_l)Q_{\mathrm{L}}}{\beta_s}. \tag{7.35}$$

The above-described procedure is used for measuring the performances of each manufactured HOM-coupler prototype on a 2-cell 801.58 MHz Cu cavity, whose results are presented in Subsection 7.2.2.

7.2 Low power RF measurements on 801.58 MHz cavities

In the framework of the collaboration between CERN and JLab to initiate SRF cavity R&D studies for the LHeC and FCC-related projects, several 801.58 MHz prototype elliptical cavities, including the 801.58 MHz Nb five-cell cavity presented in Chapter 2, were designed, fabricated, and tested during the period from 2016 to 2018 [58]. The following cavities were produced: a 1-cell and a 5-cell fine-grain high-RRR Nb cavities, two 1-cell OFHC Cu cavities for thin film coating R&D, and a 2-cell OFHC Cu cavity for R&D bench measurements. The 5-cell 801.58 MHz cavity JLab design has been adapted as the baseline for the two superconducting linac cryomodules of the PERLE ERL at IJCLab. In 2023, the first 801.58 MHz OFHC Cu 5-cell PERLE-type cavity, presented in Chapter 6, was manufactured at JLab as part of this thesis.

The main scope of this study is to test the damping performance of the fabricated HOM coupler prototypes, presented in Chapter 4, at warm temperatures. The HOM couplers were individually tested first on the 2-cell OFHC Cu cavity (refer to Subsection 7.2.2). Then, their combination into the 2P2H and 4DQW HOM-damping schemes, presented in Chapter 5, was tested on the produced 5-cell Cu cavity (refer to Subsection 7.2.3).

The summary of the measurements presented in this section includes:

(i) Evaluation of the frequency spectrum and deviation of the 2-cell and 5-cell 801.58 MHz OFHC Cu cavities.

(ii) Bead-pull measurements on the 5-cell Cu cavity to determine the identity of relevant monopole and dipole HOMs.

(iii) HOM-damping measurements, including the evaluation of the transmission (S_{21}), reflection (S_{11} and S_{22}) signals, coupling parameter (β), unloaded quality factor (Q_0), loaded quality factor (Q_L), and external quality factor (Q_ext) for the highest-R/Q HOM passbands of the 2-cell and 5-cell Cu cavities.

In the following, the measurement setup is presented. RF measurements performed on the 2-cell and 5-cell OFHC Cu cavities are discussed and compared to CST eigenmode simulations. These analyses provide insights into designing the final HOM-damping endgroups of the 5-cell 801.58 MHz Nb cavity intended for use in the PERLE ERL linacs. The 5-cell Nb cavity, which was not available at JLab during the measurement campaigns, is not covered in the present measurement survey. Since all

the mentioned cavities are suitable for PERLE R&D studies, they are referred to as PERLE-type cavities in this thesis.

7.2.1 The measurement setup

The experimental setup used for low-power RF measurements on PERLE-type Cu cavities is depicted in Figure 7.6. The purpose of this setup is to enable the execution of multiple RF tests on the same test bench, including measurements of HOM frequency, bead-pull tests, and HOM-damping measurements.

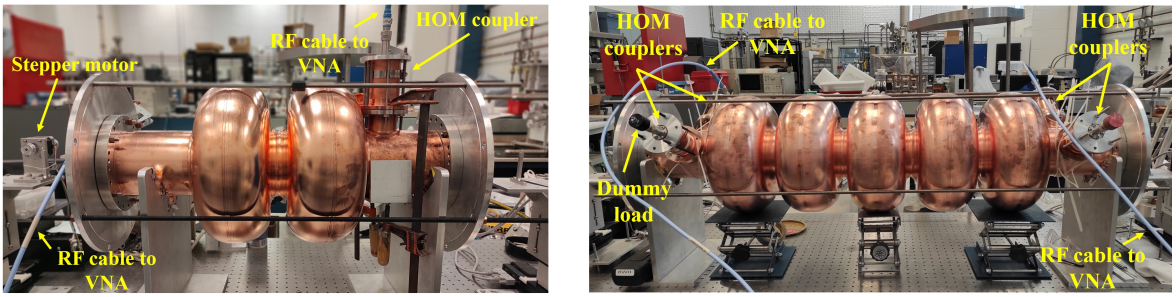

(a) 2-cell Cu cavity with one HOM coupler **(b)** 5-cell Cu cavity with four HOM couplers

Figure 7.6: Measurement setup for the 2-cell Cu cavity with one HOM coupler prototype installed on the right-hand beam pipe and a reference antenna (not visible in the picture) on the left-hand beam pipe (a) [123]. A similar setup is employed for the 5-cell Cu cavity with four HOM couplers (b). Two couplers are positioned on each side of the 5-cell cavity. Test cables are connected to a VNA. Figure (a) falls under the Creative Commons Attribution 4.0 (CC BY 4.0) license (https://creativecommons.org/licenses/by/4.0/).

The measurement setup consists of a Cu cavity equipped with one or multiple 3D-printed epoxy and Cu-coated HOM couplers (refer to Section 4.3). The cavity cells and beam pipe are clamped together, as described in Section 6.3. Couplers are connected to the beam pipe ports and secured using both metal C-clamps and cable ties. While welding offers superior RF contact between surfaces, clamping was selected as the preferred method for securing the assembly due to its practicality and suitability for the specific requirements of low-power RF measurements. Beam pipes are left open to allow the insertion of reference antennas on both sides of the cavity for the purpose of exciting HOMs (see Figure 7.7 (a)). In addition, this facilitates access to the cavity interior and permits the easy rotation and replacement of the reference antennas if stronger or weaker coupling to the cavity HOMs is required. Two stepper motors, one on each side of the cavity, enable the movement of a nylon wire, to which a Teflon bead is attached, passing through the cavity to perform bead-pull tests (see Figure 7.7 (b)).

The setup is equipped with a VNA to record the RF signal between the antennas of the experimental setup. The antennas are connected to the VNA ports using coaxial test cables. Depending on the purposes of the analysis, the RF signal between the two

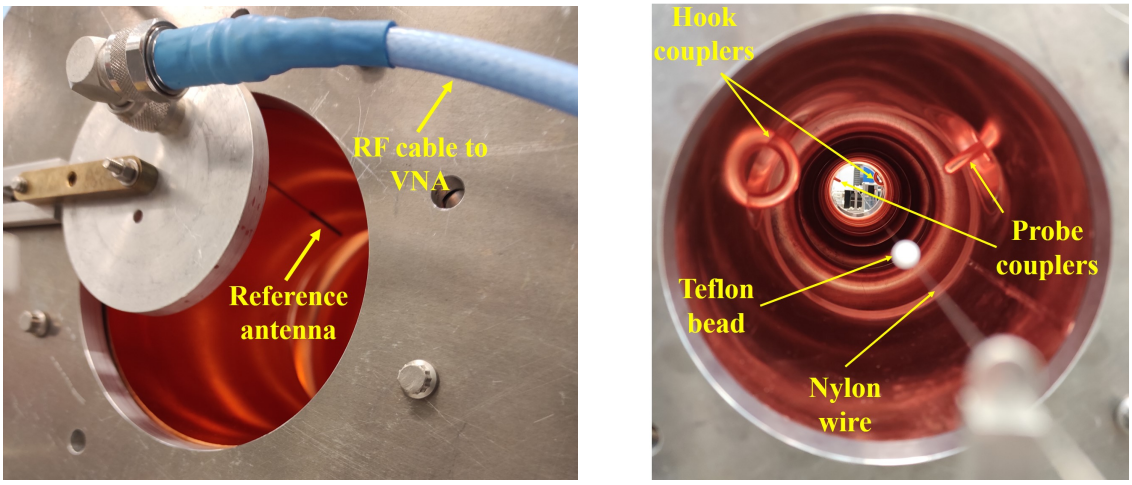

(a) Reference antenna on the 2-cell cavity **(b)** 2P2H scheme on the 5-cell cavity

Figure 7.7: Reference antenna installed on the 2-cell Cu cavity (a). Interior of the 5-cell Cu cavity with the 2P2H damping scheme (b). The Teflon bead for bead-pull tests is also shown.

ports can be measured using two reference antennas, one reference antenna and one HOM coupler, or two HOM couplers. When measuring the transmission between two couplers in a multi-coupler damping scheme, the couplers that are not involved in the measurement are terminated with 50 Ω dummy loads (see Figure 7.6 (b)). These terminations are designed to absorb all the incident power with little reflection, allowing the ports to be terminated in their characteristic impedance and ensure an accurate measurement. The collected data were analyzed using a Mathematica 13.3 [208] program called Polfit [209]. This routine uses a procedure for automatic pole fitting of complex spectral data to estimate the Q_L of each HOM. This approach permits saving time for resonance frequencies and Q_L measurements compared to direct VNA measurements, especially when measuring HOM-passbands in multi-cell cavities.

7.2.2 2-cell elliptical copper cavity

This section presents the HOM-damping measurements performed at low power and room temperature on a 2-cell 801.58 MHz PERLE-type Cu cavity with a HOM coupler mounted on one of its beam pipes. The experimental setup is shown in Figure 7.6 (a). Bench RF measurements were carried out at JLab on 3D-printed and copper-coated HOM coupler prototypes - namely probe-type, hook-type, and DQW couplers - for validating their damping performances and the adequacy of the used measurement setup. Although the couplers have been optimized based on the frequency spectrum of the 5-cell PERLE cavity, the decision to test them individually on a 2-cell cavity was made because the 5-cell Cu cavity was still under fabrication at JLab during the first HOM measurement campaign. This choice was based on the assumption that the

frequency spectrum of a 5-cell cavity is reasonably similar to that of a 2-cell cavity (see Figure 4.6). First, the frequency spectrum of the 2-cell cavity is analyzed, along with the HOM frequency deviation from the simulated resonant mode frequencies. Subsequently, Q_{ext} measurements for the FM and trapped high-R/Q HOMs for each studied coupler are presented. In particular, the dependency of the Q_{ext} on the coupler orientation is investigated to assess the best HOM-damping orientation for each of the three couplers. As part of the design criteria for the three produced couplers, the analysis aimed to demonstrate adequate FM rejection and satisfactory HOM-damping, with $Q_{\text{ext}} < 10^5$ for all relevant monopole and dipole HOMs. Measurement results and their comparison with CST simulations are detailed. It is important to note that the considerations in this study will refer only to the HOMs of the investigated 2-cell cavity. Indeed, the performance of the HOM couplers in the 5-cell cavity may vary slightly. The results shown in this section were partially presented in [123, 166].

7.2.2.1 Frequency spectrum and deviation

The frequency spectrum of the 2-cell 801.58 MHz cavity was recorded throughout the frequency range from 0.7 GHz to 1.8 GHz, including the FM and trapped high-R/Q cavity HOMs. The RF transmission was measured from a reference antenna to the HOM coupler installed on the opposite side of the cavity using a VNA (see Figure 7.6 (a)). The reference antenna was placed on-axis or off-axis for monopole and dipole mode excitation, respectively. This subsection presents only the frequency spectrum analysis of the 2-cell cavity with one DQW coupler. The perturbation introduced in the cavity is similar to the other two coupler designs. Therefore, the frequency spectra and deviations do not vary significantly from one coupler design to another. Figures 7.8 (a) and (b) illustrate, as an example, the recorded S_{21} transmission of the TM_{010}-π mode and trapped mode passbands of the 2-cell cavity with a DQW-type coupler, respectively.

The resonant modes can be identified on the VNA by distinct resonance peaks. The measured TM_{010}-π frequency was 801.577 MHz at a recorded room temperature of 23°C and humidity of 29%. The measured frequency deviates by only 3 kHz from the designed cavity frequency. Similar results were found in measurements involving the other analyzed couplers. Eigenmode analyses were carried out in CST on the 2-cell cavity with a DQW-type coupler to calculate the resonant frequencies and compare them with measurements. The simulated cavity model is depicted in Figure 7.9. PEC boundary conditions were considered for the cavity walls and beam pipe openings. Waveguide ports were applied to the reference antenna and HOM coupler terminations.

Figure 7.10 (a) depicts the comparison between the measured and simulated frequencies of the FM and concerned monopole and dipole HOMs of the 2-cell Cu cavity. Figure 7.10 (b) shows the deviation between measured and simulated mode frequencies. Table 7.1 reports the average relative frequency deviation of the modes belonging to the same passband. The largest deviation is observed for the mode passbands with longitudinal index $p = 1$. These modes are the most sensitive to frequency change due

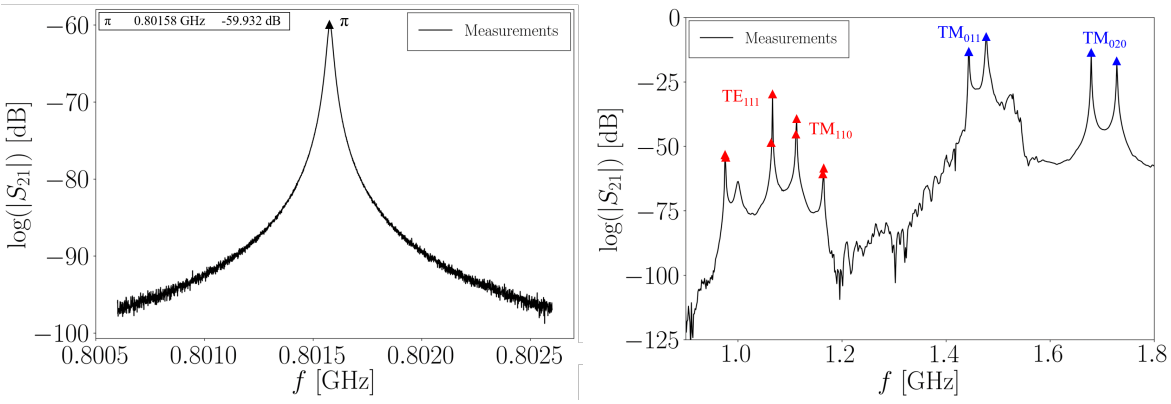

(a) TM_{010}-π mode **(b)** Spectrum from 0.9 GHz to 1.8 GHz

Figure 7.8: Measured S_{21} transmission for the 2-cell cavity with one DQW coupler. The TM_{010}-π mode is indicated by a black triangle in (a). The frequency spectrum from 0.9 GHz to 1.8 GHz, including the trapped monopole (blue triangles) and dipole (red triangles) cavity modes, is shown in (b). Both polarizations of dipole modes are indicated.

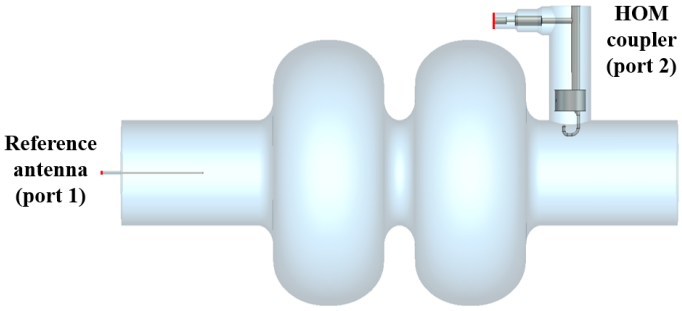

Figure 7.9: Simulated experimental setups in CST for the 2-cell 801.58 MHz cavity with a DQW-type HOM coupler and a reference antenna. Waveguide ports are indicated in red.

to errors in the cell lengths that might be caused during the equator trimming. Cell deformations occurring during the half-cell fabrication also contribute to the frequency deviation. The spring-back effect on the iris of the half-cells may result in a frequency deviation of several MHz for the cavity modes, as outlined in Section 6.1.2.

Table 7.1: Frequency deviation of mode passbands for the 2-cell cavity with a DQW coupler.

Monopole modes			Dipole modes		
Passband	$\lvert\Delta f\rvert_{ave}$ [MHz]	$(\lvert\Delta f\rvert/f)_{ave}$ [%]	Passband	$\lvert\Delta f\rvert_{ave}$ [MHz]	$(\lvert\Delta f\rvert/f)_{ave}$ [%]
TM_{010}	0.011	0.001	TE_{111}	13.379	1.311
TM_{011}	20.335	1.392	TM_{110}	2.804	0.244
TM_{020}	2.380	0.141			

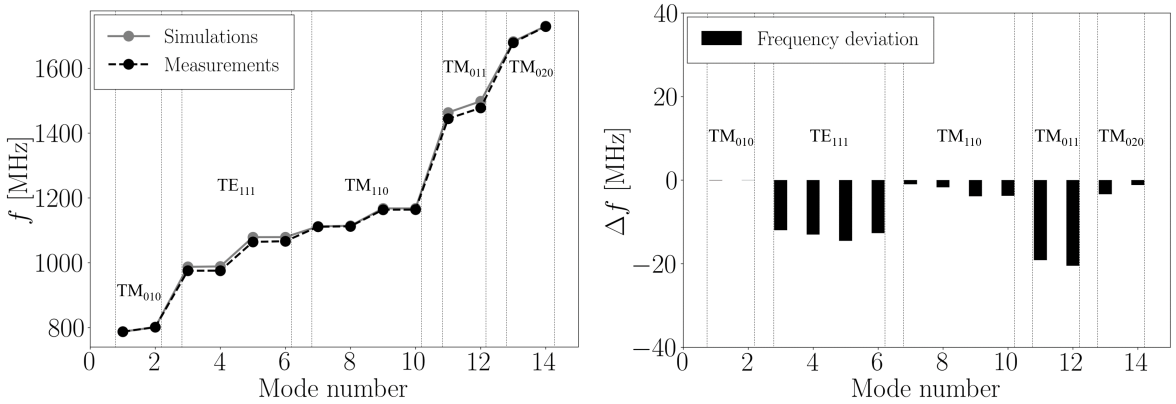

(a) Measured and simulated frequencies **(b)** Frequency deviation

Figure 7.10: Measured and simulated frequencies of the investigated modes for the 801.58 MHz Cu 2-cell cavity with one DQW-type coupler. Black and gray circles depict the measured and simulated frequencies, respectively (a). The deviation between the measured and simulated frequency of each mode is shown in (b).

7.2.2.2 Probe-type coupler: HOM measurements and simulations

This section focuses on the HOM-damping measurements and simulations of the fabricated probe-type coupler mounted on the 2-cell 801.58 MHz Cu cavity. The coupler is installed on one cavity extremity, with the antenna inserted 20 mm into the beam pipe. This value represents the nominal antenna penetration for the three coaxial HOM coupler designs investigated in this thesis (refer to Section 4.2). The other cavity side hosts a reference antenna along the cavity axis to excite monopole modes. The reference antenna is displaced in the transverse directions from the beam axis to excite dipole modes. Several coupler orientations were investigated to determine the dependency of the EM field coupling on the antenna rotation. Figure 7.11 shows the simulated CST models representing the five tested setups.

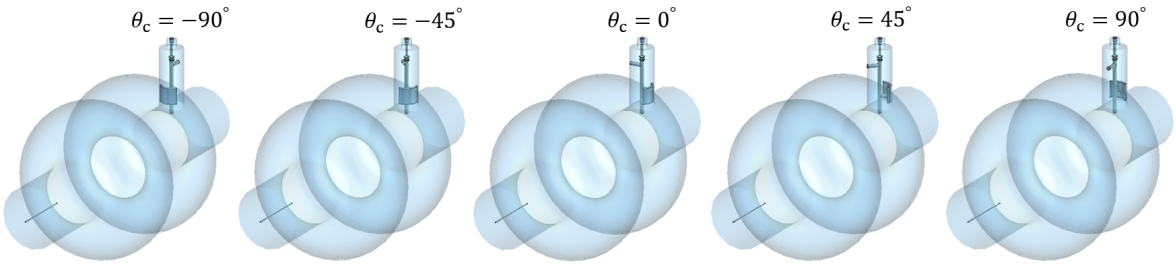

Figure 7.11: Simulated CST configurations for the 2-cell 801.58 MHz cavity with a probe-type HOM coupler and a reference antenna. The five investigated coupler orientations $\theta_c = [-90°, -45°, 0°, 45°, 90°]$ are depicted. The reference antenna and the HOM coupler are terminated with waveguide ports, while PEC boundary conditions are assigned elsewhere.

The active surface of the capacitive plate is aligned perpendicular to the longitudinal axis of the cavity at $\theta_c = 0°$. The plate is oriented to face the cavity end-cell at $\theta_c = -90°$. The capacitive plate is directed towards the beam pipe opening at $\theta_c = 90°$. Figure 7.12 illustrates the comparison between measured and simulated Q_{ext} of concerned cavity modes as a function of the probe-type coupler rotation. The Q_{ext}-values of the investigated monopole and dipole passbands show a moderate dependency on the coupler rotation. The experimental results demonstrate a satisfactory agreement with the simulated values. However, large discrepancies have been found for specific modes that might be due to weak reflection-type signals, coupler misalignment, fabrication tolerances, and weak RF contact in the assembly. The measured Q_{ext}-values of the TM_{010} passband demonstrate consistent behavior across the different coupler orientations, as they remain within the same order of magnitude, i.e., 10^8. The highest suppression of the FM occurs at $\theta_c = -45°$, yielding $Q_{ext} = 4.44 \times 10^8$. On the other hand, simulations suggest higher values for the Q_{ext} of FM passband, ranging from 1.29 $\times 10^9$ to 4.51 $\times 10^{12}$. Although values of Q_{ext} higher than 10^{10} are challenging to measure for the FM, more accurate measurements of the TM_{010}-π mode for the probe-type coupler might be obtained by improving the alignment between the capacitive plate and the coupler outer conductor in the fabrication phase (refer to Subsection 4.3.4.2). In addition, manual tuning techniques, such as contracting the coupler can through a metallic collar, might lead to higher values of the FM Q_{ext} closer to 10^9.

The findings of the measurements reveal that the fabricated probe-type coupler gives higher mitigation for the TM_{011} and TM_{020} monopole passbands, with Q_{ext}-values ranging from 8.74 $\times 10^3$ to 5.77 $\times 10^4$. For all the studied orientations, the measured monopole modes are damped below $Q_{ext} = 10^5$. Conversely, the TE_{111} and TM_{110} dipole passbands present lower damping, with Q_{ext}-values spanning from 3.77 $\times 10^4$ to 2.58 $\times 10^8$. Although a slightly higher FM rejection has been achieved at $\theta_c = -45°$, measurements suggest that both angles $\theta_c = -90°$ and $\theta_c = 0°$ may provide satisfactory FM suppression and HOM mitigation.

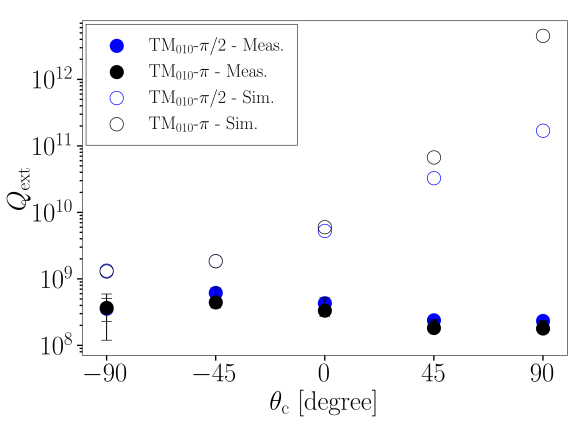

(a) TM_{010} passband

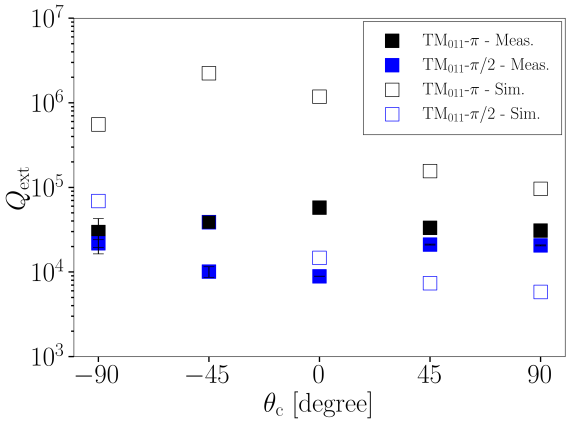

(b) TM_{011} passband

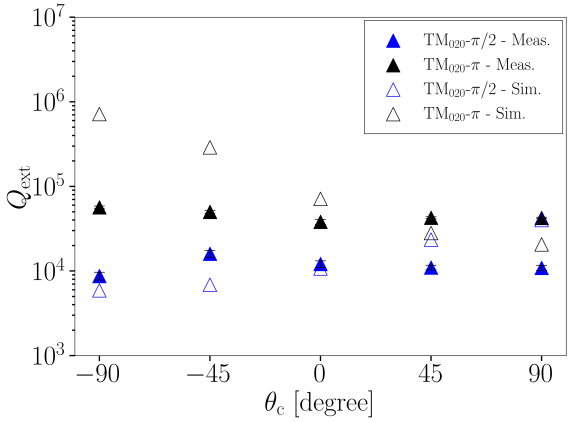

(c) TM_{020} passband

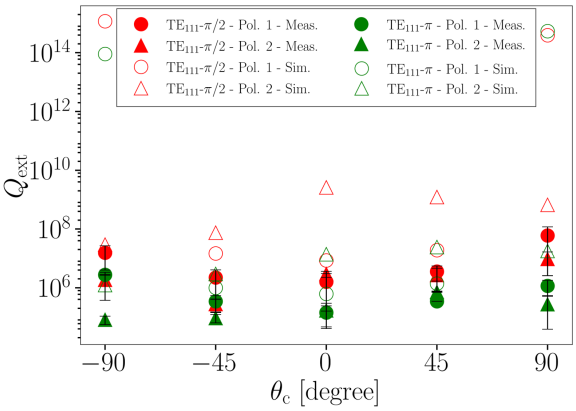

(d) TE_{111} passband

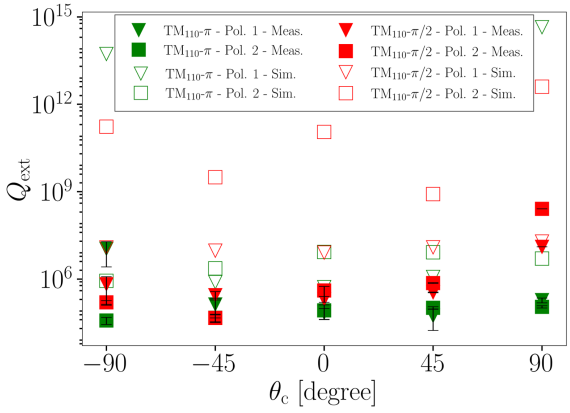

(e) TM_{110} passband

Figure 7.12: Measured ("Meas.") and simulated ("Sim.") Q_{ext} for the relevant monopole (a-c) and dipole (d-e) modes as a function of the probe coupler rotation. The coupler is installed on the right side of the 2-cell Cu cavity with an insertion depth of 20 mm into the beam tube. "Pol. 1" and "Pol. 2" depict the 1st and 2nd dipole polarizations, respectively.

7.2.2.3 Hook-type coupler: HOM measurements and simulations

This section presents the HOM measurements and simulations performed on the fabricated hook-type coupler prototype installed on the 2-cell 801.58 MHz Cu cavity. The transmission is measured from a reference antenna installed on one beam pipe opening to the HOM coupler on the opposite side of the cavity. The same considerations on the position of the reference antenna for HOM excitation, as described in the previous Subsection 7.2.2.2, apply to these measurements. An insertion depth of 20 mm for the coupler antenna into the beam tube was maintained to ensure a fair comparison with the other studied couplers. Figure 7.13 shows the simulated CST models representing the five tested experimental setups. An angle of $\theta_c = 0°$ means that the active surface of the coupling loop is oriented to be perpendicular to the axis of the cavity. The terminal straight road of the coupler is directed towards the cavity end-cell at $\theta_c = -90°$. On the other hand, the terminal road faces the beam pipe entry at $\theta_c = 90°$.

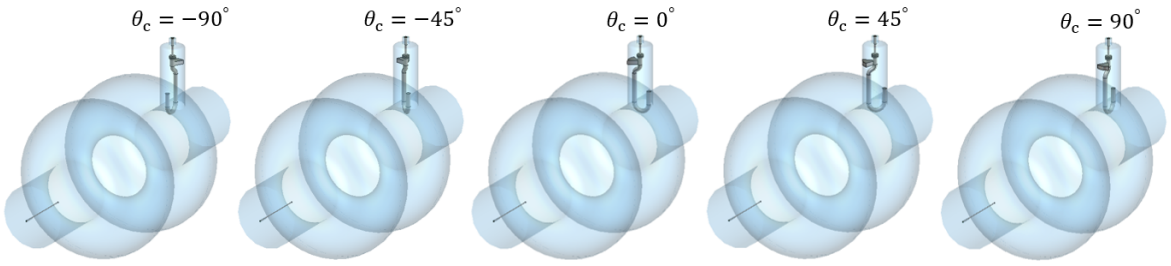

Figure 7.13: Simulated experimental setups in CST for the 2-cell 801.58 MHz Cu cavity with a hook-type HOM coupler and a reference antenna installed on the right-hand side and left-hand side of the cavity, respectively. The subfigures illustrate the five investigated coupler orientations, which are $\theta_c = [-90°, -45°, 0°, 45°, 90°]$. In the numerical model, the reference antenna and the HOM coupler are terminated with waveguide ports having a matched impedance. PEC boundary conditions are employed elsewhere.

Figure 7.14 shows the results of the investigated cavity modes for the hook-type coupler. The TM_{010} mode passband exhibits the greatest variation in response to changes in the coupler orientation. The maximum rejection of the FM is observed for $\theta_c = 0°$, with $Q_{ext} = 7.30 \times 10^9$. The measured Q_{ext} of monopole and dipole passbands show a lower sensitivity to the hook coupler rotation. The majority of the measured HOMs provide external quality factors below 10^5 for the studied orientations. Only a few modes present a slightly higher Q_{ext}. However, the first and second polarizations of the TM_{110}-$\pi/2$ mode present higher measured Q_{ext} in the order of 10^6 and 10^7 at $\theta_c = 90°$, respectively. In general, measurements reasonably agree with simulations. The significant deviations observed in specific modes could arise from various factors. The misalignment of the coupler during its mounting on the beam pipe significantly impacts the resulting Q_{ext}. Section 7.2.2.5 provides additional details about this aspect. Furthermore, reflection-type measurements for modes with small coupling to the coupler antenna can result in measurement inaccuracies. HOM measurements become

even more challenging for dipole modes, where the separate assessment of the two polarizations is typically possible only in limited cases. It is worth noting that in a single-coupler configuration, the effective dipole attenuation is obtained for only one polarization. An additional coupler on the other side of the cavity is needed to mitigate the other polarization. Finally, errors can also arise from imperfect RF contact in the clamped assembly and fabrication tolerances related to the cavity and HOM coupler. For example, a misalignment between the terminal straight road of the coupler loop and the can of the HOM coupler may alter the capacitive gap for the FM notch tuning, leading to a change in FM suppression (refer to Subsection 4.3.4.1).

The results of measurements indicate that the fabricated hook coupler provides higher levels of damping for the two studied dipole passbands (TE_{111} and TM_{110}) in most of the investigated configurations. The TM_{020} monopole passband results in a larger mitigation than the TM_{011} passband. The findings may suggest $\theta_c = 0°$ and $\theta_c = 45°$ as potential optimal angles for rejecting the FM and damping the studied HOMs using the hook-type coupler. Surprisingly, simulations revealed a lower rejection of the FM at $\theta_c = 45°$. A similar trend was observed for $\theta_c = 90°$. These discrepancies between measurements and simulations may be due to the source of errors mentioned above. Therefore, for the studied hook coupler, the orientation $\theta_c = 0°$ may be preferred for the FM rejection and mitigation of HOMs.

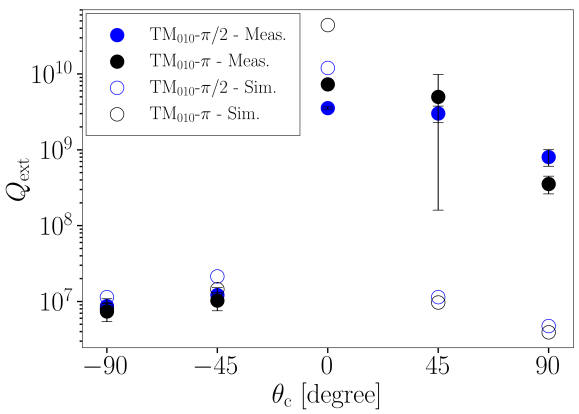

(a) TM_{010} passband

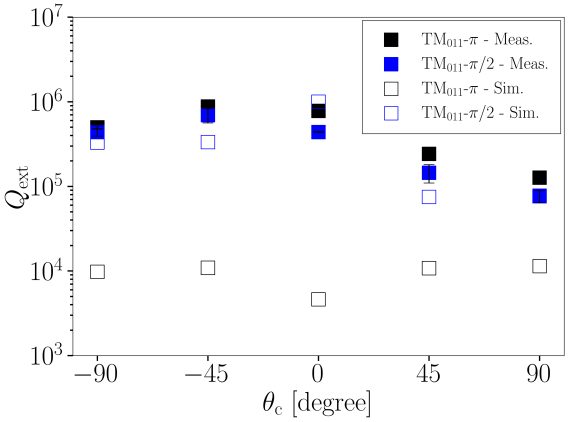

(b) TM_{011} passband

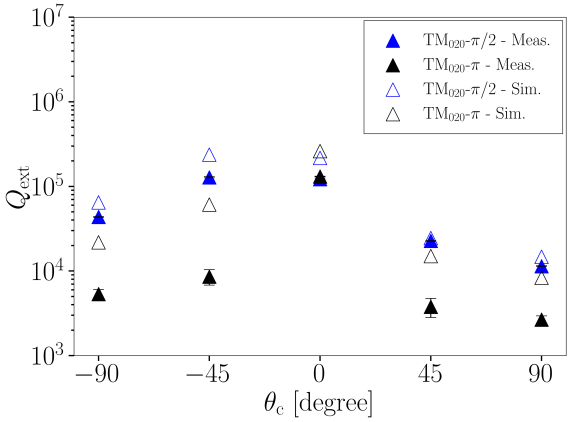

(c) TM_{020} passband

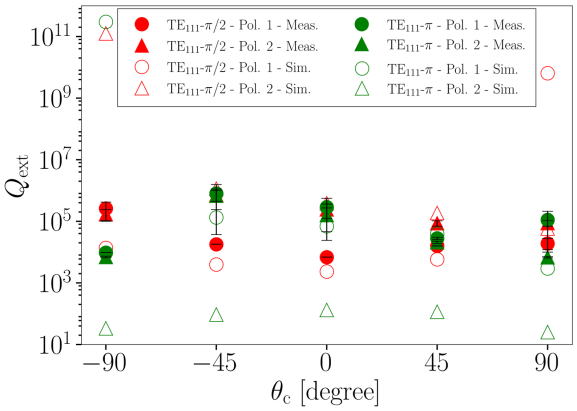

(d) TE_{111} passband

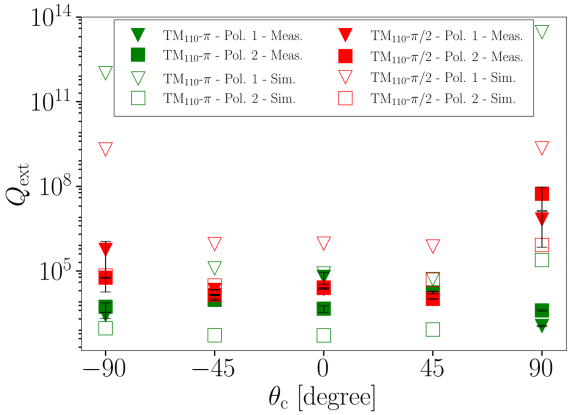

(e) TM_{110} passband

Figure 7.14: Measured ("Meas.") and simulated ("Sim.") Q_{ext} for the relevant monopole (a-c) and dipole (d-e) modes as a function of the hook coupler rotation. The coupler is installed on the right side of the 2-cell Cu cavity with an insertion depth of 20 mm into the beam tube. "Pol. 1" and "Pol. 2" depict the 1st and 2nd dipole polarizations, respectively.

7.2.2.4 DQW-type coupler: HOM measurements and simulations

This section illustrates the HOM measurements on the fabricated DQW coupler prototype installed on the 2-cell Cu cavity and compares them with CST simulations. The RF signals are measured from a reference antenna mounted on one beam pipe entry to the HOM coupler on the opposite cavity side. An insertion depth of 20 mm for the coupler antenna and consistent measurement conditions employed for the previously analyzed HOM couplers were kept. The five measured and simulated coupler configurations on the 2-cell 801.58 MHz cavity are depicted in Figure 7.15. An angle of $\theta_c = 0°$ signifies that the effective surface of the antenna loop is aligned perpendicular to the cavity axis. The terminal straight part of the loop is directed towards the cavity end-cell at $\theta_c = -90°$, while it faces the beam pipe opening at $\theta_c = 90°$.

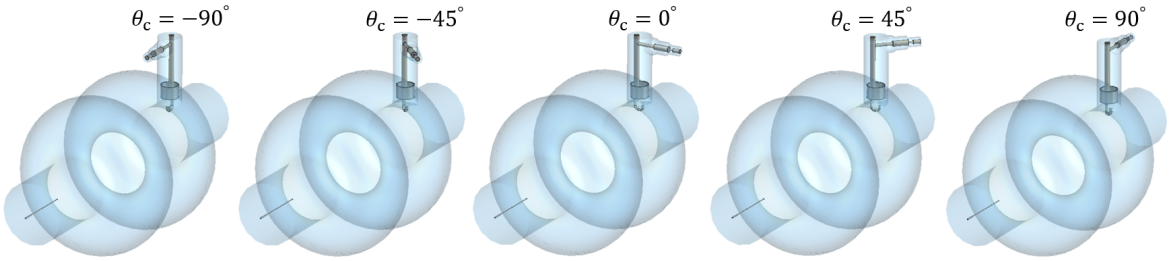

Figure 7.15: Simulated experimental setups in CST for the 2-cell 801.58 MHz cavity with a DQW-type HOM coupler and a reference antenna mounted on the cavity's right and left sides, respectively. The subfigures show the five investigated coupler orientations, which are $\theta_c = [-90°, -45°, 0°, 45°, 90°]$. The numerical model features waveguide ports at the exit of the reference antenna and the HOM coupler, with PEC boundary conditions applied elsewhere.

Figure 7.16 illustrates the results of the measurements and simulations for the investigated cavity modes across various DQW coupler orientations. The experimental findings demonstrate a reasonable agreement with the simulated values. The significant deviations found for specific modes and coupler orientations could be due to fabrication tolerances, coupler misalignment, weak RF contact in the assembly, and small reflection-type signals. The TM_{010} passband presents the largest Q_{ext} change in relation to the coupler orientation. The highest measured FM suppression was achieved at $\theta_c = -90°$, with a corresponding value of $Q_{ext} = 1.88 \times 10^{10}$. The measured monopole and dipole HOMs provide Q_{ext}-values below 10^5, except for the 2nd polarization of the TM_{110}-$\pi/2$ mode ($Q_{ext} = 1.85 \times 10^6$) and the TM_{020}-$\pi/2$ mode ($Q_{ext} = 4.33 \times 10^6$) at $\theta_c = 45°$. The findings may indicate $\theta_c = 45°$ and $\theta_c = -90°$ as potential optimal orientations for damping HOMs. However, the angle $\theta_c = 45°$ provides a relative low rejection ($Q_{ext} = 1.10 \times 10^9$) of the FM compared to the $\theta_c = -90°$. Therefore, $\theta_c = -90°$ may be considered as the most suitable orientation for both rejecting the FM and damping HOMs using the DQW coupler.

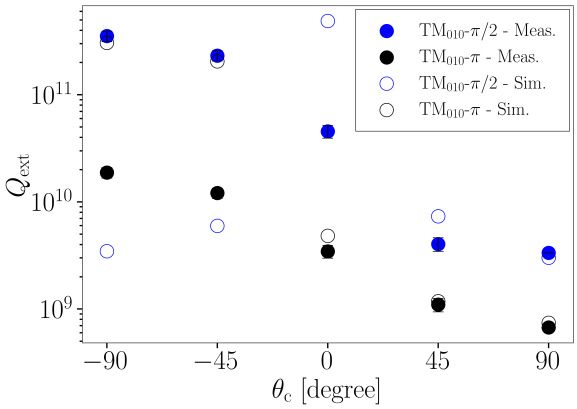

(a) TM_{010} passband

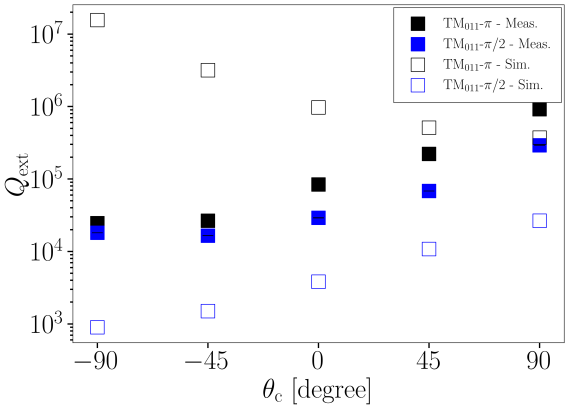

(b) TM_{011} passband

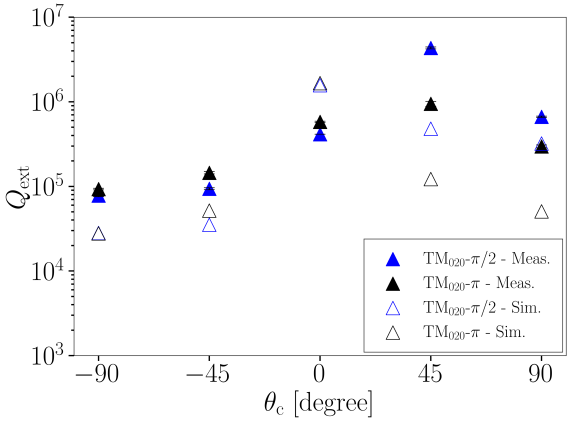

(c) TM_{020} passband

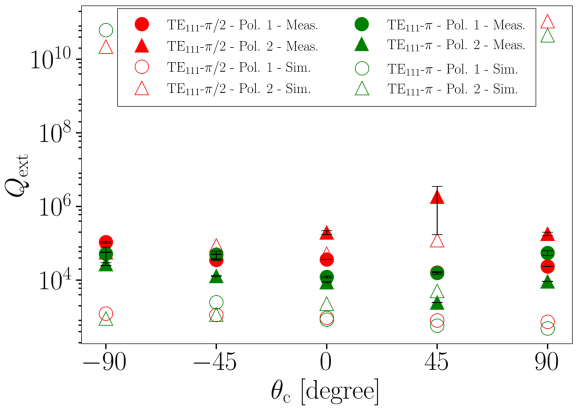

(d) TE_{111} passband

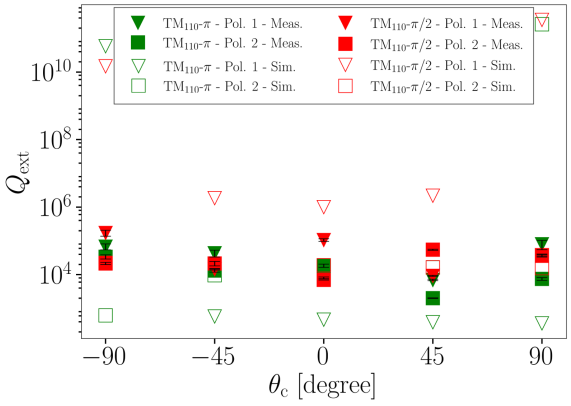

(e) TM_{110} passband

Figure 7.16: Measured ("Meas.") and simulated ("Sim.") Q_{ext} for the studied monopole (a-c) and dipole (d-e) modes as a function of the DQW coupler rotation. The coupler is installed on the right side of the 2-cell Cu cavity with an insertion depth of 20 mm into the beam tube. "Pol. 1" and "Pol. 2" depict the 1st and 2nd dipole polarizations, respectively.

7.2.2.5 Influence of the coupler antenna tilt

HOM couplers are typically designed to couple with cavity modes through the electric or magnetic fields. The orientation of the cavity fields with respect to the plane parallel to the effective surface of the coupler determines the coupling strength for a specific mode. Consider a HOM coupler featuring a loop-shaped antenna, whose active surface is perfectly perpendicular to the cavity axis, as the hook-type coupler at $\theta_c = 0°$ (see Figure 7.13). In simulations, the pick-up loop plane is assumed to be parallel to the magnetic field of the TM_{01} beam-pipe mode to reject the magnetic coupling of the antenna to the FM. In these conditions, the magnetic coupling is nearly zero. Although simulations assume perfect alignment of a plane with respect to a reference surface, in reality, it may be distorted or twisted. The tilt of the coupler, referred to as $\delta\theta_c$, perturbs the mode patterns in the beam pipe, resulting in a change in the EM field coupling. The 2-cell 801.58 MHz cavity with a DQW coupler was simulated in CST to assess the sensitivity of the computed external quality factors of FM and HOMs to small coupler rotations. The simulated coupler tilt ranges from -2.5 to 2.5 degrees with respect to $\theta_c = -90°$, which is the nominal angular position of the DQW antenna in the considered numerical model (refer to Figure 7.15).

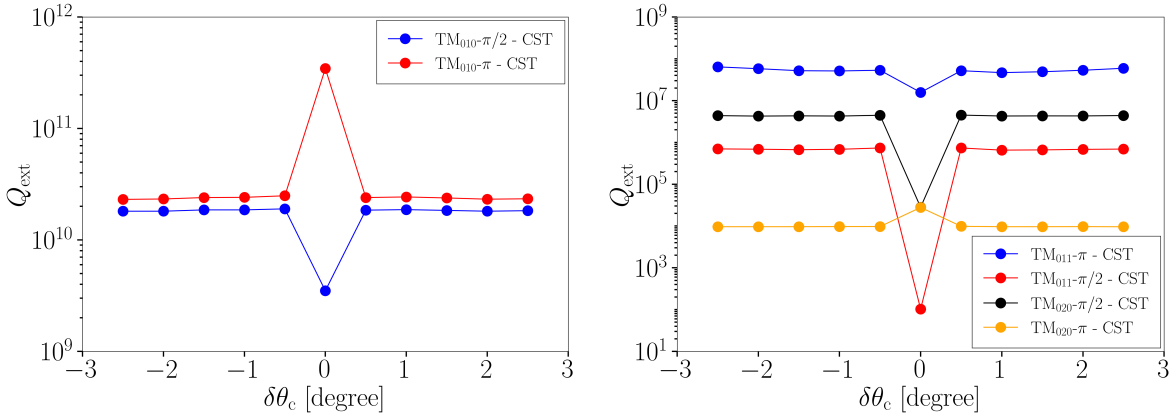

(a) TM_{010} passband **(b)** TM_{011} and TM_{020} passbands

Figure 7.17: External quality factor of relevant monopole modes as a function of the small coupler rotation $\delta\theta_c$: TM_{010} passband (a), TM_{011} and TM_{020} passbands (b).

Figures 7.17 and 7.18 depict the results of the influence of the coupler antenna tilt on the external quality factor of the concerned monopole and dipole modes, respectively. The simulated FM rejection reduces by one order of magnitude when a small tilt of $\pm 0.5°$ is introduced in the coupler antenna. Conversely, the TM_{010}-$\pi/2$ mode exhibits the opposite behavior. The simulated tilt effect reduces the coupling (i.e., Q_{ext} increases) for most of the modes belonging to the TM_{011} and TM_{020} passbands, especially for the $\pi/2$ modes where the Q_{ext} raises from two to the three orders of magnitude for a tilt of $\pm 0.5°$. On the other hand, the coupling of the TM_{020}-π mode

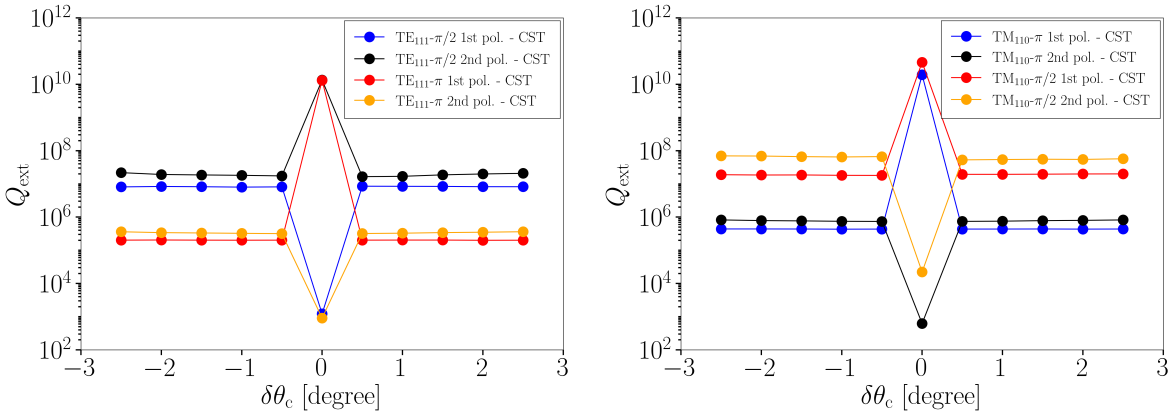

(a) TE_{111} passband **(b)** TM_{110} passband

Figure 7.18: External quality factor of relevant dipole modes as a function of the coupler tilt: TE_{111} (a) and TM_{110} (b) passbands. The two polarizations of the studied dipole passbands are illustrated.

increases (i.e., Q_{ext} decreases) by one order of magnitude. The TE_{111} and TM_{110} dipole passbands are the most affected by the change in simulated damping resulting from the tilt of the coupler antenna. The first polarization of the TE_{111}-$\pi/2$ mode and the second polarization of the TE_{111}-π mode show a simulated increase in Q_{ext} by three orders of magnitude for a tilt of $\pm 0.5°$. The other two polarizations exhibit a lower Q_{ext} for the same amount of tilt. Surprisingly, the Q_{ext} of the first polarization of the TE_{111}-π modes decreases by five orders of magnitudes in the same coupler tilt conditions. Similar changes in damping due to the coupler tilt were observed for the TM_{110} passband. Overall, the variation of the external quality factor as a function of the simulated tilt remains almost symmetrical with respect to the nominal coupler position for small angle variations. The Q_{ext} undergoes in a drastic change when simulating a tilt of $\pm 0.5°$, while remains almost stable from $1°$ to $2.5°$ and from $-1°$ to $-2.5°$. It is worth noticing that these considerations apply specifically for small angular changes of the DQW coupler from its nominal angular position at $\theta_c = -90°$.

Figure 7.19 illustrates the measured Q_{ext} of the DQW coupler at its optimal damping orientation, i.e., $\theta_c = -90°$, along with the simulated Q_{ext}-values for the same angle and a tilt of $\pm 0.5°$. Most simulated values align more closely with measurements when considering a small coupler tilt. This is particularly valid in this specific analyzed scenario for the FM and most dipole modes. However, for the other analyzed modes, the deviation surprisingly increases. This effect may depend on whether the antenna is coupling to the HOMs through the magnetic or electric fields. In conclusion, the simulated effect of the antenna tilt may represent one of the potential causes of the discrepancies found between measurements and simulations, especially for the dipole modes. Depending on the EM coupling to the modes, both the quantitative and qualitative aspects of this simulated analysis may change for other angular positions or even

for other couplers. Additionally, while small variations of the coupler angle lead to a significant change in Q_{ext} in simulations, this aspect results less prominent for small antenna tilts in practical measurements.

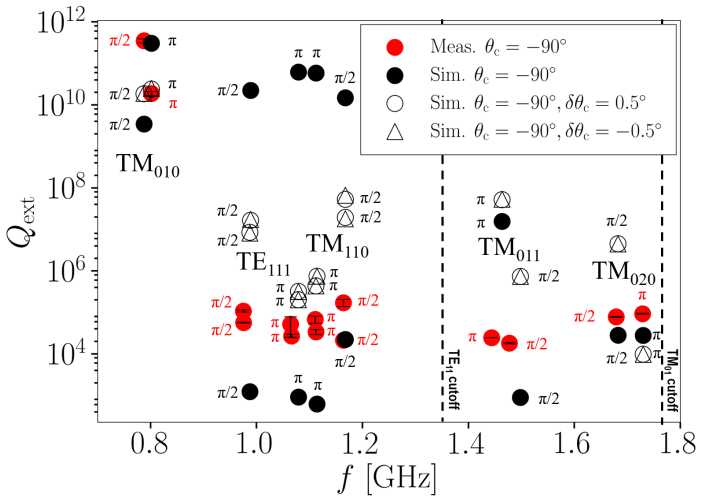

Figure 7.19: Measured (red dots) and simulated (black dots) Q_{ext}-values for the DQW coupler at the optimal position $\theta_c = -90°$ on the 2-cell 801.58 MHz cavity. The simulated values for coupler tilts of 0.5° (white and black contoured dots) and −0.5° (white and black contoured triangles) are depicted. The phase advance of each mode is reported. The dashed lines represent the cutoff frequencies of the TM_{01} and TE_{11} beam pipe modes, respectively.

7.2.2.6 Summary of the HOM measurement results for the 2-cell cavity

Three designs of HOM couplers have been fabricated and tested on a 2-cell PERLE-type 801.58 MHz Cu cavity. The measured Q_{ext}-values align reasonably with the corresponding simulated values. The results of the measurements reveal that the three couplers provide satisfactory levels of FM rejection and damping of HOMs for specific coupler angular positions, notably $\theta_c = 0°$ for the hook-type coupler, $\theta_c = -90°$ for both probe-type and DQW couplers. Figure 7.20 depicts the measured damping performances of the three couplers at their optimal orientations, as determined by measurements.

The DQW-type coupler emerges as the most effective solution for damping both monopole and dipole HOMs of the PERLE 2-cell cavity. In addition, it presents the highest FM rejection among the three studied couplers. The hook coupler remains a valid option for mainly damping dipole modes, with the additional capability of mitigating monopole modes to a slightly lesser extent. The probe coupler stands as a suitable solution only for damping monopole modes below a reasonable mitigation level, in accordance with its electric-coupling design nature.

This study has permitted the initial validation of the design of HOM couplers optimized for the 801.58 MHz PERLE-type cavities. The manufactured HOM coupler prototypes have demonstrated remarkable performances, considering the existing

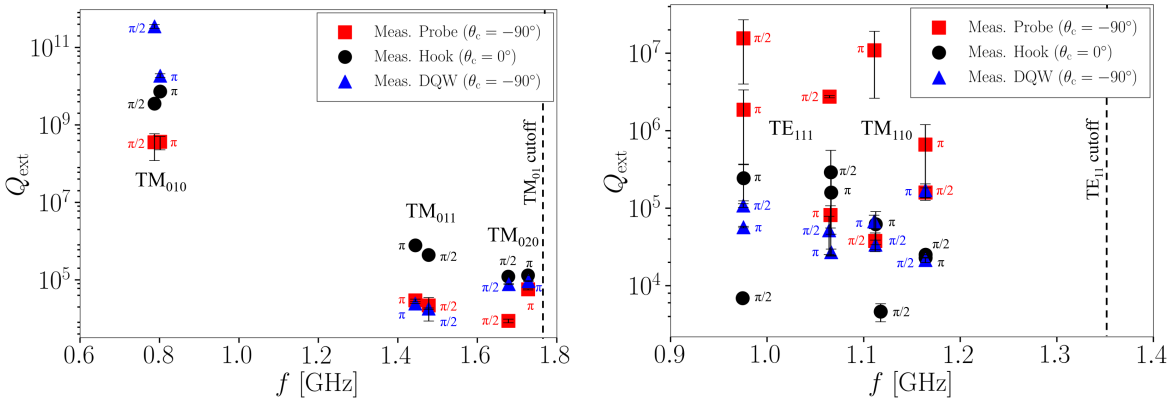

(a) Monopole modes **(b)** Dipole modes

Figure 7.20: Measured Q_{ext}-values for the optimal orientation of probe-type, hook-type, and DQW coupler on a 2-cell 801.58 MHz cavity. The orientation of each coupler antenna refers to Figures 7.11, 7.13 and 7.15. The phase advance for each mode is indicated. The dashed vertical lines in (a) and (b) correspond to the cutoff frequencies of the TM_{01} and TE_{11} beam pipe modes, respectively.

limitations of 3D-printing and copper-coating techniques, which are still considered pioneering in this context (refer to Section 4.3). Further studies are required to enhance the coupler FM rejection by improving the alignment of the antenna to the coupler shell, which is particularly susceptible to material shrinkage, or incorporating innovative tuning mechanisms in future designs. Subsequent to this study, additional couplers have been produced at CERN for the final measurement phase in the 5-cell 801.58 MHz Cu cavity, which will be described in the next section.

7.2.3 5-cell elliptical copper cavity

This section describes the low-power RF measurements performed on the 801.58 MHz 5-cell Cu cavity. Experiments were initially conducted on the bare cavity to analyze the frequency spectrum and HOM frequency deviations compared to the simulated resonant frequencies. Subsequently, two suitable HOM-damping schemes were tested. The first scheme features 2 Probe-type and 2 Hook-type couplers (2P2H scheme), while the second employs 4 DQW-type couplers (4DQW scheme). The results of the measurements and their comparison with simulations are reported in the following sections.

7.2.3.1 Frequency spectrum and deviation

The resonant frequencies of the FM and several monopole and dipole HOMs were measured at room temperature for the 5-cell bare cavity. The RF transmission and reflection through the cavity were recorded across the frequency range from 0.7 GHz

to 1.8 GHz. This range is characterized by the presence of trapped HOMs that can potentially cause coupled-bunch instabilities during the ERL operation (see Subsection 2.2.2). The measurements were carried out using a VNA connected to two reference antennas installed at the opposite beam pipes. Their position was adjusted during the measurements to excite and enhance the visualization of different types of modes. The two antennas were positioned on the cavity axis to excite monopole modes, while they were placed off-axis in opposite directions to measure dipole modes.

Figure 7.21 (a) depicts the measured S_{21} transmission of the TM_{010} mode passband of the 5-cell bare cavity. The five modes composing the TM_{010} passband were correctly identified. The cavity was successfully tuned to the target frequency of 801.58 MHz by tightening the threaded roads that secure the cavity cells. Figure 7.21 (b) illustrates the measured S_{21} transmission for the frequency range of the trapped cavity modes. The HOM passbands are identifiable in the VNA as groups of resonance peaks. A higher Q_L for a certain mode results in a greater S_{21} amplitude at the resonance frequency, along with a narrow and more pronounced resonance peak. On the other hand, modes with lower Q_L lead to a reduced S_{21} amplitude, resulting in a broader resonance peak.

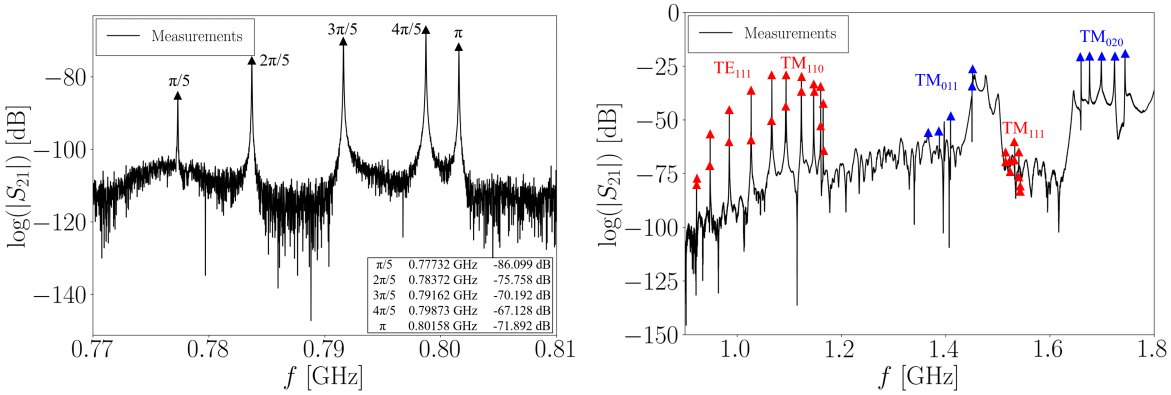

(a) TM_{010}-passband **(b)** Spectrum from 0.9 GHz to 1.8 GHz

Figure 7.21: Measured S_{21} transmission for the bare cavity using two reference antennas. The TM_{010}-passband is shown in (a). The frequency spectrum from 0.9 GHz to 1.8 GHz, containing the trapped modes, is shown in (b). Blue and red triangles indicate the relevant monopole and dipole HOM passbands, respectively. Both dipole mode polarizations are indicated in (b). The phase advance per cell of TE_{111}, TM_{020} and TM_{012} mode passbands takes values from $\pi/5$ to π. The phase of TM_{011}, TM_{110} and TM_{021} modes shifts from π to $\pi/5$.

Different environmental factors, including room temperature, humidity, and pressure, influence the accuracy of the measurements. The thermal expansion or contraction of cavity components can alter their dimensions and impact the resonant frequency of the modes. Assuming a small finite change in cavity volume ΔV, and considering that the active length L_{act} of a 5-cell cavity is predominant with respect to the other two spatial dimensions, it is possible to estimate the change in the resonant frequency Δf_n of a mode n due to the free thermal expansion as [210]

$$\frac{\Delta f_n}{f_n} = -\frac{\Delta L}{L_{\text{act}}} = -\alpha_{\text{L}} \Delta T, \tag{7.36}$$

where f_n is the resonant frequency of the mode n, α_{L} the linear thermal expansion coefficient and ΔT the temperature gradient. The TM_{010}-π mode resulted in a measured frequency of 801.578 MHz at a room temperature of 23.6°C and humidity of 29.2%. For a 1°C temperature variation, assuming $\alpha_{\text{L}} = 17.7 \times 10^{-6}$ 1/°C for the OFHC Cu [211], the frequency sensitivity to the room temperature for the 5-cell cavity is approximately 14.2 kHz. The resonance frequencies are also sensitive to the clamping force acting on the cell equators to secure the different cavity parts. Following the cavity manipulation during the installation and alignment of the HOM couplers, the FM frequency shifted to 801.924 MHz. This 346 kHz frequency change can be due to the deformation caused by the tightening of the threaded rods on the cavity cells. Considering the calculated average trimming parameter on the cell equators of 1.51 MHz/mm, this frequency shift was due to an average reduction of 229 µm in the equator flat length per cavity cell.

Eigenmode analyses were conducted using CST on the 5-cell bare cavity to calculate the resonant frequencies and Q_0-values of trapped modes between 0.7 GHz and 1.8 GHz. PEC boundary conditions were applied to cavity walls and beam pipe ends. The perturbation method was used to compute Q_0-values of HOMs, considering the electrical conductivity value of copper at room temperature (5.8×10^7 S/m). Figure 7.22 (a) compares the measured and simulated frequencies of the FM and the most relevant trapped monopole and dipole modes for the 5-cell Cu cavity. Figure 7.22 (b) illustrates the frequency deviations between measured and simulated frequencies for the investigated modes. Each mode is associated with its respective passband.

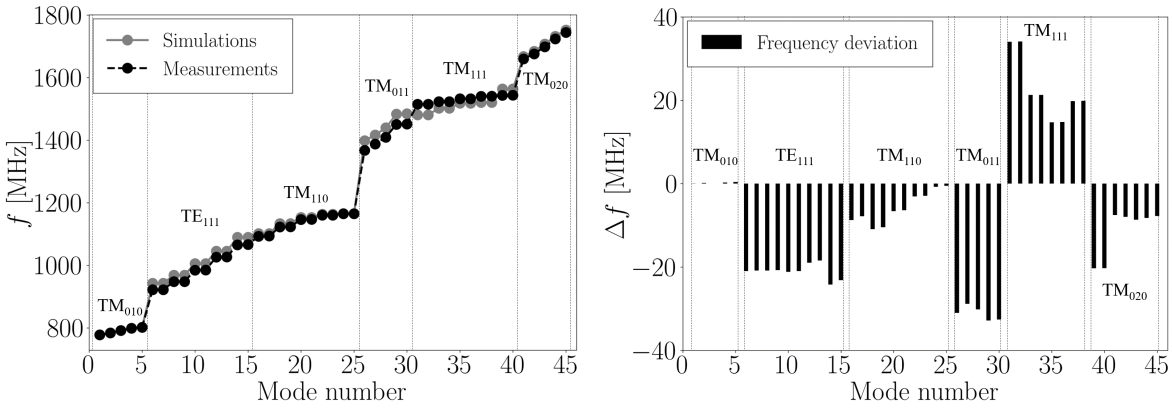

(a) Measured and simulated frequencies **(b)** Frequency deviation

Figure 7.22: Comparison between measured and simulated frequencies of the investigated modes for the 801.58 MHz Cu 5-cell bare cavity. Black circles represent measured frequencies, while gray circles correspond to simulated frequencies (a). The deviation between the measured and simulated frequencies of each mode is depicted in (b).

The average relative frequency deviation among modes within each examined passband ranges from 0.02% to 2.20% (see Table 7.2). This corresponds to an average absolute frequency difference of 0.18 MHz and 31.07 MHz between calculated and measured frequencies, respectively. These measurements provide an initial estimate of the actual frequency variation caused by mechanical tolerances during cavity fabrication and tuning.

Table 7.2: Average frequency deviation of modes within the FM and HOM passbands of the 5-cell cavity.

Monopole modes			Dipole modes		
Passband	$\lvert\Delta f\rvert_{\text{ave}}$ [MHz]	$(\lvert\Delta f\rvert/f)_{\text{ave}}$ [%]	Passband	$\lvert\Delta f\rvert_{\text{ave}}$ [MHz]	$(\lvert\Delta f\rvert/f)_{\text{ave}}$ [%]
TM_{010}	0.18	0.02	TE_{111}	21.01	2.13
TM_{011}	31.07	2.20	TM_{110}	5.80	0.52
TM_{020}	8.01	0.47	TM_{111}	22.05	1.44

Among the monopole and dipole HOMs, those characterized by a longitudinal index $p = 1$ deviate the most from their simulated frequencies. These modes are highly sensitive to changes in the total cavity length and, in turn, the most affected by frequency deviations. Variations of the physical dimensions in radial and azimuthal directions can also influence the resonant frequency of a mode. During the fabrication process of a cavity, errors can occur, yielding discrepancies in the individual cavity cell lengths compared to the design specifications. The global error, especially in the longitudinal direction, tends to accumulate in a multi-cell cavity. As a result, the iris-to-iris cavity length can become longer or shorter than the initially designed length, leading to a frequency shift for these modes. After assembling the cavity cells, the cavity length was measured and found to be approximately 2 cm longer than the designed value of 89.905 cm. This discrepancy corresponds to an average deviation of 2 mm in each individual half-cell length, which can be attributed to the intentional trimming of the equator extra length or fabrication errors. Furthermore, the equator radius in the fabricated half-cells may deviate from the designed value, which can impact the resonant frequency of a mode. Often, the radii of the fabricated half-cell equators are shorter than the intended length due to deformations and errors during the fabrication process. Lastly, the deformation on the iris of the half cells, caused by the springback effect during deep-drawing, can also result in a frequency spread of several MHz, as described in Section 6.1.2.

Due to the relatively large frequency variations found for certain modes, such as TM_{011}, TE_{111}, and TM_{111}, it is fundamental to control them in the Nb cavity 801.58 MHz model and assess their proximity to the harmonics of the circulating bunch. The simulated frequency shifts between the resonant frequencies of the cavity HOMs and the closest lower and higher bunch harmonics are evaluated in Subsection 2.2.2. Ultimately, it is crucial to quantify the frequency spread between the measured HOM

frequencies and the bunch harmonics, as illustrated in Figures 7.23 (a) and (b) for the measured monopole and dipole modes, respectively.

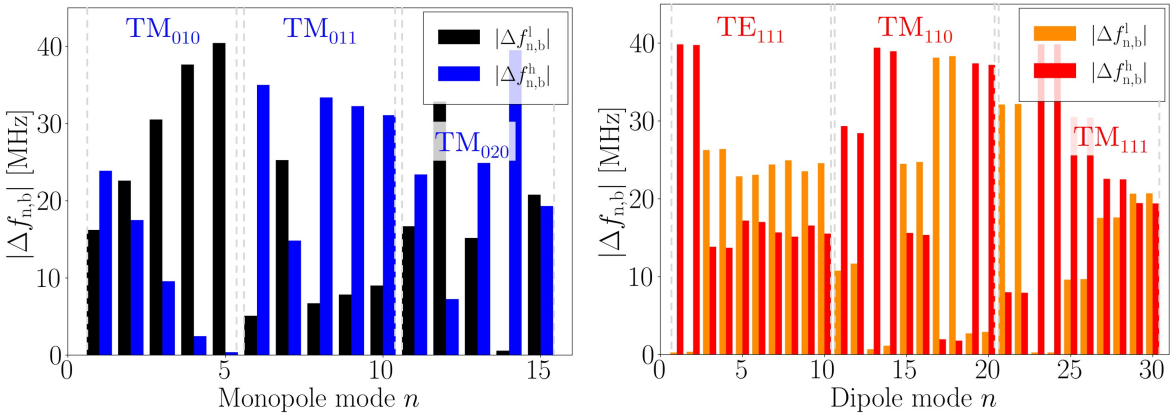

(a) Monopole modes **(b)** Dipole modes

Figure 7.23: Frequency shift between the measured resonant frequency of a mode n and its closest lower and higher bunch harmonics. The absolute difference between the mode frequency and its closest lower-frequency harmonic $|\Delta f^{\mathrm{l}}_{n,\mathrm{b}}|$ is depicted in black for monopole modes (a) and orange for dipole modes (b). The frequency shift to the nearest higher-frequency harmonic $|\Delta f^{\mathrm{h}}_{n,\mathrm{b}}|$ is illustrated in blue for monopole modes (a) and red for dipole modes (b). The resonant frequency associated with each mode is depicted in Figure 7.22.

The frequency spread ranges from 0.57 MHz to 39.51 MHz. The TM_{011} and TM_{020}-type modes are positioned at least 6 MHz away from their closest beam current line, except for the low-$(R/Q)_{\parallel}$ TM_{020}-$4\pi/5$ mode (mode no. 14 in Figure 7.23 (a)), which is separated by 0.57 MHz from its nearest harmonic. The frequency spread of dipole HOMs varies from 0.25 MHz for the low to 39.82 MHz. The frequency shifts of the high-$(R/Q)_{\perp}$ TE_{111}-$3\pi/5$ and TE_{111}-$4\pi/5$ modes (modes no. 5-6 and no. 7-8 in Figure 7.23 (b)) are 17 MHz and 15 MHz, respectively. These modes, whose simulated frequency shift was about 3 MHz (refer to Figure 2.9 (b)), are positioned in the measured cavity spectrum sufficiently away from the beam spectral lines to exclude the possibility of resonant effects. Due to the relatively small frequency shift of only 1 MHz from the nearest harmonic, the high-$(R/Q)_{\perp}$ TM_{110}-$4\pi/5$ mode (modes no. 13-14 in Figure 7.23 (b)) needs to be carefully monitored in the final Nb cavity design. Further analyses regarding the expected HOM frequency spread in the PERLE Nb cavities remain to be studied and are beyond the scope of this analysis.

7.2.3.2 Bead-pull measurements

In general, the identification of HOMs from scattering parameter measurements, as detailed in Subsection 7.2.3.1, can be challenging for a multi-cell cavity. The presence of crossing HOMs passbands, especially at higher frequencies where the spectrum

becomes denser, along with the frequency deviations because of manufacturing tolerances, can complicate the mode identification process. Consequently, the mode identity of the studied HOMs was confirmed using the bead-pull measurements (refer to Section 6.4). The procedure consists of measuring the electric field profile of monopole and dipole HOMs through perturbation and comparing it to the corresponding simulated normalized electric field amplitude. In general, the bead is moved by the stepper motors through the cavity to measure the electric field of the transverse magnetic (TM) monopole modes along the nominal particle bunch trajectory. The longitudinal electric field vanishes on the cavity axis for both TM and TE (transverse electric) dipole modes. As our objective is to capture both the longitudinal and transverse components of the electric field, dipole modes are measured with a transverse offset [212]. In our experimental setup, this is achieved by displacing the bead 10 mm away from the cavity center in the vertical direction using the two motors. The measured and simulated normalized electric field amplitude of two monopole HOMs are presented in Figure 7.24.

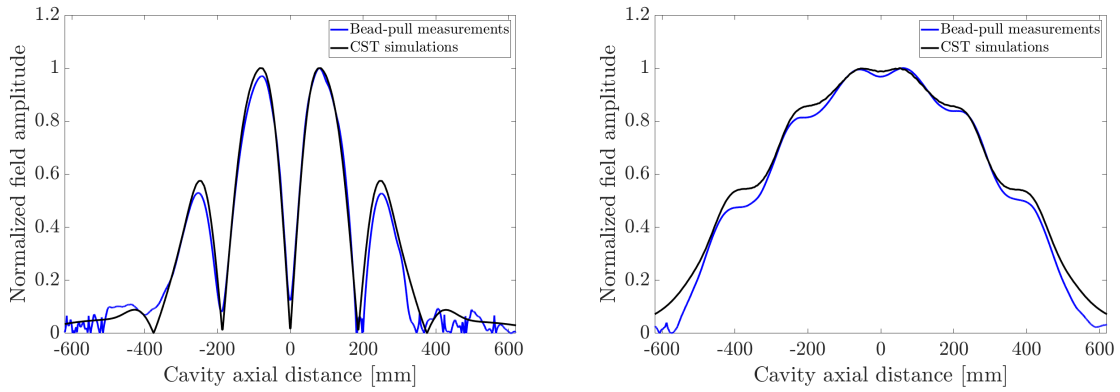

(a) E-field amplitude of TM_{011}-π mode **(b)** E-field amplitude of TM_{020}-$\pi/5$ mode

Figure 7.24: Measured (blue line) and simulated (black line) normalized field profile for the TM_{011}-π mode (a) and TM_{020}-π mode (b) of the 5-cell 801.58 MHz Cu bare cavity.

7.2.3.3 Unloaded quality factor

The standard procedure to measure the unloaded quality factor Q_0 of the cavity modes foresees the measurement of the transmission and reflection signals between an input (port 1) and a pick-up antenna (port 2) installed in the cavity under test. This allows for the calculation for each mode of the coupling parameters β_1 and β_2 for the two ports, as well as the evaluation of Q_L, in order to evaluate the Q_0-values using the equation (7.9). An alternative, more straightforward approach is to calculate the unloaded quality factor from the equation (1.89), assuming $Q_0 \approx Q_L$. This assumption is valid when the external quality factor Q_{ext} of the HOMs is significantly elevated,

i.e., $1/Q_{\text{ext}} \approx 0$. In this case, the Q_{L}-values of the HOMs are mostly dominated by the losses on the cavity walls. This can be achieved using two probe-type antennas with lengths shorter than the beam pipe length to minimize the coupling to the EM field. This alternative method, despite the potential for increased measurement error compared to the standard procedure, was used for the RF measurement on the 5-cell cavity due to the large number of modes that needed to be measured. Measurements were conducted using two 50 mm long probe-type antennas, one on each side of the cavity. Hook-shaped antennas having the same lengths were used for more accurate measurements of the S_{21} and Q_{L}-values of dipole modes. The resulting unloaded quality factors for the potentially dangerous monopole and dipole passband, compared with frequency-domain simulations, are shown in Figure 7.25. The Q_0-deviation from simulated values is depicted in Figure 7.26.

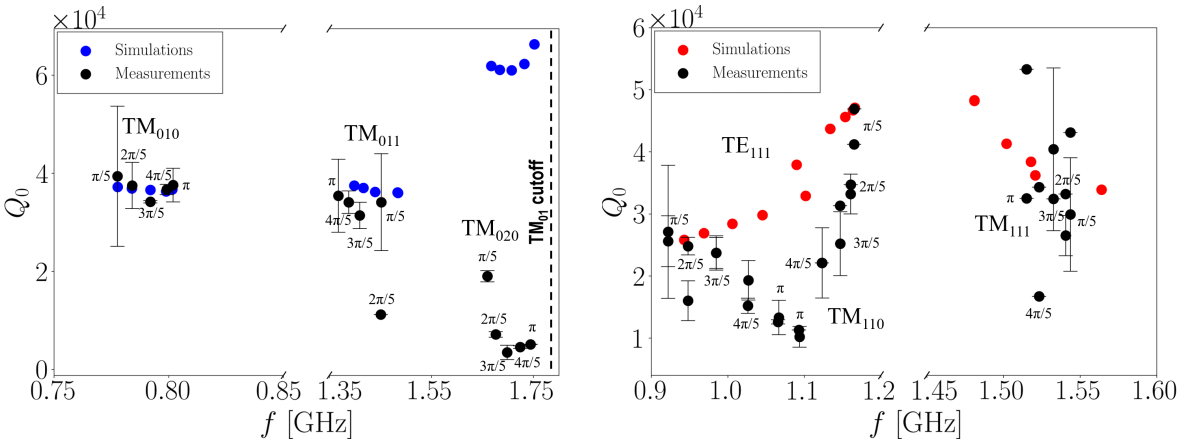

(a) Monopole HOMs **(b)** Dipole HOMs

Figure 7.25: Measured and simulated unloaded quality factors of monopole modes (a) and both polarizations of dipole modes (b) of the 5-cell PERLE cavity. Error bars correspond to multiple measurements conducted using the VNA and fitted in Polfit. Two 50 mm long reference antennas were used for the measurements, one on each cavity beam pipe. The dashed vertical line in (a) denotes the cutoff frequency of the TM_{01} beam pipe mode.

Results show that, for the majority of the studied modes, the simulated Q_0-values are higher than the measured ones. This arises from the assumption that cavity surfaces have superior quality and are in perfect contact with each other in simulations. The simulated Q_0-values for the TM_{010}-passband closely align with measurements. The discrepancy between measurements and simulation for most of the studied monopole and dipole HOMs is less than 60%. A higher spread ($\sim$ 100%) is observed for the TM_{011}-$2\pi/5$ mode (mode no. 9 in Figure 7.26 (a)) and for certain modes within the investigated dipole passband, such as TE_{111}-π mode (modes no. 9-10 in Figure 7.26 (b)) and TM_{110}-π mode (no. 11-12 in Figure 7.26 (b)). The spread increases further for higher frequencies, especially for HOMs whose frequencies are close to the TM_{01} beam

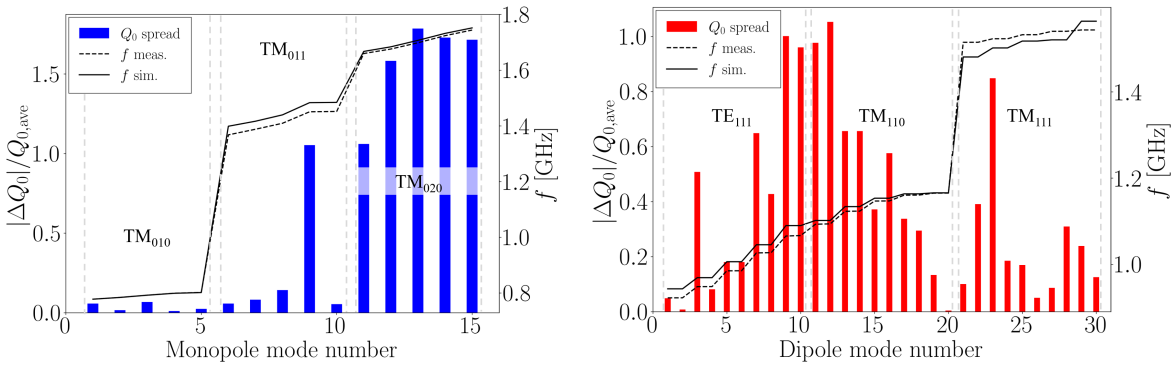

(a) Monopole HOMs **(b)** Dipole HOMs

Figure 7.26: Relative spread of the Q_0-values for monopole modes (a) and both polarizations of dipole (b) modes of the 5-cell PERLE cavity.

pipe cutoff frequency. In these cases, the measurements are also affected by the setup conditions at the entries of the beam pipes, which can be either open or closed during the RF measurements. For example, the simulated Q_0-values of the TM$_{020}$-passband deviate in average from measurements by approximately 150%.

Multiple factors may contribute to the deviations between measurements and simulations observed in several modes. The reference antenna length plays an important role in the precision of these measurements as it determines the coupling to the resonant modes. This, in turn, could impact the validity of our initial assumption, i.e., $Q_0 \approx Q_L$, for these specific measurements. Nevertheless, using 50 mm long antennas during tests yielded satisfactory Q_0-value measurements due to reduced coupling to the resonant modes. Imperfections on the cavity surfaces and weak RF contact between parts in the clamped assembly can result in a lower Q_0-value than the simulated one. Furthermore, S_{21}-measurements for modes with weak coupling to the used antennas can lead to measurement inaccuracy. This is particularly true for the measurements of dipole modes, which are typically characterized by the presence of a double peak on the S_{21} signal. In these cases, the measurement of the first polarization is influenced by the presence of the excited second polarization and vice versa. The two polarizations of the dipole modes could only be measured separately at the VNA in a few instances. The observed discrepancies align with findings in previous studies conducted by Papke *et al.* [213] involving RF measurements on similar cavities. This indicates the consistency of these discrepancies for the conducted RF measurements.

7.2.3.4 HOM-damping measurements and simulations

HOM-damping measurements were conducted at room temperature on the manufactured 5-cell 801.58 MHz elliptical Cu cavity equipped with four 3D-printed and copper-coated HOM coupler prototypes for the relevant monopole and dipole mode passbands

(see Figure 7.6 (b)). The study focused on HOM measurements of the 2P2H and 4DQW damping endgroups. The positioning of HOM couplers on the cavity was executed as illustrated in Figure 7.27. The two couplers on the left-hand beam pipe are positioned 78 mm from the straight wall of the adjacent end-cell, while the couplers on the opposite side are at a distance of 69 mm from their neighboring end-cell. The two couplers on each beam pipe are mounted to form an angle of 120° between their axes. A penetration depth of 20 mm for the coupler antenna into the beam tube was set for all the couplers. These technical specifications were chosen based on mechanical integration and HOM-damping considerations discussed in Chapter 5. Figure 7.27 depicts the simulated CST models representing the two tested experimental setups. The measurements were compared to eigenmode simulations to validate the adequacy of our measurement setup (refer to Subsection 7.2.1) in measuring Q_{ext} of cavity modes.

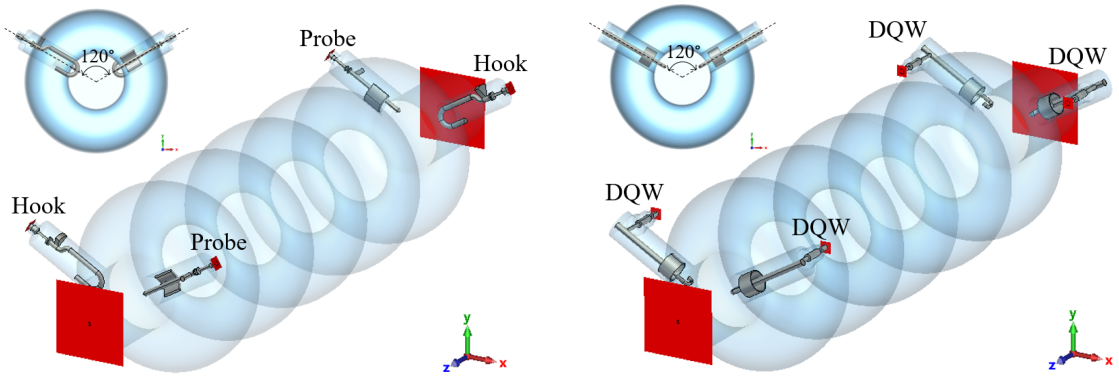

(a) 5-cell cavity with 2P2H scheme **(b)** 5-cell cavity with 4DQW scheme

Figure 7.27: Simulated setup in CST including the 5-cell 801.58 MHz cavity equipped with HOM couplers: (a) 2P2H and 4DQW (b) schemes. Waveguide ports are indicated in red.

PEC boundary conditions are applied to the cavity walls and HOM coupler surfaces. Beam pipe entries and HOM couplers are terminated with WG ports to simulate the HOM power propagating into the ports. The lossy CST eigenmode solver is used to calculate the resonant frequencies and Q_{ext}-values for the investigated modes. The measurement procedure employed is described in Section 7.2.1. Since our focus is on measuring the overall damping performance of the multi-coupler scheme, the loaded quality factor, or total Q, could be measured between two couplers only while terminating the other two couplers with dummy loads. First, the loaded quality factor Q_{L} is determined from the resonant frequency and 3 dB bandwidth of the measured S_{21} transmission for each monopole and dipole mode. Using the Q_0-values measured on the 5-cell bare cavity in Section 7.2.3.3, the external quality factor for each mode n in the analyzed damping schemes could be calculated as

$$Q_{\text{ext},n} = \left(\frac{1}{Q_{\text{L},n}} - \frac{1}{Q_{0,n}} \right)^{-1} . \tag{7.37}$$

The resulting Q_{ext}-values for the potentially dangerous monopole and dipole passbands, compared with frequency-domain simulations, for the 2P2H and 4DQW damping structures are shown in Figures 7.28 and 7.29, respectively.

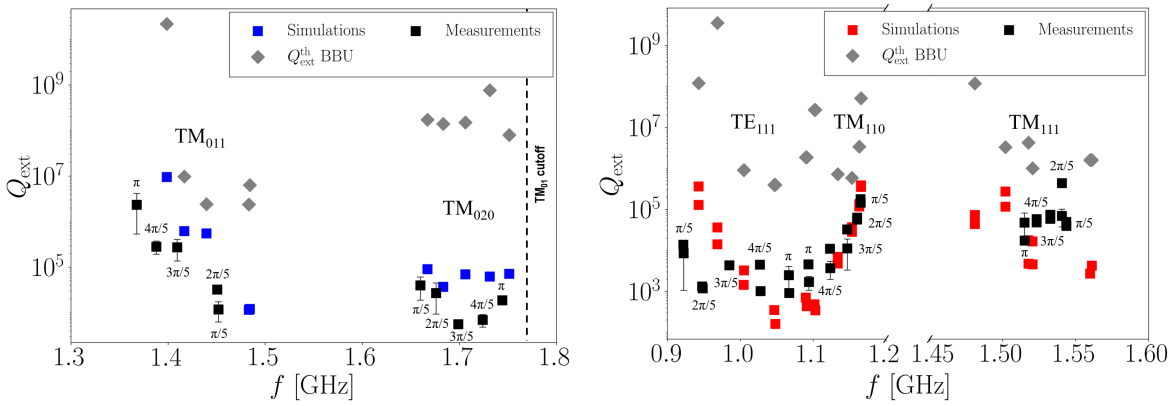

(a) Monopole HOMs - 2P2H scheme **(b)** Dipole HOMs - 2P2H scheme

Figure 7.28: Measured and simulated Q_{ext} of monopole modes (a) and both polarizations of dipole modes (b) for the 2P2H damping scheme on the 5-cell PERLE cavity. Error bars reflect Q_{ext} variation observed in distinct measurements. One hook-type and probe-type coupler are installed on each side of the cavity, each with a penetration depth of 20 mm into the cutoff tube. The critical Q_{ext}-values (gray diamonds) are computed for the current $I_{\text{b,op}}$=120 mA.

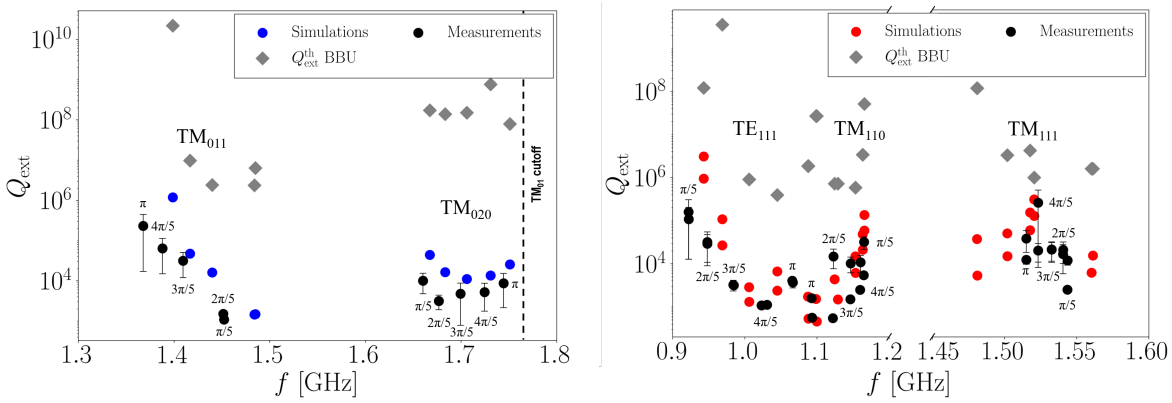

(a) Monopole HOMs - 4DQW scheme **(b)** Dipole HOMs - 4DQW scheme

Figure 7.29: Measured and simulated Q_{ext} of monopole modes (a) and both polarizations of dipole (b) modes for the 4DQW damping scheme on the 5-cell PERLE cavity. Error bars reflect Q_{ext} variation observed in distinct measurements. Two DQW couplers are placed on each side of the cavity, each with a penetration depth of 20 mm into the cutoff tube. The critical Q_{ext}-values (gray diamonds) are computed for the current $I_{\text{b,op}}$=120 mA.

The results demonstrate a satisfactory agreement between measured and simulated external quality factor values for both analyzed damping schemes. For the majority of

modes, the measured Q_{ext}-values range between 10^3 and 10^5, and they are lower than the simulated ones. Some modes provide external quality factors higher than 10^5. For example, by referring to the 2P2H damping scheme, the TM_{011}-π mode at 1.368 GHz has $Q_{\text{ext}} = 2.34 \times 10^6$. However, this mode possesses $R/Q_{\parallel}$=6×10^{-3} Ω, which is the lowest R/Q-value among modes of the TM_{011} passband (see Table 3.1), and it safely damped below its BBU threshold. The same mode exhibits $Q_{\text{ext}} = 2.31 \times 10^5$ in the 4DQW damping scheme. The second polarization of TM_{111}-$2\pi/5$ mode shows the highest measured Q_{ext} among the trapped dipole modes, reaching 4.4×10^5 in the 2P2H scheme. This mode has the highest transverse impedance ($(R/Q)_{\perp} Q_{\text{ext}} \approx 2 \times 10^5$ kΩ/m) among the modes of the TM_{111} passband. Nevertheless, this HOM is mitigated with $Q_{\text{ext}} = 2.1 \times 10^4$ in the 4DQW scheme. In both damping schemes, the measured HOMs exhibit a safety margin of at least one order of magnitude compared to the simulated BBU Q_{ext} thresholds for the PERLE accelerator operating at a beam current of 120 mA. The measurements suggest that the analyzed 4DQW damping scheme demonstrates higher efficiency in damping the majority of confined monopole and dipole HOMs below their BBU stability limits than the 2P2H damping scheme (see Figure 7.30), confirming the validity of our simulation predictions.

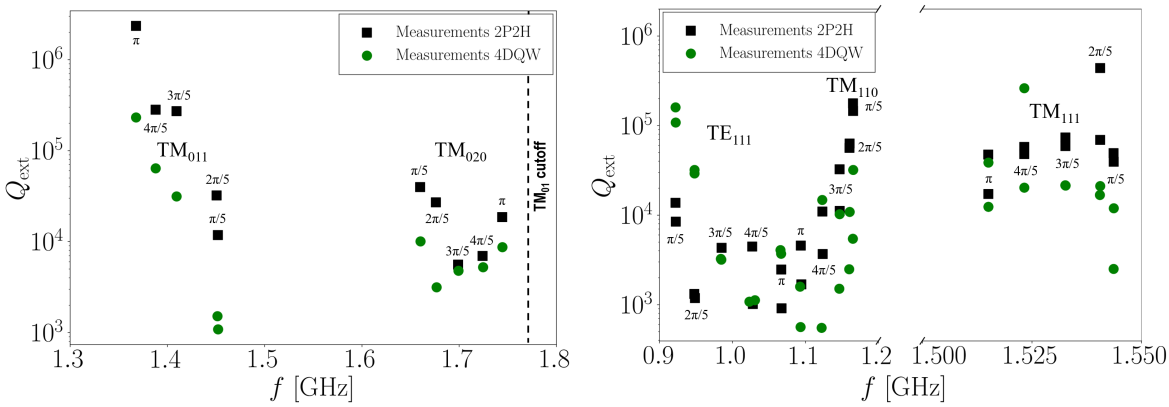

(a) Monopole HOMs **(b)** Dipole HOMs

Figure 7.30: Measured external quality factors for the 2P2H and 4DQW HOM-damping schemes. The HOM couplers are installed on the 5-cell Cu cavity as depicted in Figure 7.6 (b). The orientation of each coupler antenna is illustrated in Figure 7.27. The phase advance for each mode is indicated.

The discrepancies observed between measured and simulated Q_{ext}-values could be due to various factors. The orientation of each coupler antenna is crucial in damping HOMs. As described in Subsection 7.2.2.5 and demonstrated in our previous work [123], a small simulated tilt $\delta\theta_{\text{c}}$ of the coupler antenna in CST (for example, $\pm 0.5°$ with respect to the design position) can influence its coupling to the electromagnetic field of HOMs. This changes the simulated Q_{ext} up to several orders of magnitudes for certain modes. Moreover, only in limited cases, the S_{21} signal was measured separately for the

two polarizations of dipole modes. The coexistence of both polarizations in the dipole mode signal can lead to inaccuracies in measuring Q_{L} when the amplitude of their S_{21}-values is comparable. Finally, cavity surface imperfections, errors in manufacturing the cavity, and the HOM couplers, as well as the weak RF contact in the clamped assembly, are possible reasons for the found Q_{ext} deviations.

Conclusions and perspectives

The PERLE facility study envisions building a compact three-pass ERL based on SRF technology. Its main goal is demonstrating the high-current (20 mA injection beam current), continuous wave, multi-pass operation with SRF cavities at 801.58 MHz to validate options for future higher-energy machines, such as the 50 GeV ERL foreseen for the LHeC and the FCC-eh. The regenerative multi-pass BBU is a relevant phenomenon in high-current ERL, like PERLE. The main motivation for this thesis was to design, build, test, and analyze coaxial HOM couplers for the PERLE cavities, with the ultimate goal of proposing several damping options capable of mitigating HOMs below BBU instability limits. This work considers the 500 MeV PERLE ERL configuration.

The PERLE accelerator complex layout, the SRF cavity design, and HOM identification were covered in Chapter 2. The 5-cell 801.58 MHz Nb cavity design built at JLab was selected for the PERLE project. Potentially dangerous monopole and dipole HOMs have been identified using eigenmode simulations in CST. The first monopole passband (TM_{011}) and the first two dipole passbands (TE_{111}, TM_{110}) are the most problematic parasite modes due to their high R/Q values. These HOMs may lead to beam instabilities if not adequately damped. The proximity of the HOMs to the beam harmonics has also been assessed to prevent the potential voltage buildup from their possible resonant interaction with the highest current harmonics. Simulation results show that concerned HOMs are sufficiently separated from their nearest beam harmonic to exclude the possibility of resonant effects with the circulating beam. The power consumption of the cryogenic system has also been evaluated. The static and dynamic losses for each of the two PERLE linacs are estimated to be $P_{\mathrm{st}} = 37.4$ W and $P_{\mathrm{dyn}} = 107.5$ W, respectively. The required AC wall power per linac is roughly $P_{\mathrm{t,AC}} = 108$ kW. The total input power needed per cavity was evaluated in the on-crest and off-crest ERL operating scenarios. Given the cavity nominal gradient of 22.4 MV/m, the total beam power per cavity of 1.23 MW, and assuming a microphonic detuning of 60 Hz and a fixed input coupler with $Q_{\mathrm{L,0}} = 2.5 \times 10^6$, the estimated input power per cavity is 103 kW for the considered off-crest scenario and 92 kW for the on-crest scenario. The required input power can be further reduced by controlling the microphonics effect through a Ferro-Electric Fast Reactive Tuner (FE-FRT).

The BBU instabilities were discussed in Chapter 3. The longitudinal and transverse impedance thresholds were analytically calculated for the PERLE cavity considering

an operating beam current of 120 mA. The resulting longitudinal impedance threshold follows the fit equation $Z_{\parallel}^{\text{th}}[\text{k}\Omega] = 2.12 \times 10^5 f^{-1}[\text{GHz}]$, while transverse impedance threshold value is $Z_{\perp}^{\text{th}} = 5.23 \times 10^5$ kΩ/m and is independent of the frequency. The impedance thresholds were used to compute the critical external quality factors for concerned HOMs above which BBU instabilities may occur. The critical Q_{ext} were compared with simulation results from Lancaster's BBU-tracking model, revealing similar trends. Results also demonstrate that Ampere level threshold currents can be achieved in PERLE when considering typical Q_{ext} ranging from 10^3 to 10^5.

The RF transmission of three coaxial HOM couplers, namely the probe (P), hook (H), and DQW couplers, has been optimized to damp the dangerous HOMs of the 5-cell 801.58 MHz PERLE cavity while preserving the fundamental mode efficiency (see Chapter 4). Simulations were performed using the CST frequency domain solver. The high-impedance HOMs and FM notch filter requirements for the selected designs have been globally satisfied. The DQW-type design emerges as the most advantageous solution for damping simultaneously the first monopole and the first two dipole passbands. After optimizing their RF transmission, prototypes of each HOM coupler were fabricated to test their performance in 2-cell and 5-cell 801.58 MHz Cu PERLE cavities. The HOM coupler prototypes were 3D printed in epoxy resin (Accura 25 and Accura 48 HTR) and then copper-coated using an electroplating process. The study has successfully demonstrated the feasibility of copper-plating for 3D-printed epoxy-based HOM couplers, confirming that the applied carbon substrate facilitates copper adhesion to the polymer surfaces. Yet, the coating technique did not allow full control of copper deposit homogeneity throughout the process. The Accura 48 HTR epoxy emerges as a better-suited material for electrolytic copper-plating because of its higher stiffness and thermal stability than the Accura 25. 3D-scanning measurements were performed on each manufactured coupler to assess the shape deviation between the ideal 3D CAD model and the actual geometry. The metrological analyses suggest that most of the measured surface regions fall within the set tolerance range of $\pm$ 0.5 mm after the coating process. Furthermore, the estimated average coating thickness on coupler surfaces spans from approximately 200 µm to 350 µm, successfully exceeding the minimum coating average thickness of 30 µm required to ensure the desired electrical conductivity properties in the considered operating frequency range of the studied HOM couplers.

The optimized HOM coupler designs were combined into two HOM endgroups and simulated with the 5-cell 801.58 MHz PERLE cavity (refer to Chapter 5). The HOM-damping performance and thermal behavior due to RF-heating were studied for two HOM endgroups: the 2 Probe-type and 2 Hook-type couplers (2P2H scheme) and 4 DQW-type couplers (4DQW scheme). An adapted version of the SPL-type fundamental power coupler was also included in the simulations. Wakefield and eigenmode simulations were performed in CST to compute the longitudinal and transversal cavity impedances. Both analyzed HOM-damping schemes lower the cavity impedance

below the BBU instability limits. The 4DQW damping scheme demonstrates stronger HOM damping for both longitudinal and transverse impedances compared to the 2P2H option. Furthermore, its symmetrical design ensures the preservation of dipole HOM symmetry. The average HOM power of the 5-cell cavity in the 500 MeV PERLE version is estimated to be approximately 103 W. The HOM power deposited by the beam into the cavity and extracted through HOM couplers was also evaluated in the time domain, considering the beam-filling pattern dependency. The couplers of the 4DQW endgroup exhibit a higher rate of HOM power extraction compared to the couplers of the 2P2H scheme. Because of the relatively short longitudinal bunch length of 3 mm foreseen for PERLE, a large amount of HOM power propagates through the cavity beam pipes. The inclusions of beamline absorbers between cavity tubes allowed the absorption of part of the propagating HOM power within the tolerable power heat flux limits. The RF-heating analyses performed in COMSOL Multiphysics demonstrated that in the 2P2H damping scheme, the maximum temperature on the coupler parts is successfully lowered below the quench limit under the simulated conduction cooling conditions. The 4DQW scheme experiences a quench under the same cooling conditions due to the higher rate of HOM power absorption. Simulating additional convective cooling through He-channels on the DQW coupler inner conductor has successfully lowered the maximum temperature below the quench limit. Therefore, cooling channels are needed for the safe operation of Nb DQW couplers in the superconducting state.

The first Cu 5-cell 801.58 MHz cavity was manufactured at JLab (see Chapter 6) for conducting low-power RF R&D bench measurements. Frequency deviations of resonant modes from the ideal cavity shape due to mechanical tolerances, and mainly to the springback effect, were evaluated. Dumbbell measurements were performed on the cavity half-cells. The assembled cavity was successfully tuned at the 801.58 MHz target frequency. Bead-pull measurements on the fundamental mode indicate that a satisfactory field flatness of 96% was achieved.

Low-power RF measurements on the 2-cell and 5-cell 801.58 MHz PERLE-type Cu cavities were performed at JLab (refer to Chapter 7). The frequency spectrum of both cavities was analyzed. The mode passbands reporting the largest average relative frequency deviations from the simulated frequency spectrum are the ones with longitudinal index $p = 1$. These modes are the most sensitive to errors due to the equator trimming. The springback effect might also be the cause of the frequency deviation of several MHz detected on the measured cavity mode passbands. The fabricated HOM couplers were tested individually on the 2-cell PERLE-type cavity, and their optimal damping orientations were determined. The experimental findings demonstrate a reasonable agreement with the simulated eigenmode results. Measurements confirm that the DQW coupler is the most effective solution for damping both monopole and dipole HOMs. HOM-damping measurements were conducted on the 5-cell Cu cavity with the manufactured 2P2H and 4DQW HOM endgroups. Bead-pull measurements were conducted to identify HOMs based on their field profile. The measured Q_{ext}-values of concerned resonant modes agree reasonably with the corresponding simulated values.

The experimental results show that the two analyzed HOM-damping options provide adequate mitigation of HOMs below the BBU instability Q_{ext} thresholds. Moreover, the 4DQW damping scheme performs better in damping confined cavity modes, confirming the validity of our simulation predictions.

This thesis has initiated the groundwork for the design, optimization, fabrication, and experimental performance validation of the HOM coupler endgroups intended for the fully dressed 5-cell cavity for PERLE. It has encompassed multiple disciplines, including beam dynamics, radio-frequency domain, and combined RF-heating effects. The simulation work has culminated in fabricating a copper cavity prototype from scratch. Furthermore, HOM coupler prototypes were manufactured using an innovative approach based on the combined epoxy-based 3D-printing technology with a copper-coated technique suitable for RF applications. Low-power RF measurements have been finally performed to validate the performance of the produced HOM coupler prototypes. Nevertheless, certain aspects of the HOM coupler and cavity designs can be further refined and studied in the future, in view of the production of Nb HOM couplers to be installed in the final 5-cell 801.58 MHz Nb cavities. These include the design of cooling channels and thermal intercepts to mitigate the RF-heating of Nb HOM couplers and beamline absorbers. The FM notch detuning of Nb couplers due to thermal contraction and the multipacting effect needs to be studied. Further studies are needed to limit the deformations associated with the shrinkage during coupler 3D printing and subsequent copper coating and improve the copper deposit homogeneity. The springback effect and mechanical tolerances needed to be carefully addressed during the Nb elliptical cavity fabrication. Conducting low-power RF measurements on a soldered cavity for better RF contact and enhancing the measurement setup, such as including a bipolar HOM excitation device able to separate the two polarization of dipole modes, might reduce the discrepancies observed between measurement and simulations in the future.

A 5-cell cavity and HOM couplers for PERLE

In the context of this thesis, three 3D-printed epoxy and copper-coated HOM coupler prototypes were fabricated. The HOM couplers were mounted on the beam pipes of both the 2-cell and 5-cell 801.58 MHz Cu cavities developed for PERLE to assess their damping performances. The mechanical designs of the probe-type, hook-type, and DQW-type PERLE HOM couplers are depicted in Figures A.1, A.2, and A.3, respectively. Figure A.4 illustrates the mechanical design of the 5-cell 801.58 MHz PERLE cavity. The mechanical drawings were performed by Samuel Roset and Gilles Olivier at IJCLab based on the specifications provided by the thesis author.

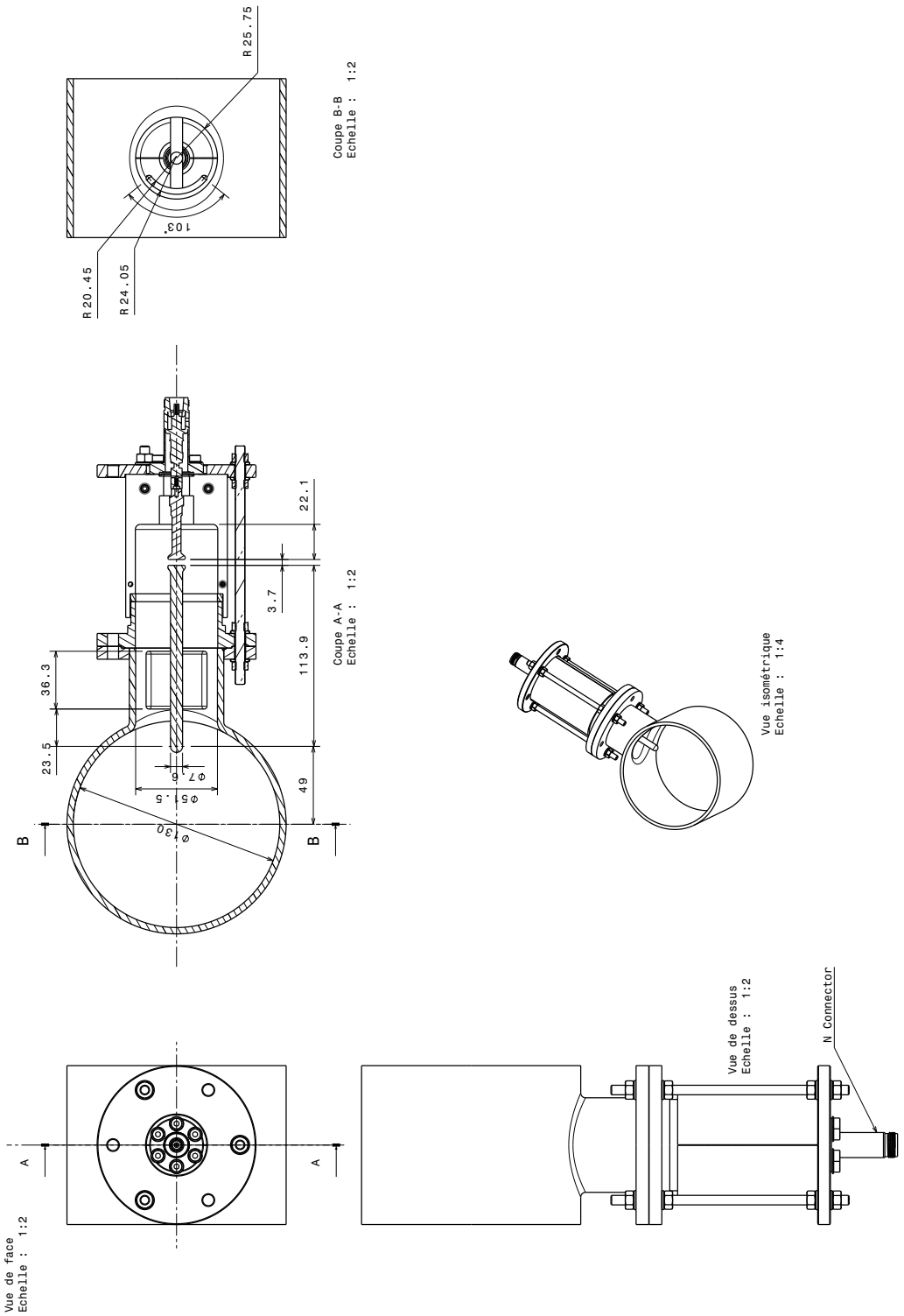

Figure A.1: Mechanical design of the probe-type PERLE HOM coupler.

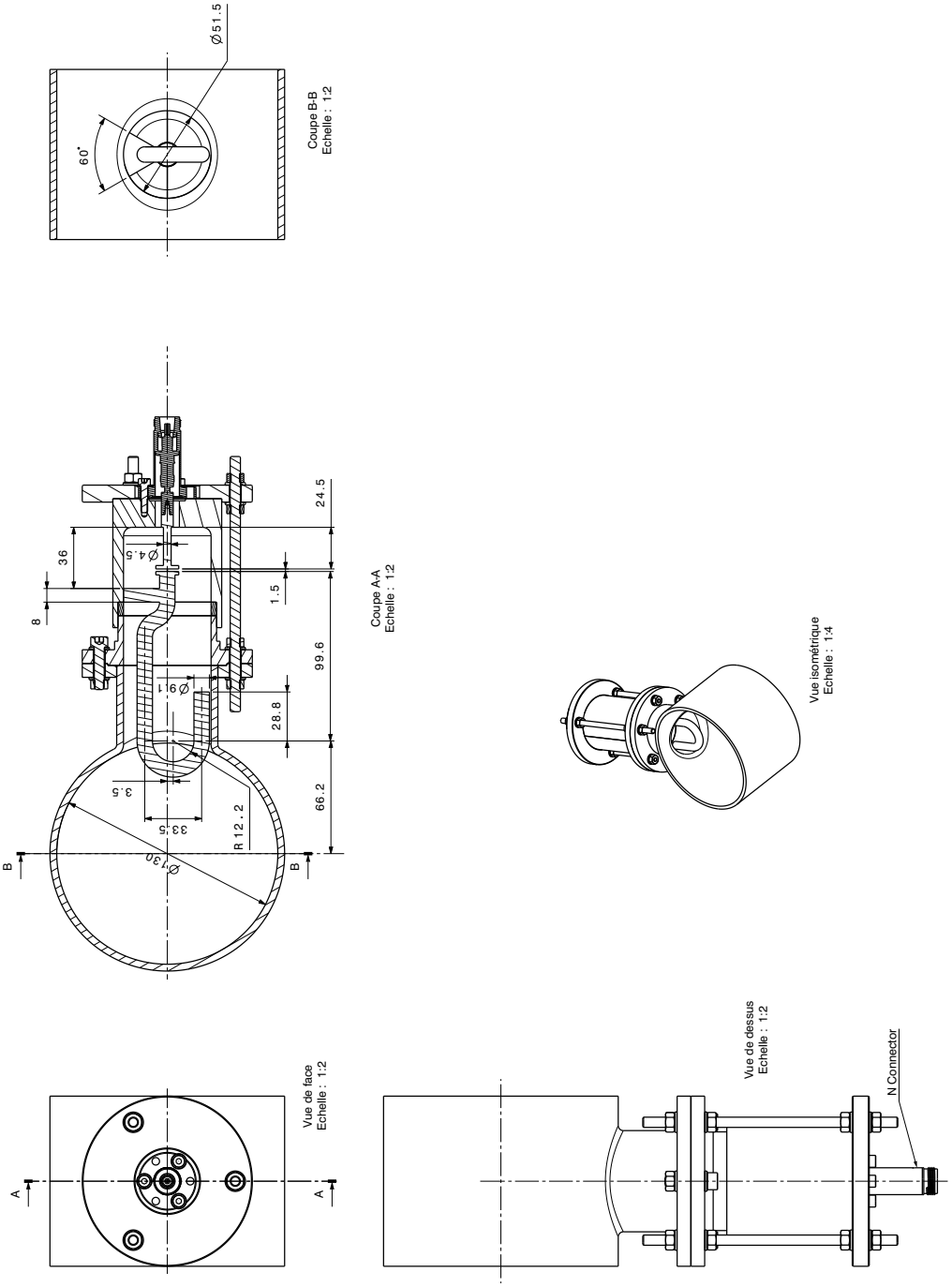

Figure A.2: Mechanical design of the hook-type PERLE HOM coupler.

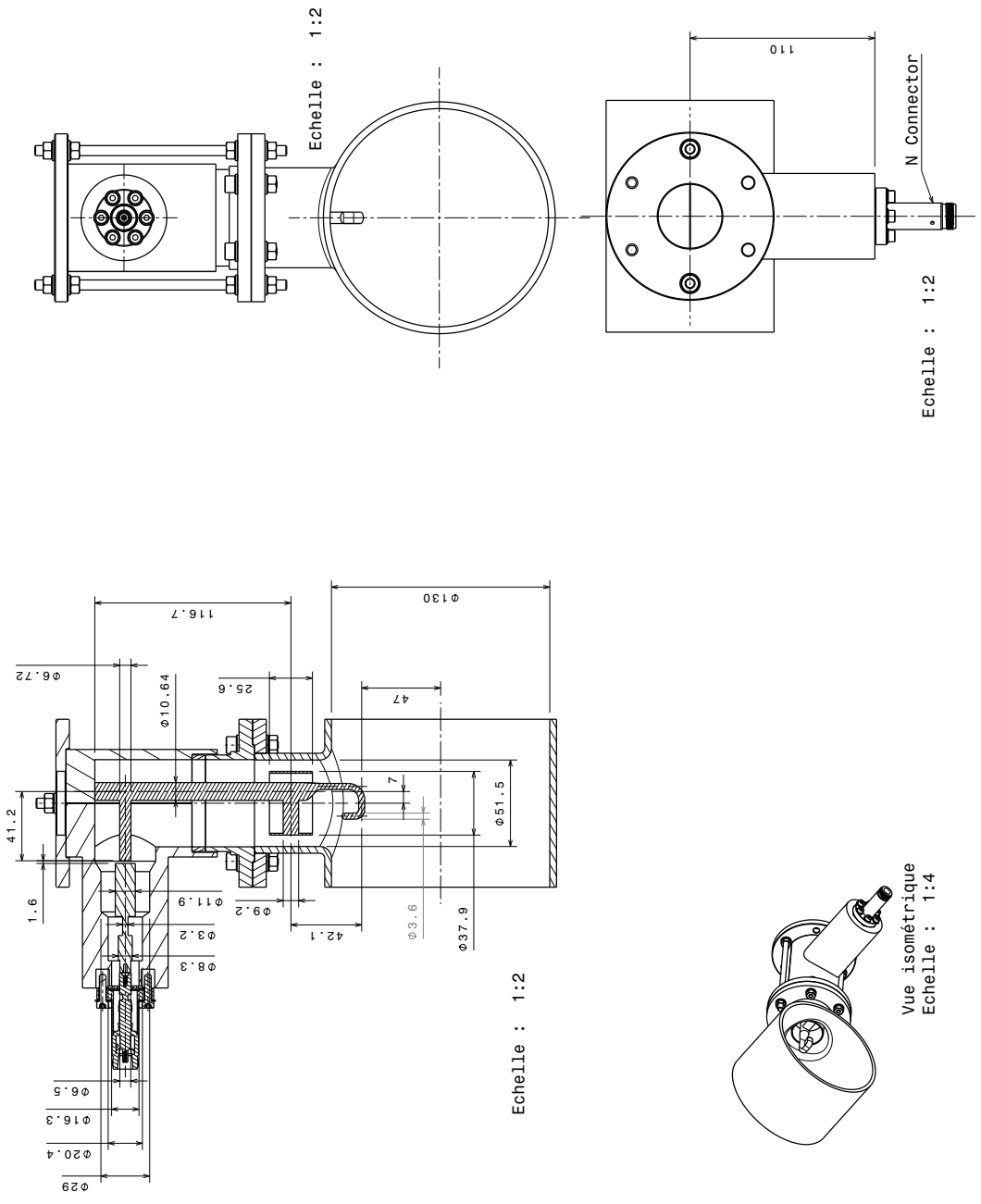

Figure A.3: Mechanical design of the DQW-type PERLE HOM coupler.

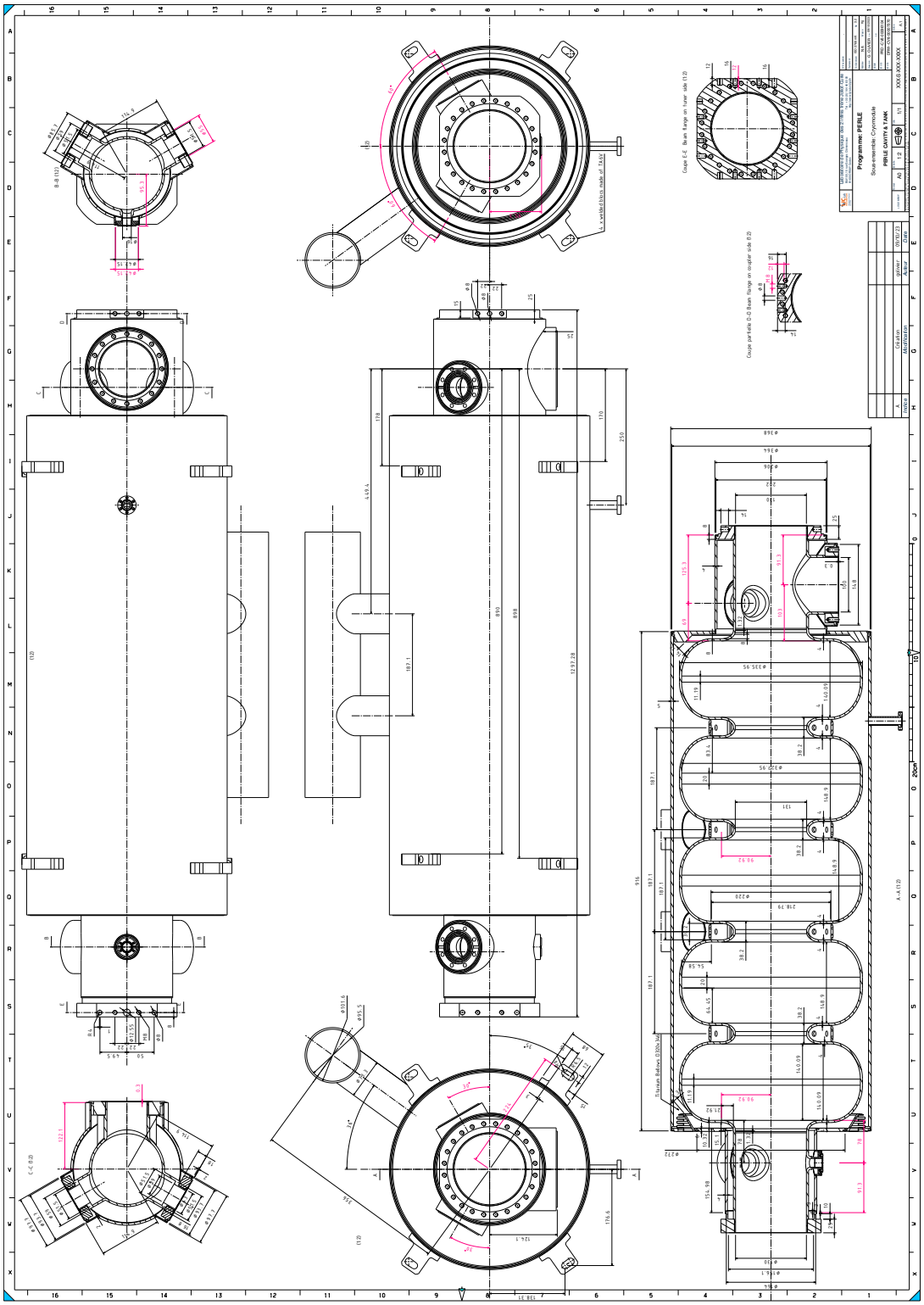

Figure A.4: Mechanical design of the 5-cell 801.58 MHz PERLE cavity.

Symbols

Symbol	Unit	Description
a_e	m	minor half-axis of the iris ellipse for the end-half-cell
A_e	m	major half-axis of the equatorial ellipse for the end-half-cell
a_k	$\mathrm{V}/\sqrt{\Omega}$	incident wave
a_m	m	minor half-axis of the iris ellipse for the middle-half-cell
A_m	m	major half-axis of the equatorial ellipse for the middle-half-cell
b_e	m	major half-axis of the iris ellipse for the end-half-cell
B_e	m	minor half-axis of the equatorial ellipse for the end-half-cell
b_k	$\mathrm{V}/\sqrt{\Omega}$	reflected wave
$b_{i,k}(t)$	$\sqrt{\mathrm{W}}$	signal excited in mode k of port i in the time-domain
$\underline{b}_{i,k}$	$\sqrt{\mathrm{W}}$	signal excited in mode k of port i in the frequency domain
b_m	m	major half-axis of the iris ellipse for the middle-half-cell
B_m	m	minor half-axis of the equatorial ellipse for the middle-half-cell
B_pk	T	peak magnetic field of FM on the cavity surface
$B_\mathrm{pk,0}$	T	peak magnetic field of FM on the coupler surfaces
$B_{\mathrm{pk},k}$	T	peak magnetic field of FM on the coupler surfaces at iteration k
$\underline{\mathbf{B}}$	T	phasor of the magnetic flux density
$\underline{\mathbf{B}}_n$	T	magnetic flux density of mode n
$\mathbf{B}(\mathbf{r}, t)$	T	magnetic flux density
$\underline{B}_x$	T	x-component of the magnetic flux density
$\underline{B}_y$	T	y-component of the magnetic flux density
$\underline{B}_z$	T	z-component of the magnetic flux density
c	m/s	speed of light in vacuum
$c_{\mathrm{D},i}$	m	ith geometrical parameter of the DQW coupler
$C_{\mathrm{D},i}$	F	ith capacitance of the DQW coupler equivalent circuit
$C_\mathrm{D,nf}$	F	notch filter capacitance of the DQW coupler equivalent circuit

Symbol	Unit	Description
$c_{\mathrm{H},i}$	m	ith geometrical parameter of the hook-type coupler
$C_{\mathrm{H},i}$	F	ith capacitance of the hook-type coupler equivalent circuit
$C_{\mathrm{H,nf}}$	F	notch filter capacitance of the hook-type coupler equivalent circuit
c_p	J/(kg·K)	specific heat capacity at constant pressure
$c_{\mathrm{P},i}$	m	ith geometrical parameter of the probe-type coupler
$C_{\mathrm{P},i}$	F	ith capacitance of the probe-type coupler equivalent circuit
$C_{\mathrm{P,nf}}$	F	notch filter capacitance of the probe-type coupler equivalent circuit
$d_{\mathrm{D},i}$	m	ith geometrical parameter of the DQW coupler
$d_{\mathrm{H},i}$	m	ith geometrical parameter of the hook-type coupler
$d_{\mathrm{P},i}$	m	ith geometrical parameter of the probe-type coupler
$dz_{\mathrm{BLA},i}$	m	incremental axial distance from the center of the BLA to the cavity iris
$\underline{\mathbf{D}}$	C/m^2	phasor of the electric flux density
$\mathbf{D}(\mathbf{r},t)$	C/m^2	electric flux density
e	C	electron charge
E_{acc}	V/m	cavity accelerating gradient
E_{b}	eV	beam energy in the recirculation arc for a two-pass machine
E_{b}^{m}	eV	beam energy at checkpoint m in a multi-pass machine
E_{dump}	eV	energy extracted at the dump of an ERL
E_{inj}	eV	injection energy in a ERL
$E_{\mathrm{p},i}$	V/m	peak axial electric field in the ith cell
E_{pk}	V/m	peak electric field of FM on the cavity surface
$E_{\mathrm{p,max}}$	V/m	maximum peak axial electric field among cells
$E_{\mathrm{p,min}}$	V/m	minimum peak axial electric field among cells
$\underline{\mathbf{E}}$	V/m	phasor of the electric field strength
$\underline{\mathbf{E}}_n$	V/m	electric field strength of mode n
$\underline{E}_r$	V/m	r-component of the electric field strength
$\underline{E}_x$	V/m	x-component of the electric field strength
$\underline{E}_y$	V/m	y-component of the electric field strength
$\underline{E}_z$	V/m	z-component of the electric field strength
$\underline{E}_\varphi$	V/m	φ-component of the electric field strength
$\underline{E}_0$	V/m	amplitude of the electric field strength
$\mathbf{E}(\mathbf{r},t)$	V/m	electric field strength
$\mathbf{E}_0(\mathbf{r})$	V/m	amplitude vector of the electric field strength
f	Hz	frequency
f_0	Hz	operating frequency
f_{b}	Hz	bunch repetition frequency

Symbol	Unit	Description
$f_{\mathrm{cut}}^{(\mathrm{TE}_{11})}$	Hz	cutoff frequency of the TE_{11} beam pipe mode
$f_{\mathrm{cut}}^{(\mathrm{TM}_{01})}$	Hz	cutoff frequency of the TM_{01} beam pipe mode
f_n	Hz	frequency of mode n
f_{target}	Hz	target frequency of an ideal half-cell
f_π	Hz	dumbbell frequency of the TM_{010}-π mode
$f_{\pi,\mathrm{D}}$	Hz	π-mode frequency of the lower half-cell in a dumbbell
$f_{\pi,\mathrm{e}}$	Hz	π-mode frequency of the end-cell dumbbell
$f_{\pi,\mathrm{P,D}}$	Hz	perturbed π-mode frequency of the lower half-cell
$f_{\pi,\mathrm{m}}$	Hz	π-mode frequency of the mid-cell dumbbell
$f_{\pi,\mathrm{P,U}}$	Hz	perturbed π-mode frequency of the upper half-cell
$f_{\pi,\mathrm{U}}$	Hz	π-mode frequency of the upper half-cell in a dumbbell
$f_{\pi/2}$	Hz	dumbbell frequency of the TM_{010}-$\pi/2$ mode
$f_{\pi/2,\mathrm{P,D}}$	Hz	perturbed $\pi/2$-mode frequency of the lower half-cell
$f_{\pi/2,\mathrm{P,U}}$	Hz	perturbed $\pi/2$-mode frequency of the upper half-cell
$\underline{\mathbf{F}}_n$	N	Lorentz force of mode n
F_{e}	N	extraction force
F_{h}	N	blank holder force
$\underline{F}_{i,k}$	$\sqrt{\mathrm{V/A}}$	weighting transfer function of mode k of port i
F_{p}	N	punch force
G	Ω	geometry factor of the fundamental mode
G_0	S	shunt admittance
G_{c}	S	admittance of the equivalent circuit of a cavity
$\underline{\mathbf{H}}$	A/m	phasor of the magnetic field strength
h_{Kap}	$\mathrm{W/(m^2{\cdot}K)}$	Kapitza conductance
$\underline{\mathbf{H}}_0$	A/m	magnetic field strength of the FM
$\underline{\mathbf{H}}_{\mathrm{tan},0}$	A/m	$\underline{\mathbf{H}}_0$ tangential to the cavity surface
$\underline{\mathbf{H}}_n$	A/m	magnetic field strength of mode n
$\underline{\mathbf{H}}_{\mathrm{tan},n}$	A/m	$\underline{\mathbf{H}}_n$ tangential to the cavity surface
$\underline{H}_z$	A/m	z-component of the magnetic field strength
$\underline{H}_0$	A/m	amplitude of the magnetic field strength
$\mathbf{H}(\mathbf{r}, t)$	A/m	magnetic field strength
$\underline{I}_b$	A	total beam current seen by a cavity
$\underline{I}_{\mathrm{b,acc}}$	A	accelerating beam current vector
$\underline{I}_{\mathrm{b,dec}}$	A	decelerating beam current vector
$\underline{I}_b(\omega_n)$	A	beam spectrum of an accelerator
$I_{\mathrm{b,op}}$	A	operating beam current
$I_{\mathrm{b},0}$	A	average beam current
$I_{\mathrm{b,i}}$	A	fraction of beam current in the ith frequency region
$i_{\mathrm{b}}(t)$	A	current of the single Gaussian bunch
$I_{\mathrm{b,tot}}$	A	total beam current up to 39 GHz

Symbol	Unit	Description
$I_{\mathrm{D,g}}$	A	current delivered by an ideal current source in the DQW coupler equivalent circuit
I_{g}	A	current delivered by an ideal current source
$I_{\mathrm{H,g}}$	A	current delivered by an ideal current source in the hook-type coupler equivalent circuit
$\hat{I}_n$	1	normalized Fourier spectrum of the beam current
I_k	A	current at the terminal pair k
$I_{\mathrm{P,g}}$	A	current delivered by an ideal current source in the probe-type coupler equivalent circuit
$I_{\mathrm{s},n}$	A	surface current of mode n
I_{th}	A	BBU threshold current
j	1	complex unit
$\underline{\mathbf{J}}$	$\mathrm{A/m^2}$	phasor of the electric current density
$\mathbf{J}(\mathbf{r},t)$	$\mathrm{A/m^2}$	electric current density
$\mathbf{J}_{\mathrm{i}}(\mathbf{r},t)$	$\mathrm{A/m^2}$	impressed electric current density
$\mathbf{J}_{\mathrm{d}}(\mathbf{r},t)$	$\mathrm{A/m^2}$	convection electric current density
J_m	1	mth order Bessel function
J'_m	1	derivative of mth order Bessel function
k	1/m	wave number
k_{B}	J/K	Boltzmann constant
k_0	1/m	wave number of the FM
k_{cc}	1	cell-to-cell coupling factor
K_i	1	total number of modes defined at port i
k_n	1/m	wave number of mode n
k_r	1/m	radial propagation constant
k_z	1/m	longitudinal propagation constant
$k_{\parallel}$	V/C	total longitudinal loss factor
$k_{\parallel,0}$	V/C	longitudinal loss factor of FM
$k_{\parallel,\mathrm{HOM}}$	V/C	total longitudinal loss factor of HOMs
$k_{\parallel,n}$	V/C	longitudinal loss factor of mode n
$k_{\perp,n}$	V/Cm	kick factor of mode n
$l(s)$	m	path length difference between the arbitrary trajectory of the particle and its nominal trajectory
$l_{\mathrm{D},i}$	m	ith geometrical parameter of the DQW coupler
$l_{\mathrm{H},i}$	m	ith geometrical parameter of the hook-type coupler
$l_{\mathrm{P},i}$	m	ith geometrical parameter of the probe-type coupler
ℓ	m	electron mean free path
L	m	half-cell length of the middle-cell of a cavity
L_{act}	m	active length of a cavity
L_{BLA}	mm	length of the BLA

Symbol	Unit	Description
L_{bp}	m	length of the beam pipe
L_{c}	H	inductance of the equivalent circuit of a cavity
L_{cav}	m	length of a cavity
L_{cell}	m	cell length of a cavity
L_{e}	m	length of the half-end cell of an elliptical cavity
L_{eq}	m	remaining extra length on the equator after trimming
$L_{\mathrm{D,nf}}$	H	notch filter inductance of the DQW coupler equivalent circuit
$L_{\mathrm{H,nf}}$	H	notch filter inductance of the hook-type coupler equivalent circuit
L_{p}	m	length of a pillbox cavity
$L_{\mathrm{P,nf}}$	H	notch filter inductance of the probe-type coupler equivalent circuit
$M_{\mathrm{H},i}$	H	coupling inductance of the hook-type coupler equivalent circuit
$M_{\mathrm{P},i}$	H	coupling inductance of the probe-type coupler equivalent circuit
M_{ij}	m	(i,j) element of the beam transfer matrix
M_{ij}^{lm}	m	element of the beam transfer matrix from checkpoint l to checkpoint m in a multi-pass machine
$\mathbf{M}(\mathbf{r},t)$	A/m	magnetic polarization vector
$\mathbf{n}$	1	normal unit vector
$N_{\mathrm{b,acc}}$	1	number of accelerating bunches
$N_{\mathrm{b,dec}}$	1	number of decelerating bunches
N_{c}	1	number of checkpoints in a multi-pass machine
N_{cell}	1	number of cavity cells
N_h	1	maximum considered harmonic number
N_{p}	1	number of passes in a multi-pass ERL
n_{wave}	1	number of waves per cycle
P_{b}	W	total beam power per cavity
$P_{\mathrm{BLA,0}}$	W	power dissipated in the absorber by the FM
$P_{\mathrm{BLA,HOM}}$	W	HOM power absorbed by the BLA
$P_{\mathrm{BLA},(i)}$	W	total HOM power at ith beam line absorber approximated up to 39 GHz
$P_{\mathrm{BLA,tot}}$	W	total RF power absorbed by the BLA
$P_{\mathrm{bp},(i)}$	W	total HOM power at beam pipe port i approximated up to 39 GHz
P_{c}	W	power dissipated in the cavity walls
P_{cer}	W	total power absorbed on the ceramic window due to the ensemble of modes N

Symbol	Unit	Description
$P_{\mathrm{cer},0}$	W	power absorbed on the ceramic window due to FM
$P_{\mathrm{c},0}$	W	power dissipated in the cavity walls by the FM
$P_{\mathrm{c},n}$	W	power dissipated in the cavity walls by a mode n
$P_{\mathrm{D},(i)}$	W	total HOM power approximated for the DQW coupler at port i up to 39 GHz
P_{ds}	W	total dissipated power on the coupler surfaces due to the ensemble of modes N
$P_{\mathrm{ds},0}$	W	dissipated power on the coupler surfaces due to FM
$P_{\mathrm{ds},0,k}$	W	dissipated power on the coupler surfaces due to FM at iteration k
P_{dyn}	W	total dynamic power losses in the Helium bath
P_{e}	W	emitted power
P_{ext}	W	external power loss
$P_{\mathrm{ext},n}$	W	external power loss of mode n
P_{f}	W	power propagating toward the cavity
$P_{\mathrm{FPC},(i)}$	W	total HOM power approximated for the Fundamental Power Coupler at port i up to 39 GHz
P_{h}	W	HOM power approximated between 2.5 GHz and 39 GHz
$P_{\mathrm{H},(i)}$	W	total HOM power approximated for the hook-type coupler at port i up to 39 GHz
P_{HOM}	W	total HOM power deposited by the beam into the cavity
$P_{\mathrm{HOM,ave}}$	W	average HOM power deposited by the beam into the cavity
$P_{\mathrm{HOM},n}$	W	HOM power of mode n
P_{i}	W	HOM power propagating through the port i
P_{in}	W	input power
P_{in}^{*}	W	minimum input power per cavity at $Q_{\mathrm{L},0}^{*}$
P_{kly}	W	klystron power
P_{loss}	W	power loss
P_{l}	W	HOM power up to 2.5 GHz
P_{m}	W	HOM power up between 2.5 GHz and 4 GHz
$P_{\mathrm{nd},n}$	W	undamped HOM power of a trapped mode n
$P_{\mathrm{ports,HOM}}$	W	HOM power the HOM power going out from the cavity through
$P_{\mathrm{P},(i)}$	W	total HOM power approximated for the probe-type coupler at port i up to 39 GHz
P_{r}	W	reflected power
$\mathbf{P}(\mathbf{r},t)$	$\mathrm{C/m^2}$	electric polarization vector
P_{st}	W	total static power loss
P'_{st}	W/m	static power loss per unit length
P_{t}	W	power coming out of the fixed output coupler

Symbol	Unit	Description
$P_{\mathrm{t,AC}}$	W	total AC wall power
P_{tot}	W	total HOM power approximated up to 39 GHz
$P_{\mathrm{wake,HOM}}$	W	beam-induced HOM power calculated from wake impedance
q	C	electric charge
Q	1	quality factor
Q_0	1	unloaded quality factor of the fundamental mode
$Q_{0,n}$	1	unloaded quality factor of mode n
Q_{b}	C	bunch charge
$Q_{\mathrm{BLA},0}$	1	quality factor of the BLA at FM frequency
Q_{ext}	1	external quality factor
$Q_{\mathrm{ext},l}$	1	external quality factor of the strong-coupled antenna
$Q_{\mathrm{ext},n}$	1	external quality factor of mode n
$Q_{\mathrm{ext},s}$	1	external quality factor of the weak-coupled antenna
$Q_{\mathrm{ext},1,n}$	1	external quality factor of port 1 for mode n
$Q_{\mathrm{ext},2,n}$	1	external quality factor of port 2 for mode n
$Q^{\mathrm{th}}_{\mathrm{ext}\parallel,n}$	1	required Q_{ext} for a monopole mode n to avoid BBU
$Q^{\mathrm{th}}_{\mathrm{ext}\perp,n}$	1	required Q_{ext} for a dipole mode n to avoid BBU
Q_{L}	1	loaded quality factor
$Q_{\mathrm{L},0}$	1	loaded quality factor of FM
$Q^{*}_{\mathrm{L},0}$	1	optimum loaded quality factor of FM
$Q_{\mathrm{L},n}$	1	loaded quality factor of mode n
Q_n	1	quality factor of mode n
$\mathbf{q}_{\mathrm{rad}}$	$\mathrm{W/m^2}$	heat flux emitted from a surface by radiation
Q_v	$\mathrm{W/m^3}$	volumetric heat source
$\mathbf{r}$	m	position vector
R^2	1	coefficient of determination
r_{b}	m	radius of the spherical dielectric bead
r_{p}	m	beam offset from the cavity axis in the predominant mode polarization
$R_{\mathrm{BCS}}(T)$	Ω	BCS resistance
R_{BLA}	mm	inner radius of the BLA
R_{bp}	m	beam pipe radius
R_{eq}	m	equator radius of an elliptical cavity
R_{i}	m	iris radius of an elliptical cavity
R_k	Ω	reference resistance related to a source or a load
R_{p}	m	radius of a pillbox cavity
R_{res}	Ω	residual resistance
R_{s}	Ω	surface resistance
$R_{\mathrm{s},0}(T)$	Ω	temperature-dependent surface resistance of FM

Symbol	Unit	Description
R/Q	Ω	geometric shunt impedance
$(R/Q)_n$	Ω	geometric shunt impedance of mode n
$(R/Q)_\parallel$	Ω	longitudinal geometric shunt impedance
$(R/Q)_{\parallel,0}$	Ω	longitudinal geometric shunt impedance of FM
$(R/Q)_{\parallel,n}$	Ω	longitudinal geometric shunt impedance of mode n
$(R/Q)_\perp$	Ω	transversal geometric shunt impedance
$(R/Q)_{\perp,n}$	Ω	transversal geometric shunt impedance of mode n
$(R/Q)_{\perp\mathrm{x},n}$	Ω	transversal geometric shunt impedance of mode n in x-direction
$(R/Q)_{\perp\mathrm{y},n}$	Ω	transversal geometric shunt impedance of mode n in y-direction
RRR	1	Residual (electrical) Resistivity Ratio
s	m	distance of the test charge behind the exciting particle
S_{11}	1	input reflection coefficient
S_{22}	1	output reflection coefficient
S_{12}	1	transmission from port 2 to port 1
S_{21}	1	transmission from port 1 to port 2
$S_{21}(f_n)$	dB	S_{21} measurement of mode n
$S_{i(k),j(l)}$	dB	S-parameter between the mode k and l of ports i and j
S_{ll}	dB	reflected signal to the strongly-coupled antenna
S_{ss}	dB	reflected signal to the weakly-coupled antenna
S_t	Hz/m	trimming parameter
$S_{\mathrm{t,m}}$	Hz/m	trimming parameter for the middle-cell dumbbell
$S_{\mathrm{t,e}}$	Hz/m	trimming parameter for the end-cell dumbbell
t	s	time
t_b	s	bunch spacing in time domain
T	K	temperature
T_amb	K	ambient temperature
T_bath	K	bath temperature
T_c	K	critical temperature
T_max	K	maximum temperature on the coupler surfaces
t_0	s	time period of FM
$t_{\mathrm{D},i}$	m	ith geometrical parameter of the hook-type coupler
t_r	s	recirculation time of a two-pass machine
t_r^{lm}	s	recirculation time from checkpoint l to checkpoint m in a multi-pass machine
U	J	stored energy
U_0	J	energy of the fundamental mode
$U_{\mathrm{b},n}$	J	deposited energy by N_b bunches into a mode n
u_{mn}	1	nth root of the mth order Bessel function

Symbol	Unit	Description
u'_{mn}	1	nth root of the mth order Bessel function derivative
U_n	J	energy of mode n
$U_{q,n}$	J	deposited energy by the charge into a mode n
$\mathbf{v}$	m/s	particle's velocity
V_{acc}	V	accelerating voltage of the FM of a cavity
V_{c}	V	voltage of the equivalent circuit of a cavity
V_k	V	voltage at the terminal pair k
$v_i^{(n)}$	1	relative field amplitude of mode n in the ith cell
V_{RF}	V	total required voltage for the cavities
$V_{\mathrm{s},1}$	V	voltage source at port 1
$V_{\mathrm{s},2}$	V	voltage source at port 2
$\underline{V}_{\parallel,n}$	V	accelerating voltage of mode n
$\underline{\mathbf{V}}_{\perp,n}$	V	transverse voltage vector
$\underline{V}_{\perp\mathrm{x},n}$	V	transverse voltage of mode n in x-direction
$\underline{V}_{\perp\mathrm{y},n}$	V	transverse voltage of mode n in y-direction
$\mathbf{w}$	V/C	wake function
$\mathbf{W}(\mathbf{r}, s)$	V/C	wake potential
$w_{\parallel}$	V/C	longitudinal component of the wake function
$W_{\parallel}$	V/C	longitudinal component of the wake potential
$\mathbf{W}_{\perp}$	V/C	transversal wake potential
$w_{\mathrm{H},i}$	m	ith geometrical parameter of the hook-type coupler
$x(\zeta)$	m	horizontal displacement of the particle from the nominal trajectory
$x'(\zeta)$	rad	particle angle in the horizontal plane from the nominal trajectory
x_{p}	m	offset from the axis in x-direction
X_{s}	Ω	surface reactance
$y(\zeta)$	m	vertical displacement of the particle from the nominal trajectory
$y'(\zeta)$	rad	particle angle in the vertical plane from the nominal trajectory
y_{p}	m	offset from the axis in y-direction
Z_{D}	Ω	characteristic impedance of the transmission line connected to the output port of the DQW coupler
$Z_{\mathrm{D},i}$	Ω	characteristic impedance of the ith transmission line of length $l_{\mathrm{D},i}$ of the DQW coupler
Z_{H}	Ω	characteristic impedance of the transmission line connected to the output port of the hook-type coupler
$Z_{\mathrm{H},i}$	Ω	characteristic impedance of the ith transmission line of length $l_{\mathrm{h},i}$ of the hook-type coupler

Symbol	Unit	Description
Z_{P}	Ω	characteristic impedance of the transmission line connected to the output port of the probe-type coupler
$Z_{\mathrm{P},i}$	Ω	characteristic impedance of the ith transmission line of length $l_{\mathrm{P},i}$ of the probe-type coupler
Z_n^{th}	Ω	impedance threshold of mode n
$Z_{\parallel}$	Ω	longitudinal impedance
$Z_{\parallel,n}^{\mathrm{th}}$	Ω	longitudinal impedance threshold of mode n
$\mathbf{Z}_{\perp}$	Ω	transversal impedance
$Z_{\perp}$	Ω/m	magnitude of the transversal impedance
$Z_{\perp,n}^{\mathrm{th}}$	Ω/m	transversal impedance threshold of mode n
$\underline{Z}_{\mathrm{s}}$	Ω	surface impedance
Z_0	Ω	impedance of free space
α_{H}	degree	geometrical parameter of the hook-type coupler
α_{P}	degree	geometrical parameter of the probe-type coupler
α_{L}	1/K	linear thermal expansion coefficient
α_{γ}	Np/m	attenuation constant
α_{w}	degree	wall slope angle of a cavity cell
β	1	coupling factor
β_l	1	coupling parameter of the strongly-coupled antenna
β_{opt}	1	optimum coupling factor
β_s	1	coupling parameter of the weakly-coupled antenna
β_{γ}	rad/m	phase constant
β_1	1	coupling parameter of the antenna at port 1
β_2	1	coupling parameter of the antenna at port 2
Γ	1	reflection coefficient
$\underline{\gamma}$	1/m	propagation constant of the wave
$\underline{\Delta}$	eV	energy gap of the superconductor
$\tan(\delta_{\mathrm{e}})$		electric loss tangent
ΔE_{b}	eV	energy gain (or energy lost) through an SC linac in an ERL
Δf	Hz	frequency deviation
Δf_{3dB}	Hz	cavity bandwidth
δf_{m}	Hz	microphonic detuning
δf_n	Hz	frequency shift of mode n due to a bead inside the cavity
Δf_n	Hz	change in the resonant frequency of mode n
$\left\lvert\Delta f_{n,\mathrm{b}}^{\mathrm{l}}\right\rvert$	Hz	frequency shift between the resonant frequency of mode n and its nearest lower-frequency bunch harmonic
$\left\lvert\Delta f_{n,\mathrm{b}}^{\mathrm{h}}\right\rvert$	Hz	frequency shift between the resonant frequency of mode n and its nearest higher-frequency bunch harmonic
δf_0	Hz	static detuning

Symbol	Unit	Description
Δf_0	Hz	intrinsic cavity bandwidth
Δh_c	m	estimated local thickness change on a surface
ΔL	m	change in cavity length
ΔL_t	m	simulated trimmed extra length on the half-cell equator
$\Delta L_\mathrm{t,D}$	m	trimmed extra length of the lower half-cell
$\Delta L_\mathrm{t,e}$	m	trimmed length on the equator of end-cell dumbbell
$\Delta L_\mathrm{t,m}$	m	trimmed length on the equator of middle-cell dumbbell
$\Delta L_{\mathrm{t},i}$	m	trimmed length on the cell equator at machining round i
$\Delta L_\mathrm{t,U}$	m	trimmed extra length of the upper half-cell
ΔL_tot	m	total removed length on the half-cell equator
$\delta_{n,i}$	1	Kronecker delta
$\Delta p/p$	1	fractional momentum deviation of the particle from the nominal trajectory
ΔQ_0	1	unloaded quality factor deviation
$\Delta S_{11}(f_0)$	dB	difference between the on-resonance and off-resonance reflected signal at port 1
δ_s	m	skin depth
$\Delta S_{22}(f_0)$	dB	difference between the on-resonance and off-resonance reflected signal at port 2
ΔT	K	temperature gradient
Δu_n	m	measured shape deviation in the normal direction
ΔV	m^3	small finite change in cavity volume
$\delta\theta_\mathrm{c}$	degree	small tilt of the coupler antenna
$\delta\phi$	degree	S_{21} phase variation
$\delta\phi_n$	degree	S_{21} phase variation of mode n due to a bead
$\delta\phi_{\mathrm{p},i}$	degree	peak phase variation in the ith cell due to a bead
$\delta\phi_\mathrm{p,max}$	degree	maximum peak phase variation among cells due to a bead
$\delta\phi_\mathrm{p,min}$	degree	minimum peak phase variation among cells due to a bead
$\Delta\omega_n$	1/s	angular half-power bandwidth of mode n
ϵ	1	total hemispherical emissivity of the surface
ε	F/m	permittivity
ε'	F/m	real part of the complex permittivity
ε''	F/m	imaginary part of the complex permittivity
ε_0	F/m	permittivity of free space
ε_r	1	relative permittivity
ε'_r	1	real part of the complex relative permittivity
ε'_r0	1	real part of the complex relative permittivity at zero frequency
$\varepsilon'_{\mathrm{r}\infty}$	1	real part of the complex relative permittivity at infinity frequency

Symbol	Unit	Description
ε_r''	1	imaginary part of the complex relative permittivity
ζ	m	particle position along a nominal trajectory
η_b	1	ratio between klystron power and beam power
η_c	1	Carnot efficiency
η_ff	1	field flatness
η_t	1	technical efficiency of the cryogenic plant
θ_c	degree	rotation angle of the coupler
κ	W/(m·K)	thermal conductivity
λ	m	wavelength
λ_0	m	wavelength at FM frequency
λ_L	m	London penetration depth
μ	H/m	permeability
μ_0	H/m	permeability of free space
μ_r	1	relative permeability
ξ_c	1	bunch shape function
$\xi_{V,n}^{(\mathrm{Dip})}$	1	voltage scaling factor for dipole HOMs
$\xi_{V,n}^{(\mathrm{Mon})}$	1	voltage scaling factor for monopole HOMs
ϱ	kg/m^3	volumetric mass density
$\underline{\rho}$	C/m^3	phasor of the electric charge density
$\rho(\mathbf{r}, t)$	C/m^3	electric charge density
$\boldsymbol{\Sigma}$	m^2	arbitrary surface
σ	S/m	electric conductivity
σ_n	S/m	electric conductivity in the normal conducting state
σ_SB	W/(m^2·K^4)	Stefan–Boltzmann constant
σ_z	m	RMS bunch length in the longitudinal direction
τ_e	s	relaxation time constant of the dielectric material
τ_L	s	time constant of the loaded cavity
τ_n	s	decay time of the HOM field
ϕ	1	phase advance per cell
ϕ_n	1	phase advance per cell of the mode n
$\phi_0(\mathbf{r})$	1	initial phase angle
χ_e	1	electric susceptibility
χ_m	1	magnetic susceptibility
ψ	degree	tuning angle
$\psi_{\mathrm{acc},i}$	degree	angular position of the ith accelerating bunch
ψ_b	degree	beam phase with respect to the FM E-field crest
$\psi_{\mathrm{dec},k}$	degree	angular position of the kth decelerating bunch
$\boldsymbol{\Omega}$	m^3	arbitrary domain
ω	1/s	angular frequency

Symbol	Unit	Description
ω_0	$1/\mathrm{s}$	angular frequency of the fundamental mode
ω_n	$1/\mathrm{s}$	angular frequency of mode n
$\omega_{mnp}^{(\mathrm{TM})}$	$1/\mathrm{s}$	angular frequency of TM modes in a pillbox cavity
$\omega_{mnp}^{(\mathrm{TE})}$	$1/\mathrm{s}$	angular frequency of TE modes in a pillbox cavity
$\omega_{\mathrm{p},0}$	$1/\mathrm{s}$	lowest angular frequency in the passband
$\omega_{\mathrm{p},\pi}$	$1/\mathrm{s}$	highest angular frequency in the passband
$\mathbf{\Omega}_\mathrm{s}$	m^3	solid domain
$\mathbf{\Omega}_\mathrm{v}$	m^3	vacuum filled domain
$\Im$		imaginary part of a complex number
$\Re$		real part of a complex number
$\partial\mathbf{\Omega}_\mathrm{c}$	m^2	surface of an HOM coupler or a cavity
$\partial\mathbf{\Omega}_\mathrm{s}$	m^2	boundary of the solid domain
$\partial\mathbf{\Omega}_\mathrm{v}$	m^2	boundary of the vacuum domain
∇	$1/\mathrm{m}$	gradient operator
$\nabla_\perp$	$1/\mathrm{m}$	transverse gradient operator
$\nabla\cdot$	$1/\mathrm{m}$	divergence operator
$\nabla\times$	$1/\mathrm{m}$	curl operator
∇^2	$1/\mathrm{m}^2$	Laplace operator
$\cdot^*$	1	complex conjugate operator

Bibliography

[1] I. Bazarov *et al.*, "The Energy Recovery Linac (ERL) as a driver for X-ray producing insertion devices," in *Proc. of the 2001 Particle Accelerator Conf. (PACS2001)*, Chicago, Illinois, USA, June 2001, pp. 230–232. doi: 10.1109/PAC.2001.987478.

[2] L. Merminga, D. R. Douglas, and G. A. Krafft, "High-Current Energy-Recovering Electron Linacs," *Annual Review of Nuclear and Particle Science*, vol. 53, no. 1, pp. 387–429, 2003. doi: 10.1146/annurev.nucl.53.041002.110456.

[3] M. Tigner, "A possible apparatus for electron clashing-beam experiments," *Il Nuovo Cimento (1955-1965)*, vol. 37, no. 3, pp. 1228–1231, 1965. doi: 10.1007/BF02773204.

[4] T. I. Smith, H. A. Schwettman, R. Rohatgi, Y. Lapierre, and J. Edighoffer, "Development of the SCA/FEL for use in biomedical and materials science experiments," *Nuclear Instruments and Methods in Physics Research Section A: Accelerators, Spectrometers, Detectors and Associated Equipment*, vol. 259, no. 1-2, pp. 1–7, September 1987. doi: 10.1016/0168-9002(87)90421-9.

[5] D. W. Feldman *et al.*, "Energy recovery in the Los Alamos free electron laser," *Nuclear Instruments and Methods in Physics Research Section A: Accelerators, Spectrometers, Detectors and Associated Equipment*, vol. 259, no. 1-2, pp. 26–30, September 1987. doi: 10.1016/0168-9002(87)90425-6.

[6] G. R. Neil *et al.*, "Sustained Kilowatt Lasing in a Free-Electron Laser with Same-Cell Energy Recovery," *Phys. Rev. Lett.*, vol. 84, pp. 662–665, January 2000. doi: 10.1103/PhysRevLett.84.662.

[7] S. Benson *et al.*, "High power operation of the JLab IR FEL driver accelerator," in *Proceedings of the 2007 IEEE Particle Accelerator Conference (PAC)*, Albuquerque, NM, USA, June 2007, pp. 79–81. doi: 10.1109/PAC.2007.4440128.

[8] S. Benson *et al.*, "High power lasing in the IR Upgrade FEL at Jefferson Lab," in *Proceedings of the 2004 FEL Conference*, Trieste, Italy, Aug. 29 - Sept. 3, 2004, pp. 229–232.

[9] C. Adolphsen *et al.*, *European Strategy for Particle Physics - Accelerator R&D Roadmap*. CERN Yellow Reports: Monographs, 2022. doi: https://doi.org/10.23731/CYRM-2022-001.

[10] L. Jones, J. McKenzie, K. Middleman, B. Militsyn, Y. M. Saveliev, and S. Smith, "The ALICE Energy Recovery Linac–Project overview and injector performance," in *Journal of Physics: Conference Series*, vol. 298, p. 012007, IOP Publishing, 2011. doi: 10.1088/1742-6596/298/1/012007.

[11] S. Bogacz *et al.*, "CEBAF-ER Experiment Proposal," PAC22 Proposal, PR-02-102, Jefferson Lab, June 2002. `https://www.jlab.org/exp_prog/proposals/02/PR02-102.pdf`.

[12] C. Tennant *et al.*, "CEBAF-ER: Extending the Frontier of Energy Recovery at Jefferson Lab," in *Proc. of the 11th Workshop on RF Superconductivity*, Lübeck/Travemünder, Germany, September 2003, pp. 249–253.

[13] A. Richter *et al.*, "Operational Experience at the S-DALINAC," in *Proc. of the 5th European Particle Accelerator Conference (EPAC'96)*, Sitges, Spain, June 1996, p. 110.

[14] G. Hoffstaetter *et al.*, "CBETA design report, Cornell-BNL ERL test accelerator," *arXiv preprint, arXiv:1706.04245*, 2017. doi: 10.48550/arXiv.1706.04245 .

[15] S. Fukuda *et al.*, "RF source of compact ERL in KEK," in *Proc. of the 1st International Particle Accelerator Conference (IPAC'10)*, vol. 10, Kyoto, Japan, May 2010, pp. 3981–3983.

[16] F. Hug, K. Aulenbacher, R. Heine, B. Ledroit, and D. Simon, "MESA-an ERL project for particle physics experiments," in *Proc. of the 28th Linear Accelerator Conference (LINAC'16)*, vol. 28, East Lansing, MI, USA, September 2016, 313–315.

[17] H. Padamsee, J. Knobloch, and T. Hays, *RF superconductivity for accelerators*. John Wiley & Sons, 2008.

[18] D. Angal-Kalinin *et al.*, "PERLE. Powerful energy recovery linac for experiments. Conceptual design report," *Journal of Physics G: Nuclear and Particle Physics*, vol. 45, p. 065003, May 2018. doi: doi.org/10.1088/1361-6471/aaa171.

[19] J. L. Abelleira Fernandez *et al.*, "A Large Hadron Electron Collider at CERN: Report on the Physics and Design Concepts for Machine and Detector," *Journal of Physics G: Nuclear and Particle Physics*, vol. 39, p. 075001, June 2012. doi: 10.1088/0954-3899/39/7/075001.

[20] P. Agostini *et al.*, "The Large Hadron–Electron Collider at the HL-LHC," *Journal of Physics G: Nuclear and Particle Physics*, vol. 48, p. 110501, Dec. 2021. doi: 10.1088/1361-6471/abf3ba.

[21] F. Marhauser, "Next generation HOM-damping," *Superconductor Science and Technology*, vol. 30, p. 063002, May 2017. doi: 10.1088/1361-6668/aa6b8d .

[22] J. C. Maxwell, *A Treatise on Electricity and Magnetism*, vol. 1. Oxford: Clarendon Press, 1873.

[23] C. A. Balanis, *Advanced engineering electromagnetics*. John Wiley & Sons, 2012.

[24] T. Flisgen, J. Heller, and U. van Rienen, "Recapitulation of electromagnetism," *CERN Yellow Reports: School Proceedings*, vol. 5, pp. 69–69, Dec. 2018. doi: https://doi.org/10.23730/CYRSP-2018-005.69.

[25] U. Van Rienen, *Numerical Methods in Computational Electrodynamics: Linear Systems in Practical Applications*, vol. 12. Springer Science & Business Media, 2001.

[26] H. Guo, P. Arbenz, and B. Oswald, "Realistic 3-dimensional eigenmodal analysis of electromagnetic cavities using surface impedance boundary conditions," in *Proc. of the 11st International Computational Accelerator Physics Conference (ICAP 2012)*, Rostock-Warnemünde, Germany, August 2012, pp. 161–163.

[27] J. G. Van Bladel, *Electromagnetic fields*, vol. 19. John Wiley & Sons, 2007.

[28] Computer Simulation Technology, CST Studio Suite 2023. https://www.3ds.com/products-services/simulia/products/cst-studio-suite/.

[29] J.-M. Jin, *The finite element method in electromagnetics*. John Wiley & Sons, 2002.

[30] J. D. Jackson, *Classical electrodynamics*. John Wiley & Sons, 1999.

[31] F. Marhauser, "Higher Order Modes (HOMs)," *USPAS Education in Beam Physics and Accelerator Technology, SRF Hands-on Course*, Thomas Jefferson Lab, USA, January 2015. `https://indico.jlab.org/event/98/contributions/7448/attachments/6309/8357/4T_-_HOMs.pdf`.

[32] F. Gerigk, "Cavity types," in *Proceedings of the CAS-CERN Accelerator School: RF for Accelerators*, November 2011, pp. 277–298. doi: 10.5170/CERN-2011-007.

[33] T. P. Wangler, *RF Linear accelerators*. John Wiley & Sons, 2008.

[34] S. Belomestnykh and V. Shemelin, "High-β cavity design – A tutorial," in *Proc. of the 12th International Workshop on RF Superconductivity (SRF 2005)*, Cornell University, Ithaca, NY, USA, July 2005.

[35] W. Panofsky and W. Wenzel, "Some considerations concerning the transverse deflection of charged particles in radio-frequency fields," *Review of Scientific Instruments*, vol. 27, pp. 967–967, Nov. 1956. doi: 10.1063/1.1715427.

[36] R. Appleby, G. Burt, J. Clarke, and H. Owen, *The science and technology of particle accelerators*. Taylor & Francis, 2020. doi: 10.1201/9781351007962.

[37] Y. Yang, A. Nassiri, G. Waldschmidt, D. Li, and H. Chen, "Wakefield characterization in an asymmetric superconducting deflecting cavity," *Physical Review Special Topics-Accelerators and Beams*, vol. 17, no. 3, p. 032001, March 2014. doi: 10.1103/PhysRevSTAB.17.032001.

[38] A. Godeke, "A review of the properties of Nb_3Sn and their variation with A15 composition, morphology and strain state," *Superconductor Science and Technology*, vol. 19, p. R68, June 2006. doi: 10.1088/0953-2048/19/8/R02.

[39] F. London and H. London, "The electromagnetic equations of the supraconductor," *Proceedings of the Royal Society of London. Series A-Mathematical and Physical Sciences*, vol. 149, no. 866, pp. 71–88, March 1935. doi: 10.1098/rspa.1935.0048.

[40] W. Singer, A. Ermakov, and X. Singer, "RRR-measurement techniques on high purity niobium," DESY, Hamburg, Germany, Rep. TTC-Report 2010-02, 2010. `https://bib-pubdb1.desy.de/record/91801/files/TTC-Report%202010-02.pdf`.

[41] D. D'Elia, "A method to evaluate RRR of superconducting cavities," CERN, Geneva, Switzerland, Rep. CERN-HIE-ISOLDE-PROJECT-Note-0014, Sep. 2012. `https://cds.cern.ch/record/1477732/files/HIE-ISOLDE-PROJECT-Note-0014.pdf`.

[42] G. Ciovati, P. Dhakal, and G. R. Myneni, "Superconducting radio-frequency cavities made from medium and low-purity niobium ingots," *Superconductor Science and Technology*, vol. 29, no. 6, p. 064002, 2016. doi: 10.1088/0953-2048/29/6/064002.

[43] A. B. Pippard and W. L. Bragg, "An experimental and theoretical study of the relation between magnetic field and current in a superconductor," *Proceedings of the Royal Society of London. Series A. Mathematical and Physical Sciences*, vol. 216, pp. 547–568, Feb. 1953. doi: 10.1098/rspa.1953.0040.

[44] G. Ciovati, "AC/RF superconductivity," in *Proceedings of the CAS-CERN Accelerator School: Superconductivity for Accelerators*, Jan. 2014, pp. 57-75. doi: 10.5170/CERN-2014-005.57.

[45] D. C. Mattis and J. Bardeen, "Theory of the anomalous skin effect in normal and superconducting metals," *Physical Review*, vol. 111, p. 412, July 1958. doi: 10.1103/PhysRev.111.412.

[46] J. Bardeen, L. N. Cooper, and J. R. Schrieffer, "Theory of superconductivity," *Physical review*, vol. 108, p. 1175, Dec. 1957. doi: 10.1103/PhysRev.108.1175.

[47] F. Zimmermann, "Accelerator physics for ILC and CLIC," CERN, Geneva, Switzerland, Rep. CERN-ATS-2010-056, CLIC-Note-820, May 2010. `https://cds.cern.ch/record/1269881/files/CERN-ATS-2010-056.pdf`.

[48] S. A. Bogacz *et al.*, "Beam dynamics driven design of powerful energy recovery linac for experiments," *Phys. Rev. Accel. Beams*, vol. 27, p. 031603, Mar. 2024. doi: 10.1103/PhysRevAccelBeams.27.031603 .

[49] C. Barbagallo *et al.*, "Higher Order Modes Investigation in the PERLE Superconducting RF Cavity," in *Proc. of the 31st International Linear Accelerator Conference (LINAC'22)*, Liverpool, UK, 28 Aug. - 2 Sep. 2022, pp. 731–734. doi:10.18429/JACoW-LINAC2022-THPOJO21.

[50] S. Bogacz *et al.*, "PERLE - Lattice Design and Beam Dynamics Studies," in *Proc. of the 9th International Particle Accelerator Conference (IPAC'18)*, Vancouver, BC, Canada, 29 Apr. - 4 May 2018, pp. 4556–4559. doi: https://doi.org/10.18429/JACoW-IPAC2018-THPMK105.

[51] D. Pellegrini, A. Latina, D. Schulte, and S. A. Bogacz, "Beam-dynamics driven design of the LHeC energy-recovery linac," *Phys. Rev. ST Accel. Beams*, vol. 18, p. 121004, Dec. 2015. doi: 10.1103/PhysRevSTAB.18.121004.

[52] A. Fomin, L. Perrot, J. Michaud, R. Abukeshek, C. Guyot, and S. A. Bogacz, "Lattice design of 250 MeV version of PERLE," in *Proc. of the 14th International Particle Accelerator Conference (IPAC'23)*, Venice, Italy, May 2023, pp. 2151–2153. doi: 10.18429/JACoW-IPAC2023-TUPL171.

[53] W. Kaabi and A. Stocchi, "PERLE: A Novel Facility for ERL Development and Applications in Multi-turn Configuration and High-power Regime," *Acta Phys. Polon. Supp.*, vol. 16, pp. 7–A21, Sept. 2023. doi: 10.5506/APhysPolBSupp.16.7-A21.

[54] V. Shemelin, S. G. Zadeh, J. Heller, and U. van Rienen, "Systematical study on superconducting radio frequency elliptic cavity shapes applicable to future high

energy accelerators and energy recovery linacs," *Phys. Rev. Accel. Beams*, vol. 19, p. 102002, Oct 2016. 10.1103/PhysRevAccelBeams.19.102002.

[55] S. Belomestnykh *et al.*, "Superconducting RF linac for eRHIC," in *Proc. of the 26th International Linear Accelerator Conference (LINAC'12)*, Tel Aviv, Israel, Sept. 2012, pp. 321–323.

[56] R. Rimmer *et al.*, "The JLAB ampere-class cryomodule conceptual design," in *Proc. of the 10th European Particle Accelerator Conference (EPAC'06)*, Edinburgh, Scotland, June 2006, pp. 490–492.

[57] M. Liepe *et al.*, "Progress on superconducting RF work for the Cornell ERL," in *Proc. of the 3rd International Particle Accelerator Conference (IPAC'12)*, New Orleans, Louisiana, USA, May 2012, pp. 2381–2383.

[58] F. Marhauser *et al.*, "802 MHz ERL cavity design and development," in *Proc. of the 9th International Particle Accelerator Conference (IPAC'18)*, Vancouver, BC, Canada, 29 Apr. - 4 May 2018, pp. 3990–3992. doi: 10.18429/JACoW-IPAC2018-THPAL146 .

[59] F. Marhauser *et al.*, "Design, Fabrication, and Test Results of 802 MHz Prototype Cavities for CERN's LHeC and FCC Initiatives," Rep. JLAB-TN-18-019, JLab, Newport News, VA, USA, April 2018.

[60] V. Shemelin, "Optimal choice of cell geometry for a multicell superconducting cavity," *Phys. Rev. ST Accel. Beams*, vol. 12, p. 114701, Nov. 2009. doi: 10.1103/PhysRevSTAB.12.114701.

[61] F. Marhauser, "Tuning recipe for SRF cavities." JLab. Unpublished, 2010.

[62] F. Marhauser, Private communication, JLab. 2021.

[63] H. Wang and J. Guo, "Bead-pulling measurement principle and technique used for the SRF cavities at JLab," *USPAS Education in Beam Physics and Accelerator Technology, SRF Practices and Hands-on Measurements*, Thomas Jefferson Lab, USA, Jan. 2015. `https://indico.jlab.org/event/98/contributions/7452/attachments/6308/8356/Bead-pull_Measurement_Principle_Lecture_Haipeng_v8.pdf`.

[64] F. Marhauser, "JLAB SRF cavity fabrication errors, consequences and lessons learned," in *Proc. of the 2nd International Particle Accelerator Conference (IPAC'11)*, San Sebastián, Spain, Sept. 2011, pp. 346–348.

[65] E. Chojnacki, E. Smith, R. Ehrlich, V. Veshcherevich, and S. Chapman, "Cryogenic heat load of the Cornell ERL main LINAC cryomodule," in *Proc. of the 14th*

International Conference on RF Superconductivity (SRF 2009), Berlin, Germany, Sept. 2009, pp. 638–642.

[66] S. Aull, O. Brunner, A. Butterworth, and N. Schwerg, "Material options for the superconducting rf system of the Future Circular Collider," CERN, Geneva, Switzerland, Rep. CERN-ACC-2018-0019, June 2018. https://cds.cern.ch/record/2625126.

[67] N. R. Chevalier, T. Junquera, J.-P. Thermeau, L. M. Romão, and D. Vandeplassche, "Cryogenic system for the MYRRHA superconducting linear accelerator," in *AIP Conference Proceedings*, vol. 1573, pp. 315–322, American Institute of Physics, Jan. 2014. doi: 10.1063/1.4860717.

[68] F. Zimmermann *et al.*, "Electrical Power Budget for FCC-ee," in *Proc. of the 7th International Particle Accelerator Conference (IPAC'16)*, Busan, Korea, May 2016, pp. 3828–3831. doi: 10.18429/JACoW-IPAC2016-THPOR024.

[69] C. Rode and D. Proch, "Cryogenic optimization for cavity systems," in *Proc. of the 4th International Conference on RF Superconductivity (SRF'89)*, KEK, Tsukuba, Japan, Aug. 1989, pp. 751–753.

[70] G. H. Hoffstaetter, S. M. Gruner, M. Tigner, *et al.*, "Cornell Energy Recovery Linac - Science Case and Project Definition Design Report," *Cornell University*, 2013.

[71] L. Merminga and J. R. Delayen, "On the optimization of Q_{ext} under heavy beam loading and in the presence of microphonics," Rep. JLab-TN-96-022, JLab, Newport News, VA, USA, May 1996. https://www.jlab.org/uspas11/MISC/Beam%20loading%20TN.pdf.

[72] E. Montesinos, "SPL Power Coupler - Possible Proposed Designs," Review of SPL RF Power Couplers, CERN, March 2010. https://indico.cern.ch/event/86123/contributions/1264596/attachments/1079384/1539615/SPL_power_coupler_possible_design_part_I.pdf.

[73] G. P. Segurana, I. R. Bailey, and P. H. Williams, "Construction of self-consistent longitudinal matches in multipass energy recovery linacs," *Physical Review Accelerators and Beams*, vol. 25, p. 021003, Feb. 2022. doi: 10.1103/PhysRevAccelBeams.25.021003.

[74] J. Delayen, "RF fundamentals and beam loading," *USPAS Education in Beam Physics and Accelerator Technology, University of Maryland*, USA, June 2008. https://uspas.fnal.gov/materials/08UMD/RF_Fundamentals.pdf.

[75] S. Posen and M. Liepe, "Mechanical optimization of superconducting cavities in continuous wave operation," *Phys. Rev. ST Accel. Beams*, vol. 15, p. 022002, Feb 2012. doi: 10.1103/PhysRevSTAB.15.022002.

[76] R. Zeng, A. Sunesson, S. Molloy, and A. Johansson, "Investigation to reduce power overhead required in superconducting rf cavity field control," in *Proc. of the 4th International Particle Accelerator Conference (IPAC'13)*, Shanghai, China, May 2013, pp. 3013–3015.

[77] N. C. Shipman *et al.*, "Ferro-Electric Fast Reactive Tuner Applications for SRF Cavities," in *Proc. of the 12th International Particle Accelerator Conference (IPAC'21)*, Campinas, SP, Brazil, May 2021, pp. 1305-1310. doi: 10.18429/JACoW-IPAC2021-TUXC03.

[78] E. Pozdeyev, "Regenerative multipass beam breakup in two dimensions," *Physical Review Special Topics - Accelerators and Beams*, vol. 8, p. 054401, May 2005. doi: 10.1103/PhysRevSTAB.8.054401.

[79] K. Yokoya, "Cumulative beam breakup in large scale linacs," Rep. DESY-86-084, DESY, Hamburg, Germany, August 1986. `https://inspirehep.net/files/c30ec0fed1dce9d21eb97e54c2080343`.

[80] C. Song and G. Hoffstaetter, "Beam breakup simulations for the Cornell x-ray ERL," in *2007 IEEE Particle Accelerator Conference (PAC)*, Albuquerque, New Mexico, June 2007, pp. 1227–1229. doi: 10.1109/PAC.2007.4441038.

[81] J. J. Bisognano and M. L. Fripp, "Requirements for longitudinal HOM damping in superconducting recirculating linacs," in *Proceedings of the 1988 Linear Accelerator Conference*, Williamsburg, Virginia, USA, Oct. 1988, pp. 388–390.

[82] A. Wolski, *Beam dynamics in high energy particle accelerators*. World Scientific, 2014.

[83] K. L. Brown, F. Rothacker, D. C. Carey, and F. C. Iselin, "Transport: A Computer Program for Designing Charged Particle Beam Transport Systems," Rep. SLAC-91, Rev.3, UC-28, SLAC, May 1983. `https://lss.fnal.gov/archive/nal/fermilab-nal-091.pdf`.

[84] K. L. Brown, "First-and second-order matrix theory for the design of beam transport systems and charged particle spectrometers," Rep. SLAC-75, Rev.2, SLAC, August 1967. doi: 10.2172/4742148.

[85] S. Setiniyaz, R. Apsimon, and P. H. Williams, "Filling pattern dependence of regenerative beam breakup instability in energy recovery linacs," *Physical Review Accelerators and Beams*, vol. 24, p. 061003, June 2021. doi: 10.1103/PhysRevAccelBeams.24.061003.

[86] G. Krafft, J. Bisognano, and S. Laubach, "Calculating beam breakup in superconducting linear accelerators," Tech. Rep. CEBAF-PR-90-39, JLab, Newport News, VA, USA, February 1990. https://www.osti.gov/biblio/882282.

[87] G. H. Hoffstaetter and I. V. Bazarov, "Beam-breakup instability theory for energy recovery linacs," *Physical Review Special Topics-Accelerators and Beams*, vol. 7, p. 054401, May 2004. doi: 10.1103/PhysRevSTAB.7.054401.

[88] L. Merminga, I. Campisi, D. Douglas, G. Krafft, J. Preble, and B. Yunn, "High average current effects in energy recovery linacs," in *Proceedings of the 2001 Particle Accelerator Conference (PACS2001)*, Chicago, IL, USA, June 2001, pp. 173–175. doi: 10.1109/PAC.2001.987462.

[89] B. C. Yunn, "Expressions for the threshold current of multipass beam breakup in recirculating linacs from single cavity models," *Physical Review Special Topics-Accelerators and Beams*, vol. 8, p. 104401, Oct. 2005. doi: 10.1103/PhysRevSTAB.8.104401.

[90] C. Barbagallo *et al.*, "HOM-damping studies in a multi-cell elliptical superconducting RF cavity for the multi-turn energy recovery linac PERLE," in *Proc. of the 66th ICFA Advanced Beam Dynamics Workshop on Energy Recovery Linacs*, vol. arXiv:2409.13798v1, Cornell University, Ithaca, NY, USA, Oct. 2022. doi: 10.48550/arXiv.2409.13798.

[91] H. Zheng, F. Meng, and J. Zhai, "HOM coupler design for CEPC cavities," in *Proc. of the 18th International Conference on RF Superconductivity (SRF'17)*, Lanzhou, China, July 2017, pp. 115–119. doi: 10.18429/JACoW-SRF2017-MOPB028.

[92] H. Zheng, J. Zhai, and J. Gao, "HOM Analysis and HOM Coupler Preliminary Design for CEPC," in *International ICFA Mini-Workshop on High Order Modes in SC Cavities*, Warnemünde, Germany, Aug. 2016. https://indico.cern.ch/event/465683/contributions/2269334/attachments/1325991/1990745/HOM_analysis_and_HOM_coupler_preliminary_design_for_CEPC.pdf.

[93] S. A. Bogacz, Private communication, JLab. 2022.

[94] MATLAB, *Version R2022b*. The MathWorks, Natick, MA, USA, 2022.

[95] V. Lebedev, "OptiMX - Computer code for linear and non-linear optics calculations," 2008.

[96] K. Papke, F. Gerigk, and U. van Rienen, "Comparison of coaxial higher order mode couplers for the CERN Superconducting Proton Linac study," *Physical Review Accelerators and Beams*, vol. 20, p. 060401, June 2017. doi: 10.1103/PhysRevAccelBeams.20.060401.

[97] W. Lou and G. Hoffstaetter, "Beam breakup current limit in multiturn energy recovery linear accelerators," *Physical Review Accelerators and Beams*, vol. 22, p. 112801, Nov. 2019. doi: 10.1103/PhysRevAccelBeams.22.112801 .

[98] S. Setiniyaz, R. Apsimon, P. H. Williams, C. Barbagallo, S. A. Bogacz, R. Bodenstein, and K. Deitrick, "Beam Breakup Instability Studies of Powerful Energy Recovery Linac for Experiments," *arXiv preprint, arXiv:2409.02798*, 2024. doi: 10.48550/arXiv.2409.02798.

[99] C. D. Tennant, *Studies of energy recovery linacs at Jefferson laboratory: 1 GeV demonstration of energy recovery at CEBAF and studies of the multibunch, multipass beam breakup instability in the 10 kW FEL upgrade driver*. PhD thesis, College of William & Mary - Arts & Sciences, 2006.

[100] C. Song and G. H. Hoffstaetter, "Longitudinal BBU Threshold Current in Recirculating Linacs," Rep. ERL-06-04, Cornell Laboratory for Accelerator-based Science and Education (CLASSE), Cornell University, Ithaca, NY, USA, August 2006. `https://www.classe.cornell.edu/~hoff/papers/ERL06-04.pdf`.

[101] D. Sagan, "Bmad - Software toolkit for charged-particle and X-ray simulations," 1996. `https://www.classe.cornell.edu/bmad/`.

[102] S. Setiniyaz, R. Apsimon, and P. Williams, "Implications of beam filling patterns on the design of recirculating energy recovery linacs," *Physical Review Accelerators and Beams*, vol. 23, p. 072002, July 2020. doi: 10.1103/PhysRevAccelBeams.23.072002 .

[103] S. Setiniyaz, Private communication, JLab. 2023.

[104] D. Boussard and T. P. R. Linnecar, "The LHC Superconducting RF System," Rep. LHC-Project-Report-316, CERN, Geneva, Switzerland, December 1999. `https://cds.cern.ch/record/410377`.

[105] A. Mosnier, S. Chel, X. Hanus, A. Novokhatski, and G. Flynn, "Design of a heavily damped superconducting cavity for SOLEIL," in *Proc. of the 17th Particle Accelerator Conf. (PAC'97)*, Vancouver, Canada, May 1997, pp. 1709–1711.

[106] J. Sekutowicz, "Higher Order Mode coupler for Tesla," in *Proc. of the 6th Workshop on RF Superconductivity*, Newport News, Virginia, USA, Oct. 1993.

[107] R. Rimmer, "Waveguide HOM damping studies at JLab," in *International Workshop on Higher-Order-Mode Damping Superconducting RF Cavities*, Cornell University, Ithaca, NY, USA, Oct. 2010. `https://www.classe.cornell.edu/Events/HOM10/rsrc/LEPP/Events/HOM10/Agenda/TA1_Rimmer.pdf`.

[108] R. Eichhorn *et al.*, "Cornell's HOM Beamline Absorbers," in *Proceedings of the 4th International Particle Accelerator Conference (IPAC'13)*, Shanghai, China, May 2013, pp. 2441–2443.

[109] S. Wang, J. Guo, R. Rimmer, and H. Wang, "JLEIC SRF Cavity RF Design," in *Proceedings of the 8th International Particle Accelerator Conference (IPAC'16)*, Busan, Korea, May 2016, pp. 2522–2524. doi:10.18429/JACoW-IPAC2016-WEPMW039.

[110] J. Holzbauer, "RF theory and design - notes," *US Particle Accelerator School*, Grand Rapids, MI, USA, June 2012. `https://uspas.fnal.gov/materials/12MSU/RF_Design_Lecture_Notes.pdf`.

[111] A. Butterworth, O. Brunner, R. Calaga, and E. Jensen, "The RF system for FCC-ee," *Proceedings of Science*, vol. EPS-HEP2015, 2015. doi:10.22323/1.234.0525.

[112] J. Mitchell, G. Burt, R. Calaga, S. Verdú-Andrés, and B. P. Xiao, "DQW HOM Coupler Design for the HL-LHC," in *Proc. of the 9th International Particle Accelerator Conference (IPAC'18)*, Vancouver, BC, Canada, April 29 - May 4, 2018, pp. 3663–3666. doi: 10.18429/JACoW-IPAC2018-THPAL018.

[113] W. Fang, W. Er-Dong, Z. Bao-Cheng, and Z. Kui, "Measuring the performance of the coaxial HOM coupler on a 2-cell TESLA-shape copper cavity," *Chinese Physics C*, vol. 33, p. 440, June 2009. doi: 10.1088/1674-1137/33/6/007.

[114] F. Marhauser, T. Elliot, and R. Rimmer, "Investigations on absorber materials at cryogenic temperatures," in *2009 IEEE Particle Accelerator Conference (PAC)*, Vancouver, Canada, May 2009, pp. 2799–2801.

[115] S. Gorgi Zadeh, *Accelerating cavity and higher order mode coupler design for the Future Circular Collider*. PhD thesis, Universität Rostock, Mar. 2021.

[116] R. Rimmer *et al.*, "The JLAB Ampere-Class cryomodule," in *Proc. of the 12th International Workshop on RF Superconductivity (SRF'05)*, Cornell University, Ithaca, New York, USA, 2005, pp 567–570.

[117] P. Sotirios, "Higher Order Mode Couplers Optimization for the 800 MHz Harmonic System for HL-LHC," Rep. CERN-STUDENTS-Note-2014-114, CERN, Geneva, Switzerland, Aug. 2014. `https://cds.cern.ch/record/1751451`.

[118] E. Häbel, V. Rödel, F. Gerigk, and Z. T. Zhao, "The Higher-Order Mode Dampers of the 400 MHz Superconducting LHC Cavities," Rep. CERN-SL-98-008-RF, CERN, Geneva, Switzerland, May 1997. `https://cds.cern.ch/record/349383`.

[119] C. G. Montgomery, R. H. Dicke, and E. M. Purcell, *Principles of microwave circuits*. IET, 1987.

[120] H. Padamsee *et al.*, "Design challenges for high current storage rings," *Part. Accel.*, vol. 40, pp. 17–41, Aug. 1991.

[121] F. Gerigk, "Design of higher-order mode dampers for the 400 MHz LHC superconducting cavities," First thesis (Studienarbeit), Technische Universität Berlin, 1997.

[122] J. Mitchell, *Higher Order Modes and Dampers for the LHC Double Quarter Wave Crab Cavity*. PhD thesis, Lancaster University, Oct. 2019.

[123] C. Barbagallo *et al.*, "First coaxial HOM coupler prototypes and RF measurements on a copper cavity for the PERLE project," in *Proc. of the 14th International Particle Accelerator Conference (IPAC'23)*, Venice, Italy, 2023, pp. 89–92. doi: 10.18429/JACoW-IPAC2023-MOPA025.

[124] 3D Systems, "Accura 25 Datasheet." `https://www.3dsystems.com/sites/default/files/2020-11/3d-systems-accura-25-datasheet-us-a4-2020-09-23-a-print.pdf`.

[125] 3D Systems, "Accura 48 Datasheet." `https://www.3dsystems.com/sites/default/files/2020-11/3d-systems-accura-48-htr-datasheet-a4-us-2020-09-11-a-print.pdf`.

[126] R. V. Broeck, "CERN Polymer Laboratory," CERN-Poster-2019-931, CERN, Geneva, Switzerland, 2019. `https://cds.cern.ch/record/2695152`.

[127] S. Clément, "3D-printing of HOM couplers," in *PERLE Collaboration Meeting*, CERN, Geneva, Switzerland, 2023. `https://indico.cern.ch/event/1266985/contributions/5449146/`.

[128] P. Maurin, "Copper-coating for PERLE project". CERN, Geneva, Switzerland, Unpublished internal document, 2023.

[129] HandySCAN BLACK® 3D Scanner. `https://get.creaform3d.com/lp-handyscan-3d/`.

[130] J. P. Rigaud, "Inspection report of the Accura 25 Hook coupler after coating". CERN, Geneva, Switzerland, EDMS 2787740, 2022.

[131] J. P. Rigaud, "Inspection report of the Accura 48 HTR Probe coupler antenna before coating". CERN, Geneva, Switzerland, EDMS 2787740, 2023.

[132] J. P. Rigaud, "Inspection report of the Accura 48 HTR Probe coupler antenna after coating". CERN, Geneva, Switzerland, EDMS 2787740, 2023.

[133] J. P. Rigaud, "Inspection report of the Accura 48 HTR Probe coupler shell before coating". CERN, Geneva, Switzerland, EDMS 2787740, 2023.

[134] J. P. Rigaud, "Inspection report of the Accura 48 HTR Probe coupler shell after coating". CERN, Geneva, Switzerland, EDMS 2787740, 2023.

[135] J. P. Rigaud, "Inspection report of the Accura 48 HTR half-block DQW coupler antenna before coating". CERN, Geneva, Switzerland, EDMS 2901961, 2023.

[136] J. P. Rigaud, "Inspection report of the Accura 48 HTR half-block DQW coupler antenna after coating". CERN, Geneva, Switzerland, EDMS 2901961, 2023.

[137] J. P. Rigaud, "Inspection report of the Accura 48 HTR half-block DQW coupler shell before coating". CERN, Geneva, Switzerland, EDMS 2901961, 2023.

[138] J. P. Rigaud, "Inspection report of the Accura 48 HTR half-block DQW coupler shell after coating". CERN, Geneva, Switzerland, EDMS 2901961, 2023.

[139] L. Lü, J. Y. H. Fuh, and Y.-S. Wong, *Laser-induced materials and processes for rapid prototyping*. Springer Science & Business Media, 2001.

[140] R. Gerard, Private communication, CERN. 2024.

[141] G. Ciovati, H. Tian, and S. G. Corcoran, "Buffered electrochemical polishing of niobium," *Journal of Applied Electrochemistry*, vol. 41, pp. 721–730, 2011.

[142] T. Weiland and R. Wanzenberg, "Wake fields and impedances," *Lect. Notes Phys.*, vol. 400, pp. 39–79, 1992. doi: 10.1007/3-540-55250-226.

[143] M. Migliorati and L. Palumbo, "Multibunch and multiparticle simulation code with an alternative approach to wakefield effects," *Phys. Rev. ST Accel. Beams*, vol. 18, p. 031001, Mar 2015. doi: 10.1103/PhysRevSTAB.18.031001.

[144] F. Reimann and U. H. Van Rienen, "Wakefields - An Overview," *CERN Yellow Reports: School Proceedings*, vol. 1, pp. 125–125, 2018. doi: 10.23730/CYRSP-2018-001.125.

[145] M. Ferrario, M. Migliorati, and L. Palumbo, "Wakefields and Instabilities in Linear Accelerators," pp. 357–375, 2014. CAS - CERN Accelerator School: Advanced Accelerator Physics Course, Trondheim, Norway, 18-29 Aug 2013. doi: 10.5170/CERN-2014-009.357.

[146] M. Dohlus and R. Wanzenberg, "An Introduction to Wake Fields and Impedances," *CERN Yellow Rep. School Proc.*, vol. 3, p. 15, 2017. doi: 10.23730/CYRSP-2017-003.15.

[147] L. Palumbo, V. G. Vaccaro, and M. Zobov, "Wake fields and impedance," in *CERN Accelerator School: Course on Advanced Accelerator Physics*, Laboratori Nazionali di Frascati, Sept. 2003, pp. 331–390. doi: 10.5170/CERN-1995-006.331.

[148] Y. Chin, "Advances and applications of ABCI," in *Proc. of the 15th International Conference on Particle Accelerators*, Washington, DC, USA, May 1993, pp. 3414–3416. doi: 10.1109/PAC.1993.309668.

[149] H. Wang, R. Rimmer, and F. Marhauser, "Simulations and measurements of a heavily HOM-damped multi-cell SRF cavity," in *2007 IEEE Particle Accelerator Conference (PAC)*, Albuquerque, New Mexico, 2007, pp. 2496–2498.

[150] F. Marhauser, R. Rimmer, and H. Wang, "Narrowband and broadband impedance budget of the 1497 MHz HOM-damped five cell high current cavity," Rep. JLAB-TN-08-002, JLab, Newport News, VA, USA, 2008.

[151] F. Marhauser, R. Rimmer, K. Tian, and H. Wang, "Enhanced method for cavity impedance calculations," in *Proc. of the 23rd Particle Accelerator Conference (PAC'09)*, Vancouver, BC, Canada, 2009, pp. 4523–4525.

[152] G. Van Rossum and F. L. Drake Jr, "Python tutorial," 1995.

[153] H. W. Pommerenke, J. D. Heller, S. G. Zadeh, and U. van Rienen, "Computation of lossy higher order modes in complex SRF cavities using Beyn's and Newton's methods on reduced order models," *International Journal of Modern Physics A*, vol. 34, no. 36, p. 1942037, 2019. doi: 10.1142/S0217751X19420375.

[154] F. Marhauser *et al.*, "Calculations for RF cavities with dissipative material," in *Proc. of the 17th Int. Conf. RF Superconductivity (SRF'15)*, Whistler, Canada, 2015, pp. 1056–1060.

[155] I. Karpov, R. Calaga, and E. Shaposhnikova, "High order mode power loss evaluation in future circular electron-positron collider cavities," *Phys. Rev. Accel. Beams*, vol. 21, p. 071001, Jul 2018. doi: 10.1103/PhysRevAccelBeams.21.071001.

[156] A. Lunin, T. Khabiboulline, N. Solyak, A. Sukhanov, and V. Yakovlev, "Resonant excitation of high order modes in the 3.9 GHz cavity of the Linac Coherent Light Source," *Phys. Rev. Accel. Beams*, vol. 21, p. 022001, Feb 2018. doi: 10.1103/PhysRevAccelBeams.21.022001.

[157] G.-T. Park, J. Guo, F. Marhauser, R. Rimmer, H. Wang, and S. Wang, "Beam Impedance Study on a Harmonic Kicker for the CCR of JLEIC," in *Proceedings of the ICFA Advanced Beam Dynamics Workshop on Energy Recovery Linacs (ERL'19)*, Berlin, Germany, Sept. 2019, pp. 116–119. doi: 10.18429/JACoW-ERL2019-WEPNEC22.

[158] B. Aune *et al.*, "Superconducting TESLA cavities," *Phys. Rev. ST Accel. Beams*, vol. 3, p. 092001, Sept. 2000. doi: 10.1103/PhysRevSTAB.3.092001.

[159] D. Gong, J. Gao, H. Zheng, J. Zhai, and P. Sha, "Beam-induced HOM power in CEPC collider ring cavity," *Radiation Detection Technology and Methods*, vol. 3, pp. 1–10, March 2019. doi: 10.1007/s41605-019-0098-y.

[160] B. W. Zotter and S. Kheifets, *Impedances and Wakes in High Energy Particle Accelerators*. World Scientific, 1998.

[161] S. G. Zadeh, T. Flisgen, R. Calaga, and U. van Rienen, "HOM damping options for the Z-Pole operating scenario of FCC-ee," *Journal of Physics: Conference Series*, vol. 1350, p. 012007, Nov. 2019. doi: 10.1088/1742-6596/1350/1/012007.

[162] A. Tsakanian, H.-W. Glock, A. Velez, and J. Knobloch, "Study on HOM power levels in the BESSY VSR module," in *Proc. of the 8th Int. Particle Accelerator Conf.(IPAC'17)*, Copenhagen, Denmark, May 2017, pp. 982–985. doi: 10.18429/JACoW-IPAC2017-MOPVA052.

[163] T. Flisgen, H.-W. Glock, A. Tsakanian, *et al.*, "Estimation of dielectric losses in the BESSY VSR Warm Beam Pipe Absorbers," in *Proc. of the 9th International Particle Accelerator Conference (IPAC'18)*, Vancouver, BC, Canada, May 2018, pp. 3185–3188. doi: 10.18429/JACoW-IPAC2018-THPAF085.

[164] G. Olivier, Private communication, IJCLab. 2023.

[165] S. Blivet, Private communication, IJCLab. 2024.

[166] C. Barbagallo *et al.*, "Simulations and first RF measurements of coaxial HOM coupler prototypes for PERLE SRF cavities," in *Proc. of the 21st Int. Conf. RF Supercond. (SRF'23)*, Grand Rapids, MI, USA, 2023, pp. 831–834. doi: 10.18429/JACoW-SRF2023-WEPWB103.

[167] F. Marhauser, "PERLE Cavity Design and Results and First Thoughts on HOM-Couplers," PERLE HOM Coupler Meeting, CERN, Oct. 2019. `https://indico.in2p3.fr/event/19904/contributions/75731/attachments/55322/72889/PERLE_HOM_WorkshopV1.pdf`.

[168] E. Montesinos, "CERN SPL Fundamental Power Coupler - Progress report," SPL Meeting, CERN, Dec. 2012. https://indico.cern.ch/event/216370/contributions/441388/attachments/345697/482085/SPL_couplers_December_2012.pdf.

[169] Toshiba Ceramics Co., LTD, "CERASIC-B©."

[170] Y. Takeuchi, T. Abe, T. Kageyama, and H. Sakai, "RF dielectric properties of SiC ceramics and their application to design of HOM absorbers," in *Proceedings of the 2005 Particle Accelerator Conference (PAC'05)*, Knoxville, Tennessee, USA, May 2005, pp. 1195–1197.

[171] W. Xu *et al.*, "High-power test results for a cylindrical-shell silicon carbide higher-order-mode damper," *Phys. Rev. Accel. Beams*, vol. 27, p. 031601, Mar. 2024. doi: 10.1103/PhysRevAccelBeams.27.031601.

[172] S. G. Zadeh, "HOM damping study of the 800 MHz UROS5 cavity," CERN, Dec. 2023. https://indico.cern.ch/event/1349840/.

[173] A. Mosnier, "Developments of HOM couplers for superconducting cavities," in *Proc. of the 4th Workshop on RF Superconductivity*, KEK, Tsukuba, Japan, 1989, pp. 378–396.

[174] N. Solyak, M. Awida, A. Hocker, T. Khabibobulline, and A. Lunin, "Higher Order Mode Coupler Heating in Continuous Wave Operation," *Physics Procedia*, vol. 79, pp. 63–73, 2015. doi: 10.1016/j.phpro.2015.11.063.

[175] COMSOL Multiphysics 5.6. https://www.comsol.com/.

[176] D. W. Hahn and M. N. Özisik, *Heat conduction*. John Wiley & Sons, 2012.

[177] H. Guo, P. Arbenz, and B. Oswald, "Realistic 3-Dimensional eigenmodal analysis of electromagnetic cavities using surface impedance boundary conditions," in *Proc. of the 11th International Computational Accelerator Physics Conference (ICAP 2012)*, Rostock-Warnemünde, Germany, Aug. 2012, pp. 161–163.

[178] K. Mittag, "Kapitza conductance and thermal conductivity of copper niobium and aluminium in the range from 1.3 to 2.1 K," *Cryogenics*, vol. 13, pp. 94–99, Feb. 1973. doi: 10.1016/0011-2275(73)90132-X.

[179] A. Boucheffa and M. Francois, "Kapitza conductance of niobium for superconducting cavities in the temperature range 1.6 K, 2.1 K," in *Proc. of the 1995 Workshop on RF Superconductivity (SRF1995)*, Gif-sur-Yvette, 1995, pp. 659–663.

[180] T. Khabiboulline, "Engineering for Particle Accelerators," *USPAS Education in Beam Physics and Accelerator Technology, SRF cavity design, RF measurements and tuning*, Rohnert Park, CA, USA, July 2017. https://uspas.fnal.gov/materials/24RohnertPark/Engineering/Engineering%20for%20particle%20accelerators%20-%20USPAS%20July%202024%20-%20TKhabiboulline.pdf.

[181] K. Sang-ho, D. Marc, J. Dong-o, and S. Ronald, "Higher-order-mode (HOM) power in elliptical superconducting cavities for intense pulsed proton accelerators," *Nuclear Instruments and Methods in Physics Research Section A: Accelerators, Spectrometers, Detectors and Associated Equipment*, vol. 492, p. 10, Oct. 2002. doi: 10.1016/S0168-9002(02)01286-X.

[182] J. Halbritter, "FORTRAN program for the computation of the surface impedance of superconductors," Tech. Rep. 3/70-6, Kernforschungszentrum, Karlsruhe (West Germany). Institut fuer Experimentelle Kernphysik, 1970. doi: 10.5445/IR/270004230.

[183] N. Valles *et al.*, "Record quality factor performance of the prototype Cornell ERL main linac cavity in the horizontal test cryomodule," in *Proc. of the 16st International Conference on RF Superconductivity (SRF'13)*, Paris, France, Sep. 2013, pp. 300–304.

[184] J. Turneaure, J. Halbritter, and H. Schwettman, "The surface impedance of superconductors and normal conductors: The Mattis-Bardeen theory," *Journal of Superconductivity*, vol. 4, pp. 341–355, 1991.

[185] J. Apeland, "Thermal analysis of HOM coupler for HG-Cavity," Tech. Rep. EDMS No. 1772707, CERN, 2017.

[186] D. M. Pozar, *Microwave engineering*. John Wiley & Sons, 2011.

[187] MarkeTech, "Single-crystal sapphire." https://www.matweb.com/search/DataSheet.aspx?MatGUID=dc842aba6fa24c48b7e0155ee448d6f0.

[188] M. H. Awida, I. Gonin, T. Khabiboulline, and V. P. Yakovlev, "Modeling of Thermal Quench in Superconducting RF Cavities," *IEEE Transactions on Applied Superconductivity*, vol. 30, pp. 1–8, March 2020. doi: 10.1109/TASC.2020.2978437.

[189] S. Verdu-Andres *et al.*, "Cryogenic RF performance of Double-Quarter Wave cavities equipped with HOM filters," in *Proc. of the 10th International Particle Accelerator Conference (IPAC'19)*, Melbourne, Australia, May 2019, pp. 3043-3046. doi: 10.18429/JACoW-IPAC2019-WEPRB098.

[190] V. Shemelin and P. Carriere, "Frequency control in the process of a multicell superconducting cavity production," *Review of Scientific Instruments*, vol. 83, Apr. 2012. doi:10.1063/1.4705985.

[191] H. Park, S. D. Silva, J. R. Delayen, A. Hutton, and F. Marhauser, "First test results of superconducting twin axis cavity for ERL applications," in *Proc. of the 29th Linear Accelerator Conf. (LINAC'18)*, Beijing, China, Sept. 2018, pp. 398–401. doi: 10.18429/JACoW-LINAC2018-TUPO032.

[192] M. Gao, Q. Wang, L. Li, and C. Liu, "Comprehensive energy-saving method for sheet metal forming," *The International Journal of Advanced Manufacturing Technology*, vol. 104, pp. 2273–2285, July 2019. doi:10.1007/s00170-019-04022-4.

[193] G. Grose, Private communication, JLab. 2022.

[194] T. Khabiboulline, N. Solyak, and V. Yakovlev, "Experiments on HOM spectrum manipulation in a 1.3 GHz ILC SC cavity," in *Proc. of the 2011 Particle Accelerator Conference(IPAC'11)*, New York, NY, USA, 2011.

[195] FARO® 8-axis Edge FaroArm® & Scan Arm. https://www.faro.com/fr-FR/Resource-Library/Tech-Sheet/techsheet-8-axis-edge-faroarm-scanarm.

[196] E. Drachuk, Private communicationn JLab. 2022.

[197] S. An, Z. Liping, T. Yazhe, Y.-m. Li, and Y.-S. Cho, "A method to measure the frequencies of individual half cells in a dumbbell cavity," *Review of Scientific Instruments*, vol. 79, Oct. 2008. doi:10.1063/1.2987686.

[198] G.-T. Park, Private communication, JLab. 2023.

[199] S. Overstreet, Private communication, JLab. 2023.

[200] M. Ge, Private communication, JLab. 2023.

[201] S. An, Z. Liping, T. Yazhe, L. Yingmin, G. Changyi, and Y. Cho, "PEFP dumbbell frequency and length tuning of a low-beta SRF cavity," in *Proc. of the 11th European Particle Accelerator Conference (EPAC2008)*, Genoa, Italy, June 2008, pp. 823–825.

[202] W. W. Hansen and R. F. Post, "On the Measurement of Cavity Impedance," *Journal of Applied Physics*, vol. 19, pp. 1059–1061, April 2004.

[203] T. Jurgens, "Equations for bead pull cavity measurements," Rep. Fermilab-LU-159, Fermilab, Batavia, IL, USA, April 1990. `https://lss.fnal.gov/archive_notes/linac/fermilab-lu-159.pdf`.

[204] MatWeb, MatWeb Materials Database, "Polytetrafluoroethylene (PTFE)." `https://www.matweb.com/search/DataSheet.aspx?MatGUID=4e0b2e88eeba4aaeb18e8820f1444cdb`.

[205] H. Hahn, R. Calaga, P. Jain, E. C. Johnson, and W. Xu, "HOM identification by bead pulling in the Brookhaven ERL cavity," *Nuclear Instruments and Methods in Physics Research Section A: Accelerators, Spectrometers, Detectors and Associated Equipment*, vol. 734, pp. 72–78, Jan. 2014. doi: 10.1016/j.nima.2012.12.065.

[206] F. Caspers, P. McIntosh, and T. Kroyer, "RF engineering - basic concepts," in *Proceedings of the CERN Accelerator School (CAS)*, Ebeltoft, Denmark, June 2010. https://cas.web.cern.ch/sites/default/files/afternoon%20courses/Daresbury-2007/basic-concepts-v6.pdf.

[207] A. D'Elia, "Design and characterization of the power coupler line for HIE-ISOLDE high beta cavity," CERN, Geneva, Switzerland, HIE-ISOLDE-PROJECT-Note-0011, Aug. 2011. https://cds.cern.ch/record/1436073/files/HIE-ISOLDE-PROJECT-Note-0011.pdf.

[208] W. R. Inc., "Mathematica, Version 13.3." Champaign, IL, 2023.

[209] C. Potratz, H. Glock, U. van Rienen, and F. Marhauser, "Automatic pole and Q-value extraction for RF structures," in *Proc. of the 2011 International Particle Accelerator Conference (IPAC'11)*, San Sebastián, Spain, 2011, pp. 2241–2243.

[210] G. T. Park, J. Guo, M. Marchlik, R. A. Rimmer, S. Overstreet, and H. Wang, "Harmonic kicker cavity for high power operation," *Physical Review Accelerators and Beams*, vol. 26, no. 9, p. 091002, 2023. doi: 10.1103/PhysRevAccelBeams.26.091002.

[211] MatWeb, MatWeb Materials Database, "Oxygen-free high conductivity Copper." https://www.matweb.com/search/DataSheet.aspx?MatGUID=0db21ddedce14e16993ee5cbdf97878d.

[212] T. Weiland, U. van Rienen, P. Hülsmann, W. Müller, and H. Klein, "Investigations of trapped higher order modes using a 36-cell test structure," *Physical Review Special Topics-Accelerators and Beams*, vol. 2, p. 042001, April 1999. doi: 10.1103/PhysRevSTAB.2.042001.

[213] K. Papke, F. Gerigk, and U. van Rienen, "Progress of HOM coupler for CERN SPL Cavities," in *Proc. 5th International Particle Accelerator Conference (IPAC 2014)*, Dresden, Germany, 2014, pp. 2568–2570. doi: 10.18429/JACoW-IPAC2014-WEPR.

Résumé étendu en français

Introduction

Les accélérateurs de particules ont été largement utilisés tout au long du vingtième siècle dans dans de nombreux domaines, dont l'industrie, la médecine et la recherche fondamentale. Parmi les applications notables, nous pouvons citer les sources de rayonnement synchrotron (RS) et les lasers à électrons libres (LEL), qui génèrent des faisceaux de photons pour les études de physique atomique, moléculaire et la biologie, mais également les collisionneurs de hadrons et d'électrons-ions pour la recherche en physique nucléaire et des particules. Historiquement, les anneaux de stockage ont satisfait la demande de faisceaux de photons hautement cohérents et à haute luminosité moyenne [1]. Cependant, leurs performances sont limitées par l'équilibre entre l'amortissement par rayonnement et l'excitation quantique. Cela restreint la minimisation de l'émittance et de la longueur des paquets de particules. Les accélérateurs linéaires (Linacs) peuvent produire des faisceaux avec une faible émittance, une faible dispersion en énergie et une courte longueur de paquet. Cependant, leur utilisation est limitée à l'accélération de faisceaux à faible courant moyen (de l'ordre du mA ou moins) en raison d'une consommation importante de puissance radiofréquence (RF).

Les accélérateurs linéaires à récupération d'énergie (ERLs) représentent un concept prometteur pour générer des faisceaux d'électrons à haut courant avec une puissance RF considérablement réduite par rapport aux Linacs traditionnels. Les ERLs combinent l'efficacité d'un anneau de stockage avec les caractéristiques supérieures du faisceau d'un Linac. L'ERL se positionne comme une option attrayante pour un certain nombre d'applications dont les futures sources de lumière [2]. La notion de récupération d'énergie a été introduite par M. Tigner [3] en 1965, initialement pour sa mise en œuvre dans un collisionneur. Elle se fonde sur le principe que les champs de cavité RF, en synchronisant correctement l'arrivée des paquets d'électrons dans le Linac, peuvent accélérer et décélérer le même faisceau [2]. Le schéma le plus simple d'un ERL implique une seule recirculation. Un faisceau d'électrons est injecté dans le Linac depuis un photo-injecteur de haute luminosité et il est accéléré à travers des cavités RF. Si la longueur du chemin de recirculation est conçue pour être un nombre entier plus la moitié de la longueur d'onde du champ RF d'accélération, après son utilisation, le faisceau retourne au Linac déphasé de 180° par rapport au champ RF et il est alors décéléré à travers les cavités RF. L'énergie du faisceau décéléré est récupérée et utilisée

pour accélérer les paquets d'électrons suivants. Par la suite, le faisceau décéléré quitte le Linac avec une énergie approximativement égale à l'énergie d'injection et il est dirigé vers un absorbeur de faisceau. Le faisceau décéléré compense la charge du faisceau accéléré, permettant l'accélération de faisceaux à haut courant avec une consommation minimale de puissance RF.

Depuis la première démonstration de récupération d'énergie au Stanford Superconducting Accelerator FEL [4], plusieurs installations d'ERLs ont été conçus, construits et exploités à travers le monde. Les principaux paramètres d'un ERL sont le courant du faisceau d'électrons et l'énergie du faisceau [9]. Le record de puissance du faisceau est détenu par le laser à électrons libres ERL IR (infrarouge) Upgrade à JLab, qui a fonctionné avec plus de 1,1 MW de puissance de faisceau [8]. Ce faisceau n'a nécessité qu'environ 300 kW de puissance RF pour être accéléré, mettant en évidence l'économie d'énergie comme motivation derrière la construction d'un ERL [2]. Dans une époque où la sobriété énergétique est cruciale et la durabilité énergétique essentielle pour la société, la minimisation de la consommation d'énergie constitue un défi prioritaire pour les futurs accélérateurs. Ainsi, les ERLs représentent une étape essentielle vers l'avenir durable des applications de physique à haute énergie. Pour la prochaine génération d'ERL à fort courant, l'utilisation de cavités supraconductrices à radiofréquence (RF) est la solution la plus efficace pour réduire significativement la consommation d'énergie [17, p. 45]. Au cours des prochaines décennies, quatre ERLs devraient être construits. Ils utiliseront des cavités supraconductrices RF pour atteindre des niveaux de puissance du faisceau de l'ordre de plusieurs mégawatts. Cela ouvrira la voie au développement et à la construction de complexes d'accélérateurs de plusieurs gigawatts pour des études de physique à haute énergie [9].

Dans ce contexte, PERLE (Powerful Energy Recovery Linac for Experiments) [18], discuté dans cette thèse, est la seule proposition d'un ERL multi-tour en mode continu avec une puissance de faisceau de 10 MW. Le faisceau d'électrons de 20 mA sera accéléré à travers des cavités RF supraconductrices lors de trois passages de recirculation pour atteindre l'énergie cible de 500 MeV. PERLE est prévu pour être hébergé au Laboratoire de Physique des 2 Infinis Irène Joliot-Curie (IJCLab) à Orsay. Il servira de démonstrateur pour acquérir l'expérience nécessaire au développement du Large Hadron-electron Collider (LHeC) [19, 20] envisagé au CERN. De plus, PERLE ouvrira la voie à la prochaine génération d'ERLs compacts et puissants adaptés aux applications nécessitant des faisceaux à haute énergie et à haut courant, telles que la diffusion Compton inverse, les sources de refroidissement d'ions à haute énergie, et les collisionneurs électron-ion.

Motivation et objectif de la thèse

Dans les ERLs multi-tours à fort courant, comme PERLE, l'instabilité de Beam Breakup (BBU) constitue un phénomène limitant les performances pour un fonctionnement stable [2]. Cet effet émerge de l'interaction entre le faisceau d'électrons circulant et les

modes des cavités excités parasites, connus sous le nom de modes d'ordre supérieur (HOMs). Les modes monopolaires induits par le faisceau peuvent augmenter la charge cryogénique du Linac, tandis que les modes dipolaires peuvent dévier le faisceau lors des passages suivants dans les cavités. Pour atténuer ces effets, la prochaine génération d'ERLs à fort courant nécessite des cavités SRF avec des exigences d'amortissement élevées des HOMs [21]. Aujourd'hui, divers concepts pour amortir les HOMs potentiellement dangereux peuvent être utilisés. Les solutions d'amortissement existantes utilisent principalement des coupleurs HOM coaxiaux et à guide d'ondes, des absorbeurs de ligne de faisceau, ou une combinaison de ceux-ci installés sur le tube faisceau des cavités pour absorber les HOMs.

Cette thèse vise à concevoir, construire, tester et analyser des coupleurs HOM coaxiaux pour les cavités de PERLE. L'objectif ultime est de proposer des options pour atténuer les HOM des cavités et assurer le fonctionnement stable de l'ERL. Plusieurs designs de coupleurs HOM coaxiaux ont été analysés et optimisés en fonction du spectre de fréquence de la cavité PERLE pour répondre aux exigences de BBU. La performance de la cavité équipée des coupleurs HOM a été évaluée numériquement. Les coupleurs HOM optimisés ont été fabriqués et testés individuellement ainsi qu'en combinaisons multi-coupleurs à température ambiante dans des prototypes de cavités en cuivre conçues pour PERLE afin d'évaluer leurs performances d'amortissement. Les simulations ont été validées en les comparant aux résultats obtenus à partir des mesures sur les prototypes des cavités RF et des coupleurs HOM.

Contenu de la thèse

Le chapitre 1 discute des principes de base de la théorie électromagnétique et des cavités RF. Le chapitre 2 présente l'accélérateur PERLE et la cavité elliptique 5-cellules en niobium résonante à 801,58 MHz proposée pour ses Linacs. Les paramètres RF et le spectre des HOM de la cavité 5-cellules sont discutés. Les pertes de chaleur statiques et dynamiques de la cavité ainsi que les exigences en puissance sont également évalués. Le phénomène d'instabilité de BBU est présenté au chapitre 3. Les seuils d'impédance longitudinale et transversale sont calculés pour la cavité PERLE, ainsi qu'une estimation du courant de faisceau maximal atteignable.

Le chapitre 4 présente un aperçu des mécanismes existants d'amortissement des modes d'ordre supérieur, tels que les coupleurs HOM et les absorbeurs de ligne de faisceau, utilisés pour extraire la puissance HOM des cavités. L'optimisation de la transmission RF de trois modèles de coupleurs coaxiaux HOM est présentée. Les processus utilisés dans l'impression 3D et les techniques de revêtement de surface en cuivre employées pour fabriquer les coupleurs HOM optimisés sont détaillés, ainsi que les mesures métrologiques effectuées sur leurs composants principaux.

Le chapitre 5 décrit la théorie des impédances longitudinales et transversales, ainsi que la puissance HOM générée par le faisceau. Les techniques numériques employées pour calculer les quantités susmentionnées sont également discutées. Les coupleurs

HOM optimisés sont combinés en deux structures d'amortissement différentes (ou groupes d'extrémité HOM) et ils sont comparés en termes d'impédance et d'extraction de la puissance HOM. L'absorption de la puissance HOM via des absorbeurs de ligne de faisceau est également présentée. Enfin, la charge thermique dynamique sur les surfaces des coupleurs est examinée. Plusieurs techniques de refroidissement sont proposées pour prévenir le risque de perte de supraconductivité dans les coupleurs HOM et la cavité.

Le chapitre 6 présente le premier prototype de cavité PERLE en cuivre à 5 cellules et à 801,58 MHz fabriqué dans le cadre de cette thèse pour valider les performances d'amortissement des HOMs de deux groupes d'extrémité HOM. Le processus de fabrication et les écarts géométriques des cellules de la cavité dus aux tolérances de fabrication sont décrits. Les mesures de type "dumbbell" et le processus de "découpage" effectué sur les cellules pour accorder la cavité à sa fréquence de fonctionnement sont également discutés. De plus, les mesures de "bead-pull" effectuées sur la cavité à 5 cellules sont présentées.

Le chapitre 7 traite des mesures RF à faible puissance réalisées sur les cavités PERLE de type cuivre à 2 et 5 cellules et à 801,58 MHz équipées des coupleurs HOM fabriqués. L'étude inclut l'évaluation du spectre de fréquence des cavités, les mesures de "bead-pull" des modes pertinents, ainsi que les mesures de performance d'amortissement des HOM pour les prototypes de coupleurs HOM.

Synthèse des résultats et conclusions

Dans cette thèse, des coupleurs HOM coaxiaux pour les cavités PERLE ont été conçus, fabriqués, testés et analysés, avec pour objectif principal de proposer plusieurs options d'amortissement capables de réduire les HOMs en dessous des limites d'instabilité de BBU. Cette étude a pris en compte la configuration ERL à 500 MeV pour le projet PERLE.

Le layout de l'accélérateur PERLE, la conception de la cavité SRF et l'identification des HOMs ont été traités dans le chapitre 2. La cavité Nb 5-cellules à 801,58 MHz construite au JLab a été sélectionnée pour le projet PERLE. Les HOMs monopolaires et dipolaires potentiellement dangereux ont été identifiés à l'aide des analyses fréquentielles en utilisant le logiciel CST Studio Suite®. Les modes de la première bande passante monopolaire (TM_{011}) et les deux premières bandes passantes dipolaires (TE_{111}, TM_{110}) ont été identifiés comme les plus problématiques en raison de leurs valeurs élevées de R/Q (rapport entre l'impédance shunt et le facteur de qualité de la cavité). Ces HOMs peuvent entraîner des instabilités du faisceau s'ils ne sont pas suffisamment amortis. La proximité des HOMs avec les harmoniques du spectre du faisceau a également été évaluée. Cela permet de prévenir l'augmentation potentielle de la tension due à leur possible interaction résonante avec les harmoniques de courant de grande amplitude. Les résultats des simulations montrent que les HOMs concernés sont suffisamment éloignés de leur harmonique de faisceau le plus proche pour exclure

la possibilité d'effets résonants avec le faisceau traversant les cavités.

La consommation de puissance du système cryogénique a également été évaluée. Les pertes statiques et dynamiques pour chacun des deux Linacs de PERLE sont estimées à $P_{\mathrm{st}} = 37.4$ W and $P_{\mathrm{dyn}} = 107.5$ W, respectivement. La puissance en régime alternatif requise par chaque Linac est d'environ $P_{\mathrm{t,AC}} = 108$ kW. La puissance RF totale à fournir par cavité a été évaluée dans les scénarios de fonctionnement ERL "sur la crête" et "hors crête". Étant donné le gradient nominal de la cavité de 22,4 MV/m, la puissance totale du faisceau par cavité est de 1,23 MW. En supposant une désaccord microphonique de 60 Hz et un coupleur de puissance avec $Q_{\mathrm{L},0} = 2.5 \times 10^6$, la puissance d'entrée estimée par cavité est de 103 kW pour le scénario "hors crête" considéré et de 92 kW pour le scénario "sur la crête". La puissance RF requise peut être réduite davantage en contrôlant les effets de microphonie grâce à un système d'accord en fréquence (FE-FRT).

Les instabilités BBU ont été discutées dans le chapitre 3. Les seuils d'impédance longitudinale et transversale ont été calculés analytiquement pour la cavité PERLE en considérant un courant de faisceau total de 120 mA. Le seuil d'impédance longitudinale résultant suit l'équation $Z_{\parallel}^{\mathrm{th}}[\mathrm{k}\Omega] = 2.12 \times 10^5 f^{-1}[\mathrm{GHz}]$, tandis que la valeur du seuil d'impédance transversale est $Z_{\perp}^{\mathrm{th}} = 5.23 \times 10^5$ kΩ/m et elle est indépendante de la fréquence. Les seuils d'impédance ont été utilisés pour calculer les facteurs de qualité externes critiques pour les HOM concernés, au-delà desquels des instabilités BBU peuvent se produire. Les Q_{ext} critiques ont été comparés aux résultats de simulation du code de suivi de particules développé à l'université de Lancaster, révélant des tendances en bon accord. Les résultats montrent également que des courants seuil au niveau de l'Ampère peuvent être atteints sur PERLE en considérant des Q_{ext} typiques allant de 10^3 à 10^5.

La transmission RF de trois coupleurs HOM coaxiaux, notamment les coupleurs probe (P), hook (H) et DQW, a été optimisée pour amortir les HOM dangereux de la cavité PERLE à 5 cellules et à 801,58 MHz tout en préservant l'efficacité du mode fondamental (cf. chap. 4). Les simulations ont été réalisées en utilisant le solveur en domaine fréquentiel du logiciel CST. Les exigences d'amortissement des HOMs à haute impédance et du filtre coupe-bande du mode fondamental ont été globalement satisfaites pour les conceptions des coupleurs HOM étudiés. Le coupleur DQW apparaît comme la solution la plus avantageuse pour amortir simultanément la première bande passante monopolaire et les deux premières bandes passantes dipolaires. Après avoir optimisé leur transmission RF, des prototypes de chaque coupleur HOM ont été fabriqués pour tester leurs performances dans des cavités en cuivre à 2 cellules et 5 cellules de typologie PERLE à 801,58 MHz. Les prototypes de coupleurs HOM ont été imprimés en 3D en résine époxy (Accura 25 et Accura 48 HTR), puis recouverts de cuivre par électrodéposition. L'étude a démontré avec succès la faisabilité du cuivrage pour des coupleurs HOM en résine époxy imprimés en 3D, confirmant que le substrat de carbone appliqué facilite l'adhésion du cuivre aux surfaces polymères.

Cependant, la technique d'électrodéposition utilisée n'a pas permis de contrôler pleinement l'homogénéité du dépôt de cuivre tout au long du processus. L'époxy Accura 48 HTR s'est révélé être plus approprié pour le cuivrage par électrodéposition en raison de sa rigidité et de sa stabilité thermique supérieures à celles de l'Accura 25. Les mesures de reconstruction numérique 3D ont été réalisées sur chaque coupleur fabriqué pour évaluer les écarts de forme entre le modèle idéal du CAO 3D et la géométrie réelle. Les analyses métrologiques suggèrent que la plupart des régions de surface mesurées se situent dans la plage de tolérance définie de ± 0,5 mm après le processus de revêtement. De plus, l'épaisseur moyenne estimée du revêtement sur les surfaces des coupleurs varie d'environ 200 µm à 350 µm. Cette épaisseur dépasse avec succès l'épaisseur moyenne minimale de revêtement de 30 µm requise pour assurer les propriétés de conductivité électrique désirées dans la plage de fréquence de fonctionnement considérée des coupleurs HOM étudiés.

Les coupleurs HOM optimisés, décrits dans le chapitre 4, ont été regroupés en deux configurations appelées groupes d'extrémités HOM, puis simulés avec la cavité 5 cellules de PERLE à 801,58 MHz (cf. chap. 5). Les performances d'amortissement des HOM et le comportement thermique dû au chauffage RF ont été étudiés pour ces deux configurations : deux coupleurs HOM de type Probe et deux de type Hook (schéma 2P2H), ainsi que quatre coupleurs de type DQW (schéma 4DQW). De plus, une version adaptée du coupleur de puissance de type SPL a été incluse dans les simulations. Les simulations de champs de sillage (*wakefields*) et de modes propres (*eigenmodes*) ont été effectuées pour calculer les impédances longitudinales et transversales de la cavité. Les deux schémas d'amortissement des HOM analysés abaissent l'impédance de la cavité en dessous des limites d'instabilité BBU. Le schéma d'amortissement 4DQW montre une atténuation des HOM plus efficace pour les impédances longitudinales et transversales par rapport à l'option 2P2H. De plus, sa conception symétrique garantit la préservation de la symétrie des HOM dipolaires. La puissance moyenne des HOM de la cavité à 5 cellules dans la version PERLE à 500 MeV est estimée à environ 103 W. La puissance des HOM déposée par le faisceau dans la cavité et extraite par les coupleurs HOM a également été évaluée dans le domaine temporel, en tenant compte de la dépendance au mode de remplissage de l'accélérateur. Les coupleurs du groupe d'extrémités 4DQW présentent un taux d'extraction de puissance des HOM plus élevé par rapport aux coupleurs du schéma 2P2H. En raison de la longueur de paquet longitudinal relativement courte de 3 mm prévue pour PERLE, une grande quantité de puissance HOM se propage à travers les tubes faisceau de la cavité. L'introduction d'absorbeurs de faisceau entre les tubes de la cavité a permis l'absorption d'une partie de la puissance HOM propagée, tout en restant dans les limites de flux thermique de puissance tolérables. Les analyses de chauffage RF ont montré que, dans le schéma d'amortissement 2P2H, la température maximale des parties du coupleur est abaissée avec succès sous la limite de quench dans les conditions de refroidissement par conduction simulées. Le schéma 4DQW subit un quench dans les mêmes conditions de refroidissement en raison du taux plus élevé d'absorption de puissance HOM. La sim-

ulation d'un refroidissement convectif supplémentaire à travers des canaux à hélium dans le conducteur interne du coupleur DQW a permis de réduire avec succès la température maximale en dessous de la limite de quench. Par conséquent, des canaux de refroidissement sont nécessaires pour le fonctionnement sécurisé des coupleurs niobium DQW dans l'état supraconducteur.

La première cavité cuivre à 5-cellules et à 801,58 MHz a été fabriquée à Jefferson Laboratory (JLab) aux États-Unis (cf. chap. 6) pour réaliser des mesures expérimentales de radiofréquences à faible puissance. Les écarts de fréquence des modes résonants par rapport à la forme idéale de la cavité, dus aux tolérances mécaniques et principalement à l'effet de retour élastique, ont été évalués. Des mesures de type "dumbbell" ont été effectuées sur les demi-cellules de la cavité. La cavité assemblée a été correctement réglée à la fréquence cible de 801,58 MHz. Les mesures de type "bead-pull" sur le mode fondamental indiquent qu'une planéité de champ satisfaisante de 96% a été atteinte.

Des mesures RF à faible puissance sur les cavités cuivre de type PERLE à 2-cellules et à 5-cellules à 801,58 MHz ont été réalisées à JLab (cf, chap. 7). Le spectre de fréquences des deux cavités a été analysé. Les bandes passantes des modes présentant les plus grandes déviations relatives moyennes par rapport au spectre de fréquences simulé sont celles avec l'indice longitudinal $p = 1$. Ces modes sont les plus sensibles aux erreurs dues au découpage de l'équateur des demi-cellules de la cavité. L'effet de retour élastique sur les demi-cellules pourrait également être à l'origine de la déviation de fréquence de plusieurs mégahertz détectée sur les bandes passantes des modes de la cavité mesurée. Les coupleurs HOM fabriqués ont été testés individuellement sur la cavité 2-cellules de type PERLE, et leurs orientations d'amortissement optimales ont été déterminées. Les résultats expérimentaux montrent un accord relatif avec les résultats des simulations des modes propres. Les mesures confirment que le coupleur DQW est la solution la plus efficace pour amortir les HOMs monopolaires et dipolaires. Les mesures d'amortissement des HOM ont été effectuées sur la cavité cuivre 5-cellules avec les groupes d'extrémités HOM 2P2H et 4DQW fabriqués. Des mesures de "bead-pull" ont été réalisées pour identifier les HOMs en fonction de leur profil de champ. Les valeurs simulées de Q_{ext} des modes résonants concernés sont en accord relatif avec les valeurs mesurées correspondantes. Les résultats expérimentaux montrent que les deux options d'amortissement des HOM analysées fournissent une atténuation adéquate des HOM en dessous des seuils de Q_{ext} d'instabilité BBU. De plus, le schéma d'amortissement 4DQW offre de meilleures performances pour amortir les modes confinés de la cavité, confirmant ainsi la validité de nos prédictions par la simulation.

Perspectives

Cette thèse a initié les bases pour la conception, l'optimisation, la fabrication et la validation expérimentale des performances des structures d'amortissement HOM destinés à la cavité à 5-cellules pour PERLE. Elle a englobé plusieurs disciplines, y compris

la dynamique des faisceaux, le domaine des radiofréquences et les effets combinés du chauffage radiofréquence. Les études par simulation ont abouti à la fabrication d'un prototype de cavité en cuivre depuis le départ. De plus, des prototypes de coupleurs HOM ont été fabriqués en utilisant une approche innovante combinant la technologie d'impression 3D à base de résine époxy avec une technique de cuivrage adaptée aux applications RF. Des mesures à faible puissance ont finalement été réalisées pour valider les performances des prototypes de coupleurs HOM produits. Néanmoins, certains aspects des conceptions des coupleurs HOM et des cavités peuvent être approfondis en vue de la production de coupleurs HOM en niobium devant être installés dans les cavités finales niobium 5-cellules à 801,58 MHz. Cela inclut la conception de canaux de refroidissement et d'interceptions thermiques pour atténuer le chauffage RF des coupleurs HOM en niobium et des absorbeurs de faisceau. L'accord en fréquence des filtres coupe-bande des coupleurs en niobium en raison de la contraction thermique et de l'effet multipactor doivent également être étudiés. Des études supplémentaires sont nécessaires pour limiter les déformations associées au retrait lors de l'impression 3D des coupleurs et du recouvrement ultérieur en cuivre, ainsi que pour améliorer l'homogénéité du dépôt de cuivre. Les effets de retour élastique et les tolérances mécaniques doivent être soigneusement pris en compte lors de la fabrication des cavités elliptiques en niobium. La réalisation de mesures RF à faible puissance sur une cavité soudée pour améliorer le contact RF et l'amélioration du dispositif de mesure, notamment en incluant un dispositif d'excitation HOM bipolaire capable de séparer les deux polarisations des modes dipolaires, pourrait réduire les écarts observés entre les mesures et les simulations dans le futur.